# Biophysical aspects of T cell activation

Anna Sawicka

## To cite this version:

Anna Sawicka. Biophysical aspects of T cell activation. Cellular Biology. Université Sorbonne Paris Cité, 2018. English. NNT : 2018USPCB079 . tel-02511830

HAL Id: tel-02511830
https://theses.hal.science/tel-02511830v1

Submitted on 19 Mar 2020

**Université Paris Descartes**
**Centre des Recherches Interdisciplinaires (CRI)**
**Ecole doctorale 474 "Frontières du Vivant"**

*CNRS UMR7646 Laboratoire d'Hydrodynamique de l'Ecole polytechnique (LadHyX)*
*INSERM U932 Immunité et Cancer de l'Institut Curie*

# Aspects biophysiques de l'activation des cellules T

Par Anna Sawicka

Thèse de doctorat de biophysique

Dirigée par Julien Husson et Claire Hivroz

Présentée et soutenue publiquement le 8 octobre 2018

Devant un jury composé de :

| | | | |
|---|---|---|---|
| Philippe Bousso | DR | Institut Pasteur | Rapporteur |
| Arpita Upadhyaya | Assoc. Prof. | University of Maryland | Rapportrice |
| Jérôme Delon | CR | Institut Cochin | Examinateur |
| Kheya Sengupta | DR | Université Aix-Marseille | Examinatrice |
| Claire Hivroz | DR | Institut Curie | Directrice de thèse |
| Julien Husson | Assist. Prof. | Ecole polytechnique | Directeur de thèse |

# Biophysical aspects of T-cell activation

by

## Anna Sawicka

- doctoral thesis -

in biophysics and immunology
defended on 8.10.2018 in Paris.

Jury:

| | |
|---|---|
| Arpita Upadhyaya, | rapportrice |
| Philippe Bousso, | rapporteur |
| Jérôme Delon, | examinateur |
| Kheya Sengupta, | examinatrice |
| Claire Hivroz, | directrice de thèse |
| Julien Husson, | directeur de thèse |

# Résumé

## Aspects biophysiques de l'activation des cellules T

Les cellules T jouent différents rôles dans la réponse immunitaire adaptative : elles stimulent les cellules B à produire les anticorps ; elles sécrètent les cytokines qui dirigent l'action des autres cellules immunitaires ; elles tuent les cellules du corps infectées ou porteuses de mutations ; elles assurent la mémoire immunitaire, permettant de répondre plus vite en cas de nouvelle infection avec le même pathogène. Toutes les cellules T s'activent quand elles reconnaissent leur antigène spécifique : un peptide court présenté par le complexe majeur d'histocompatibilité exprimé à la surface de la cellule présentatrice d'antigène. La liaison du récepteur de cellules T (TCR, ang. T cell receptor) à cet antigène initie la cascade de transduction de signal dans la cellule T ; ce processus mène aux modifications du cytosquelette, aux changements dans l'expression des gènes, et à la prolifération des cellules T. Récemment, il a été découvert que quand les cellules T reconnaissent l'antigène, elles poussent et tirent sur les cellules présentatrices d'antigène. Même si ces forces mécaniques ont été l'objet de recherches intenses pendant ces dernières années, leur nature et leur rôle restent toujours largement méconnus.

La caractérisation des forces générées par les cellules T était l'objectif de ma recherche doctorale. J'ai mesuré les forces avec la technique appelée "micropipette force probe", qui utilise une micropipette en verre comme un cantilever de rigidité connue. Cette technique a permis de mesurer la force maximale et la vitesse de génération des forces, et, en même temps, de capturer l'image de la morphologie des cellules de profil. J'ai trouvé que les cellules T humaines, primaires, au repos, CD4+, activées avec les anticorps contre les molécules CD3 et CD28, suivent une succession de changements de morphologie, pendant laquelle elles génèrent des forces. Cette succession était qualitativement identique pour les lymphoblastes CD4+, un modèle des cellules T activées. Ensuite, j'ai étudié cette succession d'événements dans le contexte biologique de l'activation des cellules T.

Les cellules T interagissent avec les cellules présentatrices d'antigène qui ont des propriétés mécaniques différentes. J'ai donc changé la rigidité de la micropipette utilisée comme sonde, afin de mesurer la réponse des cellules T à des cibles de rigidité différentes. J'ai trouvé que les forces générées par les cellules T sont mécanosensibles, car la vitesse de génération des forces de poussée et de traction changeaient avec la rigidité de la micropipette. Ensuite, j'ai étudié les

conditions nécessaires à la génération des forces. Les forces étaient liées au processus d'activation, car l'attachement des anticorps aux molécules CD45 n'a pas conduit à la génération des forces. Pour étudier la contribution aux forces des différents acteurs du cytosquelette d'actine, j'ai utilisé différents inhibiteurs du remaniement du cytosquelette. L'influence la plus grande sur la génération de forces a été trouvée avec SMIFH2, un inhibiteur des formines. Ces protéines jouent donc probablement un rôle important dans le processus d'activation des cellules T.

La recherche décrite dans cette thèse contribue à la compréhension des aspects biophysiques de l'activation des cellules T. Elle montre que la génération des forces est un des événements les plus précoces de l'activation des lymphocytes T, et qu'elle est modifiée par la rigidité de la cible des cellules T. Dans le futur, la recherche liant la génération des forces avec la cascade biochimique de transduction de signal induit par le TCR sera nécessaire pour décrire la base de la mécanosensibilité des cellules T. Cette recherche sera complétée par l'étude des fonctions des forces dans le processus de l'activation des lymphocytes T en conditions normales et pathologiques.

# Abstract

## Biophysical aspects of T cell activation

T cells play many roles in the adaptive immune response: they stimulate B cells for the production of antibodies; they secrete cytokines, which guide the action of other immune cells; they kill infected or mutated cells of the body; they assure the immune memory, staying ready to respond upon another infection with the same pathogen. All T cells activate when they recognise their specific antigen: a short peptide presented on the major histocompatibility complex on the surface of the antigen-presenting cell. The binding of the T cell receptor (TCR) to this antigen triggers a cascade of signalling events inside the T cell, resulting in cytoskeleton modifications, changes in the expression levels of different genes, and proliferation. One of the early responses of T cells to the antigen recognition is force generation. T cells, upon TCR triggering, push and pull on the antigen-presenting cell. Although the body of research concerning these forces has been recently growing, their nature and role is still largely unknown.

The goal of my PhD project was to characterise the pushing and pulling forces generated by T cells. I measured the forces with the micropipette force probe, which uses a glass micropipette as a cantilever of known bending stiffness. The technique allowed to measure the maximal force generated by T cells and the speed at which T cells generated forces (force rate), and, simultaneously, to track the morphology of cells as seen from the side. These experiments revealed that human primary resting CD4+ T cells, when activated with antibodies against CD3 and CD28 molecules, followed a sequence of morphology changes and force generation. This sequence was qualitatively the same for CD4+ T lymphoblasts, a model of effector T cells. The sequence was then studied in the biological context of T cell activation.

As different antigen-presenting cells, with which T cells interact in the body, were shown to have different mechanical properties, I varied the bending stiffness of the micropipette probe, to measure the response of T cells to targets of different stiffness. The force rate changed with this bending stiffness, indicating that force generation in T cell activation is a mechanosensitive process. Next, the conditions necessary for force generation were investigated. Binding to antibodies against CD45 molecule did not result in force generation, suggesting that force generation is specific to TCR triggering. To dissect the contribution of

the different components of the actin cytoskeleton to the process, T cells were treated with different cytoskeleton inhibitors. The largest influence was found with SMIFH2, an inhibitor of formins, suggesting an important role for formins in force generation in early T cell activation.

This work contributes to the understanding of the biophysical aspects of T cell activation. It shows that force generation is incorporated into the early events of the activation process, and is directly influenced by the stiffness of the T cell target. Further work is needed to link the force generation with the signalling pathways induced by TCR triggering, to explain the molecular basis of T cell mechanosensitivity. This link will open the possibility of functional studies of forces in T cell activation, to answer the open questions regarding the function of T cells in physiology and pathology of the immune system.

# Streszczenie

## Zagadnienia biofizyczne w procesie aktywacji limfocytów T

Limfocyty T (limfocyty grasicozależne) pełnią różnorodne role w układzie odporności nabytej: stymulują limfocyty B (szpikozależne) do produkcji przeciwciał; wydzielają cytokiny kierujące działaniem innych komórek układu odpornościowego; zabijają zainfekowane i zmutowane komórki własnego organizmu; są podstawą pamięci immunologicznej, pozostając w gotowości na wypadek ponownej infekcji tym samym patogenem. Wszystkie limfocyty T ulegają aktywacji (rozpoczynają działalność), gdy rozpoznają specyficzny antygen - krótki peptyd - swoim receptorem (TCR, z ang. T cell receptor). TCR łączy się z peptydem umieszczonym na kompleksie głównego układu zgodności tkankowej na powierzchni komórki prezentującej antygen. To połaczenie rozpoczyna kaskadę sygnalizacyjną wewnątrz limfocyta T, skutkującą reorganizacją cytoszkieletu, zmianami w poziomie ekspresji genów, i proliferacją limfocytów. Jedną z wczesnych odpowiedzi limfocytów na rozpoznanie antygenu są siły: limfocyty T, których TCR został związany, pchają i ciągną komórkę prezentującą antygen. Choć podjęte zostały w ostatnim czasie badania nad tymi siłami, mechanizm ich powstawania i ich rola w procesie aktywacji limfocytów T są wciąż w dużej mierze nieznane.

Celem mojego projektu doktorskiego było scharakteryzowanie pchania i ciągnięcia w procesie aktywacji limfocytów T. Do mierzenia sił użyłam szklanej mikropipety o znanej sztywności, która zgina się pod wpływem wywartej siły. Technika ta, nazwana "micropipette force probe" w naszym artykule (co do sensu można to przetłumaczyć jako dynamometr oparty na mikropipecie), pozwoliła na zmierzenie maksymalnych sił i szybkości przyrostu sił wywieranych przez limfocyty T, przy równoczesnym śledzeniu zmian w morfologii komórek. Eksperymenty te pokazały, że ludzkie limfocyty T CD4+, aktywowane przeciwciałami skierowanymi przeciwko cząsteczkom CD3 i CD28, przechodzą przez ciąg zmian morfologicznych, w które wpisane są siły. Ten ciąg zmian był jakościowo taki sam dla limfoblastów CD4+, które stanowią model aktywowanych (efektorowych) limfocytów T. W moich badaniach zajęłam się następnie wpisaniem tego ciągu zmian w szerszy kontekst biologiczny aktywacji limfocytów T.

Komórki prezentujące antygen, z którymi limfocyty T wchodzą w interakcje w trakcie inicjacji odpowiedzi immunologicznej, mają różne własności mechaniczne. Aby zbadać, jak limfocyty T reagują na obiekty o różnej sztywności, zmieniałam sztywność mikropipet użytych w eksperymentach. Szybkość przyrostu siły, zarówno dla pchania jak i dla ciągnięcia, zmieniała się wraz z tą sztywnością, co oznacza, że siły wywierane przez limfocyty T są mechanowrażliwe. Zbadałam również warunki konieczne dla pojawienia się sił. Związanie przeciwciałami cząsteczek CD45 na powierzchni limfocytów T nie doprowadziło do sekwencji pchania i ciągnięcia, co pozwala sądzić, że opisywane siły są specyficzne dla procesu aktywacji. Wpływ różnych komponentów cytoszkieletu na siły został zbadany przy użyciu chemicznych inhibitorów. Największy wpływ miał inhibitor formin (SMIFH2) wskazując na ważną rolę tych białek w generowaniu sił na początku procesu aktywacji limfocytów T.

Badania przedstawione w tej pracy doktorskiej przyczyniają się do zrozumienia biofizycznych zagadnień w procesie aktywacji limfocytów T. Pokazują, że mechaniczne siły są wpisane w początek procesu aktywacji, i że siły te zmieniają się pod wpływem sztywności obiektu, z którym oddziaływują limfocyty T. W przyszłości, badania łączące powstawanie sił z biochemiczną kaskadą sygnalizacyjną posłużą do wytłumaczenia molekularnych podstaw mechanowrażliwości limfocytów T. To połączenie pozwoli na zbadanie roli sił w procesie aktywacji limfocytów T, aby uzupełnić brakujące informacje na temat funkcjonowania limfocytów T w fizjologii i patologii układu odpornościowego.

# Acknowledgements

My gratitude goes in the first place towards my supervisors, Claire and Julien, for creating the project which - nearly miraculously - fitted all the scientific interests I could have after my Master studies, and then for all the explanations and discussions that helped me to navigate between biology and immunology on one side and physics and mechanics on the other (and for doing all of this in Paris). Special thanks for the permanent literature review.

I would say that apart from the broadening of my scientific horizons, the greatest benefit of a co-advised PhD is the opportunity to meet twice as many great people. I would like to thank the members of the two groups that I worked with, and of the neighbouring groups in the two research institutions: Lionel Guillou, Alexandra Zak, Avin Babataheri, Stéphanie Dogniaux, Michael Saitakis, Olga Chashchina, Thévy Lok, Raphaël Tomasi, Maria Gusseva, Brenna Hogan, Belen Garcia-Rodriguez, Antoine Barizien, Teja Jammalamadaka, Olivier Penalver, Gabriel Amselem, Xiu-Yu Wang, Sidney Perkins, Alexandra Hauguel, Laurence Bataille, Jean-Marie Carpier, Mélanie Chabaud, and the group leaders: Abdul Barakat and Charles Barroud. Thank you for your support, for the collaboration on various projects, and for lunches at Magnan, of course.

Thank you to the previous PhD students in both labs for the inspiration and support that I drew from their theses: Lionel Guillou, Raphaël Tomasi, Nathalie Bufi, Anita Kumari.

Thank you to Sofie Leon & Maria Molina-Calavita, and David Tareste for the follow-up provided by CRI, to Sylvie Hénon and Philippe Bousso for being my thesis committee advisors, to the FdV PhD students and to all the people that I met at this “carrefour des rencontres intéressantes”.

I would like to thank Do Chi Toai Vu, Caroline Frot, and Daniel Guy for their technical support in the daily work. And, as the administrative slalom between different institutions can be sometimes challenging, I would like to thank Elodie Kaslikowski, Lili Oliva and Tien Clabaut from CRI, Elodie Mieville-Penkova and Cassandra Mamotte from Institut Curie, Delphine Lhuillier, Thérèse Lescuyer and Audrey Lemarechal from Ecole polytechnique, Vanessa Faelens, Isabelle Lecoeur and Gislaine Montebello from Paris Descartes University, for dealing with a blond student showing up on an irregular basis.

As preparing the thesis is also a period of study, I would like to thank the instructors of the courses that I participated in: Bassam Hajj, Claire Ribrault and Livio Riboli-Sasco, David Karlin, Aurélien Baelde, and all the speakers at the EMBO Lymphocyte Antigen Receptor Signalling conference in Siena and the CellMech conference in Windermere, for providing me with masterclasses in the two disciplines that have met in my research project. I would like to thank also Kristin Sainani from the Stanford University, for her online courses on statistics and on writing.

The hand-written text on the second title page was possible thanks to my calligraphy teachers: Ewa Landowska and Basia Bodziony. I would like also to thank Ana Rewakowicz for introducing me to the basics of drawing, a skill which is very useful for a PhD student.

My family was a great team of supporters that deserves both a collective remark and individual mentions: my mum who reminded me in critical moments: „rób swoje i się nie przejmuj” (do your job and don't worry); my dad who reminded me periodically: „nie żyjesz życiem narodu” (you don't live with the life of the nation) and so that there exists life outside of the lab; my brother (older) with his programmer's work ethics; my brother (younger) who never missed a chance to be honest; and my sister whose – to put it mildly – frequent visits in Paris measured how much time I have to finish my studies. Dziękuję!

A special thank you to the donors who donated blood for research, without whom this work would not be possible.

And thank you to you, the person reading these words, for taking time to read this thesis. I hope that it proves worthy of your attention.

*To T cells*

*(I’m a big fan of your work)*

# Summary

# Introduction

The figure below shows the major object of my research: a human primary T cell, as it appears on a scanning electron microscopy image.

Figure 1. Human primary CD4+ T cell on glass coated with poly-L-lysine, imaged with scanning electron microscopy. Scale bar is 1 μm. Imaging was done by Virginie Bazin from IBPS, at Université Pierre et Marie Curie.

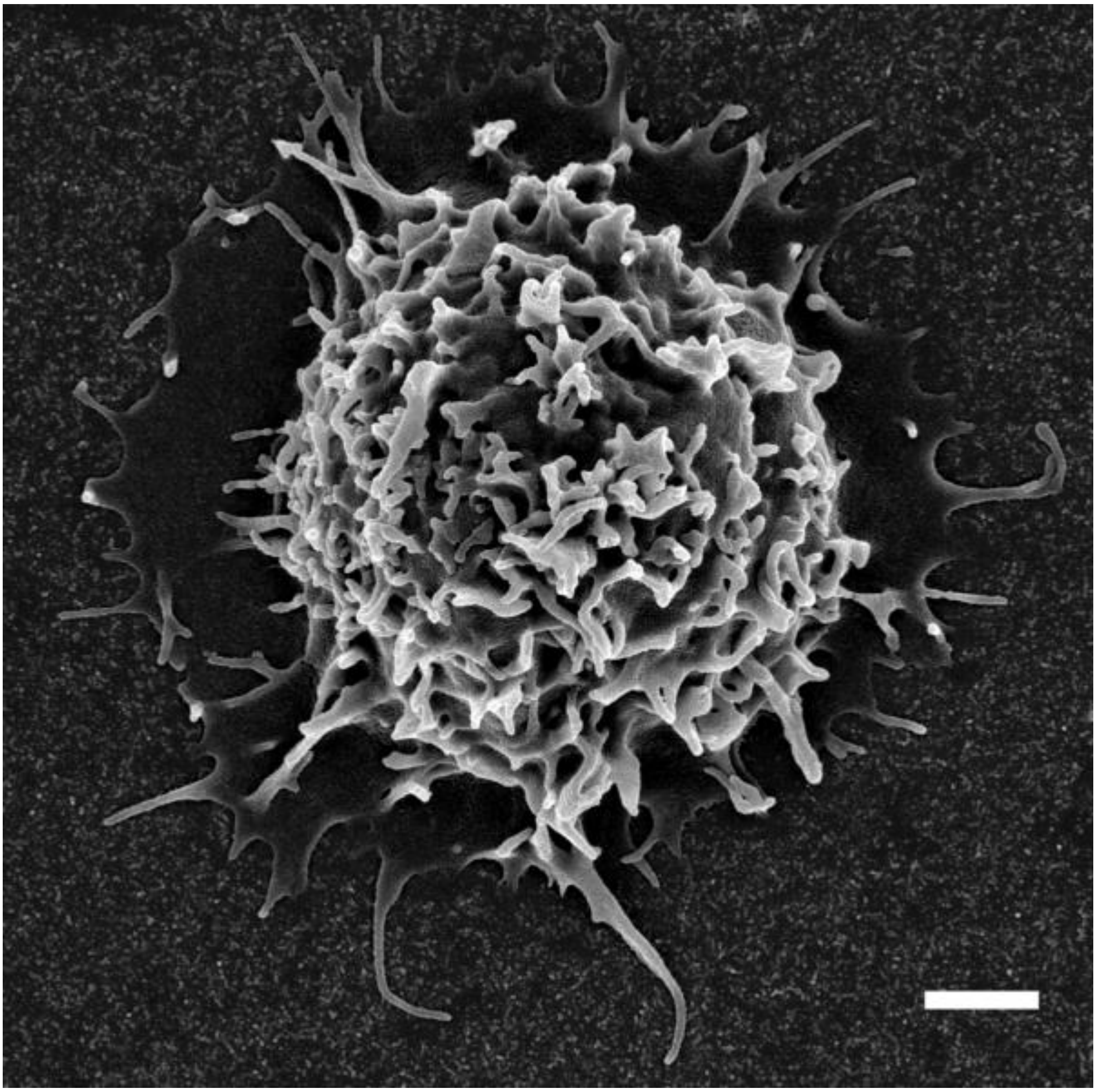

A T cell is a lymphocyte that develops in thymus. T cells form part of the adaptive immune system, as they mount a specific response when presented with an antigen specific to their particular antigen receptor.

The cell in the Figure 1 is a human CD3+CD4+ cell purified from the peripheral blood. To explain how these abbreviations for the surface markers were developed, and how these two in particular were found to identify a particular type of T cells, it is necessary to travel quite far back in time.

# 1. Historical prelude

Fifty years ago T cells were T cells already, as they were known to be these lymphocytes that develop in thymus, as opposed to B cells that were these lymphocytes that develop in bone marrow, or in bursa of Fabricius in birds (some of the early discoveries on lymphocytes – reviewed in (Good, Gabrielsen, Cooper, & Peterson, 1966) – were done in chickens; B was chosen as a reconciliating letter). Both T cells and B cells were known to circulate in the human blood, although the methods used for their purification were still under development, due to the lack of a selective marker for the two cell populations. At the end of the 1960s a curious phenomenon was observed: a population of white blood cells isolated from peripheral blood formed the so-called rosettes with sheep red blood cells (Figure 2 on the next page).

Figure 2. "Rosette-forming cells". The human white blood cells isolated from peripheral blood of healthy donors were mixed with sheep red blood cells (a few of these are indicated with black arrowheads) and imaged with a brightfield microscope. x – rosettes, o – possibly the beginning of the rosette formation, though a cell like this one would not be scored as rosette by the counting methods used at the time, * - "a polymorph" as it was called in the paper; today we would probably call it a PMN (polymorphonuclear) cell, or a granulocyte. The rosette-forming cells were – as we now know – T cells. Adapted from Fig. 2 in (Brain, Gordon, & Willetts, 1970), by permission from Wiley, copyright British Society for Immunology.

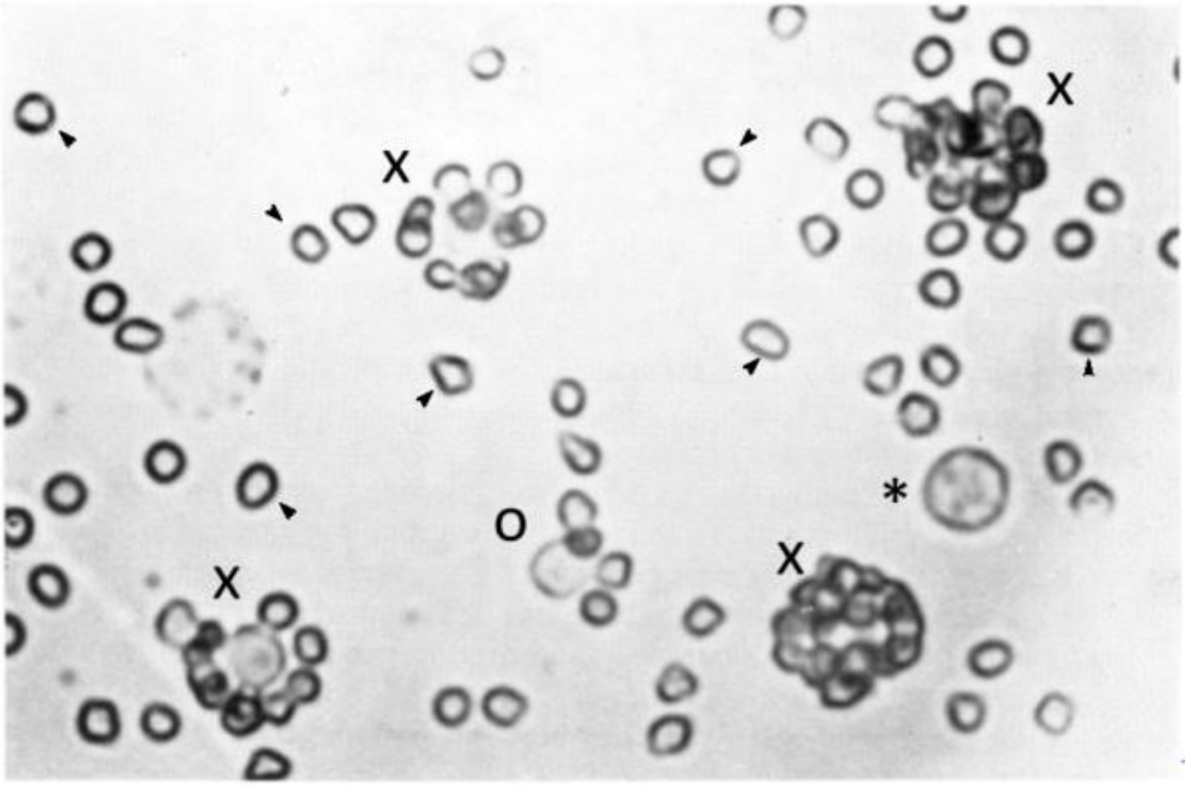

The rosette-forming cells attracted a large body of research, and soon it became clear that the formation of rosettes is a property of T cells. What is more, by modification of red blood cells with complement, a set of proteins important in the innate immune system, it was possible to select a different population of rosette-forming cells – which in turn were identified as B cells. In 1973, a method was described for purification of B cells and T cells, by the exclusion of the cells forming rosettes with particular red blood cells from the general lymphocyte population (Mendes, Tolnai, Silveira, Gilbertsen, & Metzgar, 1973) (Figure 3 on the next page).

Figure 3. Conceptual scheme of the negative selection procedure used in (Mendes et al., 1973). E: sheep red blood cells, forming rosettes with T cells, which are called "E+ cells"; HEAC: human red blood cells "activated" with rabbit serum and modified with mouse complement, forming rosettes with B cells, which are called "HEAC+ cells". During centrifugation, because of the difference in density, the rosette-forming cells sediment to the bottom layer, and are excluded from the upper, sorted population. The method relied upon the population of E+ cells and HEAC+ cells being mutually exclusive, which was the case; however, there was a population of E- HEAC- cells, therefore the HEAC- population is enriched in E+, but not exclusively E+. See details in (Mendes et al., 1973).

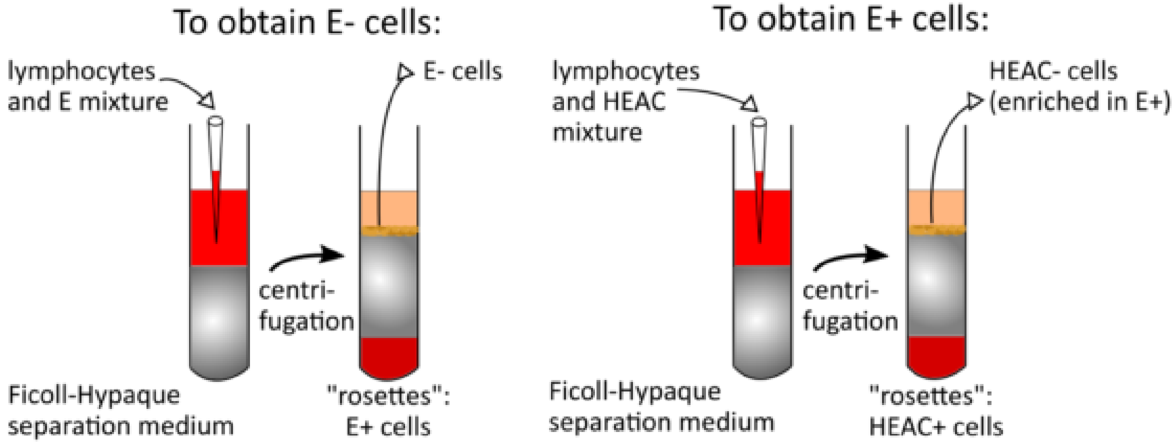

This method was used by Ellis Reinherz, Patrick Kung, Gideon Goldstein and Stuart Schlossmann, based at the Sidney Farber Cancer Institute (now known as Dana-Farber Cancer Institute) and the Ortho Pharmaceutical Company (now merged with Janssen Pharmaceuticals), to isolate human T cells from the peripheral blood. The researchers were searching for the antibodies specific for surface markers of T cells, but not B cells. They inoculated the T cells (E+ cells) into mice, collected the spleens of the mice, and fused the splenocytes with myeloma cells. This step was used to assure the "immortality" of the splenocytes in culture; the method was described in the paper (Köhler & Milstein, 1975) and allowed for the first time the production of monoclonal antibodies. An individual hybridoma – a single clone – made from the fusion of a splenocyte with a myeloma cell, could proliferate stably for a sufficiently long time (to a sufficiently large number of cells) to produce a detectable amount of antibody. For the hybridomas produced in the experiment at the Sidney Farber Cancer Institute, the supernatants from clones were assessed for reactivity against T cells and B cells, leading to the discovery of clones producing antibodies specific to the surface markers on these cells. In summary, thanks to this successful application of then cutting-edge techniques, the four researchers published a series of papers (Kung, Goldstein, Reinherz, & Schlossman, 1979; Reinherz, Kung, Goldstein, & Schlossman, 1979b, 1979a) describing the new antibodies specific for the antigens present on the surface of T cells. The antibodies were labelled OKT, with a serial number added, so OKT1, OKT2, OKT3 etc.

My focus on this one group does not mean that they were the only ones working in the field of surface markers of T cells (or, more generally, white blood cells). To the contrary, the amount of different – monoclonal – antibodies developed and published independently by different research groups led to confusion as it was not known which antibodies recognised the same surface markers, and were therefore redundant, and which distinguished different surface markers. The remedy to this problem was designed as a common enterprise, in which the participating research groups checked different antibodies "blindly", so not knowing which antigen the antibody was supposed to recognise. The project culminated in the First International Workshop on Human Leucocyte Differentiation Antigens, organised in Paris in November 1982. The major outcome of the project was the identification of 15 different antibody groups, or clusters, as the antibodies were scored with the statistical technique of cluster analysis. Each cluster was concluded to recognise the same target (the same surface marker).At that time the molecular nature of each target was not known, which is why the label “Cluster of Differentiation” (now-famous CD) was chosen. In the paper summarising the project and the workshop(Bernard & Boumsell, 1984) we can find the OKT3 and OKT4 antibodies, as belonging to, respectively, CD3 and CD4.

This description of the surface phenotype is used until now. T cells, which are the main object of my research, are recognised by the antibodies belonging to these two clusters, so they are the CD3+CD4+ cells, isolated from the peripheral blood.

In retrospect, the achievement of finding both OKT3 and OKT4 in one experiment (the second experiment described in (Kung et al., 1979)) proves a really good experimental design.

## 2. The molecular identity of the targets of CD3 and CD4.

With time, the useful CD label, apart from denoting the cluster of antibodies, started denoting also the molecule recognised with these antibodies; because by now we know the molecular targets of the antibodies grouped in CD3 and CD4.

The CD3 molecule forms part of the T cell antigen receptor (TCR) complex (Figure 4). The TCR itself consists of two chains: α and β. Each chain contains a super-variable region, unique for every T cell, that recognises the antigen. The CD3 molecule, associated with TCR, consists of four chains: two ε chains, one δ and one γ chain. The complex is completed with two ζ chains, which were renamed CD247 by the 7th International Workshop on Human Leucocyte Differentiation Antigens, as they are encoded on a different locus than the CD3 molecule. The name CD3ζ is still used in the literature; for simplicity in this thesis I call them the ζ chains. The repartition of tasks inside the complex is as follows: α and β bind the antigen, the other chains transmit the signal to the inside of the cell (this will be further described in the Early events section below).

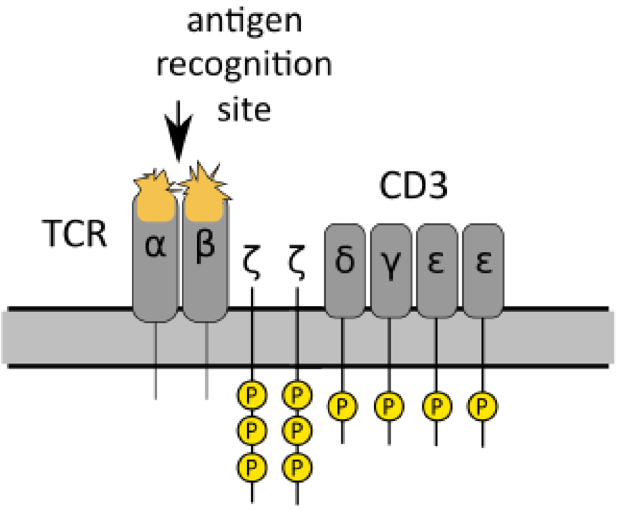

Figure 4. A schematic drawing of the TCR complex. Upon the binding of the antigen to the variable regions of the α and β chains, the immunoreceptor tyrosine-based activation motifs (ITAMs, yellow circles) can be phosphorylated and pass the signal to the inside of the cell (see the details in the Early events section below).

The above structure of the TCR complex applies to all “conventional” T cells. However, there exists also a population of the γδ T cells (reviewed in (Ferreira, 2013; Lawand, Déchanet-Merville, & Dieu-Nosjean, 2017)), in which the TCR consists of variable γ and δ chains (distinct from CD3γ and CD3δ). This population of T cells will not be discussed in this thesis, and so whenever I refer to the TCR I refer to the “conventional” αβ molecule, and whenever I refer to T cells I refer to the “conventional” T cells bearing this αβ TCR.

The CD4 molecule binds to the major histocompatibility complex (MHC) molecule on the surface of the opposing cell (Figure 5). The interactions shown in Figure 5 picture the way in which T cells recognise the antigen. The antigen that can be recognised by T cells is a short peptide presented on top of the MHC molecule. These particular molecular interactions provide a double signal to the T cell: MHC molecule denotes “self” (a cell from the same body), and the antigen serves as the control of what the “self” has met with. If the cell is healthy, it bears only “self”, "normal" peptides; if the cell is infected, or mutated, or has ingested pathogens, the MHC molecule can present the “non-self” peptides, cut out of the proteins of the pathogens, or out of the mutated proteins of this particular cell. Through this mechanism T cells are able to detect the cells that contain foreign, potentially dangerous proteins – examples include viral, bacterial, or mutated proteins. The mechanism also results in T cells interacting with other cells of their own body, and not directly with pathogens.

Figure 5. A schematic drawing of the 3D structure of the connection between T cell receptor (TCR), and major histocompatibility complex (MHC) molecule presenting the antigen (a short peptide, marked in red). The associated molecules on T cell surface, CD8 and CD4, are also shown. The illustration is based on a compilation of the solved crystal structures of the extracellular parts of the molecules. Source of the image: RCSB PDB Molecule of the Month by David S. Goodsell, doi: 10.2210/rcsb_pdb/mom_2005_3, CC-BY-4.0 license.

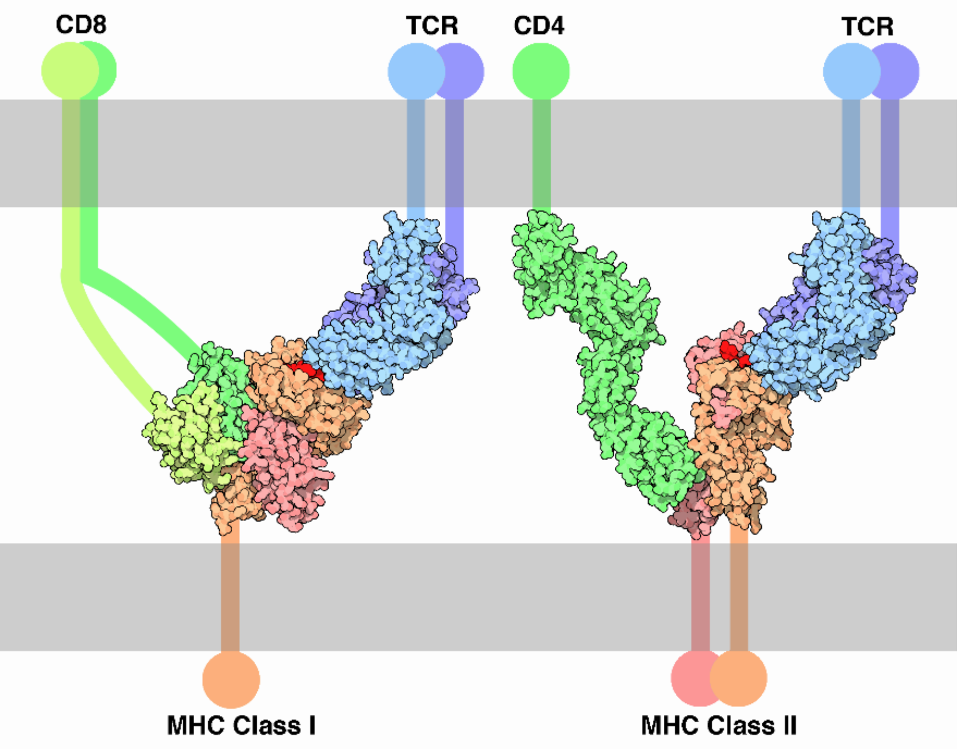

The two major T cell subpopulations: CD4+ T cells and CD8+ T cells, recognise two different classes of MHCs, as the CD4 and CD8 molecules bind, respectively, to MHC class II and MHC class I molecules (Figure 5). These molecular interactions have a direct influence on the major functions of the two subpopulations.

# 3. Functions of T cells

CD8+ T cells are cytotoxic T cells, which means that they are able to kill the cell with which they are interacting. More precisely, during the interaction that lasts about 30 minutes, a cytotoxic T cell triggers the mechanism that leads to the apoptosis of the target cell. As CD8 binds to the MHC class I molecule, which is expressed by virtually all cells of the body (except for the red blood cells), cytotoxic T cells are able to recognise their specific antigen presented by any cell of the body. This signal, combined with other molecular information, can lead to the cytotoxic activity of T cells. Cytotoxic T cells are the key component of the immunity against viruses, killing the infected cells to prevent the spread of the virus; they also have the capability to kill the cancer cells. As in my research project we decided to focus on the CD4+ T cells, the cytotoxic T cells will not be deeply discussed in this thesis; however, because of the similarities in their phenotype and development, I will discuss some of the results obtained with CD8+ T cells, to gather more information on the CD4+ T cells.

CD4+ T cells are helper T cells, which means that they help in the development and function of other cells of the immune system. This stems directly from the fact that CD4 molecule binds to MHC class II molecule, which is expressed only by a set of the cells of the body, such as dendritic cells, macrophages, B cells and, in particular conditions, also by T cells themselves. As a result, CD4+ T cells interact primarily with other cells of the immune system. CD4+ T cells perform a number of functions in the body. The "oldest" (first-characterised) two subpopulations of helper T cells were named Th1 and Th2 in 1986 (Mosmann, Cherwinski, Bond, Giedlin, & Coffman, 1986), and they were described to help the cell-mediated immunity, and antibody-mediated immunity, respectively. With time, new functional helper T cell subpopulations were identified, including Th17, Th9 and Th22. Numbers for these populations are the same as the number of the interleukin that is produced by this subset of T cells, and that identifies them. The follicular helper T cells, or Tfh, are named after the place where they perform their function: the follicles, or the germinal centres in lymph nodes, where plasma cells (activated B cells) produce antibodies. The regulatory T cells, or Treg, are also CD4+ T cells; they differ from all the above subtypes in that they slow down, or block, the immune response. A brief summary of the functions of these different subtypes of CD4+ T cells is shown in Table 1 on the next page.

Table 1. Different functional CD4+ T cell populations. Information in the table comes from the reviews (Wan & Flavell, 2009; Zhu & Paul, 2008) and the "Effector T cell markers" poster available at
http://www.abcam.com/primary-antibodies/effector-t-cell-markers
(accessed on 2018-06-04), with its list of references.

| Cell population | Function | Identified by (characteristic markers) |
|---|---|---|
| Th1 | Direct the immune response towards the cell-mediated immunity, clear the infections from intracellular pathogens. | Production of interferon γ and interleukin 2, expression of T-bet transcription factor |
| Th2 | Direct the immune response towards the antibody-mediated immunity, clear the infections from extracellular pathogens. | Production of interleukin 4, expression of GATA3 transcription factor |
| Th17 | These three subpopulations were characterised in specific cases in relation to the major functional split between Th1 and Th2 subpopulations. See examples in the references: (Bhaumik & Basu, 2017; Hirose, Iwata, Tamachi, & Nakajima, 2017; Jager, Dardalhon, Sobel, Bettelli, & Kuchroo, 2009). | Production of interleukin 17 |
| Th9 | | Production of interleukin 9 |
| Th22 | | Production of interleukin 22 |
| Tfh | Interact for long-term with B cells in follicles (germinal centres) in lymph nodes. | Place of function, production of interleukin 21 |
| Treg | Sustain immunotolerance by the suppression of self-reacting cells; stop or reduce inflammation. | CD25 surface marker, expression of FOXP3 transcription factor |

How do all these subtypes of CD4+ T cells develop? It is generally believed that a naive CD4+ T cell will develop into one or another subtype depending on the microenvironment in which it is during its activation. The process of T cell activation is triggered with the specific binding of TCR and CD4 molecule to MHC type II molecule bearing the cognate peptide; this moment is also called the antigen recognition.

# 4. Antigen-presenting cell, immunological synapse, and T cell activation

Most of the functions of T cells are linked to the antigen recognition. As this process is based on the binding of the TCR to the peptide-bearing MHC molecules (peptide-MHCs), in all cases it requires a cell partner to the T cell. This cell partner, any cell that holds a MHC with the peptide that can be recognised by the T cell, is labelled antigen-presenting cell (APC). The antigen recognition sets off the T cell activation process, which will lead to the T cell performing its function. Last major term to introduce in here is the immunological synapse, the functional interface between the T cell and the antigen-presenting cell, as T cell activation requires a close contact between the cells.

The notion of the immunological synapse began to be used widely in the scientific literature at the end of 1990s (Figure 6C), with the advent of the microscopy techniques allowing to image the protein organisation in this tight connection between a T cell and an APC. The two "citation classics" in the area of studies of the immunological synapse – (Monks, Freiberg, Kupfer, Sciaky, & Kupfer, 1998), 1685 citations and (Grakoui et al., 1999), 2051 citations, Dimensions database, checked on 30.06.2018 – illustrate the two approaches to this fluorescence imaging. The first study reports the imaging of T cell-APC conjugates with confocal fluorescence imaging, which allows to reconstruct the image of the immunological synapse from stacks of images (Figure 6A). The second one reports the imaging of T cells forming the synapse with a supported lipid bilayer, a planar membrane with the activating molecules embedded in it. As the lipid bilayer is formed on the glass coverslip, the plane of the synapse can be directly watched with the microscope (Figure 6B).

Figure 6. The birth and the career of the notion "immunological synapse". A and B. Fluorescence microscopy images of the immunological synapse reproduced from the "citation classics": A. (Monks et al., 1998), Fig. 3, reproduced by permission from Springer Nature; B. (Grakoui et al., 1999), Fig. 2, reproduced by permission from AAAS. The staining was done with antibodies recognising molecules on the T cell surface (A) and with molecules conjugated with fluorescence probes in the supported lipid bilayers with which T cells were interacting (B); colour code in both images refers to the same molecule pairs, as CD3 molecule forms part of the TCR complex which binds to peptide-MHC, and LFA-1 binds to ICAM-1. C. Number of papers in the PubMed database containing the phrase "immunological synapse" or "immune synapse" in the abstract or in the title. The search was performed on 21.06.2018. The beginning of the chart coincides perfectly with the two citation classics mentioned. However, the chart leaves out a substantial proportion of research on the interactions between T cells and APCs, and serves therefore just for illustrative purposes. In particular I note the following: one paper from 1998 on the chart is (Jurlander, 1998), not (Monks et al., 1998); the notion "immunological synapse" was used at least as early as (Paul & Seder, 1994); the analogy between the T cell-APC connection and the neuronal synapse was drawn at least as early as (Norcross, 1984) (from the reviews (Delon & Germain, 2000; Ortega-Carrion & Vicente-Manzanares, 2016), and Claire Hivroz, personal communication).

Figure 6 is shown on the next page.

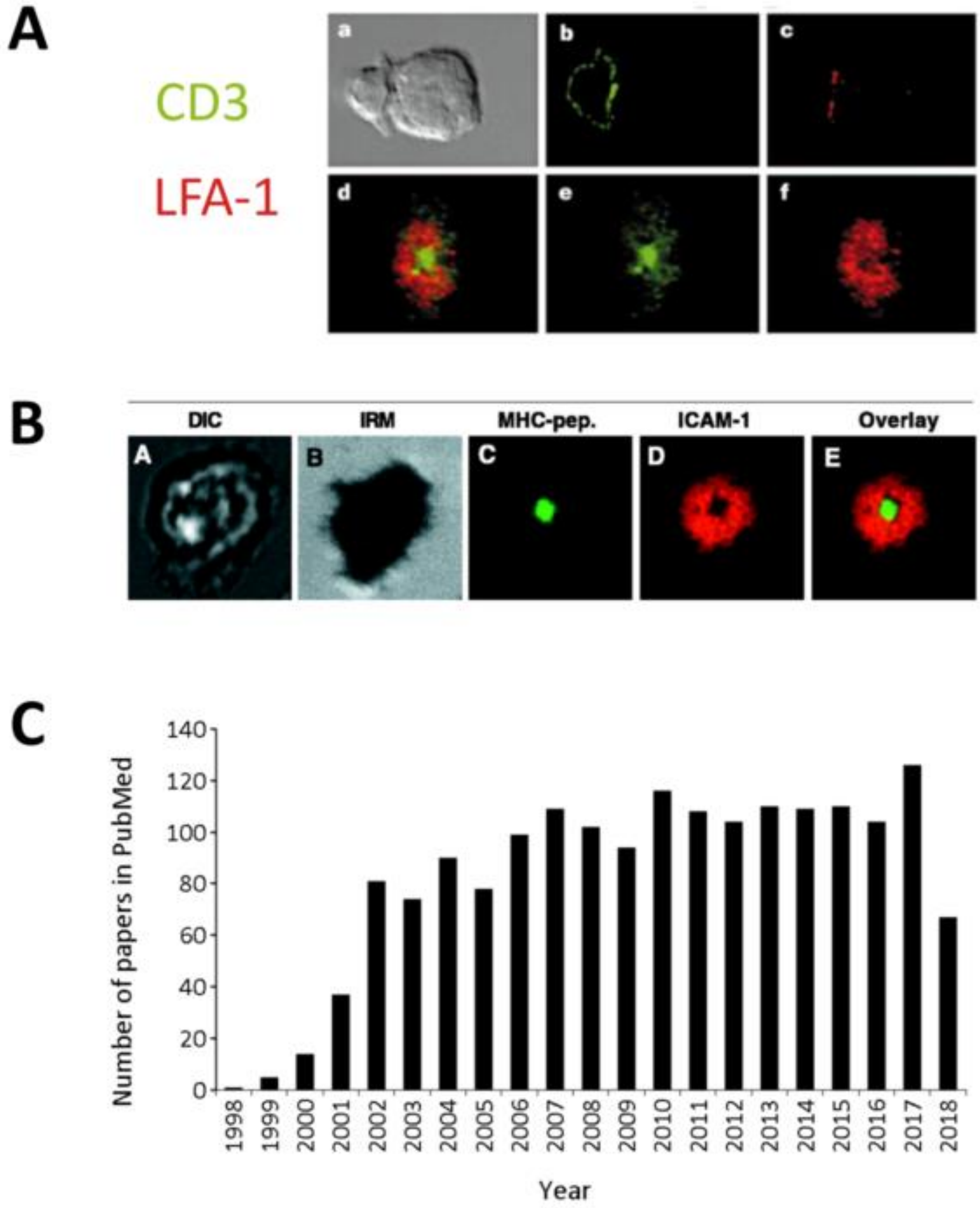

Figure 6. See legend on the previous page.

The three terms (T cell activation, antigen-presenting cell and immunological synapse) have been applied to a variety of biological processes involving T cells, both in the in vivo and in vitro studies. Here I would like to specify in which context I will use these terms in my thesis.

My study focused on human CD4+ T cells isolated from the peripheral blood. The CD4+ T cells circulating in the blood are the naive cells, which just finished their development in thymus and entered the bloodstream, or the memory cells, which were left after the infection endured by the organism, or the regulatory cells (the smallest population of the three). Together in this thesis I will call them the resting CD4+ T cells. They circulate in the body in the search for the cognate antigen. By T cell activation I mean the process of turning a resting CD4+ T cell into an effector one, so into one of the functional subtypes listed above (Table 1). This process starts in the lymph node, where resting CD4+ T cells interact with dendritic cells that have scanned the neighbouring tissue and present the antigens found there (Figure 7 on the next page). These dendritic cells are the antigen-presenting cells that I have in mind in my study, although we mimicked them with a much simpler model – a bead coated with antibodies against CD3 and CD28 molecules (see details below and in Chapter 2). The interaction between a resting CD4+ T cell and a cognate dendritic cell can last for hours, or even days; however, this stable connection needs to be formed within minutes, as T cells crawl through the dense environment in the lymph node (Bohineust, Garcia, Beuneu, Lemaître, & Bousso, 2018). The formation of this connection is the immunological synapse that I refer to.

Figure 7. Formation of immunological synapses in mice lymph nodes. OT-I T cells expressing GFP were imaged inside lymph nodes with the two-photon microscopy. A. Two frames from the recorded movie, showing high motility of T cells in lymph node when no specific peptide is presented (left), and the complete arrest of T cells when the high affinity peptide is presented (N4, right). Intermediate frames show slower migration of T cells when the peptides of lower affinity are presented. B. The tracks of individual cells were colour-coded and superimposed on one frame of the movie. Reproduced from Fig. 2D and Movie S3 in (Moreau et al., 2012), by permission from Elsevier.

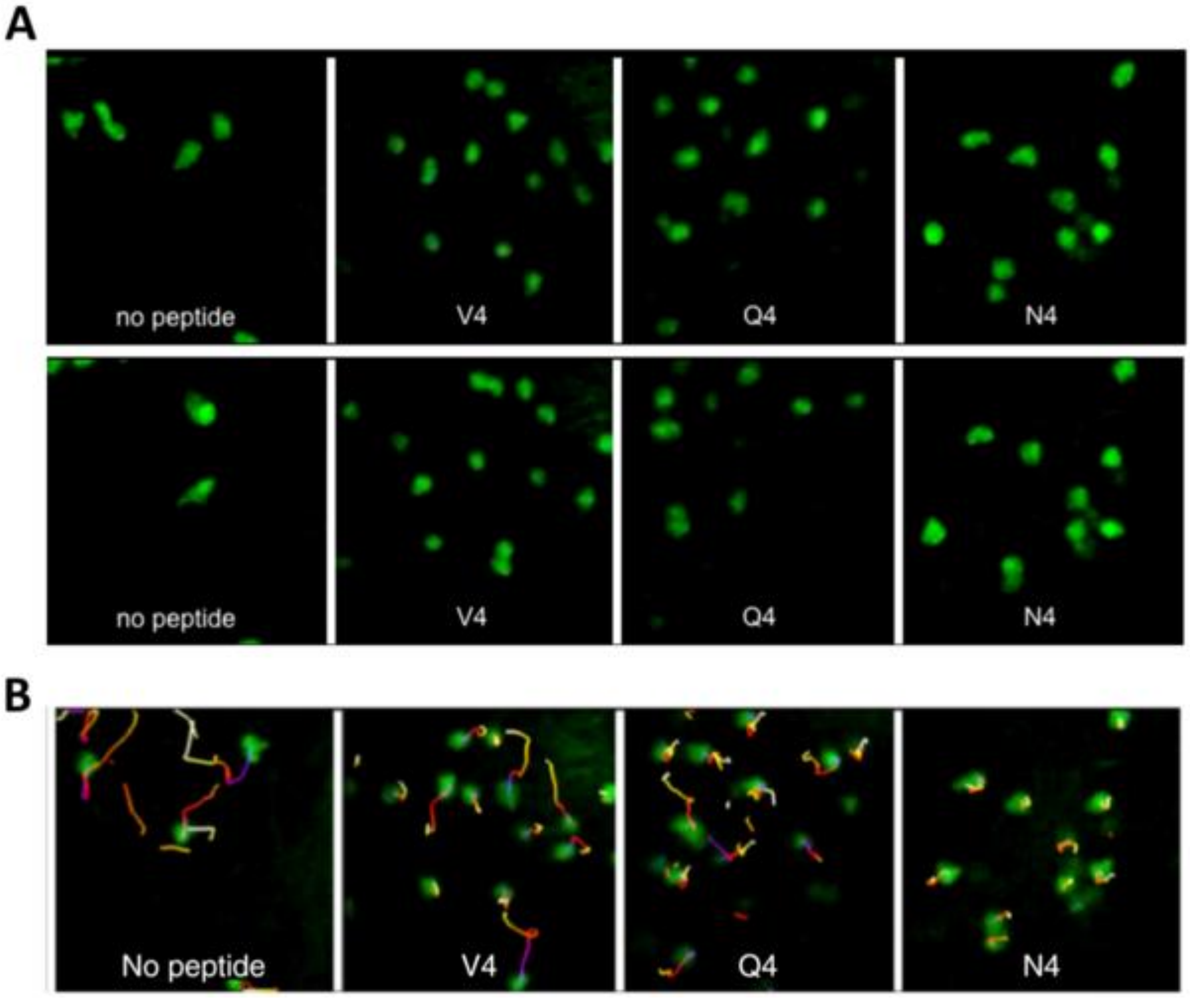

## 5. Early events in T cell activation: models of TCR triggering

Once the antigen is recognised by the TCR, a cascade of events happens inside the T cell. The precise mechanism of action of the TCR complex – the passing of the signal from the antigen binding to the whole cascade afterwards, called also the TCR triggering – is still largely unknown (reviewed in (Courtney, Lo, & Weiss, 2018; Lever, Maini, Van Der Merwe,

& Dushek, 2014; Malissen & Bongrand, 2015)). This mechanism has some remarkable properties.

On the one hand, the mechanism of TCR triggering is extremely precise, in that a TCR responding to a peptide-MHC molecule is able to distinguish minute changes in this peptide. A single amino-acid substitution in the presented peptide led to different functional responses of T cells, like cytokine production or proliferation (Allen, Matsueda, Haber, & Unanue, 1985; Evavold & Allen, 1991). The outcome of a substitution can be binary (activation to non-activation), when a substitution "switches off" the response; or gradual (more potent antigen to a less potent one), when a substitution changes the intensity of T cell response to the same concentration of the antigen. By scanning a variety of peptides, the researchers in a recent study (Lever, Lim, Kruger, et al., 2016) changed the dissociation constant of the particular TCR-peptide-MHC complex over six orders of magnitude. When IFNγ production by T cells was measured as dose-response to these different peptide-MHC molecules, the threshold value (value for which detectable amounts of IFNγ were produced) changed between 0,01 and 100 μg/ml of the peptide-MHC concentration. This range of the chemical properties of the TCR-peptide-MHC bond, and the T cell responses, was achieved only with single and double amino-acid substitutions in the activating peptide.

On the other hand, the mechanism of TCR triggering is versatile, because when the antigen recognition part of the TCR complex was artificially replaced with other molecules of different properties, the complex still retained its function of triggering the T cell response. Thus, it seems that the mechanism of the signal transmission does not depend on the particular properties of the α and β chains of TCR. CAR T cells (Chimeric Antigen Receptor) bear a receptor composed of a single, variable chain of an antibody linked to the transmembrane and intracellular domains of signalling molecules of T cells, in the simplest case they are the ζ chains. This chimeric receptor can trigger the T cell response, as CAR T cells have been shown to be active in vitro and in vivo, and have been recently approved for the therapy of lymphoblastic leukaemia and non-Hodgkin lymphomas (reviewed in (Sadelain, Brentjens, & Rivière, 2009; Salter, Pont, & Riddell, 2018)). Even more surprisingly, in a recent in vitro study (Taylor, Husain, Gartner, Mayor, & Vale, 2017), single-strand DNA molecules, chemically linked to the transmembrane and cytoplasmic part of ζ chains, were capable of triggering the functional outcomes of T cell activation (like the translocation of phosphorylated ERK to nucleus), when bound to a complementary DNA strain. This chimeric DNA-ζ chain receptor retained some of the precision of the TCR, as it was able to trigger different responses to single strand DNA molecules differing by single base in their sequence.

On top of (thus-defined) versatility and precision, TCR triggering is sensitive, in that T cells were shown in vitro to respond to a few cognate peptide-MHC complexes per cell (Huang et al., 2013; Irvine, Purbhoo, Krogsgaard, & Davis, 2002).

I did not address experimentally the question of the molecular mechanism of TCR triggering; still, this question is relevant to my work, as TCR triggering results also in force generation (see below in the section Force generation, and the results in Chapter 3). I describe below two of the proposed mechanisms of TCR triggering, to introduce the main molecular players that are important for the onset of the signalling cascade inside T cells, and thus also for the force generation in T cell activation.

Lck is a membrane-bound protein tyrosine kinase that can associate itself with the cytoplasmic part of the CD4 (or CD8) molecule. When the TCR binds to the peptide-MHC, CD4 stabilizes this link by binding to the MHC molecule (Figure 5). This association brings Lck close to the cytoplasmic tails of the TCR complex. The immunoreceptor tyrosine-based activation motifs (ITAMs)in these tails and ZAP70 (zeta-chain-associated protein kinase of 70 kDa), which is recruited to phosphorylated ITAMs, can be then phosphorylated by Lck. The kinase activity of Lck was incorporated into the kinetic proofreading model of TCR triggering (first proposed in (McKeithan, 1995)), in which the binding of TCR to specific peptide-MHC molecule initiates changes in the TCR complex (in this case exemplified by the phosphorylation of ITAMs and ZAP70). The TCR reaches the signalling-competent state only after these modifications are finished and only then the signalling cascade is started. Thus, the optimal T cell activation is reached only if the TCR is bound to peptide-MHC for a long enough time, and the activating peptides are those that allow these prolonged molecular interactions.

It should be noted that resting T cells circulating in the body constantly interact with "self" peptide-MHCs. Thus, there is a basal level of phosphorylation of ITAMs, called also "tonic signalling" (Hochweller et al., 2010). The above phosphorylation of ITAMs and ZAP70 leading to T cell activation can be described as a multi-step increase rather than a rapid switch from "off" to "on" state (Figure 8 on the next page, see also the review (Grossman & Paul, 2015)).

Figure 8. The multi-step activation and tuning of the activity of Lck and ZAP70. The active forms of the proteins perform the functions described in the main text. Reproduced from Fig. 2 in (Gaud, Lesourne, & Love, 2018), by permission from Springer Nature.

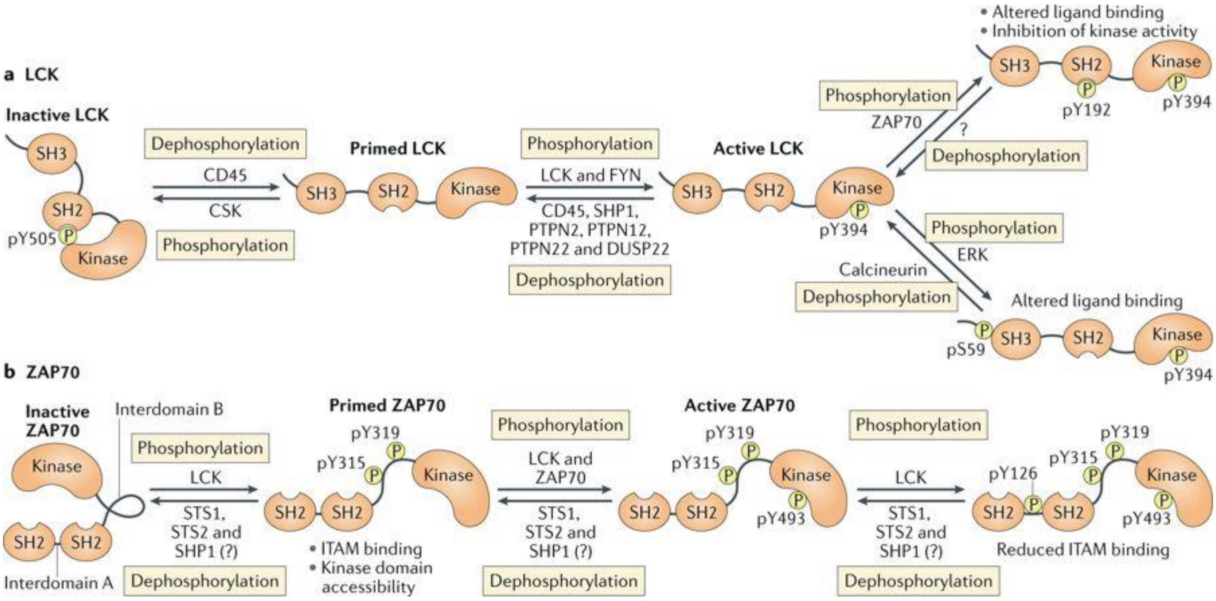

CD45 is a transmembrane protein, with a large extracellular domain and a phosphatase cytoplasmic domain. It is essential for T cell activation as it primes Lck (Figure 8). However, CD45 dephosphorylates ITAMs and ZAP70 and can be thus a negative regulator of the early signalling cascade in T cell activation. The properties of CD45 have been incorporated in the kinetic segregation model of TCR triggering (reviewed in (Davis & van der Merwe, 2006)), in which the binding of TCRs to the peptide-MHC molecules creates “close contacts” (Chang, Fernandes, Ganzinger, Lee et al., 2016), which exclude CD45 and allow Lck to phosphorylate ITAMs and ZAP70. The exclusion is based on the size of the molecules: the extracellular part of CD45 is larger than the whole TCR-peptide-MHC complex, which measures around 15 nm. Thus, when sufficient number of TCR-peptide-MHC complexes is formed, locally the membranes of T cell and antigen-presenting cell are in close contact and CD45 is excluded (Figure 9 on the next page).

Figure 9. The formation of the immunological synapse driven by the relative size of the extracellular domains of the receptors engaged on the T cell and the antigen-presenting cell. Initially, the small TCR complex is buried within large extracellular domains of CD43 and CD45. The initial engagement of integrins, such as LFA-1, allows the closer apposition of the membranes, which facilitates the formation of the TCR-peptide-MHC complexes. In the kinetic segregation model of TCR triggering, these clusters of TCR-peptide-MHC complexes allow the phosphorylation of ITAMs and ZAP70 by Lck. Lck, associated with CD4 molecule, is not included in this particular figure. Reproduced from Fig. 1 in (Delon & Germain, 2000), by permission from Elsevier.

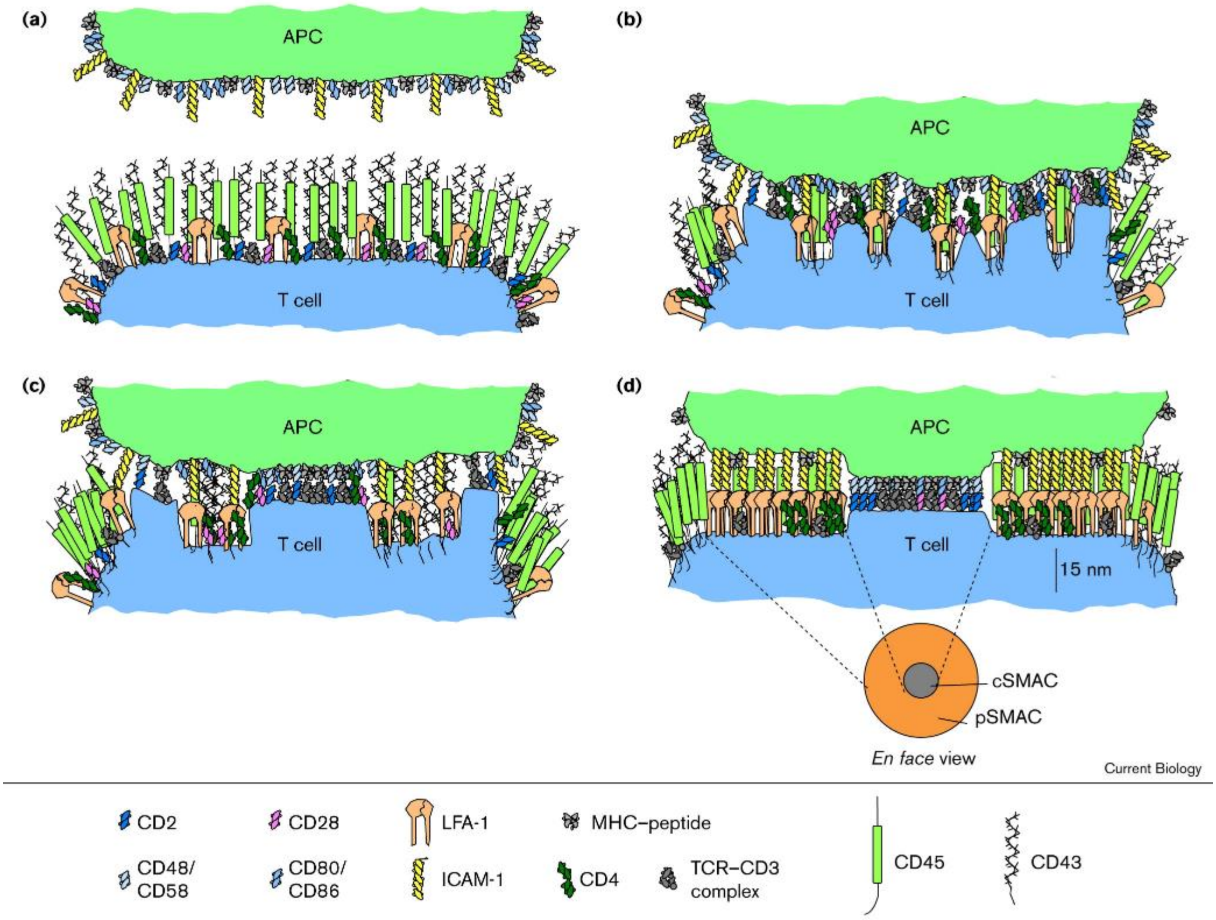

Current Biology

The molecular interplay between TCR complex, Lck, CD45, and the associated proteins, leads in the activating conditions to the signalling cascade inside T cells (Figure 10 on the next page).

Figure 10. Main signalling pathways downstream of the TCR complex. In this Introduction I focus on the pathways leading to calcium release from the endoplasmic reticulum (ER), and to the reorganisation of actin cytoskeleton (Actin polymerization). Reproduced from Fig. 1 in (Gaud et al., 2018), by permission from Springer Nature.

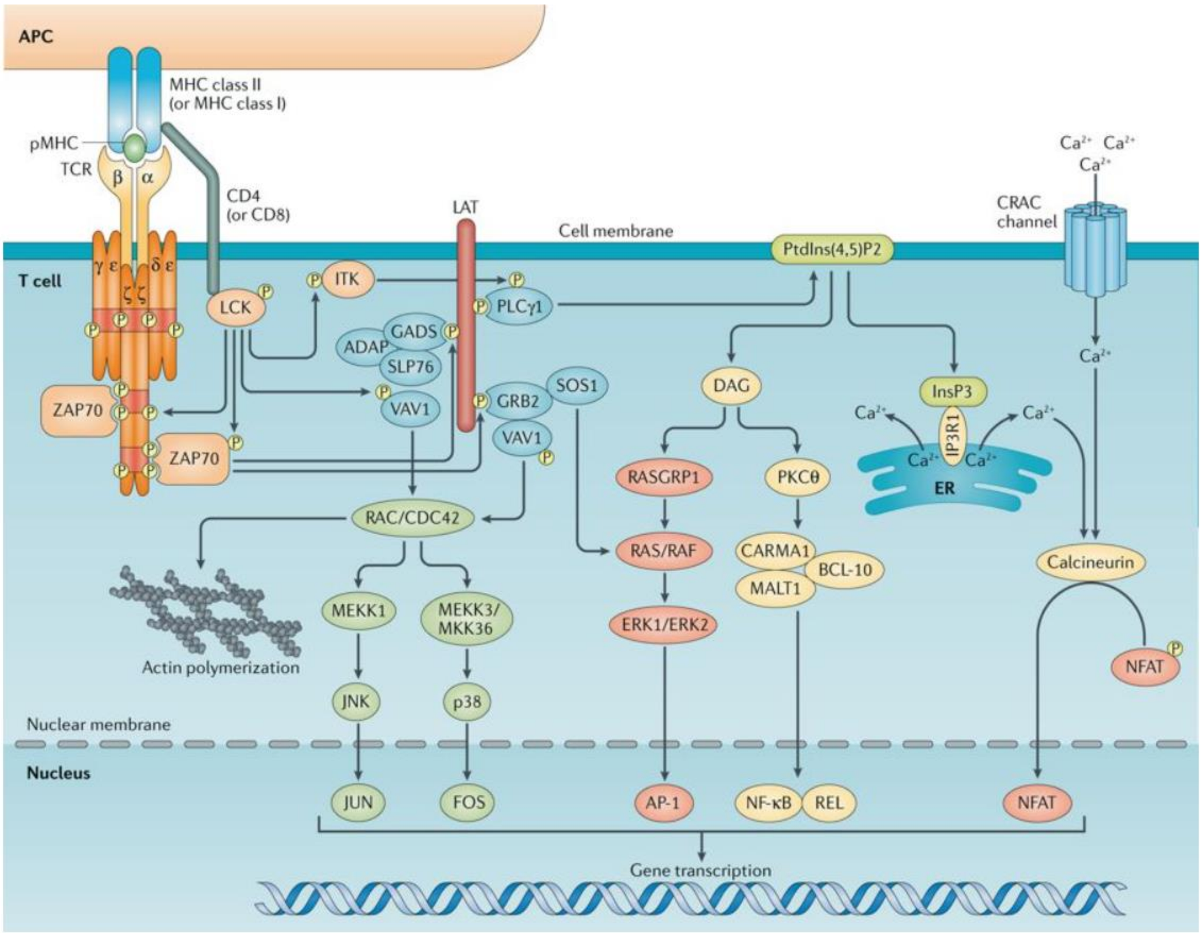

# 6. Early events in T cell activation: the signalling cascade

The activation (phosphorylation) of ZAP70 by Lck is an important step in the early signalling cascade, as ZAP70 phosphorylates LAT (linker for T cell activation) protein. LAT phosphorylation was detected a few seconds after the TCR engagement (Huse, Klein et al., 2006). LAT is a scaffolding protein, it forms the complexes known also as LAT signalosomes. From the proteins recruited to LAT several signalling pathways branch off (reviewed in (Brownlie & Zamoyska, 2013)). One of them, which requires the activity of PLCγ1, leads to the opening of the calcium channels in the membrane of the endoplasmic reticulum. Calcium ions concentration in the cytoplasm increases, leading to the opening of the calcium channels in the cell membrane (a process known as store-operated $Ca^{2+}$ entry, SOCE). This results in a sharp increase of the cytoplasm concentration of calcium ions – calcium peak – detected on the whole-cell level typically 30-40 s after TCR engagement. Calcium is an important second messenger in T cells, the calcium peak leads to the translocation to the nucleus of transcription factors such as NFAT (nuclear factor of activated T cells).

Phosphorylated LAT can bind SLP76 (SH2 domain-containing leukocyte protein of 76 kDa), an important adaptor protein. When SLP76 gets phosphorylated by ZAP70, it recruits Vav1, a guanidine-exchanging factor for small GTPases involved in the regulation of actin polymerisation (see below in the section The role of cytoskeleton). Through the ADAP molecule, there is a link between SLP76 and the integrins, such as LFA-1, which, together with the ongoing actin polymerisation, promotes the open (active) conformation of the integrins, and a sustained adhesion of T cell to the antigen-presenting cell.

For LFA-1 it has been shown that its extracellular domain gets modified due to the signalling pathways downstream of TCR (inside-out signalling), but also that its binding to its ligand on the surface of the antigen-presenting cell (ICAM-1) provides additional, modifying signals to the intracellular network of proteins (outside-in signalling, (H. Wang, Wei, Bismuth, & Rudd, 2009)). Another protein providing these additional, modifying signals, is the major costimulatory molecule on the surface of T cells, CD28 (for a review of costimulation signals provided to T cells see (L. Chen & Flies, 2013)).

CD28 binds to CD80 or CD86 on the surface of APC. This binding enhances the TCR signalling (leading to larger cytokine production, or to the strong activation of T cells with otherwise weak antigens), and provides the “survival signal”, as T cells on which CD28 was engaged, proliferate better after the TCR triggering. The discovery of coinhibitory molecules, like CTLA-4, which competes with CD28 for the binding to CD80/CD86, but has an inhibitory effect on T cell activation; or PD-1, binding to PDL-1 on the surface of APCs, led to the development of new type of cancer therapy, called the anti-checkpoint therapy. The coinhibitory molecules like CTLA-4 or PD-1 are “checkpoints” on the pathway of T cell activation, as they block the effector functions of T cells. Blocking these checkpoints enhances T cell activity, causing them to mount the response against cancer. Together with CAR T cells, anti-checkpoint therapies form the cancer immunotherapies (reviewed in (Fesnak, June, & Levine, 2016)).

CD28 provides an additional link to the cytoskeleton modifications in T cell activation, as its cytoplasmic tail recruits Vav1, and filamin A. The signalling pathways leading to the cytoskeleton reorganisation were shown to play an important role in T cell activation.

# 7. The role of cytoskeleton in early T cell activation

Cytoskeleton is a set of proteins that stabilise and dynamically change the shape of a cell, and its internal structure. It is classically divided into the three major components, based on the diameter of the filaments composing it: actin (or actomyosin), intermediate filaments, and microtubules. Intermediate filaments are the most various family as they can be composed of proteins such as vimentin, desmin, keratins, or nuclear lamins (reviewed in (Lowery, Kuczmarski, Herrmann, & Goldman, 2015)). In this introduction I focus on actin filaments and microtubules, as these two have been shown to play important roles in T cell activation.

Actin filaments (called also microfilaments, when they need to be distinguished from the actin filaments in the contractile units of muscle cells, which have a different structure) form a constantly reorganising network in all eukaryotic cells. The importance of actin dynamics in T cell activation was recognised early on through two main lines of evidence:

1) from the basic studies in different models of T cell activation (reviewed in (Dustin & Cooper, 2000)); for example it was observed that addition of actin polymerisation inhibitors aborted the calcium signalling, destabilised the contact between T cells and APCs, and decreased the cytokine production by T cells (Delon, Bercovici, Liblau, & Trautmann, 1998; Valitutti, Dessing, Aktories, Gallati, & Lanzavecchia, 1995); the involvement of cytoskeleton in the early events in T cell activation was also inferred from the observation that engaged receptors travel over the long distances in the membrane of activating T cells (Wülfing & Davis, 1998);
2) from the studies explaining the molecular basis of the Wiskott-Aldrich syndrome (WAS). WAS patients suffer from recurrent infections, prolonged bleeding due to low platelet counts, and are at a higher risk of cancers, especially blood cancers, and of autoimmune diseases. The syndrome is caused by mutations in the Wiskott-Aldrich syndrome protein (WASp), one of the proteins regulating the actin filaments nucleation through its interaction with the Arp 2/3 complex (A. S. Kim, Kakalis, Abdul-Manan, Liu, & Rosen,

2000). WASp was shown to be present near TCRs in the immunological synapse (Barda-Saad et al., 2005).

The signalling pathways leading from the TCR engagement to the actin polymerisation and the modifications of the actin network has been studied extensively (reviewed in (Acuto & Cantrell, 2000; Billadeau, Nolz, & Gomez, 2007; Comrie & Burkhardt, 2016)). The overarching pattern of actin dynamics in the plane of the immunological synapse consists of polymerisation at the periphery and the depolymerisation in the centre of the synapse, which creates the centripetal flow of actin. This flow is enabled and guided by different molecular players. I provide below a brief summary of the role of different actin-binding proteins in the early events in T cell activation.

Arp2/3 (the molecular complex containing actin-related proteins 2 and 3) is responsible for the branching of the actin filaments. In the plane of the immunological synapse, Arp2/3 promotes spreading of T cells, formation of signalling microclusters in T cell membrane, and stable contact between T cells and APC. These different functions and their spatial segregation are allowed by the interaction of Arp2/3 with different actin nucleation promoting factors such as WASp or WAVE2. These proteins are in turn activated by the small GTPases, CDC42 and Rac1, and their guanidine exchange factor (GEF) Vav1, which is downstream of SLP76 in the early signalling cascade. When the contact between a T cell and an APC is formed, WAVE2 is thought to stimulate the rapid actin polymerisation at the periphery of the immunological synapse (called dSMAC, or distal supra-molecular activation cluster, Figure 11 on the next page), whereas WASp nucleates the small actin patches (“actin foci”, (Kumari et al., 2015)) closer to the centre of the synapse (between the dSMAC and the peripheral SMAC, or pSMAC).

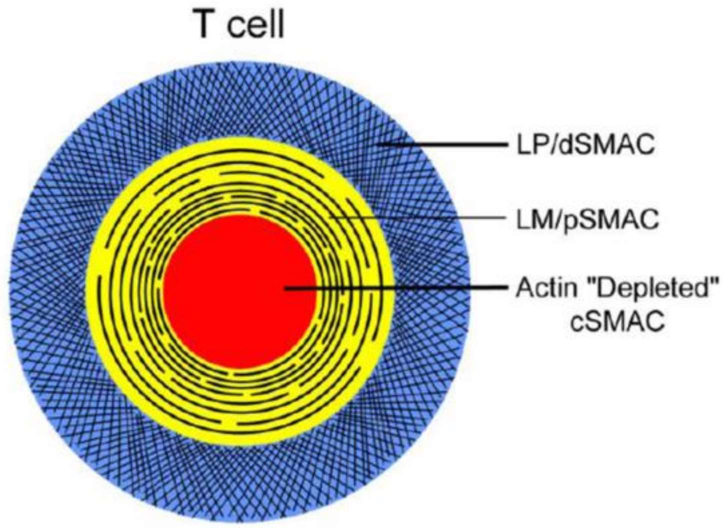

Figure 11. A schematic drawing of the three major regions of the immunological synapse: distal, peripheral, and central supra-molecular activation cluster (dSMAC, pSMAC, cSMAC). These parts of the immunological synapse were compared to the functional parts of migrating adherent cells: LP – lamellipodium, LM – lamella. Reproduced from Fig. 1 in (Hammer & Burkhardt, 2013), by permission from Elsevier.

Non-muscle myosin IIA is a molecular motor responsible for pulling of the anti-parallel actin filaments. In the plane of the immunological synapse its role is linked to the actomyosin arcs appearing in the pSMAC (Figure 11) and travelling towards the centre of the synapse, where they are disassembled(Hong, Murugesan, Betzig, & Hammer, 2017; Murugesan et al., 2016). The functional importance of these structures has been debated, as the inhibition of myosin activity led to different influence on the outcome of the activation process in different studies (reviewed in (Hammer & Burkhardt, 2013)). In particular, it is still unclear what is the relative contribution of actin polymerisation in dSMAC, myosin activity in pSMAC, and actin depolymerisation in cSMAC to the formation of the immunological synapse, and one of its hallmarks, the centripetal transport of membrane proteins, such as TCRs grouped in microclusters.

Formins are a family of proteins nucleating long linear actin filaments. There are 15 different formins in human (reviewed in (Schönichen & Geyer, 2010)), from which at least three (FMNL1, DIA1, INF2) are expressed in CD4+ T cells and were shown to be important in T cell activation (Andrés-Delgado et al., 2012; Gomez et al., 2007). Formins anchored to the T cell membrane were postulated to nucleate long actin filaments, which, once reaching the pSMAC, were organised by myosin to form the arcs, travelling in the plane of the synapse (Murugesan et al., 2016). Over the longer timescale of minutes, formins were implicated in the translocation of the centrosome towards the immunological synapse (Andrés-Delgado et al., 2012; Gomez et al., 2007). The translocation of the T cell centrosome (the microtubule organising centre of T cells is centrosome) towards the immunological synapse was first observed in 1980s (Kupfer & Dennert, 1984; Kupfer, Swain, Janeway Jr., & Singer, 1986), and it was used to explain the directional secretion of cytokines by helper T cells, and of lytic granules by cytotoxic T cells. Thus, the role of microtubule cytoskeleton in T cell activation is mostly the delivery of the specific cargo to the contact area with the antigen-presenting cell. Formins are able to interact both with actin filaments and with microtubules (Bartolini et al., 2008; Ishizaki, Morishima, et al., 2001), which places them at a binding spot of these two cytoskeleton components.

In summary, the role of different cytoskeleton-related molecules in T cell activation has not been established in details yet, but it is well known that several mechanisms drive the dynamics of cytoskeleton on the T cell-APC interface, and that this dynamics contributes to the functional events in T cell activation. The dynamics of cytoskeleton can be quantified, to some extent, with the mechanical forces exerted by T cells on the APCs.

# 8. Mechanical forces in the process of T cell activation

The cytoskeleton dynamics can be described locally, on the level of individual filaments, on the mesoscale of small assemblies, or globally, on the level of large-scale cell rearrangements. Likewise, the importance of mechanical forces generated during T cell activation was investigated on the level of individual TCRs, on the level of active foci in the plane of the immunological synapse, and on the level of the whole cell.

Molecular studies investigated the outcome of the forces applied to individual TCRs through their bond to the peptide-MHCs, or their bond to the antibodies recognising subunits of CD3 molecule. As T cells migrate when they first recognise the antigen, the movement of one membrane relative to the other exerts forces on the bound receptors. Other source of the forces exerted on the TCR is of course the internal cytoskeleton activity, described above. The importance of these forces on the molecular level are studied through their impact on the TCR-peptide-MHC bond. For a review on the structural aspects of the antigen recognition by the TCR complex, and the importance of the mechanical forces in the process, see (Moogk, Natarajan, & Krogsgaard, 2018).

In a structural study with nuclear magnetic resonance (NMR) (Kim et al. 2009) it was found that activating antibodies, in contrast to the non-activating ones, induce a torque on the CD3 molecule, suggesting this mechanical twisting of the molecule as the triggering event of the activation. This point was reinforced with the single-cell experiments with optical tweezers, in which a bead coated with non-activating anti-CD3 antibodies could induce a calcium peak in a T cell, but only if a shearing force (such that the vector of the force lies in the plane of the immunological synapse, in-plane force) was applied to the T cell membrane with the bead. For the beads coated with peptide-MHC complexes, only the combination of the peptide recognised by the TCR and this in-plane force resulted in a calcium peak, which suggested that this force is necessary for T cell activation. This opened up the possibility of the description of TCR complex as a mechanosensor.

In a study with biomembrane force probe (Hong et al., 2015), the binding of TCR to its specific, cognate peptide-MHC was described as a catch-bond: a bond the lifetime of which is extended when an external mechanical force is applied to it. As the binding to a non-specific peptide did not show this property, it was suggested that T cells use forces to discriminate between specific and non-specific peptides. This could be incorporated into the kinetic proofreading model of TCR triggering: the catch-bond would enable a prolonged interaction between TCR and peptide-MHC, which – in this model – is essential for the onset of the signalling cascade. Further support for the hypothesis that mechanical forces applied to the TCR-peptide-MHC bond increase the sensitivity and specificity of the antigen recognition process was provided in a study with optical tweezers (Feng et al., 2017).The researchers found that the application of the in-plane force (tangential force) caused a calcium peak in T cells put in contact with beads coated with sub-optimal concentration of peptide-MHCs. The out-of-plane force (normal force) caused a similar effect, but for a larger amplitude of force. In other words, the applied force allowed T cells to respond to a few peptide-MHCs, whereas without the applied force the response was only observed for thousands of peptide-MHCs engaged.

The studies discussed above tested mostly the influence of the externally applied, controlled force on T cells. DNA tension probes, a new molecular tool used to investigate forces on the molecular level, have a fluorophore attached to a DNA hairpin. The fluorophore is quenched until the hairpin unwinds after the application of the external force; this way the force applied to the probe can be measured with the increase in the fluorescence. In a design based on these probes, it was possible to show that T cells generate forces applied to the TCR complex (Liu et al., 2016). The researchers found that these forces had higher magnitude for stronger agonists, and when the integrin LFA-1 was engaged in addition to the TCR. In this second case the force was still measured on the TCR bond, which suggests that engagement of LFA-1 increased, through intracellular signalling, the strength of TCR-peptide-MHC bond. In addition, the higher magnitude of measured forces correlated with the increased ZAP70 phosphorylation, suggesting that forces applied to TCR can have a direct effect on the signalling pathways in T cells.

The forces exerted by T cells on a larger surface area are an effective sum of the forces exerted through the individual receptor bonds. The measurement of forces over these larger scales provides a description of the mechanics of the different parts of the immunological synapse. In a study with traction force microscopy (Hui, Balagopalan, Samelson, & Upadhyaya, 2015) the researchers found that in-plane, contractile (centripetal) forces were the strongest at the periphery of the Jurkat T cells interacting with polyacrylamide gels coated with antibodies against the CD3 molecule. On this scale, the in-plane forces (traction forces) can also be measured with the micropillars, structures with diameter of about 1 μm, and tuneable height which defines their stiffness. When cells are plated on top of the micropillar array, they exert the in-plane forces which bend the micropillars. Force exerted on the particular micropillar is calculated from the displacement of its tip, measured in the microscopy image. This measurement allowed to study the implication of the surface proteins in force generation, in a study where the tips of the micropillars were coated with antibodies against CD3 and CD28 molecules (Bashour et al., 2014). The researchers found that when CD28 was engaged in addition to CD3, average force per micropillar increased; this effect occurred both when anti-CD28 antibodies were attached to the micropillars and when they were added to the solution. The effect of CD28 binding could be blocked with pharmacological inhibition of PI3K, kinase implicated in the signalling pathway downstream of CD28. Altogether these results suggested that the forces generated by T cells were exerted through the TCR complex, but could be modified with the intracellular signalling downstream of CD28. With the same technique of micropillars, the strongest in-plane forces were found in the same area of the immunological synapse as the one into which the CD8+ T cells release the cytotoxic granules (Basu, Whitlock, Husson et al., 2016), suggesting a physiological role for the force development.

The micropillars and the traction force microscopy provide the measurement of forces on the subcellular or the whole cell level, but only in the plane of the immunological synapse (in-plane forces, Figure 12, right). As T cells were shown to extend protrusions into the antigen-presenting cell (Ueda, Morphew, McIntosh, & Davis, 2011), they exert forces also out-of-plane (normal to the plane of the immunological synapse, Figure 12, left). To approach these out-of-plane forces on the whole-cell level, the biomembrane force probe was used (Husson, Chemin, Bohineust, Hivroz, & Henry, 2011). In this study previously done in our group it was found that human CD4+ T cells followed a sequence of latency, pushing and pulling phases, each one with defined timing. The engagement of LFA-1 (through an antibody) together with CD3 resulted in much shorter pushing phase, and similar pulling phase; the engagement of only LFA-1 did not trigger force generation. With this setup only the pulling forces could be quantified. In a study with atomic force microscopy (AFM) (Hu & Butte, 2016) the researchers found the same sequence of latency, pushing and pulling phases, when murine T cells were put in contact with the AFM tip coated with antibodies against CD3 molecule, or with peptide-MHCs. Both pushing and pulling forces were quantified. Interestingly, in this study a cyclic movement of the AFM tip induced a calcium peak in T cells, in which actin polymerisation was inhibited with latrunculin A, suggesting that the externally applied force could rescue the effect on the signalling normally obtained with the actin cytoskeleton reorganisation inside T cells.

Figure 12. Explanation of the notions of out-of-plane and in-plane forces. Scanning electron microscopy image reproduced from Fig. 2A in (Ueda et al., 2011), it shows a murine CD4+ T cell expressing a transgenic 5c.c7 TCR (T) forming an immunological synapse with a B cell from lymphoma cell line (CH27). Scale bar is 2 μm. Drawings added on the image show the plane of the immunological synapse (black square filled white), the direction of the out-of-plane forces (red arrows) and the in-plane forces (blue arrows).

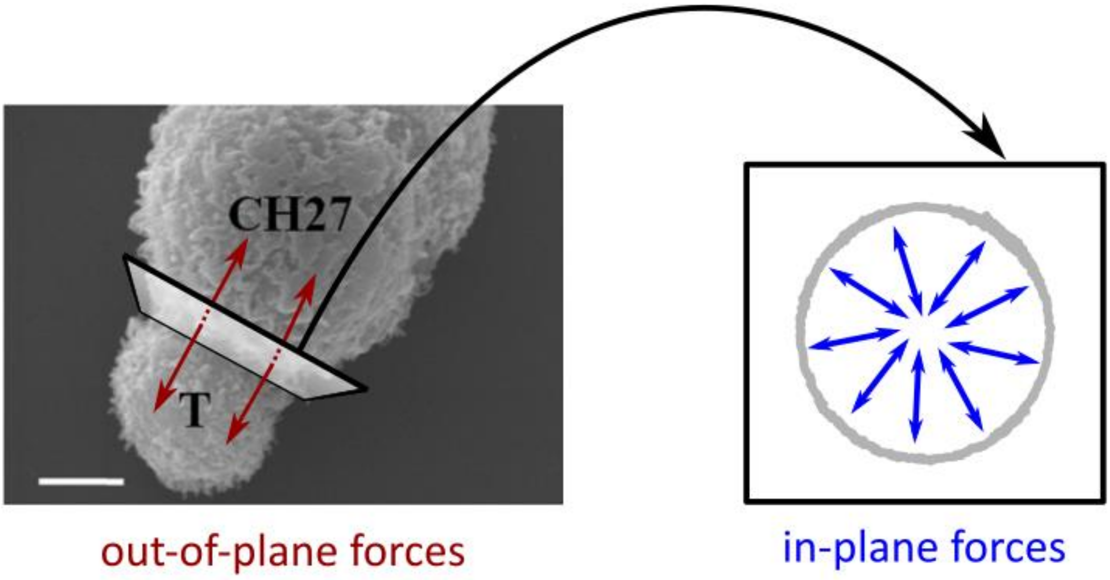

The body of research concerning the forces in the process of T cell activation began to form a few years before the beginning of my PhD studies (which was in October 2015), and it continued to be enriched during my studies. Into this landscape we wanted to incorporate the information on the pushing and pulling forces generated by T cells out of plane of the immunological synapse. Because of the results obtained previously in our group(Husson et al., 2011)–that the pulling forces generated by T cells were modified with the stiffness of their target – we decided to study these forces in the context of the mechanosensitivity of the process of T cell activation.

# 9. Mechanosensitivity of T cells

Mechanosensitivity is the ability of cells to sense the mechanical properties of their environment, including its stiffness and its shape. Several reports have indicated that T cells are mechanosensitive, as they respond differently when the activating substrate (target) has different stiffness (reviewed in (Hivroz & Saitakis, 2016)). In a study with polyacrylamide gels of different stiffness (Judokusumo, Tabdanov, Kumari, Dustin, & Kam, 2012), the production of IL-2 by T cells increased with the gel stiffness. Although the cells attached less to the gels of smaller stiffness, an increase in the concentration of cells did not increase the production of IL-2 in the way the stiffness of the gel did. It was concluded that the different stiffness of the gels induced different responses of T cells. This mechanosensitivity was mediated through the TCR complex, rather than the CD28 molecule, because when the anti-CD3 antibodies were placed on polystyrene beads mixed with cells, and the anti-CD28 antibodies on the gels of different stiffness, the production of IL-2 did not change with the gel stiffness. The opposite effect was found in a study with PDMS gels (O’Connor et al., 2012), where the cells attached to stiffer substrates proliferated less and produced less IL-2. However, the softest substrate in this study had stiffness comparable to the stiffest substrate in the (Judokusumo et al., 2012), leading to the question about the range of stiffness of the substrate which is relevant to the physiological targets of T cells.

The stiffness of the gels used for cell plating is commonly quantified as their Young’s modulus, an elastic modulus expressed in pascals. The rheological studies of cells allow to extract this parameter for living cells. Antigen-presenting cells, such as dendritic cells, are on the soft end of the spectrum of the individual cell stiffness, with Young’s modulus on the order of 0,1-1 kPa (Bufi et al., 2015). T cells circulating in the body interact also with endothelial cells, and migrate through the tissues, of much higher stiffness. This is why in the study previously done in our group (Saitakis et al., 2017) the different functional responses of T cells were tested for the gels of stiffness of 0,5 kPa, 6,4 kPa, and 100 kPa, to mimic the stiffness of these different cellular environments (to compare: (Judokusumo et al., 2012) showed different responses of T cells within the range of 10-100 kPa; in (O'Connor et al., 2012) most of the responses were compared between the gels of the stiffness of 100 kPa and more than 10 MPa). Within the range of 0,5-100 kPa, the increasing stiffness generally potentiated the activation markers such as proliferation and cytokine production. However, the gene expression analysis revealed that some of the genes were up- or downregulated only for one particular gel stiffness, suggesting that the T cell response can be fine-tuned with the substrate stiffness.

Intuitively, force generation and mechanosensitivity are linked, as we find out how stiff a presented substrate is by pressing (or pulling) on it. In cell biology, ongoing research aims to translate this intuition into particular molecular mechanisms through which cells could sense the stiffness of their environment (reviewed in (Iskratsch, Wolfenson, and Sheetz 2014; Chen et al. 2017)). My project aimed at addressing this issue in T cell activation.

*The goal of my project was to characterise the forces generated by resting CD4+ T cells, on the substrates of different stiffness. We wanted also to provide information on the mechanism of force generation, and link it to other events during T cell activation: the signalling pathways and the cytoskeleton dynamics. The outcome of my project should be a better understanding of the nature and role of forces generated by T cells in their activation process.*

# 10. Historical coda

Anthony J. Davies finished the panorama summarising the developments in T cell biology occurring during his career span (Davies, 1993) with the paragraph:

> « My broad guess is that there is still much more to be found out about the general biology of T cells and, when the molecular biologists have had their fill, future generations of PhD students will still have much to keep them entertained. »

I think that the mechanical forces and mechanosensitivity are one of these things that nowadays keep the PhD students entertained. This does not mean that the molecular biologists have finished their job already; but the techniques developed and the information gathered allow us now to broaden the scope of the research beyond the molecular components of the immunological synapse and the chemical interactions between them. The goal of this additional biophysical approach is still the same: a better understanding of the mechanism of T cell activation.

# Chapter 1: Micropipette-based techniques for biophysical study of T cell activation

T cells act as individual cells – they do not form a tissue. However, they are capable of forming, temporarily, a specialised interface with the antigen-presenting cell. This interface is called the immunological synapse, and its development leads to the T cell activation – a process which leads to T cells performing their immunological function. Two major biophysical aspects of T cell activation that I addressed in my research were such that: 1) during the formation of the immunological synapse, T cells exert forces on the antigen-presenting cell; 2) the functional outcomes of T cell activation were shown to change with the stiffness of the activating substrate, meaning that T cells are mechanosensitive.

In this chapter I describe the techniques, which we used to capture these aspects of the process of T cell activation. The chapter is divided in three sections. First, I briefly introduce the micropipettes, tools of the experimental setups, used for the positioning of cells and for the biophysical measurements. Then, I describe a new technique, the micropipette force probe, which we used for the study of the forces generated by T cells upon TCR triggering. I discuss the type of information this technique allows to obtain and how it relates to other techniques used to study T cell activation. I finish by introducing the adapted micropipette setups, which we used to obtain complementary information, asking more detailed questions about the biophysical aspects of T cell activation.

## 1.1 Characteristic parameters of the micropipettes

For each experiment, the micropipettes of particular, adapted, properties were prepared from borosilicate glass capillaries. Details on how the micropipettes were prepared and calibrated are included in the Supplement 1. Figure 13 shows a schematic drawing of a micropipette ready to use in experiment.

Figure 13. Anatomy of a micropipette. The three "functional" parts of the micropipette that can be tuned for a particular setup: the tip, the shaft, the handle. Inset shows the types of tips used in the experiments, with their major describing parameters. Left to right: straight micropipette; bent micropipette, used for "face to face" cell and target presentation (see Figure 14C); microindenter. Schematic representations in squares will be used for the setup drawings in Figures 14 and 16. The main bend is necessary to position the shaft and the tip in the focal plane of the microscope; in our setup it was fixed at 45° (see also Figure 14A). Drawings not to scale.

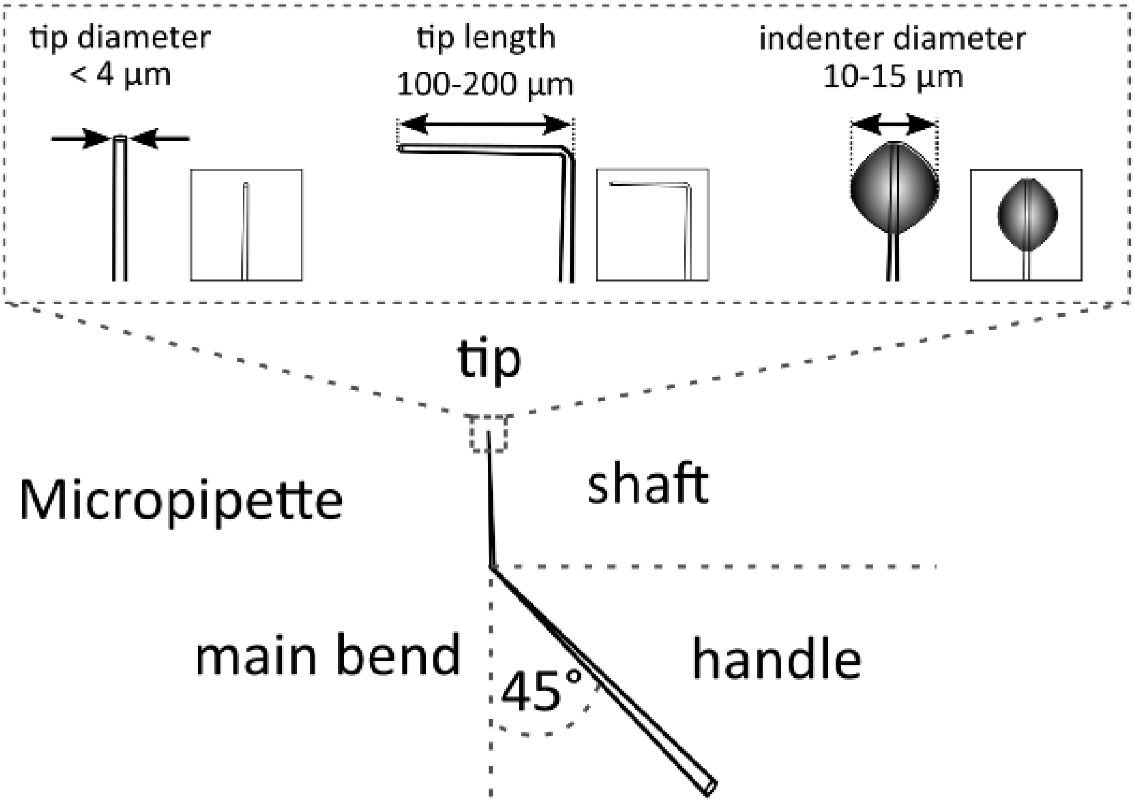

The tip part of the micropipettes was in contact with the cells during the experiments. Depending on the research question it could have different shapes (inset in Figure 13), always of micrometric size. The shaft part of the micropipettes, typically several millimetres long, defined the bending stiffness of the micropipette ($k$). Holding micropipettes, used for holding the object of interest, had a rigid shaft (marked with bold rectangles in the setup schemes in Figures 14 and 16). Measuring micropipettes, used as the force probes, had a longer and thinner shaft, and were calibrated for the measurement of their bending stiffness (rectangles with "k" in the setup schemes in Figures 14 and 16). The main parameter to tune in the holding micropipettes is the tip diameter (inset in Figure 13, left). For human primary T cells the inner diameter was typically about 2,5-3,5 µm. The main parameter to tune in the measuring micropipettes is their bending stiffness ($k$). In my experiments it was on the order of 0,1-1 nN/µm, meaning that when we tracked the displacement of the tips of these micropipettes in the microscope image, we were able to measure, and exert, forces on the order of hundreds of piconewtons to nanonewtons. This is the range of maximal forces generated by T cells (see details in Chapter 2.3). The handle part of the micropipette, several centimetres long, and 1 mm in outer diameter, was used to hold and manipulate the micropipette. During the experiment it was attached to a tube connected to the pressure system (Figure 14A), and filled with water.

# 1.2 Micropipette force probe

The standard micropipette force probe (MFP, (Sawicka et al., 2017)) setup consisted of one holding micropipette with a straight tip, and one measuring micropipette, either with a straight or with a bent tip (Figure 14 on the next page). Such setup served for a single-cell, single-target experiment – in my case a single T cell and a single bead coated with activating antibodies. The binding of the antibodies to the cell surface receptors triggered the T cell response, which was recorded in real-time in two channels: (1) the brightfield microscopy image, showing the morphology of the cell, (2) the position of the measuring micropipette, providing the amplitude of the out-of-plane force generated by the cell at a given time point (Figure 15). The technique thus provided detailed, quantitative information – mechanical and morphological – on the single-cell level.

Figure 14. Schematic drawings of the micropipette force probe setup. A: Side view (standing in the laboratory). Two micropipettes are held in the micropositioners (grey boxes). The micropipette tips are dipped in the glass-bottom Petri dish containing cells and activating beads in medium, and meet in the focal plane of the microscope objective (100× immersion oil, NA 1.3). The hydrostatic pressure in the holding micropipette ($\Delta P_{cell}$) is controlled with the level of water in the container. The pressure in the measuring micropipette ($\Delta P_{bead}$) is controlled with the syringe filled with air; in practice the bead is aspirated mostly by capillarity forces. B and C: Top view (as in the microscope image). Drawings show holding micropipettes (bold rectangles) and two types of the measuring micropipettes (thin boxes, k), in the symbolic representation. Arrows show the micropipette movement done by the operator during the experiment. Insets: sample microscope images taken during the experiment. B. This setup allows an automatic tracking of the position of the measuring micropipette, along the horizontal line in the image which crosses the micropipette tip. C. This setup keeps the axial symmetry of the cell-bead contact, and puts the micropipette shaft further away from it. The position of the tip of the micropipette needs to be tracked manually in the microscopy images. See Supplement 5 for the sample charts obtained for both setups with human T cells and activating beads.

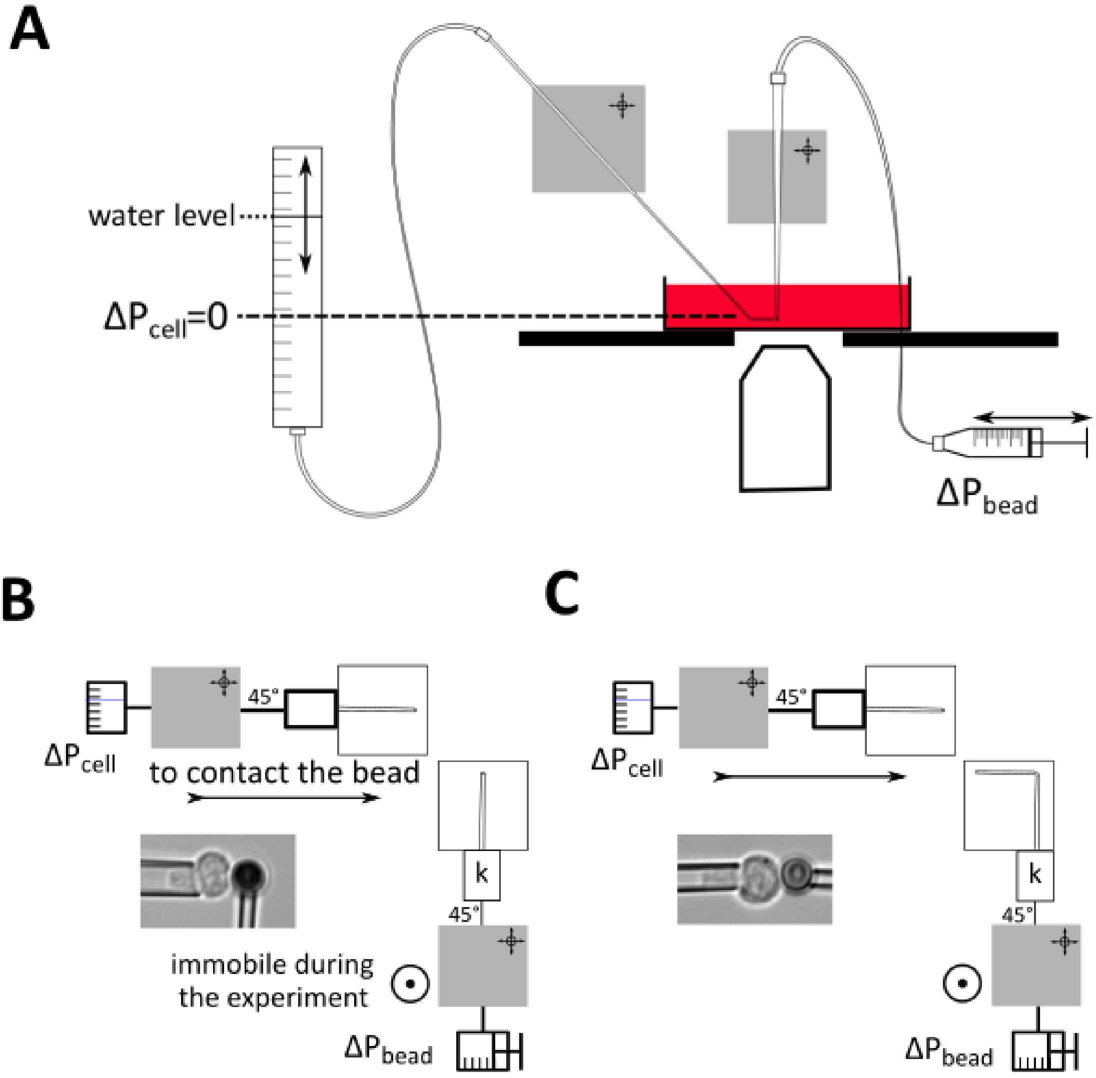

Figure 14. See legend on the previous page.

Figure 15. Micropipette Force Probe – obtained data. The chart on the right is a plot of the micropipette position (tracked along the X axis) against time. As the cell exerts forces on the bead, the measuring micropipette bends. The displacement of the tip of the micropipette ($x_{bead}$) measured on the image allows to calculate both pushing and pulling forces generated by the cell.

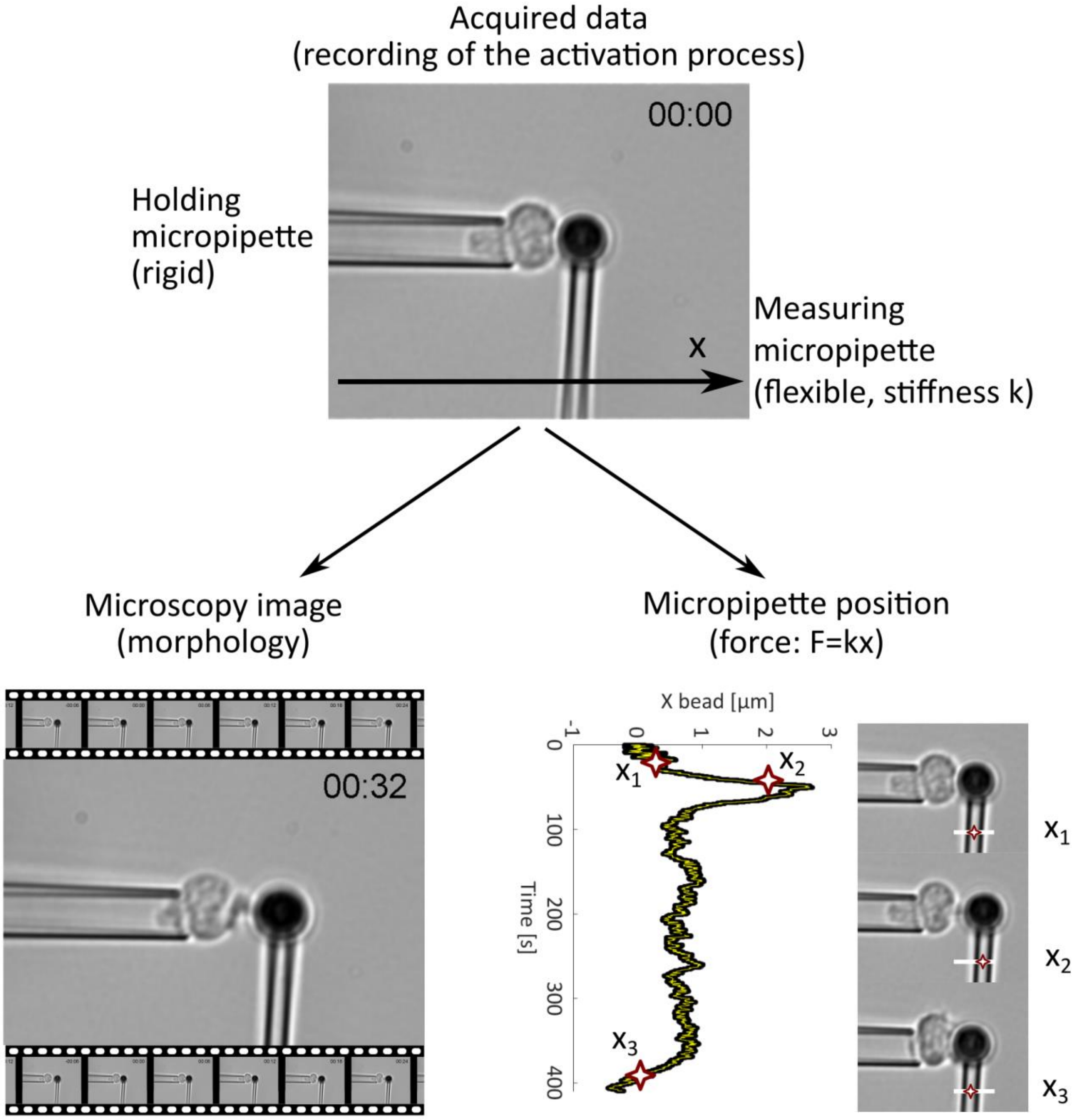

For the study of T cell activation both types of information are useful, as T cells upon contact with activating beads underwent large morphology changes (Chapter 2.1) and pushed and pulled on the bead (Chapter 2.3). I discuss below how MFP compares to other techniques applied to track force generation and morphology changes in T cell activation.

Various techniques can be applied to study forces actively generated by cells (reviewed in (Roca-Cusachs, Conte, & Trepat, 2017)). Table 2 on the next page shows these techniques, which were recently applied to study forces in T cell activation.

Table 2. Comparison of the different techniques used for the measurement of forces in T cell activation. The references cited in the "Historical reference" column are the first papers explaining the principle of measurement with the technique; for the oldest two techniques these are not the first biological applications of the technique; for the newest technique I cite two approaches which were used jointly in (Liu et al., 2016): the use of fluorescence for the detection of locally applied tension, and the use of DNA molecules as the tension sensors. The references cited in the "Application to T cell activation" column were discussed in more detail in the section 8 of the Introduction. For the explanation of the notions of "in-plane" and "out-of-plane" forces see Figure 12 in Introduction.

| Technique | Historical reference | Application to forces in T cell activation | | | |
|---|---|---|---|---|---|
| | | References | Type of the force measurement | Forces applied or measured in the studies | Stiffness of the target changed? |
| Optical tweezers | (Ashkin, 1970) | (Kim et al. 2009) | Molecular | 50 pN | No |
| | | (Feng et al., 2017) | Molecular | 8-25 pN | No |
| Atomic force microscopy | (Binnig, Quate, & Gerber, 1986) | (Hu & Butte, 2016) | Whole cell out-of-plane | 100-3000 pN | No |
| Biomembrane force probe | (Evans, Ritchie, & Merkel, 1995) | (Husson et al., 2011) | Whole-cell out-of-plane | 40-500 pN | Yes |
| | | (Hong et al., 2015) | Molecular | 5-30 pN | No |
| Traction force microscopy | (Dembo & Wang, 1999) | (Hui et al., 2015) | Subcellular or whole cell in-plane | 100-10000 pN | Yes |
| Micropillars | (Tan et al., 2003) | (Bashour et al., 2014) | Subcellular or whole cell in-plane | Per pillar: 25-200 pN | Yes |
| | | (Basu et al., 2016) | Subcellular or whole cell in-plane | Per pillar: 50-400 pN | No |
| DNA tension probes | (Liu et al. 2013; Wang and Ha 2013) | (Liu et al., 2016) | Molecular | 12 pN, 19 pN, 56 pN* | No |
| Micropipette force probe | (Sawicka et al., 2017) | (Basu et al., 2016) | Whole cell out-of-plane | 200-1000 pN | No |
| | | (Sawicka et al., 2017) | Whole cell out-of-plane | 200-1000 pN | Yes |

*three types of tension probes were used, with the maximal force that could be measured as indicated.

As it can be seen from the Table 2, the techniques used provide largely complementary information. In the studies of T cell activation different ranges of forces were measured, describing the molecular forces, exerted on the individual receptor level, or the effective sum of these forces as it appeared on subcellular or the whole cell level. The techniques allowed to measure forces exerted in the plane of the immunological synapse, or out of this plane, in the direction of the X axis in Figure 15 above. MFP measures forces out-of-plane and on the whole cell level, and in this area it can be compared mostly to atomic force microscopy (AFM) and biomembrane force probe (BFP). The main reason for the development of MFP was the possibility to measure both pushing and pulling forces, as the pushing forces could not be measured with BFP. AFM allows to measure both pushing and pulling forces, also the sensitivity and the time resolution of the AFM measurement is better than the one obtained with MFP. The advantages of MFP over AFM are more of the practical nature, based on the relative ease of use of the technique in the experiment. For instance, a single probe (micropipette in MFP, cantilever in AFM) can be re-used with multiple cells for MFP, and it has to be replaced for each cell for AFM. The morphology of the cell as seen from the side, readily available with MFP, requires a much more sophisticated setup with AFM (Chaudhuri, Parekh, Lam, & Fletcher, 2009; Ounkomol, Xie, Dayton, & Heinrich, 2009). In the context of the described mechanosensitivity of T cells, it is of particular interest to change the stiffness of the target of T cells. The bending stiffness of the measuring micropipettes can be easily changed when they are fabricated. Although AFM tips of different stiffness (spring constant) are commercially available, the tip stiffness is rarely changed in a particular set of experiments. In the study which used AFM to characterize T cell activation, the influence of stiffness of the target on the forces generated by T cells was not investigated(Hu & Butte, 2016). MFP is a low throughput technique, a typical experimental day provides data on 20-30 cells. This limitation is shared by all the techniques mentioned in the Table 2. A high-throughput technique for the study of cellular forces is yet to be developed.

For the morphology of T cells during activation, the largest amount of data was obtained with the imaging of particular proteins stained with fluorescence markers. This molecular-level information founded our understanding of the process of T cell activation (reviewed in (Kupfer and Kupfer 2003)). The recently developed super-resolution microscopy techniques, combined with fast acquisition of images, have been used to gather insight into intricate functional aspects of the formation of the immunological synapse (Cai, Marchuk, Beemiller, Beppler et al., 2017; Murugesan et al., 2016; Ritter, Asano et al., 2015). With MFP we did not aim to obtain this molecular level of precision; rather, a brightfield image, which does not require staining, was used to extract the morphological features important for force generation, as it was matched with the force information at each time point.

T cells are challenging cells, as they are small (6-8 μm diameter for resting T cells) and fast (they change the whole-cell morphology within tens of seconds, they migrate with the speed of around 15 μm/minute (Saitakis et al., 2017), an order of magnitude faster than individual HeLa cells (Shamir, Bar-On, Phillips, & Milo, 2016)). My attempt to capture the process of T cell activation – forces generated out-of-plane and the morphology seen from the side – will be discussed in Chapter 2.

## 1.3 Additional techniques

One of the advantages of the micropipette setups is that they are versatile: they can be adapted to different research questions with some changes in the micropipette fabrication and positioning, and in the parameters detected and measured during the experiment.

As we tuned the stiffness of the measuring micropipettes to test the cells' response to the targets of different stiffness, there appeared the question of the extrapolation to $k = 0$, i.e. the response of T cells to the target of negligible (vanishing) stiffness. To test experimentally this condition we tried two different approaches. In the first approach the micropipettes were like in the standard MFP setup (Figure 16A). During the experiment I corrected the position of the holding micropipette, to keep the measuring micropipette at the initial position ($x_{bead} = 0$ therefore no force, published in (Sawicka et al., 2017)). In the second approach we used two stiff, holding micropipettes facing each other (Figure 16B). During the experiment I brought the bead in contact with the cell and then retracted the bead micropipette as soon as the cell adhered to the bead. The cell therefore exerted forces against the bead floating in the medium (negligible resistance, so $k = 0$, published in (Sawicka et al., 2017)). This second approach to the micropipette experiments was used also in (Lee et al., 2015), although not to tune the stiffness of the target that the cells are faced with. I will discuss the results obtained with these approaches in the Chapter 2.3.

Figure 16. Adapted micropipette setups used in experiments, in the symbolic representation used also in Figure 14. Arrows show the micropipette movement done by the operator.Insets: sample microscope images taken during the experiments, scale bars are 10 µm. Top line: Two approaches to k=0 (cell activating against a substrate of negligible stiffness). A: correcting the holding micropipette; B: releasing the bead from its micropipette. Bottom line: Measurement of cell effective stiffness with profile microindentations. C: for resting T cells; D: during the activation process. In D, the handle part of the micropipette holding the bead is rotated in its metal holder connected to the tube (see Figure 14A), so that its tip is pointing towards other two pipettes.

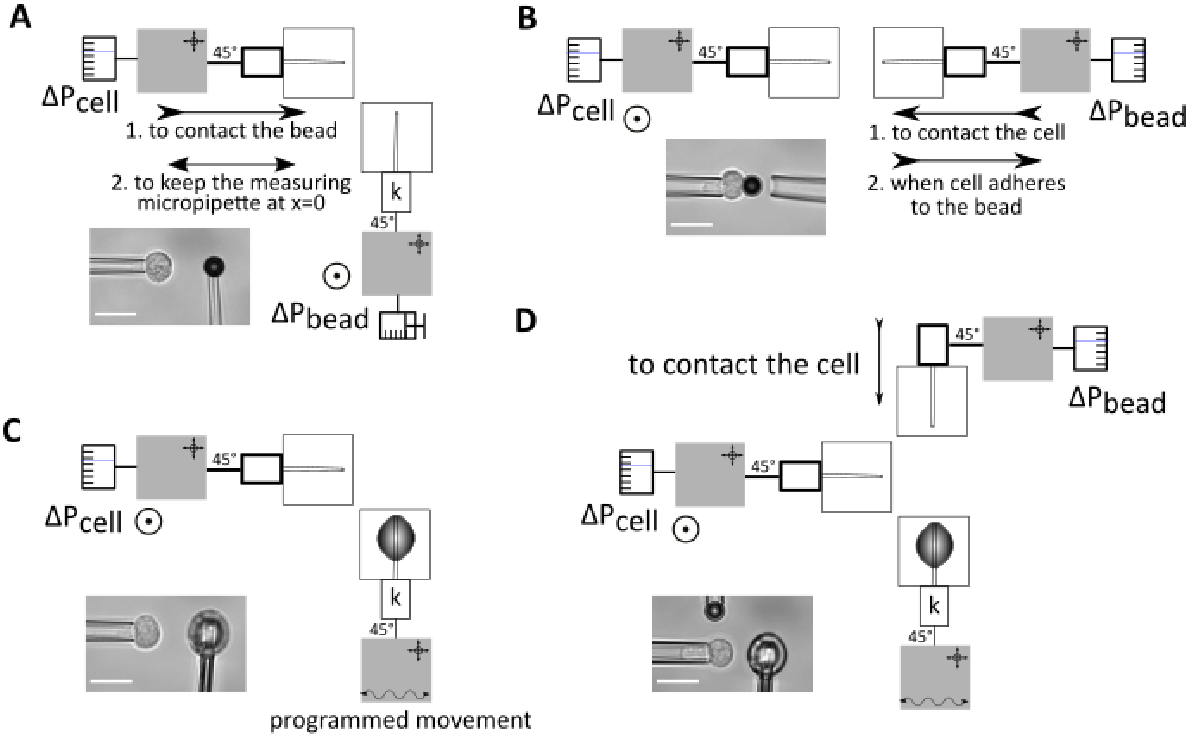

The above approaches (Figure 16A and 16B) serve to measure cells' responses to different mechanical properties of the substrate. We can also use micropipettes to probe the mechanical properties of cells. In these setups a cell was held as usual, and in the place of the measuring micropipette with the target we put a microindenter. During the experiment the base of the microindenter moves at a constant speed, so that the tip of the microindenter indents the cell with an increasing force, until the force reaches the pre-specified value. The force at each timestep is calculated by comparing the position of the base of the microindenter set on the micropositioner with the position of the tip of the microindenter obtained from the image. With this method (profile microindentation, (Guillou, Babataheri, Puech, Barakat, & Husson, 2016)) we measured the effective Young's modulus of resting T cells (Figure 16C), and resting T cells in the first minutes of the activation (Figure 16D). I will summarise these results in Chapter 2.2.

# Chapter 2: The sequence of early events in T cell activation

I used the micropipette-based techniques described in the previous chapter to study biophysical aspects of T cell activation. I focused on the first events in T cell activation, when, after TCR triggering, T cells switch from the resting, quiescent state to an active, effector one, in which they perform their immunological function.

In this chapter I describe the results obtained in the standard conditions in my experiments. I used human primary CD4+ T cells sorted negatively from peripheral blood mononuclear cells of healthy donors (cells were isolated by Stéphanie Dogniaux and Michael Saitakis, for details see Supplement 2), activated with beads coated with antibodies against CD3 and CD28 molecules (anti-CD3 and anti-CD28 antibodies, Figure 17). When put into contact with the beads, T cells followed a sequence of morphology changes (Figure 18). Inscribed into this sequence was the out-of-plane force generation (perpendicular to the synapse plane). Using micropipette force probe, I was able to quantify both pushing and pulling forces, which follow within minutes after the cell contacts the activating bead.

Figure 17. The model used in the experiments, on the molecular level. The activating antibodies bind to the CD3ε and CD28 molecules. This triggers the signalling on the cytoplasmic side of T cells: ITAM motifs (yellow circles) can be phosphorylated, and the characteristic amino acid sequences of CD28 (white circles) can recruit their binding proteins. The antibodies are covalently bound to the rigid bead surface (Dynabeads, Invitrogen Life Technologies, USA), and are immobile.

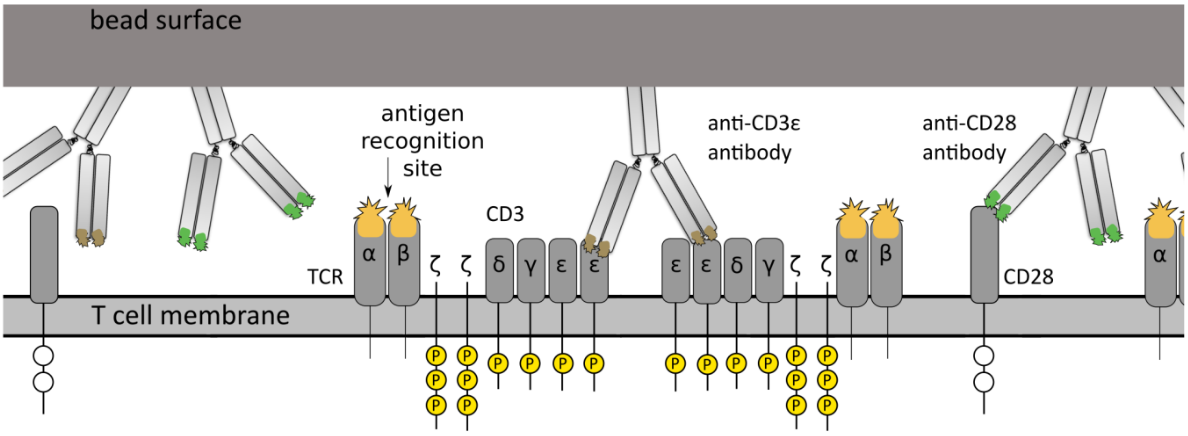

The chapter is divided into four sections. First, I set the outline, or a general map for the rest of the thesis, by describing the changes inthe morphologyof T cellsin the first few minutes after the contact was made between a T cell and an activating bead. I will refer to this sequence throughout the work. Then I move on to the mechanics of this process, discussing the change in the apparent stiffness of T cells, and the out-of-plane forces generated by T cells, which are influenced by the stiffness of the environment (in this case, the bending stiffness of the measuring micropipette). Finally, I summarise the results obtained with CD4+ T lymphoblasts, showing the same general order of events, and some quantitative differences for this model of the effector T cells. The information gathered from these experiments prepare the ground for the third chapter in which – by perturbing this fixed sequence of morphology changes – I search for the mechanism that T cells use to generate forces.

## 2.1 Timeline of events

Figure 18 on the next page shows a summary of how the sequence of events in the first minutes of T cell activation appeared in the MFP experiments. To start the experiment, I brought a cell in contact with a bead, time t=0 was set at this moment when the cell-bead couple was formed. For about 30 s there were no noticeable changes in T cell morphology, and the measuring micropipette stayed close to its initial position (position of the bead, $x_{bead} \approx 0$, waiting on the chart). Then, T cells started forming a pushing protrusion (which I call punch), appearing as a tube of approximately the same diameter along its length ($x_{bead} > 0$, pushing on the chart). Punch grew with a constant speed for about 20 s until it reached the length of 2 µm (2,0 ± 0,7 µm, mean ± SD, N = 106 cells across 14 experiments) and similar diameter (1,9 ± 0,5 µm, mean ± SD, N = 105 cells across 14 experiments, measured in the middle part of the protrusion).

Figure 18. Early events in T cell activation. A sample timetrace of the measuring micropipette with different phases of the process shown on schematic drawings (left), brightfield (middle) and scanning electron microscopy (SEM) images (right). Brightfield images show 7 different cells across 3 experiments, SEM images show 7 different cells across 2 experiments. Scale variable, the bead diameter is 4,5 µm. The shown phases have a defined time duration, reported next to the time axis as median times for crossing from one phase to another. Timetraces for two different cells were used to show the two final morphologies (below the gray box). SEM pictures are reused from Fig. 4 in (Sawicka et al., 2017), CC-BY-NC-SA 3.0 license. One of the two SEM experiments was performed by Claire Hivroz, all imaging was done by Virginie Bazin from IBPS, at Université Pierre et Marie Curie.

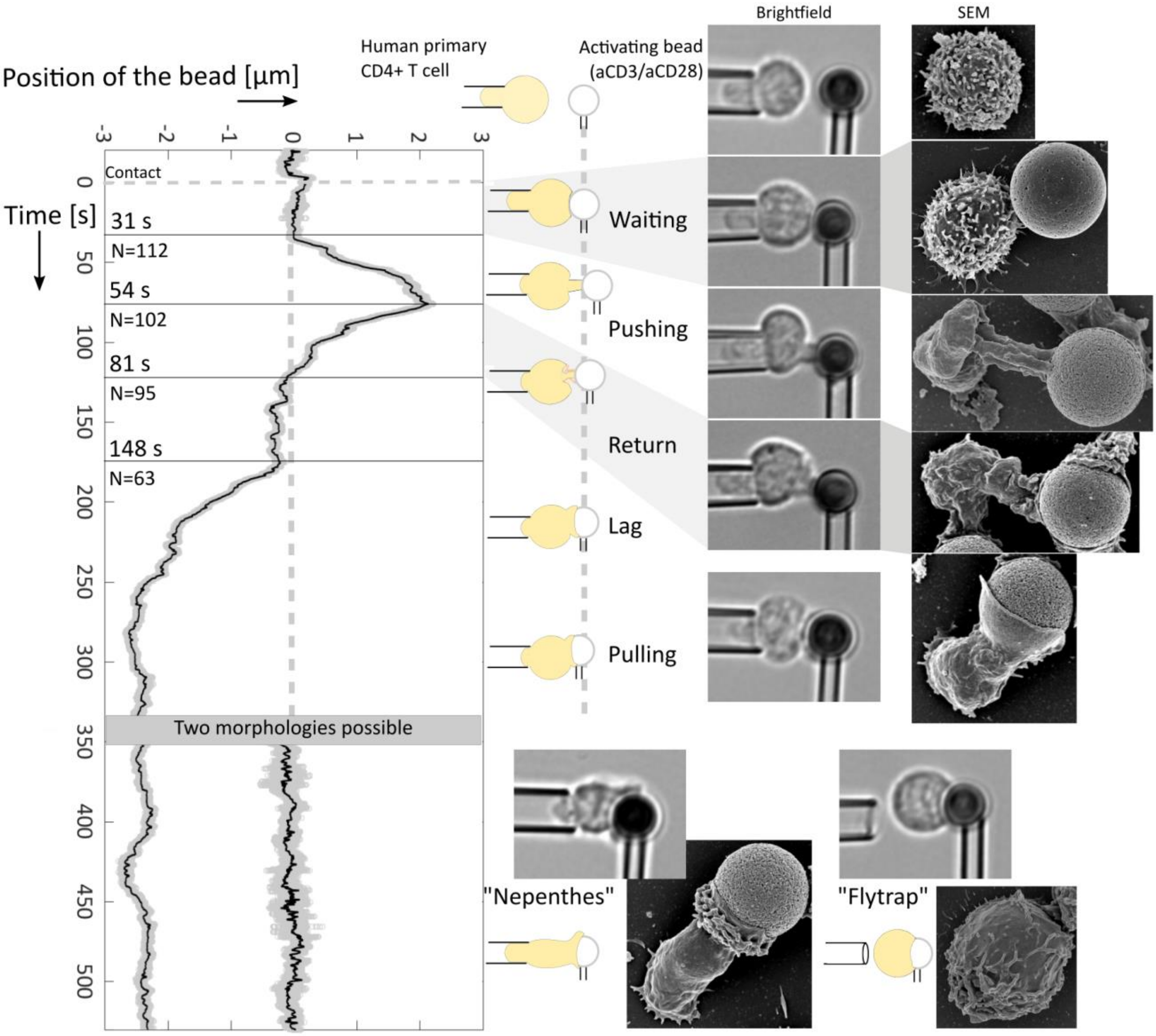

The end of the pushing was usually abrupt. The punch finished the growth, bent, or twisted, and then gradually collapsed (indicating a diminishing compressive force: $x_{bead} > 0$, return on the chart), until the punch disappeared completely and the bead returned to the initial position. The return phase lasted also for about 20 s, implying that pushing and return happened at a similar speed. This average trend could be confirmed on the individual cell level, as the return speed was correlated with the pushing speed (Spearman's correlation coefficient $\rho = 0,62$; $p < 0,001$) and the line fitted to the values, with intercept assumed at 0, had a slope of 0,94 (Figure 19A).The collapse of the punch was accompanied with a change in cell morphology: T cells gradually increased their contact area with the bead, forming a different, more spread protrusion (which I called cup). Next, for about 60 s the measuring micropipette stayed close to the initial position, meaning that cells exerted no measurable force along the X axis ($x_{bead} \approx 0$, lag on the chart in Figure 18). The cells remained active, there were ruffles or waves appearing on the cup and travelling from the bead towards the cell body. Gradually, spreading T cells started to pull the bead towards themselves ($x_{bead} <$ 0, pulling on the chart), pulling phase lasted for about 50 s. Pulling speed was not related to pushing speed (Spearman's correlation coefficient $\rho = 0,28$; $p = 0,07$; Figure 19B).

Figure 19. Typical values for pushing, return and pulling speeds. Each dot represents a T cell, the speeds were fitted to the parts of charts showing position of the bead ($x_{bead}$) versus time (see Figure 18). A. Pushing and return speeds are about equal. The fitted line has an imposed intercept at 0. N=56 cells across 8 experiments. B. Pulling speed is not correlated with pushing speed. N=45 cells across 8 experiments.

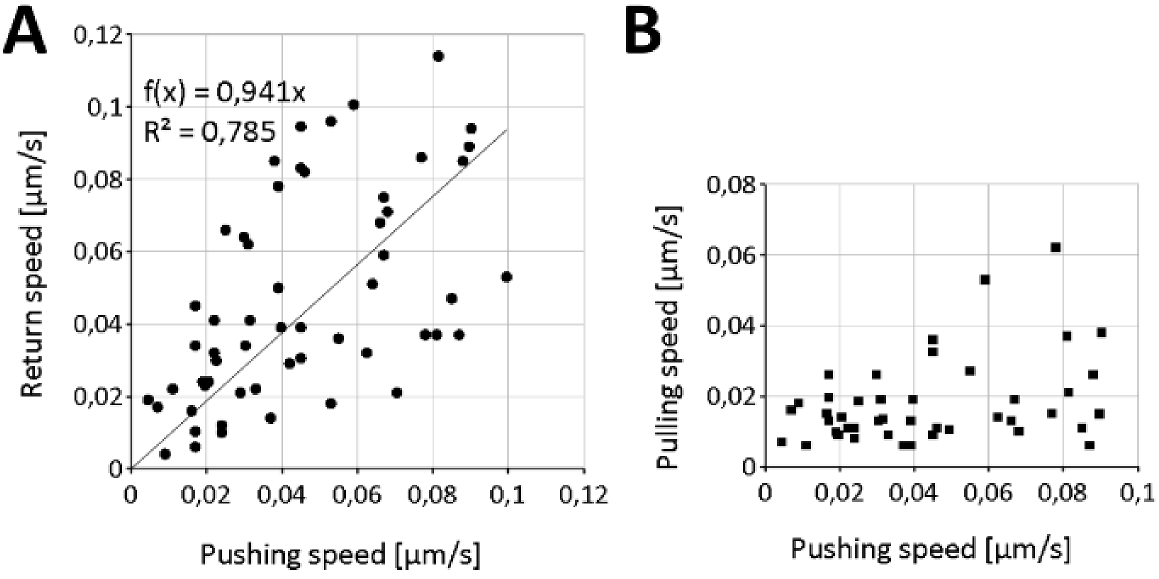

Until this point all the cells that were active (N=114 cells across 14 experiments and 5 donors) followed qualitatively all the morphology changes, with some individual quantitative differences, like the differences in speeds (Figure 19). At the end of pulling, however, the sequence of events bifurcated. 29 cells (25%) spread further on the bead, usually escaping from the holding micropipette (at this moment the measuring micropipette sprang back to $x_{bead} \approx 0$ from the maximal pulling force, trace to the right on the chart in Figure 18), whereas 47 cells (41%) stayed elongated and inside the holding micropipette. The waves initially showing on the cup started travelling on the whole cell (trace to the left on the chart in Figure 18). The remaining 38 cells either were not well aligned with the bead at the contact or pushed themselves out of the focal plane during the activation process, and so they were not clearly seen in the microscopy image and they were not assigned to any of the two types. These two morphological types – elongated and wavy versus rounded and static – repeated across the experiments often enough to get named: nepenthes, for the shape of the nepenthes flower, and flytrap, to stay close in the carnivorous plants metaphors, as they seemingly closed on the bead. As one major difference between the types seemed to be that the flytrap cells extrude themselves from the holding micropipette, the simplest explanation of the two types would be that they were only visible because of the micropipette setup, or could be even an artefact of the aspiration in the micropipette. However, we could observe similar morphologies in SEM images (Figure 18), and also in the microchamber experiments with large number of cells (see below in Chapter 3). Having ruled out a simple artefact of the method, I collected data on both morphological types, trying to find the factors that support one of the types, or quantitative differences between the two.

There were experimental days with (almost) exclusively flytrap or nepenthes cells. We hypothesized that this could be due to the individual traits of the donor whose cells were used for this particular experiment, or due to the diameter of the holding micropipette used in this particular experiment (a broader micropipette, with the same aspiration pressure applied, exerts a larger force on the cell, and could therefore prevent the formation of the flytrap cells). However, when results were summarised across several experiments performed with the cells from the same donor (Figure 20A), or plotted versus diameter of the holding micropipette (Figure 20B), no trend explaining one or the other morphology type could be found. The quantitative differences between the pushing, return, and pulling speeds, even maximal pulling force, the last event before the two types separate, were not statistically significant (Table 3). Thus, the two morphological types could still be only distinguished based on their appearance in the microscope image. It is widely recognised that morphology of cells contains the information about their physiological state; however, it is much more challenging to relate a particular morphological trait to a functional phenotype (reviewed in

(Marklein, Lam, Guvendiren, Sung, & Bauer, 2018)). Unfortunately, until now no functional difference could be found between the flytrap cells and the nepenthes cells.

Figure 20. Statistics of the flytrap and nepenthes morphological types. A. Flytrap and nepenthes types appear in all of the donors tested. Number of experiments for the donors A, B, C, D, E: 2, 3, 3, 4, 2, respectively; exact number of cells reported on the bars. B. The diameter of the holding micropipette does not influence the proportion of flytrap cells. Each dot represents one experimental day. Spearman's correlation coefficient ρ = -0,19; p = 0,56.

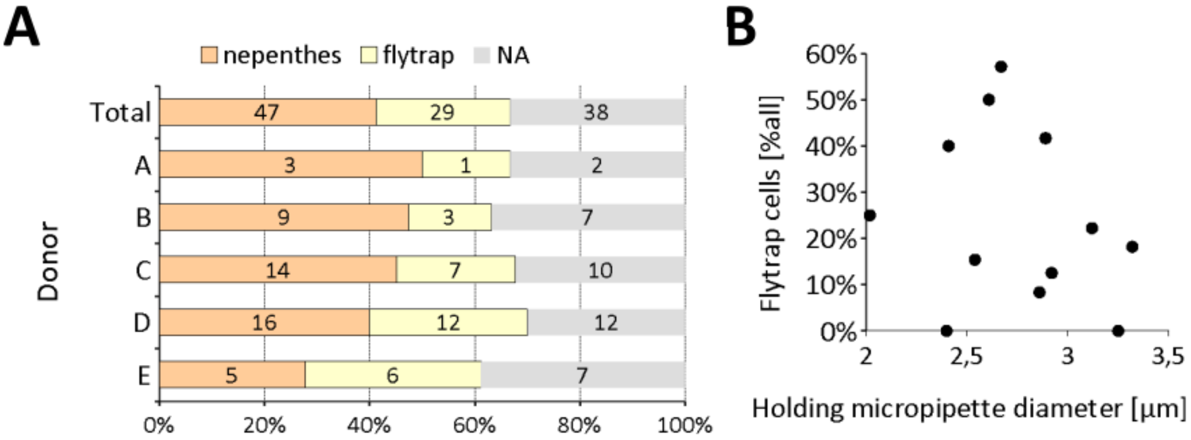

Table 3. Quantification of (no) differences between the flytrap and nepenthes cells. Values shown as means over cells from different experiments (total of 29 flytrap cells and 47 nepenthes cells across 14 experiments). Lag time calculated as the beginning of pulling minus end of return. p-values calculated with Mann-Whitney U test, N of cells for each parameter reported below the p-values as flytrap:nepenthes cells.

| Parameter | Pushing speed [µm/s] | Return speed [µm/s] | Pulling speed [µm/s] | Lag time [s] | Maximal pulling force [nN] |
|---|---|---|---|---|---|
| Flytrap cells | 0,052 | 0,055 | 0,025 | 64 | 0,56 |
| Nepenthes cells | 0,056 | 0,061 | 0,026 | 68 | 0,54 |
| p-value<br>(N) | 0,58<br>(26:40) | 0,98<br>(23:40) | 0,68<br>(20:19) | 0,81<br>(18:22) | 0,95<br>(21:22) |

All the morphology changes described above happen on the cell-bead interface, or on the "activating" side of the cell. The opposite side of the cell, aspirated in the holding micropipette, showed one important change: a sudden shortening. This observation opened up the investigation of the mechanical properties of T cells during the activation process. I will now discuss these properties, before coming back to the "activating" side, where T cells generate mechanical forces (Chapter 2.3).

## 2.2 Change in the mechanical properties of T cells

The mechanical properties of a material describe how it deforms when an external force is applied to it. Living cells are a complex material: they are composed of a lipid bilayer with proteins embedded into it (cell membrane), supported with the network of cytoskeleton proteins (cell cortex), and filled with cytoplasm, in which several major organelles (nucleus, endoplasmic reticulum, Golgi apparatus, mitochondria) form further compartments of different properties. Experiments usually do not allow to quantify independently the particular properties of these components. For this reason, the measurement of the mechanical properties of single cells relies on the extraction of the global properties, which describe the whole-cell response to the deformation. These global properties are sometimes called also "apparent" or "effective", being an effective response of all the components of the cell to the deforming force.

These effective properties were reported to change during the progression of malignant transformation of fibroblasts and epithelial cells (Guck et al., 2005), or for white blood cells in inflammatory conditions (Bufi et al., 2015). This means that the measurement of the mechanical properties of cells can be used to assess their physiological state. Recent advances in the development of the microfluidic-based setups, where the mechanical properties of the cells are extracted from the brightfield microscopy images, open the perspective for the use of the mechanical properties of cells as a clinical marker (Remmerbach et al., 2009; Toepfner et al., 2018; Tse et al., 2013).

In the laboratory setting, apart from the microfluidic setups, the mechanical properties of cells were measured with micropipette aspiration (Evans and Yeung 1989; Lee, Herant, and Heinrich 2011), optical (Yamada, Wirtz, & Kuo, 2000) and magnetic tweezers (Valberg and Feldman 1987; Laurent et al. 2002), AFM ((Rotsch, Braet, Wisse, & Radmacher, 1997), reviewed in (Li, Dang, Liu, Xi, & Wang, 2017)), and parallel plate setups (Mitrossilis et al., 2010; Thoumine & Ott, 1997). For a recent, direct comparison of the different techniques see (Wu et al., 2018). The measurement of the mechanical properties was used to explain different physiological processes in the cell, like when the mechanical properties of the cells were linked to the state of the cytoskeleton (Laurent et al. 2005; Lieber et al. 2013; Chugh, Clark, Smith, et al. 2017). Thus, the mechanical properties of a cell can show, in a quantitative manner, the underlying biological processes. The choice of the parameter describing appropriately the mechanical properties of the living cells needs to include how the cell deformation appears in the particular experimental setting.

In micropipette setups the applied aspiration pressure causes the cell deformation which appears as an extension of a part of the cell into the micropipette. In this thesis I call this aspirated part of the cell the tail. In the early micropipette aspiration experiments (Evans & Yeung, 1989) it was established that for a cell to be aspirated (for the tail to appear), a critical pressure, $\Delta P_{crit}$, needs to be applied to the micropipette. Below this pressure threshold the cell does not form the hemispherical projection inside the micropipette (does not fully enter the micropipette). Above the critical pressure the cell flows into the micropipette (the tail length increases).

One of the mechanical properties of the cells that was extracted from this situation was the surface tension ($\gamma_{cell}$). When described with this parameter, the cell is assumed to be a liquid droplet with an elastic shell, and the Laplace law is applied to the curvature between the cell and the inside of the pipette (1) and to the curvature between the cell and the outside of the pipette (2):

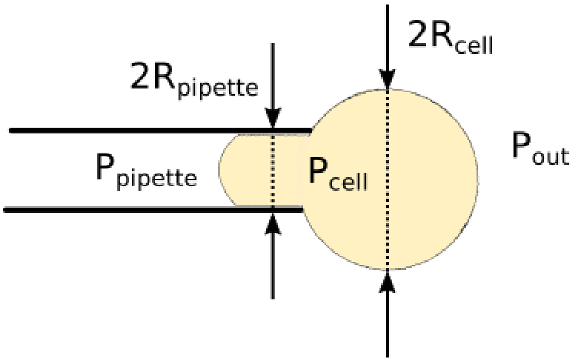

$$P_{cell} - P_{pipette} = \frac{2\gamma_{cell}}{R_{pipette}} \qquad (1)$$

$$P_{cell} - P_{out} = \frac{2\gamma_{cell}}{R_{cell}} \qquad (2)$$

$(1) - (2)$:

$$P_{out} - P_{pipette} = 2\gamma_{cell}\left(\frac{1}{R_{pipette}} - \frac{1}{R_{cell}}\right)$$

When the difference in pressure $P_{out} - P_{pipette}$ is equal to the $\Delta P_{crit}$ , the cell surface tension can be calculated as:

$$\gamma_{cell} = \frac{\Delta P_{crit}}{2\left(\frac{1}{R_{pipette}} - \frac{1}{R_{cell}}\right)}$$

In the MFP experiments a constant aspiration pressure was applied to the holding micropipette. The appearance of the tail in MFP experiments means that this applied aspiration pressure, $\Delta P_{exp}$ , was above the critical pressure: $\Delta P_{exp} > \Delta P_{crit}$

During activation (after the contact with the beads coated with anti-CD3 and anti-CD28 antibodies), the tail of T cells suddenly shortened (Figure 21A and 21B on the next page). This shortening started at the median time of 38 s, so within the same time frame as the onset of pushing forces, marking it as one of the earliest morphology changes on the whole-cell scale in the activation process. For the majority of the cells pushing preceded the tail shortening, with the biggest number of cells showing a small (less than 10 s) difference between the two events (Figure 21D). The tail shortening means that the T cell surface tension increased, as the same $\Delta P_{exp}$ was now below the critical pressure limit:

| | Cell surface tension | Critical pressure | Of which it is known that |
|---|---|---|---|
| Before the tail shortening | $\gamma_1$ | $\Delta P_{crit,1}$ | $\Delta P_{crit,1} < \Delta P_{exp}$ |
| After the tail shortening | $\gamma_2$ | $\Delta P_{crit,2}$ | $\Delta P_{crit,2} > \Delta P_{exp}$ |

Therefore $\Delta P_{crit,2} > \Delta P_{crit,1}$ and $\gamma_2 > \gamma_1$ .

Figure 21. The behaviour of the part of the cell aspirated in the holding micropipette (tail) during activation. A and B. The changes in tail length can be tracked by plotting a kymograph of the line shown in yellow in brightfield images (left). The location of three brightfield images (right) is marked with gray lines. The onset of the shortening of the tail, $t_{tail}$, is marked with a black line. Two examples of cells are shown: a flytrap cell (A) and a nepenthes cell (B). For the flytrap cells, the tail disappeared completely when they escaped from the holding micropipette (bottom image, A). For the nepenthes cells, the tail usually grew longer (bottom image, B). Time in minutes:seconds from contact. C. Timing of the earliest events in T cell activation: the onset of pushing force, $t_{push}$ (transition from waiting to pushing in Figure 18), and the onset of tail shortening, $t_{tail}$. D. For the majority of cells (yellow) pushing precedes tail shortening, $t_{push} < t_{tail}$. All times measured from the contact frame. N=97 cells across 14 experiments, 5 cells with the difference $t_{tail}$ - $t_{push}$> 100 s were excluded from all histograms for clarity.

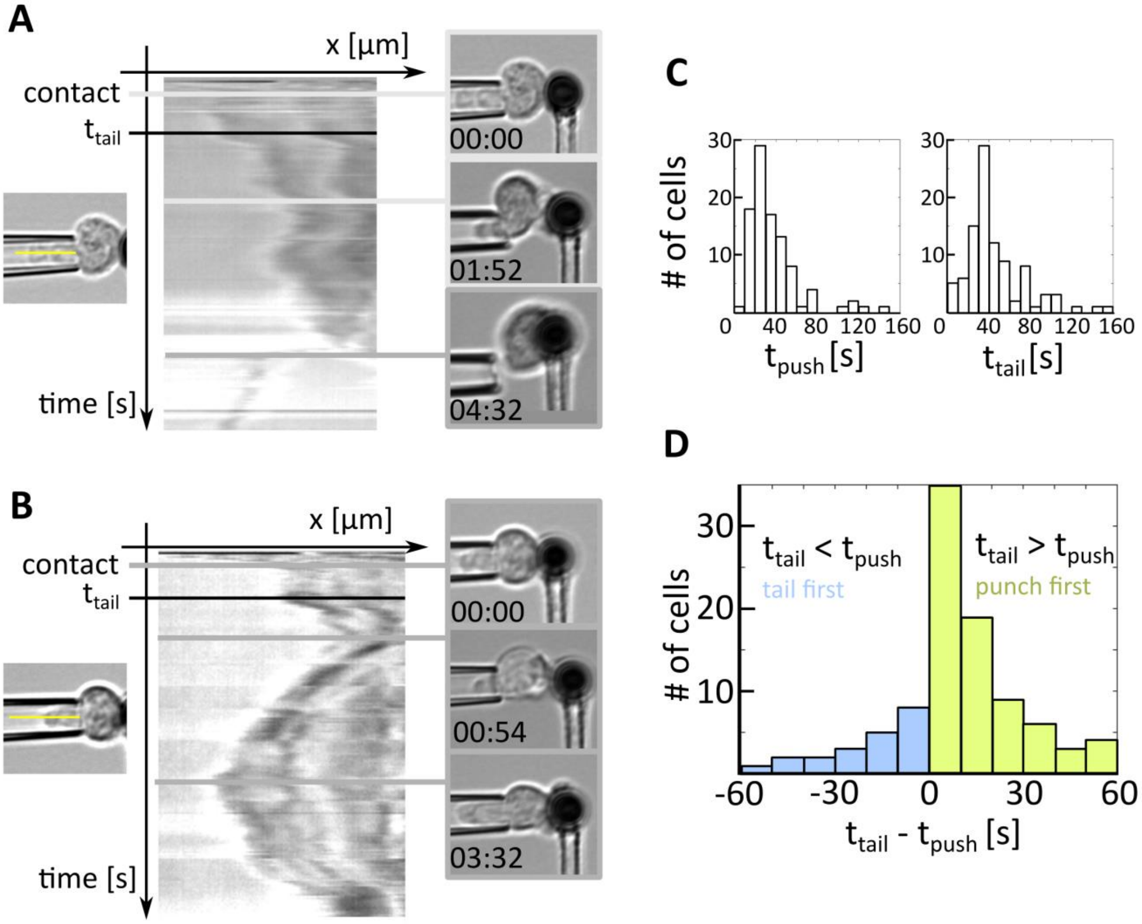

This description through the surface tension is one of the ways to say that T cells during activation become stiffer (less deformable). Qualitatively, in the MFP experiments we see an increase in the surface tension of T cells. However, with the setup used, it is not possible to quantify this change in stiffness, as the setup is not adapted to dynamically measure the surface tension.

Profile microindentation is a technique previously developed in our laboratory to measure the apparent stiffness of cells while monitoring their morphology from profile (Guillou, Babataheri, Puech, et al., 2016). The technique can address the change of the stiffness of T cells during their activation, as it allows to monitor the activation process through the observation of the cell morphology, and it provides sufficient time resolution (one measurement about every 10 s). The response of the cells to the microindentations has been described with the Hertz model, in which the indented surface is assumed to be an elastic material with a Young's modulus describing its mechanical properties. It was shown that for microindentations the Hertz model better fitted the experimental data than the model based on the surface tension (Rosenbluth, Lam, & Fletcher, 2006). Therefore, Hertz model was used for the analysis of the profile microindentations data, and the obtained from this analysis the effective Young’s modulus was used as a measure of the stiffness of T cells during activation.

Profile microindentations during activation (the setup on Figure 22A on the next page, see also Figure 16 in Chapter 1) showed an increase in the effective Young's modulus of T cells (Figure 22B), starting from 60 s after the contact with the bead, a bit later but consistent with the measured $t_{tail}$. The Young's modulus of T cells increased twice, from about 100 to 200 Pa, within this short period of several minutes after contact with the activating bead.

Figure 22. T cells increase their effective Young's modulus during the activation process. A. Sample microscope images of the measurement of the effective Young's modulus of T cells during the activation process (see also Figure 16D in Chapter 1). B. Quantification of T cell effective Young's modulus. Profile microindentations performed on resting T cells without beads (control) and on resting T cells contacted at timepoint t=0 s with an activating bead (activation). N=3-16 cells per timepoint and condition. *p<0,05; Mann-Whitney U-test.

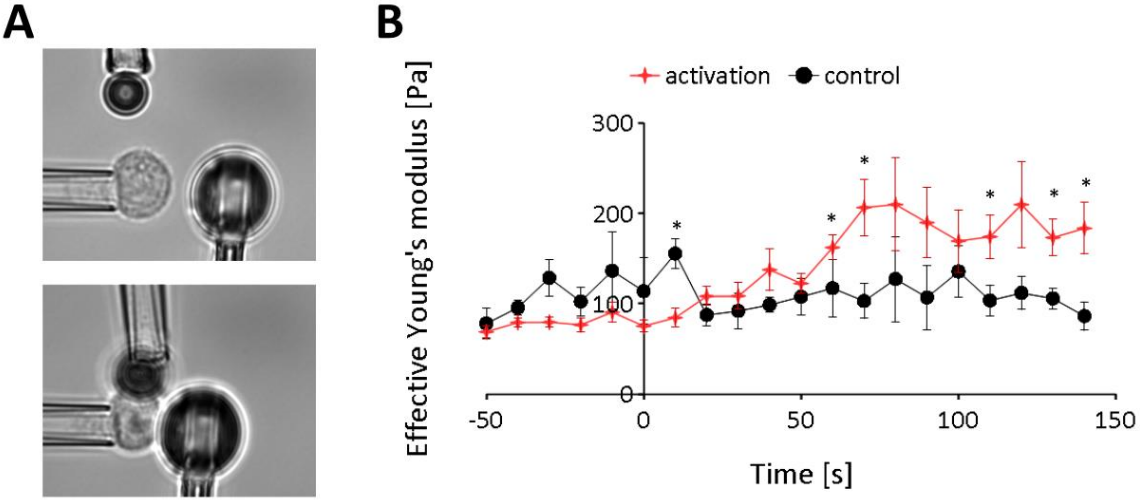

The mechanical properties mark a possible difference between flytrap and nepenthes cells (see Figure 18 in Chapter 2.1). For some of the nepenthes cells (12 of 30 nepenthes cells, or 40%, across eight experiments) the tail grew again after the initial shortening (Figure 21B), which indicates a decrease in surface tension, or a softening of the cells, at this longer time scale. In contrast, the tail of the flytrap cells never regrew (23 flytrap cells across eight experiments), suggesting that the mechanical properties of flytrap cells and nepenthes cells change differently over time. The geometry of the profile microindentations setup did not allow to quantify this putative difference in stiffness between the flytrap and the nepenthes cells, as at the moment when flytrap cells escaped from the holding micropipette their stiffness could not be measured anymore. This question could be addressed in future with an adapted experimental setup.

These results open the perspective of the mechanical characterisation of the process of T cell activation, as has been done for phagocytosis (Evans and Zhelev 1993; Herant, Heinrich, and Dembo 2005; Lee et al. 2015). The increase in the stiffness of T cells shows as an early hallmark of the process of T cell activation. The similar timing of the onset of the tail retraction and the onset of the pushing forces (Figure 21D) suggests that the increase in stiffness is linked to the force generation by T cells.

## 2.3 Pushing and pulling forces

T cells generate pushing and pulling forces during the first minutes of their activation process. With MFP experiments we could measure the forces generated during the sequence of morphology changes described in the Chapter 2.1. The first event observed after T cells contacted the bead coated with activating antibodies was the onset of the pushing force measured on the whole cell level and perpendicular to the contact area (out-of-plane). Then, after the return and lag phases, T cells develop also out-of-plane pulling forces.

We quantified both pushing and pulling forces generated by T cells with two main parameters:

1) maximal force, measured as the maximal displacement of the bead from the initial position ($x_{bead,max}$) multiplied by the bending stiffness of the measuring micropipette ($F_{max} = kx_{bead,max}$);
2) force rate, or the rate of force generation ($\frac{dF}{dt} = k\frac{dx_{bead}}{dt} = kv$). As the speed of the bead during pushing or pulling ($v$) was relatively constant over time for one cell, force rate was measured as the slope of the straight line fitted on $x_{bead}(t)$ chart, multiplied by the bending stiffness of the measuring micropipette ($k$).

We measured the forces generated by T cells when the beads were held in the measuring micropipettes of different bending stiffness ($k$). This way we wanted to check the mechanosensitivity of forces generated by T cells. The results are shown in Figure 23 (maximal force) and Figure 24 (force rate) on the next two pages. In response to the activating beads T cells generated forces reaching several hundreds of piconewtons in magnitude, at the force rates ranging from several to tens of piconewtons per second. These results indicate that force generation in T cells is mechanosensitive.

The range of stiffness used in the experiments was chosen to reflect the physiological stiffness that T cells encounter during the activation (the stiffness of the antigen-presenting cells). However, the description of the stiffness of the glass micropipettes differs from the description of the stiffness of the antigen-presenting cells, and so the quantification of the stiffness that a T cell "feels" in our setup is not straightforward. This issue will be further addressed in the Discussion.

Figure 23. Maximal force generated by human primary CD4+ T cells in contact with beads coated with anti-CD3 and anti-CD28 antibodies. The beads were held in micropipettes of different bending stiffness (k). Each data point represents a mean ± s.e.m. over one experimental day, N= 3-14 cells per data point.

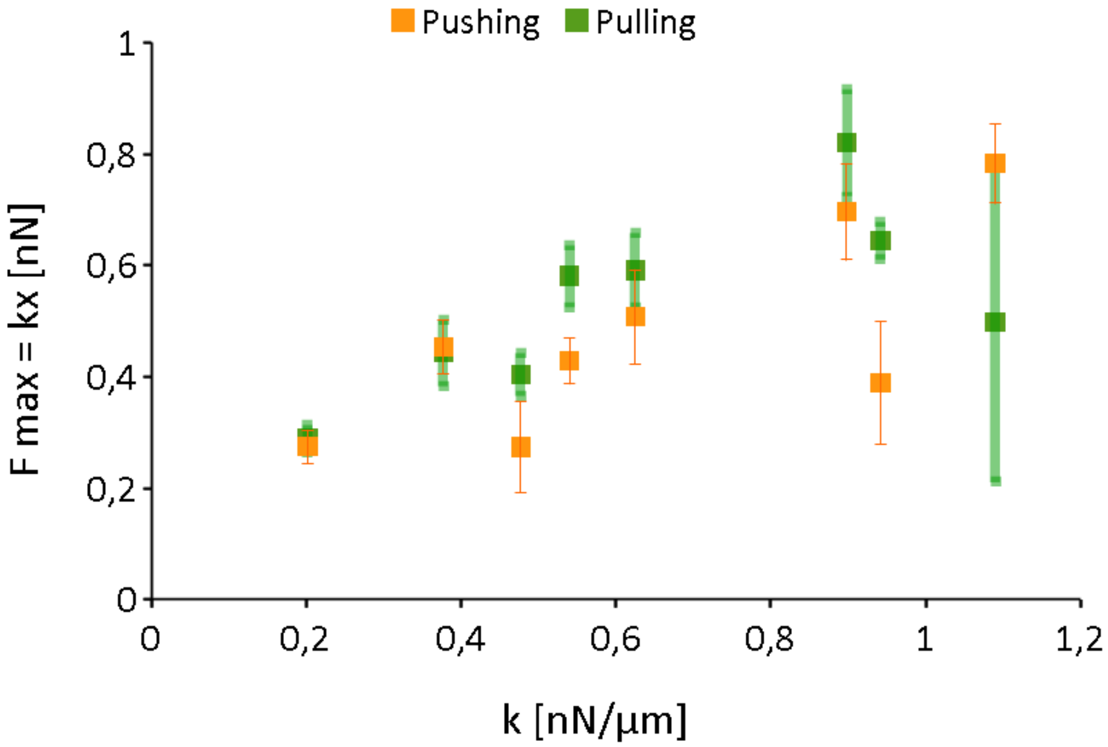

Figure 24. Force rate (the speed of force increase) generated by human primary CD4+ T cells in contact with beads coated with anti-CD3 and anti-CD28 antibodies. The beads were held in micropipettes of different bending stiffness (k). The absolute values for pushing and pulling are shown. Each data point represents a mean ± s.e.m. over one experimental day, N= 3-11 cells per data point.

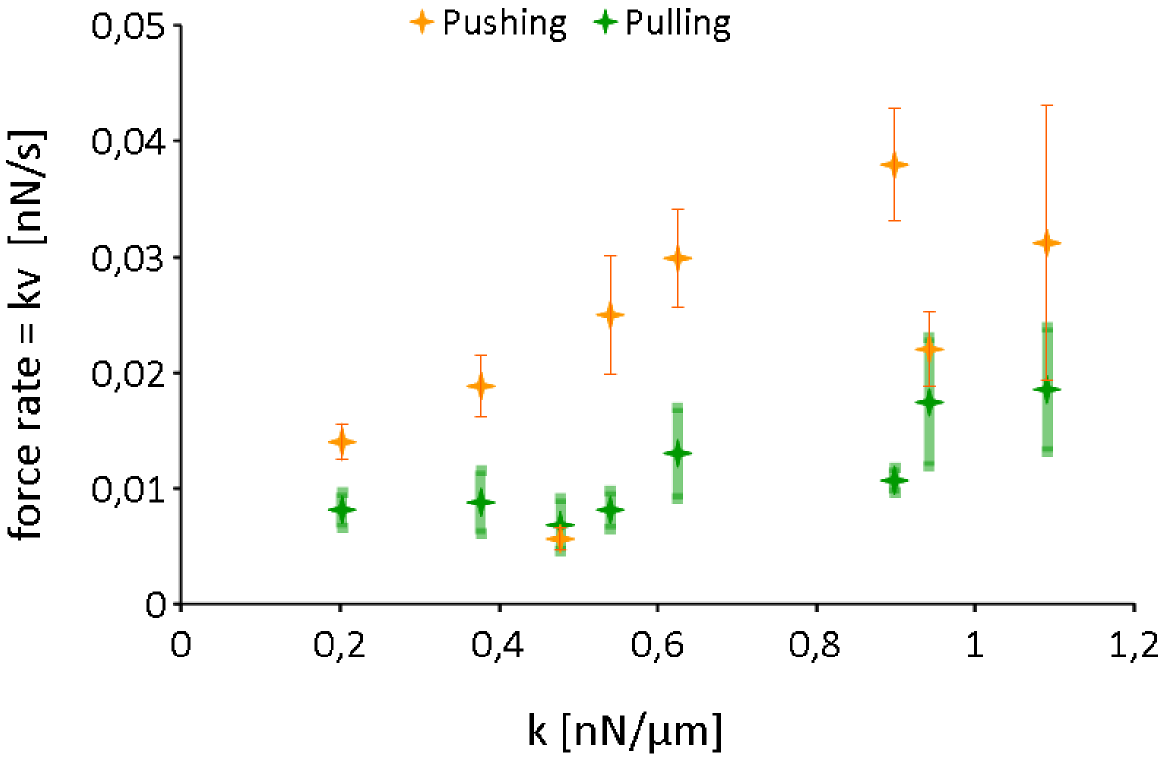

The growing punch appeared as a beam of an approximately constant diameter. As it grew, it increased the compressive force exerted on it by the micropipette with the bead (growing against a spring of the stiffness $k$, force $F$ increases linearly with the displacement $x, F = kx$). An elastic beam submitted to the compressive force above the critical value undergoes a sudden change in shape, called buckling (Figure 25). This critical value for the compressive force is described with the Euler's formula: $F_{buckling} = \frac{\pi^2 EI}{L^2}$, where $E$ is the Young's modulus of the buckling beam, $I$ is its moment of inertia, and $L$ is its length.

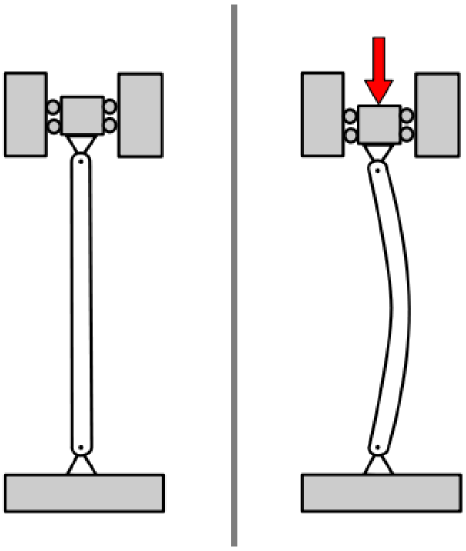

Figure 25. A schematic drawing of a buckling beam. Red arrow represents the critical force, $F_{buckling}$. Source of the image: Wikimedia Commons.

On close inspection of the $x_{bead}(t)$charts we could observe that there was a stalling, or a short break, on the pushing slope (Figure 26B). The moment when this break appeared corresponded in the movies to a sudden change in the punch morphology, appearing as a bend, or an increase in size, in the middle part of the punch (Figure 26A). We called this moment the buckling event, and measured the force corresponding to it, $F_{buckling} = kx_{buckling}$.

The measured value of $F_{buckling}$changed with the bending stiffness of the measuring micropipette, $k$ (Figure 26C). To check whether these values were consistent with the theory of mechanical buckling we derived the dependence of the $F_{buckling}$ on the bending stiffness of the measuring micropipette ($k$). From the Euler's formula:

$$F_{buckling} = \frac{\pi^2 EI}{L^2} = kL$$

as at the moment of the buckling event$x_{bead} = L$. From this,

$$L = \left(\frac{\pi^2 EI}{k}\right)^{\frac{1}{3}}$$

which substituted back to the Euler formula gives the dependence

$$F_{buckling}\left(k\right) = \left(\pi^2 EI\right)^{\frac{1}{3}} k^{\frac{2}{3}}$$

To fit this equation to the experimental data points, the Young's modulus of the punch was assumed to be equal to the measured Young's modulus of T cells, and therefore chosen at $E$ = 90 Pa (mean value measured by profile microindentations, see the control cells in Figure 22 in Chapter 2.2), the punch was assumed to be a cylinder with a moment of inertia $I = \frac{\pi D^4}{64}$, and the punch diameter $D$ was adjusted to fit the experimental data, leading to $D$ = 1,43 µm, slightly smaller than the measured in the microscope image the diameter of the punch just before the buckling event, 1,75 ± 0,08 µm (mean ± s.e.m., N=29 cells across

6 experiments). As it can be seen in the Figure 26C, the Euler's formula thus applied correctly describes the observed dependence of the buckling force on the bending stiffness of the measuring micropipette. This supports the hypothesis that the observed change in the punch morphology corresponds to the mechanical buckling.

The above analysis of the buckling force repeats the one shown in (Sawicka et al., 2017); it was developed for this study by David Gonzalez-Rodriguez. The numerical values shown here are slightly different than in the paper due to the inclusion of an improved dataset from profile microindentations, which changed the value for the Young's modulus of T cells.

Figure 26. Buckling event during T cell activation. A. Examples of the punch morphology during the buckling event. Each column shows a different cell, the frames are separated by 2 seconds. B. A close up on the pushing phase in a sample $x_{bead}(t)$ chart, with the values that can be measured on the chart. The x-values multiplied by k give the values of force that: was exerted on the cell when the cell and bead were put in contact ($x_{contact}$), was exerted by the cell when the buckling event (confirmed with the morphology of the cell) happened ($x_{buckling}$), was the maximal pushing force generated by the particular cell ($x_{max}$). C. The buckling and maximal pushing force generated by human primary CD4+ T cells in contact with beads coated with anti-CD3 and anti-CD28 antibodies. The beads were held in micropipettes of different bending stiffness (k). See text for the details on the fit. Each data point represents a mean ± s.e.m. over one experimental day, N=9-14 cells per datapoint.

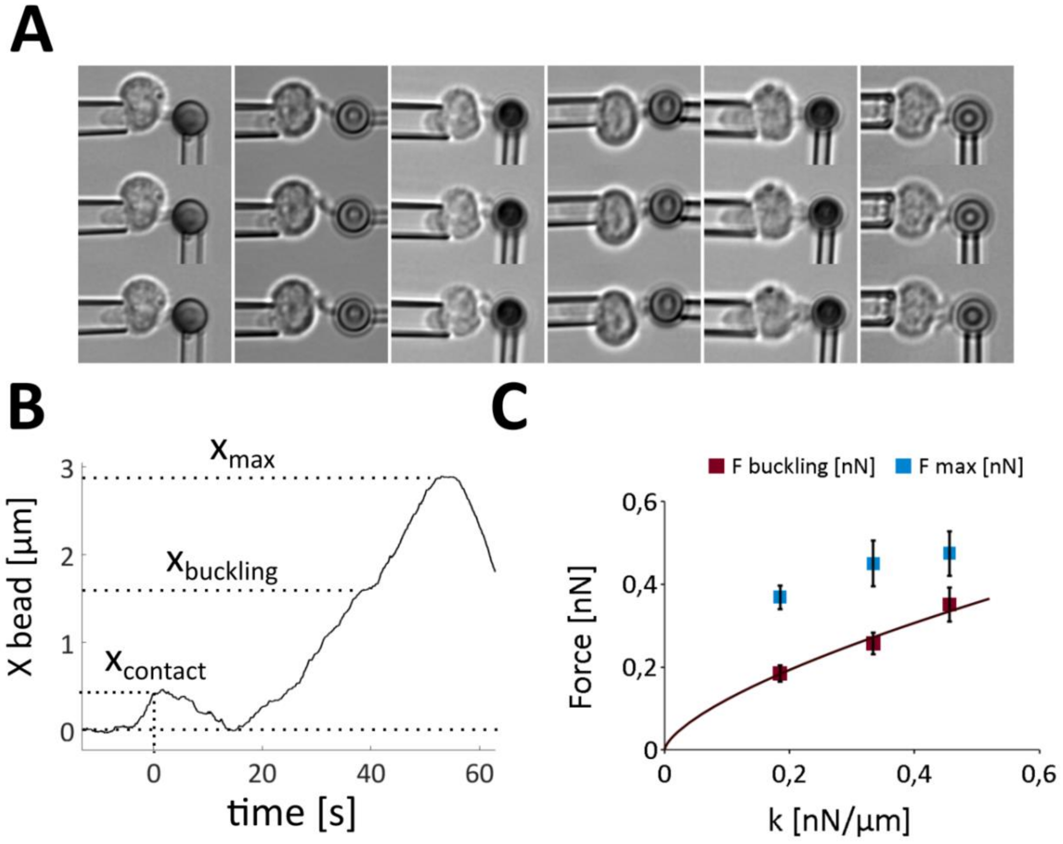

For larger bending stiffness of the measuring micropipettes we observed sometimes that the punch buckled only at its maximal length. For these cells the mechanical buckling of the punch could finish the pushing phase, meaning that the reorganisation of the punch associated with the buckling could start the process of the punch collapse. However, for many cells (as in the examples in Figure 26A), the buckling happened during the pushing, which means that after buckling the punch was still able to regrow. As a result, as $k$ decreases, the difference between the average $F_{max}$ and $F_{buckling}$ values increases (Figure 26C), suggesting that the mechanical buckling was not the only factor that limited the pushing phase, especially for the more flexible measuring micropipettes. Thus, we asked what limited the maximal pushing force exerted by T cells during the activation process, across the experiments, so for different bending stiffness of the measuring micropipette.

If T cells grew the punch until it reached a specific length, which can be approximated with the bead displacement ($x_{bead,max}$), we would see the linear relationship between $F_{max}$ and $k$ (because $F_{max} = x_{bead,max}\ k$). If T cells grew the punch for a certain time, we would see the linear relationship between $x_{bead,max}$ and pushing speed $v$(because $x_{bead,max} = tv$). The comparison of both relationships is shown in Figure 27A and 27B on the next page. Both relationships look linear, although the linear fit better describes the one shown in Figure 27B, which suggests that what was kept across the experiments was the time of pushing (duration of the pushing phase), rather than the maximal bead displacement. Indeed, the pushing time was similar across the range of stiffness tested (Figure 27D), whereas the maximal bead displacement decreased with the increasing stiffness of the measuring micropipette (Figure 27C).

Figure 27. The pushing time ($\Delta t_{push}$), rather than the maximal bead displacement ($x_{bead,max}$), is conserved for different bending stiffness of the measuring micropipette (k). See more details in the text. Each data point shows the average over cells from one experiment (N=6-14 cells per data point). Error bars are omitted here to show the general trend in the experiments. All charts report values from the same experiments.

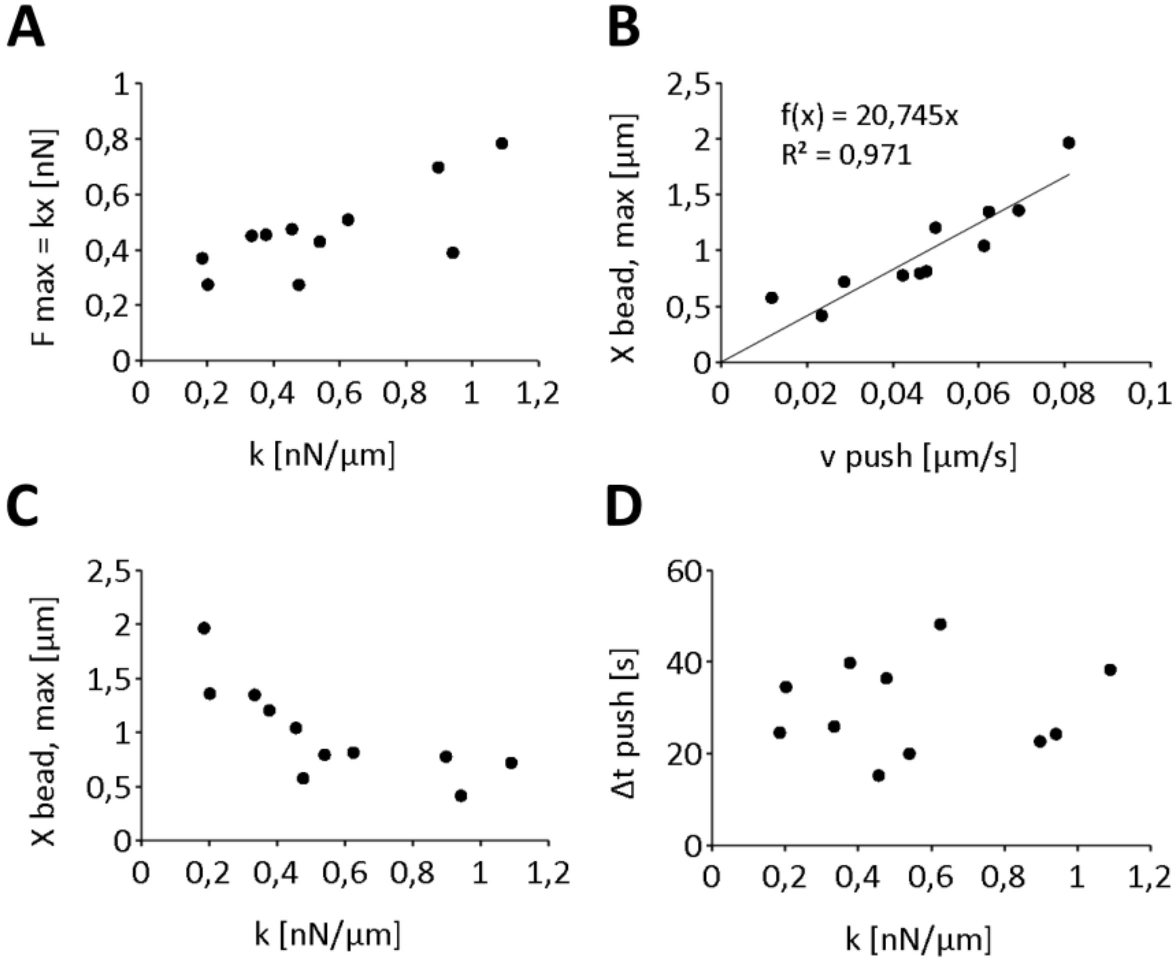

In summary, these results suggest that T cells grew the punch for a fixed time of approximately 20 s. If during this time the compressive force exerted by the bead on the punch reached the threshold value, we could observe the mechanical buckling, consistent with the buckling of an elastic cylinder. After this buckling the punch kept growing with a changed morphology, leading to maximal force being larger than the buckling force. Within the range of stiffness tested, most of the cells reached the buckling event during the pushing time, although for some cells the buckling event happened at the very end of pushing.

The role of the compressive force on the punch growth was further investigated with the micropipette setups approximating $k = 0$ (Figure 16A and 16B in Chapter 1). In the first approach, the bead was not held in the micropipette during the pushing (Figure 28A). With this approach, the punch bent quickly and it was not possible to measure its length. In the second approach, the holding micropipette was retracted as soon as the cell started pushing, to keep the measuring micropipette at the same initial position (Figure 28B), leading to a negligible compressive force exerted on the punch. The length of the punch with this approach reached 5,28 ± 2,06 µm (N=25 cells across 3 experiments), larger than the values obtained when the punch grew against a micropipette of a defined stiffness ($x_{bead}$ values in Figure 27C), suggesting that the compressive force can regulate the length of the punch.

Figure 28. Two approaches to k=0 (punch growing against a negligible compressing force). See also Figure 16A and 16B in Chapter 1. A. The bead was delivered to the cell and the micropipette was retracted as soon as the bead attached to the cell. The punch grew curved, leading to the bead being pushed out of focus. B. The holding micropipette was retracted slowly as soon as the cell started pushing, keeping the measuring micropipette at the initial position (at $x_{bead}$=0). Time in minutes:seconds, scale bar is 10 µm.

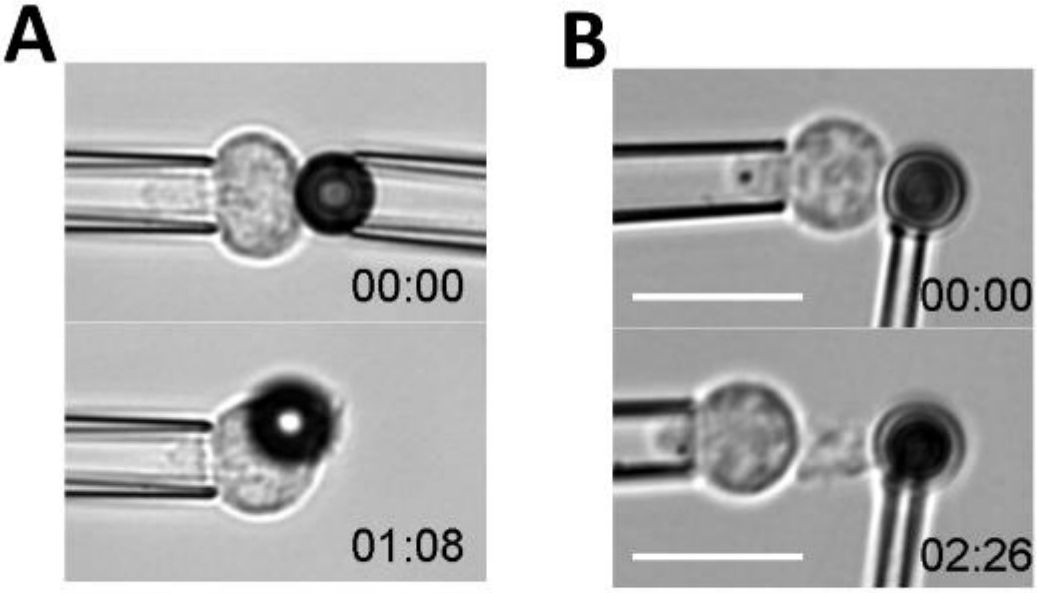

Repeating the same type of analysis for pulling – asking what limits the maximal pulling force generated by T cells during their activation process – is not feasible with the data obtained, as there is a limit on the maximal pulling force that we can measure in the MFP setup. While the cell pulls on the bead held in the measuring micropipette, the bead exerts the same force on the cell, pulling it away from the holding micropipette. When this force equals the aspiration force due to the holding micropipette, the system reaches a critical point in which a small perturbation can eject the cell from the micropipette. This is probably a reason why the measured maximal pulling force was no different for the flytrap cells and the nepenthes cells (Table 3), reflecting the limit of the measurement, not the limit of the force generation by T cells. Indeed, in the study with AFM (Hu & Butte, 2016), the measured out-of-plane pulling forces for OT-II mouse T cells reached more than 2 nN for some cells, with an average of about 1,2 nN, for AFM tips coated with anti-CD3 antibodies. The measured pulling forces in the MFP experiments were smaller than 1 nN (Figure 23).

## 2.4. Activation of lymphoblasts

All the results reported until here were obtained with the resting CD4+ T cells (circulating in the bloodstream). To provide some comparison for forces generated by resting and effector T cells, we ran the MFP experiments with a model of the effector T cells: T lymphoblasts derived in vitro from the resting T cells. To obtain T lymphoblasts the primary CD4+ T cells were activated on plastic plates coated with anti-CD3 antibodies, in the presence of soluble anti-CD28 antibodies, and then cultured for several days in the presence of IL-2 (see Supplement 2 for details).

The comparison between the values obtained in these experiments is shown in Table 4 on the next page.

Table 4. Values obtained in MFP experiments with human primary CD4+ T cells (resting) and CD4+ T lymphoblasts (see Supplement 2 for details) and beads coated with anti-CD3 and anti-CD28 antibodies. The coloured circles refer to the point where the particular value was measured, based on the general chart of the position of the tip of the measuring micropipette ($x_{bead}$) versus time (shown in the middle). Values in **bold** are discussed in the text. Values are shown as mean ± s.e.m. or as median (1st quartile : 3rd quartile) for timing, as the distributions for timing are skewed with few outliers at large values. In total, N=25 cells across 6 experiments, at average bending stiffness of the micropipette k=0,23 nN/µm (resting T cells); and N=20 cells across 2 experiments, at average bending stiffness of the micropipette k=0,26 nN/µm (T lymphoblasts); were analysed, however, for some cells not all the parameters could have been measured. For clarity of the table the N values were not shown for each parameter, but grey shading indicates that the particular value was calculated based on N ≤ 5 cells.

| | **Resting T cells** | **T lympho-blasts** |
|---|---|---|
| Waiting time [s] ○ | 28<br>(22:34) | 18<br>(12:33) |
| Pushing ends [s] ○ | 53<br>(41:63) | 55<br>(42:78) |
| Punch diameter* [µm] ○ | **1,91**±0,07 | **2,86**±0,19 |
| Punch length* [µm] ○ | **2,64**±0,10 | **3,65**±0,38 |
| Cup forms [s] ○ | 83<br>(72:119) | 70<br>(58:98) |
| Cup angle* [°] ○ | **125** ± 6 | **179**± 14 |
| Pulling starts [s] ○ | 149<br>(148:178) | 92<br>(70:125) |

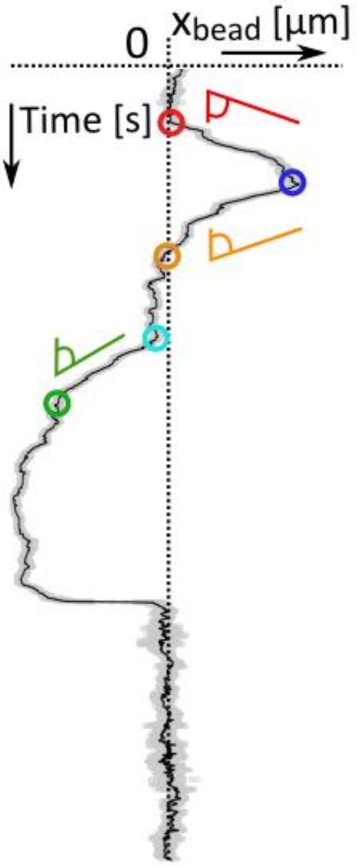

| | **Resting T cells** | **T lympho-blasts** |
|---|---|---|
| \| Pushing speed [µm/s] | 0,086±0,009 | 0,093±0,018 |
| ○ Max pushing force [nN] | 0,38± 0,04 | 0,34± 0,05 |
| \| Return speed [µm/s] | 0,089±0,011 | 0,088±0,024 |
| \| Pulling speed [µm/s] | 0,037±0,008 | 0,103±0,013 |
| ○ Max pullingforce [nN] | 0,23± 0,03 | 0,28± 0,03 |
| ○ Pulling ends [s] | 172<br>(167:227) | 119<br>(93:147) |
| Flytrap : nepenthes cells | 7 : 11 | 14 : 2 |

* see Figure 29 below for how these values were measured.

Figure 29. The measurement of the punch diameter ($D_{punch}$), punch length ($L_{punch}$) and the cup angle on a sample resting T cell put in contact with the bead coated with anti-CD3 and anti-CD28 antibodies. The blue and orange colours refer to the points marked on the chart shown in Table 4, and denote the moment during the activation process when the parameter was measured.

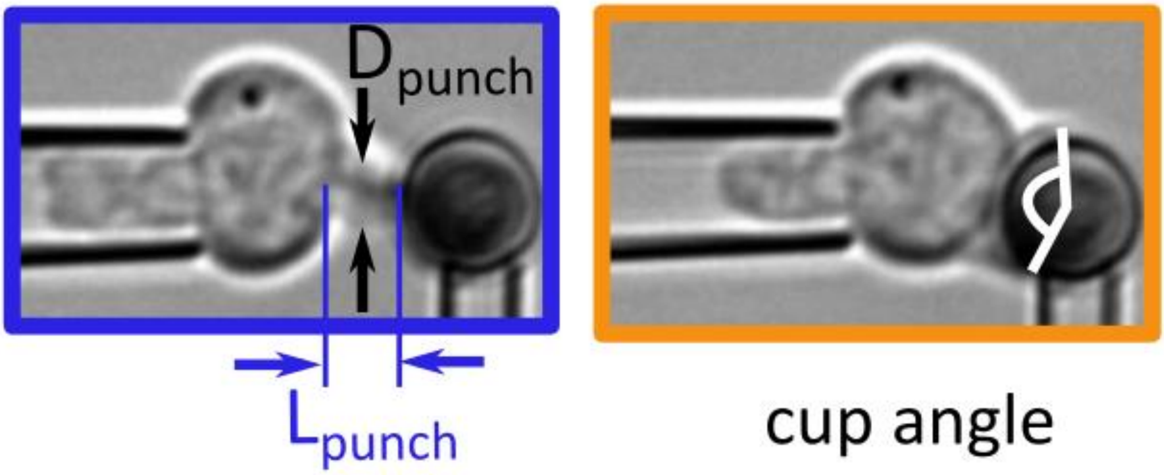

With the used model of effector T cells we do not observe strong differences in force generation between resting and effector CD4+ T cells. Qualitatively, T lymphoblasts follow the same sequence of morphology changes and force generation, quantitatively the force rates and the maximal forces are similar (Table 4). The biggest differences observed were in the morphology of the cells. T lymphoblasts generated longer and wider punches, they also spread more on the bead while they were forming the cup, which could be quantified with the measurement of the cup angle (Figure 29, right). The differences between resting T cells and T lymphoblasts for these three morphological parameters (punch length, punch diameter, cup angle) were significant at $p<0,05$ (two-sided Mann-Whitney U test). The examples of the morphology of T lymphoblasts during the MFP experiments are shown in Figure 30 on the next page.

Figure 30. An example of a CD4+ T lymphoblast put in contact with the bead coated with anti-CD3 and anti-CD28 antibodies. Left to right: the lymphoblast before contacting the bead, with characteristic protrusions, the lymphoblast during pushing, the formation of the cup. Time in minutes:seconds from contact.

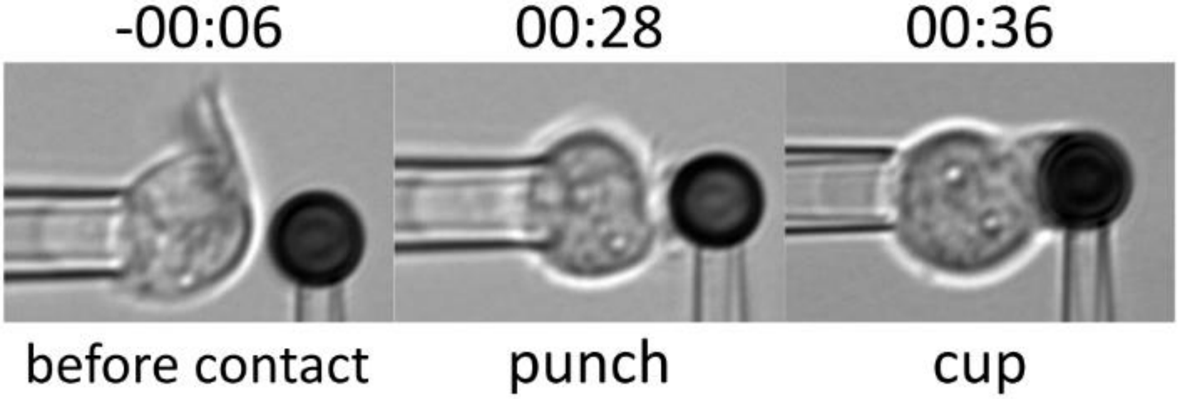

In summary, in this chapter I showed that human primary CD4+ T cells, when put in contact with beads coated with activating antibodies, followed a sequence of changes in morphology during which they generated pushing and pulling forces. This sequence repeated qualitatively also for T lymphoblasts, a model of effector T cells. We next addressed how this sequence is generated by T cells.

# Chapter 3: The mechanism of force generation in T cell activation

In the previous chapter I described the sequence of changes in morphology and of force generation that T cells follow after contacting the activating beads, coated with anti-CD3 and anti-CD28antibodies. One of the goals of my project was to explain the mechanism of force generation in T cell activation. As the force generation is directly linked with the described morphology changes, the measurable morphology changes and the timing of the events are also hallmark of the force generation. Therefore, in the experiments I performed to perturb the force generation, I measured and compared all these outcomes: the values of maximal force and force rate, the morphology of cells, and the timing of the different phases.

The chapter is divided into three sections. First, I look into what triggered the force generation, comparing the results obtained when different surface receptors of T cells were engaged. Then, I directly address the role of different cytoskeleton components in force generation, with the use of different small molecule inhibitors. Finally, in an attempt to bridge these two parts, I report the preliminary results on the signalling pathways, leading from the surface receptors to the cytoskeleton effectors of T cells.

The knowledge of the mechanism of force generation will bring us closer to the question of the function of forces in T cell activation, as once we know the mechanism, we can block it and look at the functional outcomes of the process. This will enable the studies of force generation in the different functional contexts of T cell activation, which I describe in the Perspectives section.

## 3.1 The triggering event

Around 30 s after a T cell contacted the bead coated with the antibodies against CD3 and CD28 molecules it began to develop the pushing and then pulling forces. The triggering event for the sequence of force generation and changes in morphology was therefore the contact with the coated bead. The beads were coated with the antibodies that specifically bind the receptors in the T cell membrane, but the influence of the non-specific binding of T cells to the surface cannot be neglected. It was shown for example that the contact between T cells and a glass surface coated with poly-L-lysine decreased the mobility of TCRs (or, to be more precise, the mobility of CD3ε molecules which were labelled with antibodies in Jurkat T cells) (Ponjavic et al., 2018). In the same study, the surfaces coated with fibronectin, poly-L-lysine, or unspecific antibodies (IgG purified from bovine serum) induced a calcium peak (an increase in cytoplasmic concentration of calcium ions).These events are also early signs of the T cell activation process. We asked therefore whether the morphology changes and the force generation that we observed were specific to T cell activation (TCR triggering), or were maybe dependent on the binding of T cells to a surface, or on the immobilisation of the T cell membrane proteins.

We used the MFP technique with the resting CD4+ T cells and the same beads – of the same size, and made of the same material – but coated with the antibodies against CD45, a phosphatase present on the surface of T cells, in general thought to be a negative regulator of the activation process. In this setting, we observed no force generation (Figure 31 on the next page, black trace) for all 9 of the cells tested (one experiment); consistent with the results obtained for the in-plane forces on the polyacrylamide gels coated with anti-CD45 antibodies (Hui et al., 2015).

Figure 31. MFP experiments show that force generation is specific to T cell activation. Force trace (calculated as the position of the tip of the measuring micropipette multiplied by its bending stiffness, $F=kx_{bead}$) for two different cells in MFP experiments: a resting CD4+ T cells in contact with a bead coated with anti-CD3 antibodies (anti-CD3 bead, red), and a resting CD4+ T cell in contact with a bead coated with anti-CD45 antibodies (anti-CD45 bead, black). Vertical arrows point to the contact frame, i.e. the moment when I stopped moving the micropipette holding the cell. For the anti-CD45 bead in this example I exaggerated this initial contact, to make sure that the cell is in contact with the bead.

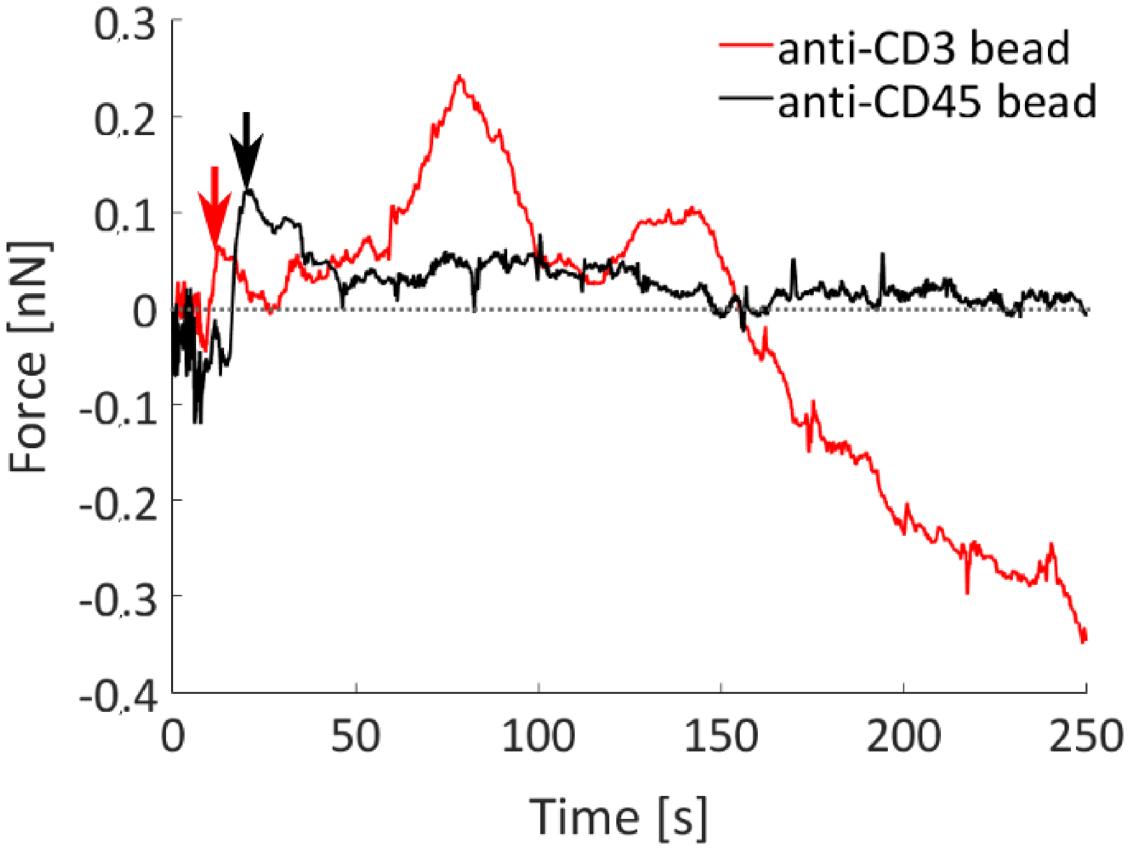

The morphology of cells put in contact with beads coated with anti-CD45 antibodies did not show any marked differences throughout the recording time (Figure 32A on the next page, bottom row). To look on the morphology of cells in more detail, we imaged with scanning electron microscopy (SEM) T cells put in contact with the beads coated with antibodies against CD45. Cells were put on slides coated with poly-L-lysine, and then beads were added on top;for details on how the slides for SEM were prepared see Supplement 3. The SEM images revealed that the membrane of T cells spread a bit on the beads coated with anti-CD45 antibodies (Figure 32B, right), but no cell reorganisation happened.

Figure 32. Morphology of resting CD4+ T cells put in contact with beads coated with anti-CD3 and anti-CD28 antibodies (anti-CD3/anti-CD28) and anti-CD45 antibodies (anti-CD45). A. MFP experiments. Images show two cells from two different experiments. Scale bar is 10 µm. B. SEM experiments. Images show two cells from two different experiments. Scale bar is 1 µm. SEM experiments were performed by Claire Hivroz and me, imaging was done by Virginie Bazin from IBPS, at Université Pierre et Marie Curie.

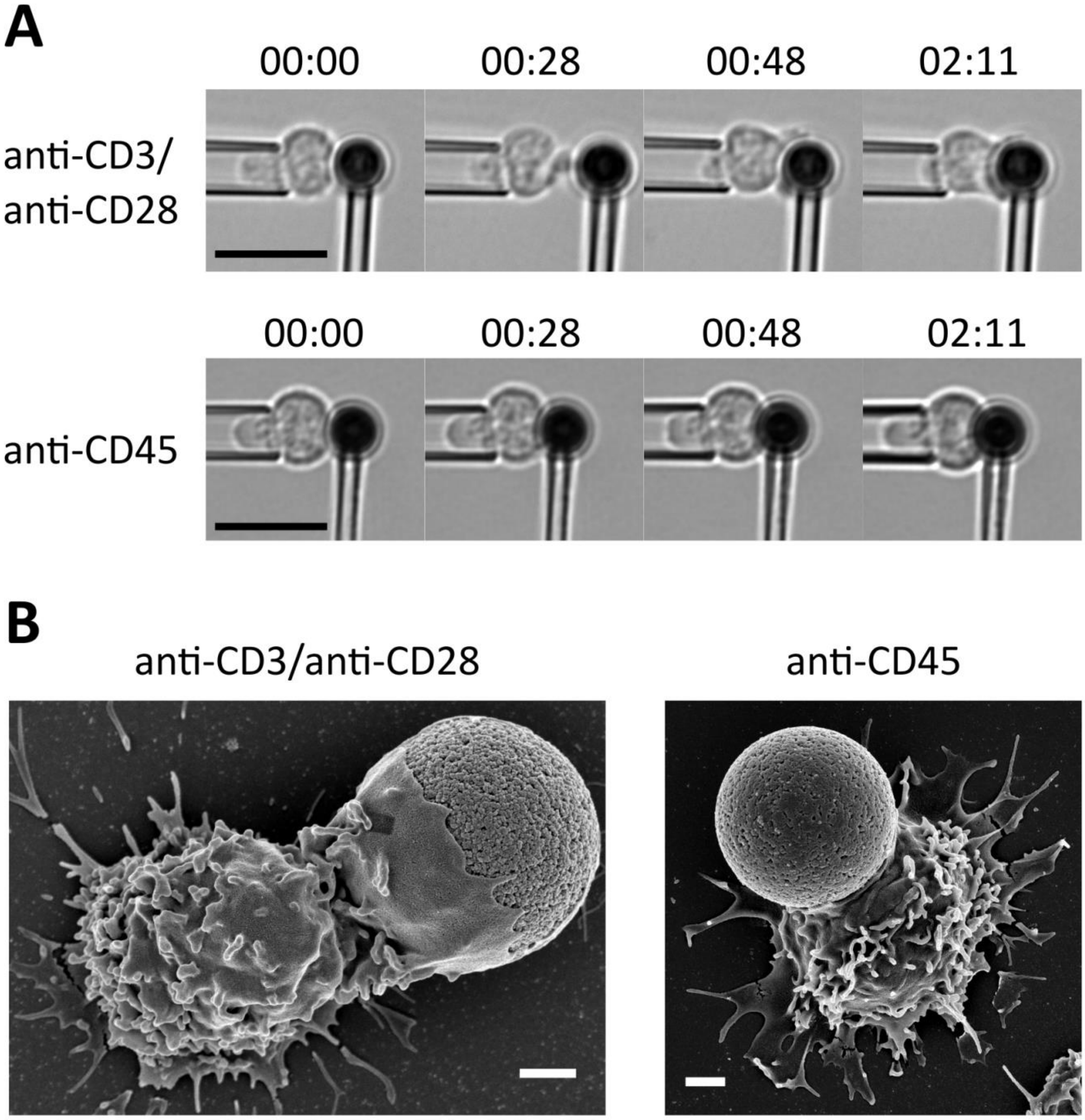

As the MFP and SEM experiments resulted in a small number of cells tested, I used a complementary approach with a simple flow microchamber, made of two rectangular coverslips (Figure 33A). On the bottom coverslip, two lines of vacuum grease, spaced by approximately 5 mm, formed the walls of the microchamber. The second, smaller coverslip covered the chamber. Such chamber was filled by capillarity forces, when a liquid (PBS or medium) was dropped on one side of the smaller coverslip (Figure 33A, right). The small volume of chamber (typically 20-40 µl) allowed quick changing of the medium during the experiment, and also concentrated the cells close to the bottom of the chamber, making them easy to track from the beginning of the recording on an inverted microscope.

Figure 33. Microchamber experiments. A. Schematic drawing of the preparation of the microchamber. The lines of vacuum grease are made with a syringe with a plastic pipette tip attached to it (left). Then the chamber is covered with the other coverslip (middle) and filled with liquid by capillarity (right). B. Recording of a microchamber movie. An area in the filled microchamber (right) is monitored with the microscope. The large image (middle) contains several hundred cell-bead couples, after zooming in (right) individual cells can be scored. o – living cell, x – "dead" cell, excluded from analysis, see the text. Scale bar is 100 µm in the middle image and 25 µm in the right image. C. Examples of cell morphology during the microchamber experiments. Resting CD4+ T cells in contact with beads coated with anti-CD3 and anti-CD28 antibodies (top row) and with anti-CD45 antibodies (bottom row). * – active cell, # – not active cell in contact with the bead. Cells are flowing from right to left. Time in minutes:seconds from the beginning of the recording.

Figure 33 is shown on the next page.

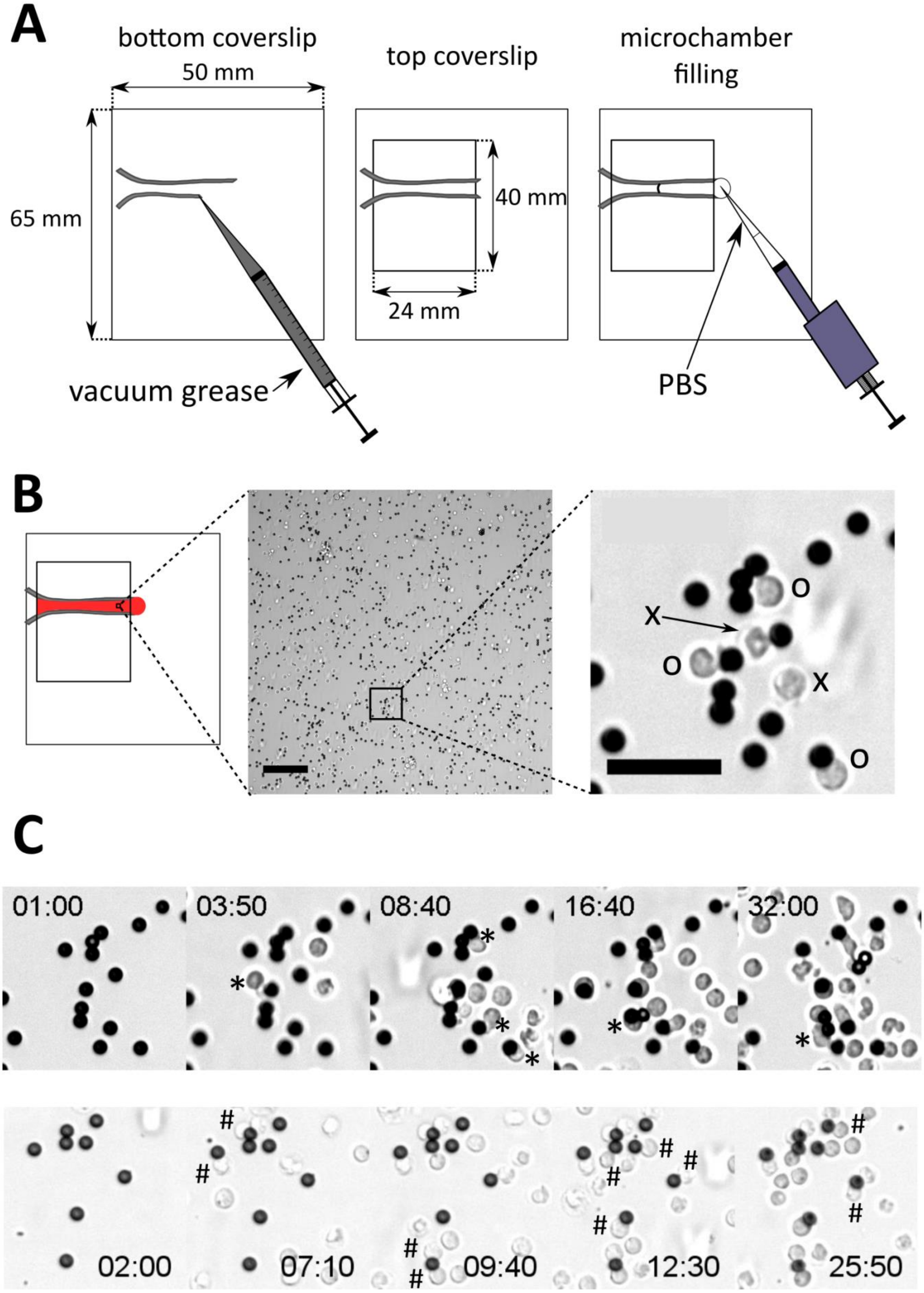

Figure 33. See legend on the previous page.

For an experiment, the chamber was first filled with bead solution in PBS. The beads sedimented and, because of lack of serum proteins, stuck to the bottom coverslip. Then the complete medium was flushed through (by aspirating liquid on the exit side of the chamber at the same time as the new liquid was added), followed with the suspension of cells. Image was acquired with 20× objective, providing general morphology information for typically 100-300 cells during 20-30 minutes of recording (Figure 33B and 33C). The morphology of active cells repeated the one known from the micropipette experiments (see Chapter 2.1), with the pushing protrusion appearing on the cell-bead interface, then collapsing into the cup structure spreading on the bead (Figure 33C, top row). After excluding from analysis cells that were visibly "dead" (see examples marked in Figure 33B), active cells formed 90% of 411 cell-bead pairs for the resting CD4+ T cells and anti-CD3/anti-CD28 beads (two experiments), and 0% of 313 cell-bead pairs for the resting CD4+ T cells and anti-CD45 beads (one experiment).

These results show that the binding to CD45 molecule on T cell surface did not induce the force generation or any large changes in morphology. Thus, the force generation, and the described above associated changes in T cell morphology, were specific to the activation process – they were triggered with the binding to the CD3 and CD28 molecules.

We were next interested in finding the minimal signal needed to start the force generation. As the signalling downstream of the CD28 molecule is known to influence, among other processes, the cytoskeleton remodelling during T cell activation, we wanted to track the force generation without this additional stimulatory signal. We used the beads coated with anti-CD3 antibodies only. Table 5 shows the comparison of the results obtained in these two conditions. The experiments showed that binding of the anti-CD3 antibodies triggered, qualitatively, the same sequence of the morphology changes and force generation (see also the example trace in red in Figure 31). However, we were able to measure some quantitative differences, mostly in cell morphology. Without the binding to CD28 (CD3 only) T cells grew longer and thicker punches, also spread further on the bead (bigger cup angle). Interestingly, there is a possible bias towards flytrap cells with anti-CD3 only beads. The difference in proportion of the flytrap cells over all the assigned cells (Table 5) gives the p-value of 0,033 (Fisher's exact test).

Table 5. Values obtained in MFP experiments with resting CD4+ T cells and beads coated both with anti-CD3 and anti-CD28 antibodies (left columns) or only with anti-CD3 antibodies (right columns). The coloured circles refer to the point where the particular value was measured, based on the general chart of the position of the tip of the measuring micropipette ($x_{bead}$) versus time (shown in the middle). Values in **bold** are discussed in the text. Values are shown as mean ± s.e.m. or as median (1st quartile : 3rd quartile) for timing, as the distributions for timing are skewed with few outliers at large values. In total, N=25 cells across 6 experiments, at average bending stiffness of the micropipette k=0,23 nN/µm (anti-CD3 anti-CD28); and N=22 cells across 2 experiments, at average bending stiffness of the micropipette k=0,21 nN/µm (anti-CD3 only); were analysed, however, for some cells not all the parameters could have been measured. For clarity of the table the N values are not shown for each parameter, but grey shading indicates that the particular value was calculated based on N ≤ 5 cells.

| | anti-CD3 anti-CD28 | anti-CD3 only |
|---|---|---|
| Waiting time [s] ○ | 28<br>(22:34) | 24<br>(18:30) |
| Pushing ends [s] ○ | 53<br>(41:63) | 63<br>(54:82) |
| Punch diameter [µm] ○ | **1,91**± 0,07 | **2,60**± 0,18 |
| Punch length[µm] ○ | **2,64**± 0,10 | **3,26**±0,25 |
| Cup forms [s] ○ | 83<br>(72:119) | 103<br>(99:136) |
| Cup angle [°] ○ | **125** ± 6 | **162**± 10 |
| Pulling starts [s] ○ | 149<br>(148:178) | 172<br>(157:237) |

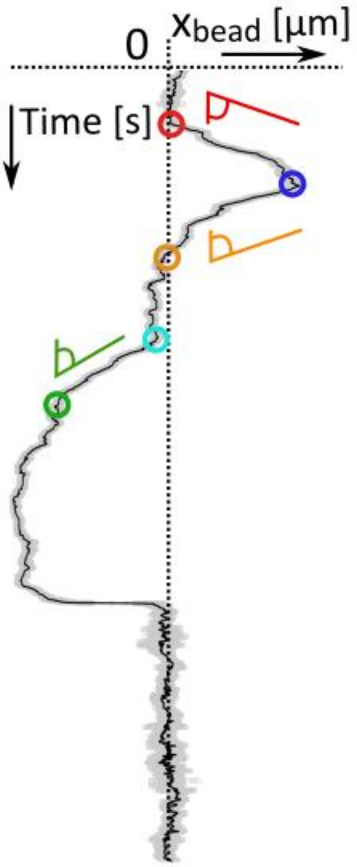

| | anti-CD3 anti-CD28 | anti-CD3 only |
|---|---|---|
| ▌ Pushing speed [µm/s] | 0,066± 0,006 | 0,064± 0,011 |
| ○ Max pushingforce [nN] | 0,38± 0,04 | 0,34± 0,06 |
| ▌ Return speed [µm/s] | 0,089± 0,011 | 0,068± 0,009 |
| ▌ Pulling speed [µm/s] | 0,037 ± 0,008 | 0,030± 0,008 |
| ○ Max pullingforce [nN] | 0,23± 0,03 | 0,22± 0,04 |
| ○ Pulling ends [s] | 172<br>(167:227) | 241<br>(230:268) |
| Flytrap : nepenthes cells | **7 : 11** | **12 : 3** |

In summary, binding to the CD45 molecules on T cell surface was not sufficient to trigger force generation; binding to the CD3ε molecules was sufficient to generate the sequence of force generation and of changes in T cell morphology.

In the kinetic segregation model, the local exclusion of CD45 molecule from the "close contacts" (Chang et al., 2016) formed by TCR-peptide-MHC complexes tips the balance towards the phosphorylation and starts the signalling cascade inside the T cell. This segregation was reported to happen in a minimal reconstituted model with liposomes interacting with supported lipid bilayer (Carbone et al., 2017), which indicates that the segregation does not require the cytoskeleton activity, and can contribute to the earliest events in T cell activation, before the cytoskeleton reorganisation is triggered through the intracellular signalling. In our system, the activating antibodies were covalently bound to the bead surface, and thus they immobilised the CD3 or CD45 molecules on T cell surface. The local organisation of the receptors on the contact area could be similar in these two situations: randomly immobilised CD3 molecules, or randomly immobilised CD45 molecules, would give a similar picture of membrane organisation. It is hard to mention the exclusion of CD45 molecules from the contact area in any of these cases. However, only the beads coated with anti-CD3 antibodies triggered the sequence of the changes in cell morphology and of force generation. It is possible that each antibody bound to CD3 molecule created this small – molecular size – exclusion of CD45 molecules. In addition, in a recent study (Al-Aghbar, Chu, Chen, & Roffler, 2018), the researchers proposed that high-affinity ligands do not require the exclusion of CD45 to trigger the T cell response. The anti-CD3 antibodies used on the beads in our study were a high-affinity ligand. Thus, our results allow to conclude that force generation requires the engagement of the TCR complex, but the model used did not allow to address the importance of the spatial segregation of the molecules in T cell membrane for the triggering of the activation process. On the further stages of the formation of the immunological synapse, the mobility of the anti-CD3 antibodies was shown to impact on the cytoskeleton organisation and on the ability of T cells to spread on the activating substrate (Dillard, Varma, Sengupta, & Limozin, 2014). It is thus likely that the mobility of activating molecules would impact on the force generation and the changes in cell morphology described here. In this context, the use of beads with mobile ligands, for example beads coated with a lipid bilayer with the activating molecules embedded into it, would be an interesting extension of the presented results.

The signalling downstream of CD28 is known to impact on the cytoskeleton reorganisation. In our setup, the engagement of CD28 did not change the magnitude of generated forces, and the force rates, as the results obtained with beads coated with only anti-CD3 antibodies, and both anti-CD3 and anti-CD28 antibodies were similar (Table 5). A different result was obtained in a study with micropillars (Bashour et al., 2014), where the co-stimulation with anti-CD28 antibodies led to almost doubling of the generated traction force per micropillar. These forces were measured in-plane, whereas the out-of-plane forces were measured with MFP. It is difficult to conclude on the role of CD28 costimulation in force generation based on these results. More experiments are needed to resolve this issue.

The binding of antibodies to the membrane receptors was the first step leading to the force generation. The further steps of the process, happening inside the T cell, result in the described changes in T cell morphology. As cytoskeleton governs the shape of a cell, these changes require a substantial reorganisation of the cytoskeleton. Thus, we decided to study the implication of the different components of the cytoskeleton in the force generation in T cell activation.

## 3.2 Cytoskeleton reorganisation

It was shown already that inhibition of actin polymerisation with latrunculin A blocked completely force generation in T cells (for T cells incubated in 0,5 μM latrunculin A, (Husson et al., 2011); or 1 μM latrunculin A, (Hu & Butte, 2016; Hui et al., 2015)). These results show that actin polymerisation is necessary for force generation. Actin filaments are nucleated and organised in cells by various proteins, including myosin, formins and Arp2/3 complex. We were interested in studying the role of these different actin-binding proteins in the force generation in T cell activation.

Non-muscle myosin II is a molecular motor responsible for pulling of the actin filaments in various types of cells. It has been shown that it is implicated in T cell activation, but its precise role is still debated (Hammer & Burkhardt, 2013). Myosin Light Chain Kinase (MLCK) activates myosin as it phosphorylates the regulatory light chain of myosin. MLCK can be inhibited with ML-7, a small molecule inhibitor (Saitoh, Ishikawa, Matsushima, Naka, & Hidaka, 1987). With MFP experiments, we studied force generation by T cells incubated with 30 μM ML-7. Results are summarised in Table 6 on the next page. The experiments showed that cells incubated with ML-7 went through, qualitatively, the same sequence of the changes in morphology and of force generation. However, we were able to measure some quantitative differences, notably in the reduced return speed.

Table 6. Values obtained in MFP experiments with resting CD4+ T cells and beads coated both with anti-CD3 and anti-CD28 antibodies, pre-treated for 30 minutes and kept during the experiment in 30 µM ML-7, MLCK inhibitor, or the same vol/vol proportion of DMSO (vehicle control). The coloured circles refer to the point where the particular value was measured, based on the general chart of the position of the tip of the measuring micropipette ($x_{bead}$) versus time (shown in the middle). Values in **bold** are discussed in the text. Values are shown as mean ± s.e.m. or as median (1st quartile : 3rd quartile) for timing, as the distributions for timing are skewed with few outliers at large values. In total, N=25 cells across 6 experiments, at average bending stiffness of the micropipette k=0,225 nN/µm (DMSO control); and N=29 cells across 2 experiments, at average bending stiffness of the micropipette k=0,208 nN/µm (ML-7, one of the experiments was performed by Julien Husson); were analysed, however, for some cells not all the parameters could have been measured. For clarity of the table the N values were not shown for each parameter, but grey shading indicates that the particular value was calculated based on N ≤ 5 cells.

| | **DMSO control** | **ML-7 30 µM** |
|---|---|---|
| Waiting time [s] ○ | 28<br>(22:34) | 29<br>(19:42) |
| Pushing ends [s] ○ | 53<br>(41:63) | 58<br>(43:104) |
| Punch diameter [µm] ○ | 1,91 ± 0,07 | 2,01± 0,12 |
| Punch length[µm] ○ | 2,64 ± 0,10 | 2,35± 0,12 |
| Cup forms [s] ○ | 83<br>(72:119) | 106<br>(75:156) |
| Cup angle [°] ○ | 125 ± 6 | 135 ± 4 |
| Pulling starts [s] ○ | 149<br>(148:178) | 144<br>(112:238) |

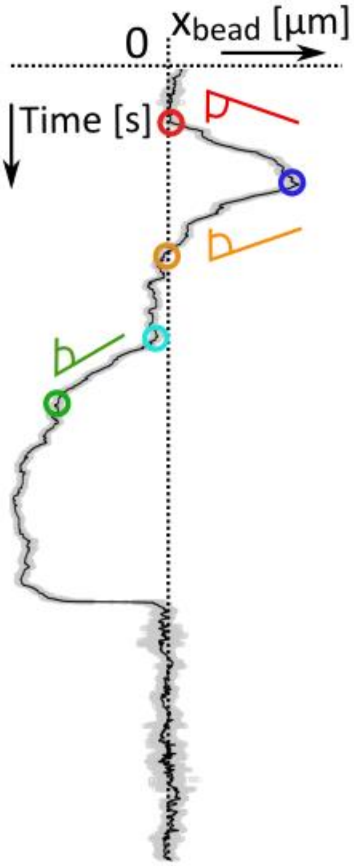

| | **DMSO control** | **ML-7 30 µM** |
|---|---|---|
| ▮ Pushing speed [µm/s] | 0,066 ± 0,006 | 0,069 ± 0,007 |
| ○ Max pushing force [nN] | 0,38± 0,04 | 0,33 ± 0,02 |
| ▮ Return speed [µm/s] | **0,089** ± 0,011 | **0,044**± 0,006 |
| ▮ Pulling speed [µm/s] | 0,037 ± 0,008 | 0,021± 0,004 |
| ○ Max pulling force [nN] | 0,23± 0,03 | 0,16 ± 0,03 |
| ○ Pulling ends [s] | 172<br>(167:227) | 185<br>(142:302) |
| Flytrap : nepenthes cells | 7 : 11 | 6 : 10 |

As the observed influence of the ML-7 inhibitor was small, we wanted to check if the inhibitor was active in T cells. The activity of MLCK results in phosphorylation of the light chain of myosin; therefore, the activity of ML-7 can be directly verified with the level of this phosphorylation. In the western blot analysis (Figure 34), the signal from phosphorylated myosin light chain (P-MLC) disappeared in ML-7 treated cells, also in the cells mixed with beads coated with anti-CD3 and anti-CD28 antibodies, recapitulating the conditions of the standard MFP experiment. This confirmed that MLCK was inhibited in T cells.

Figure 34. ML-7 treatment of cells inhibits phosphorylation of the myosin light chain (MLC). Human primary CD4+ T cells were pre-incubated for 15 minutes at 37°C with 30 µM ML-7, the MLCK inhibitor, or the vehicle (DMSO) alone. Cells were then incubated for 10 to 30 minutes with beads coated with antibodies against CD3 and CD28 molecules (activation) at 37°C in the presence of the inhibitor. Phosphorylation of the myosin light chain (MLC) was measured with western blot analysis. The gp96 protein in each lane is shown as loading control. Compared to control conditions (DMSO), the cells incubated with ML-7 show less phosphorylation of MLC, demonstrating that ML-7 is inhibiting MLCK in our conditions. Adapted from Supplemental Figure S9 in (Sawicka et al., 2017), CC-BY-NC-SA 3.0 licence. The western blot experiment was performed by Claire Hivroz.

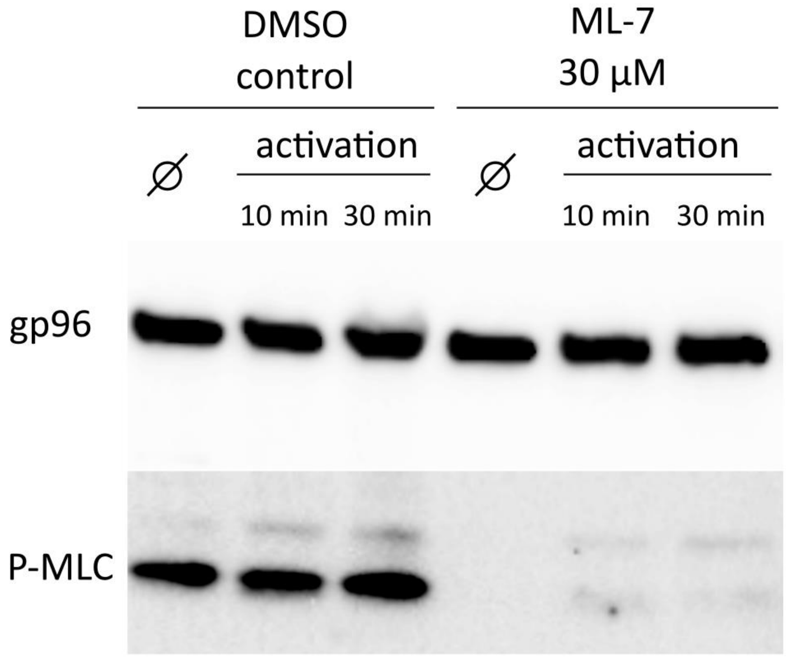

The small influence of MLCK inhibition on force generation suggests that myosin was not involved in the out-of-plane force generation and changes in cell morphology during T cell activation, especially for the pushing forces.

Formins are a family of proteins responsible for nucleating and elongating linear actin filaments. Formins are known to be implicated in T cell activation process, both as actin and microtubules nucleators. Knowing this, we were interested in the role of formins in force generation.

Inhibition of formins with small molecule inhibitor of formin homology 2 domain (SMIFH2, (Rizvi, Neidt, et al., 2009)), resulted in a perturbation of the sequence of force generation and of changes in morphology. T cells treated with 25 μM SMIFH2 produced and collapsed punches, but then, for the majority of them (22 out of 29 cells across 3 experiments, compared with 3 out of 25 cells across 6 experiments for control) did not form the cup and stayed inactive for the rest of the recording. The tail (part of the cell aspirated in the holding micropipette) also behaved abnormally, as the cells treated with SMIFH2 shortened the tail much later (median time: 107 s vs 37 s for the control cells), or did not shorten it at all (16 out of 29 cells). Quantitative analysis of the MFP experiments revealed that inhibition of formins diminished also maximal pushing force, but not pushing speed, and the maximal length and diameter of the punch (Table 7 on the next page). The return speed was also reduced, reaching the value similar to the one obtained with ML-7.

Table 7. Values obtained in MFP experiments with resting CD4+ T cells and beads coated both with anti-CD3 and anti-CD28 antibodies, pre-treated for 30 minutes and kept during the experiment in 25 µM SMIFH2, formin inhibitor, or the same vol/vol proportion of DMSO (vehicle control). The coloured circles refer to the point where the particular value was measured, based on the general chart of the position of the tip of the measuring micropipette ($x_{bead}$) versus time (shown in the middle).Values in **bold** are discussed in the text. Values are shown as mean ± s.e.m. or as median (1st quartile : 3rd quartile) for timing, as the distributions for timing are skewed with few outliers at large values. In total, N=25 cells across 6 experiments, at average bending stiffness of the micropipette k=0,225 nN/µm (DMSO control); and N=29 cells across 3 experiments, at average bending stiffness of the micropipette k=0,226 nN/µm (SMIFH2, were analysed; however, for some cells not all the parameters could have been measured. For clarity of the table the N values were not shown for each parameter, but grey shading indicates that the particular value was calculated based on N ≤ 5 cells.

| | **DMSO control** | **SMIFH2 25 µM** |
|---|---|---|
| Waiting time [s] ○ | 28<br>(22:34) | 37<br>(22:52) |
| Pushing ends [s] ○ | 53<br>(41:63) | 63<br>(47:98) |
| Punch diameter [µm] ○ | **1,91**± 0,07 | **1,70**± 0,06 |
| Punch length[µm] ○ | **2,64**± 0,10 | **2,25**± 0,13 |
| Cup forms [s] ○ | 83<br>(72:119) | 134*<br>(104:182) |
| Cup angle [°] ○ | 125 ± 6 | 149 ± 16 |
| Pulling starts [s] ○ | 149<br>(148:178) | 164<br>(145:183) |

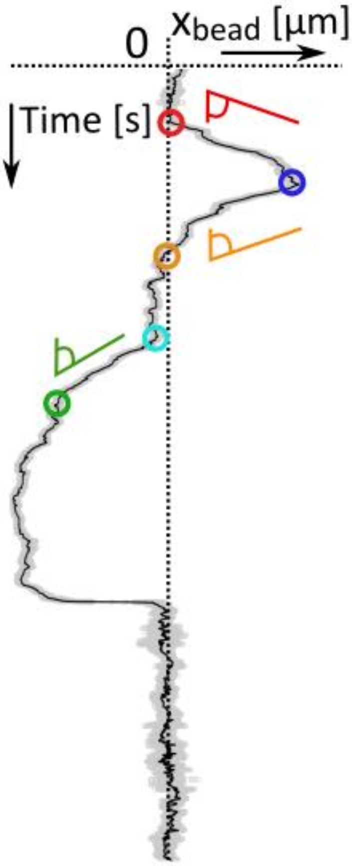

| | **DMSO control** | **SMIFH2 25 µM** |
|---|---|---|
| ▌ Pushing speed [µm/s] | **0,066**± 0,006 | **0,059**± 0,006 |
| ○ Max pushingforce [nN] | **0,38**± 0,04 | **0,25**± 0,03 |
| ▌ Return speed [µm/s] | **0,089** ± 0,011 | **0,048**± 0,009 |
| ▌ Pulling speed [µm/s] | 0,037 ± 0,008 | 0,032 ± 0,003 |
| ○ Max pulling force [nN] | 0,23± 0,03 | 0,17 ± 0,01 |
| ○ Pulling ends [s] | 172<br>(167:227) | 177<br>(154:238) |
| Flytrap : nepenthes cells | 7 : 11 | 2 : 1 |

* Cup formed only for 7 out of 29 cells treated with SMIFH2; for the rest of the cells the reported time is the moment when the punch collapsed completely.

These results indicate that formin activity was important for the formation of the cup, and that formin inhibition had a profound impact on the force generation, appearing already at the end of the pushing phase, or around 1 minute from the binding of the activating antibodies.

To gather further insight into the role of actomyosin cytoskeleton in the observed morphology changes, we treated T cells also with CK666, inhibitor of Arp2/3 complex (Nolen, Tomasevic, et al., 2009), and with para-nitroblebbistatin, the photostable variant of blebbistatin, inhibitor of myosin (Képiró et al., 2014). Figure 35 shows examples of morphology of T cells treated with different inhibitors, when they contacted the beads coated with anti-CD3 and anti-CD28 antibodies, in the microchamber experiments. The images summarise the effect of the different small molecule inhibitors of cytoskeleton on T cells.

Figure 35. The influence of the cytoskeleton inhibitors on the morphology of T cells during their activation. Human primary CD4+ T cells were pre-incubated for 30 minutes with 25 µM SMIFH2 (inhibitor of formin homology 2 domain), 25 µM CK666 (inhibitor of Arp2/3 complex), 30 µM ML-7 (inhibitor of Myosin Light Chain Kinase), 50 µM para-nitro blebbistatin (pnBleb, inhibitor of myosin ATPase activity) or the same volume of DMSO (vehicle control), and then used in microchamber experiments (see Figure 33) with the beads coated with anti-CD3 and anti-CD28 antibodies. Inhibitors were present in the medium throughout the recording. The brightfield images show examples of cell morphology during the experiment. Time in minutes:seconds, scale bar is 10 µm. ML-7 examples are taken from an experiment in which an additional 1,5x lens was used, leading to larger maginification of the image.

Figure 35 is shown on the next page.

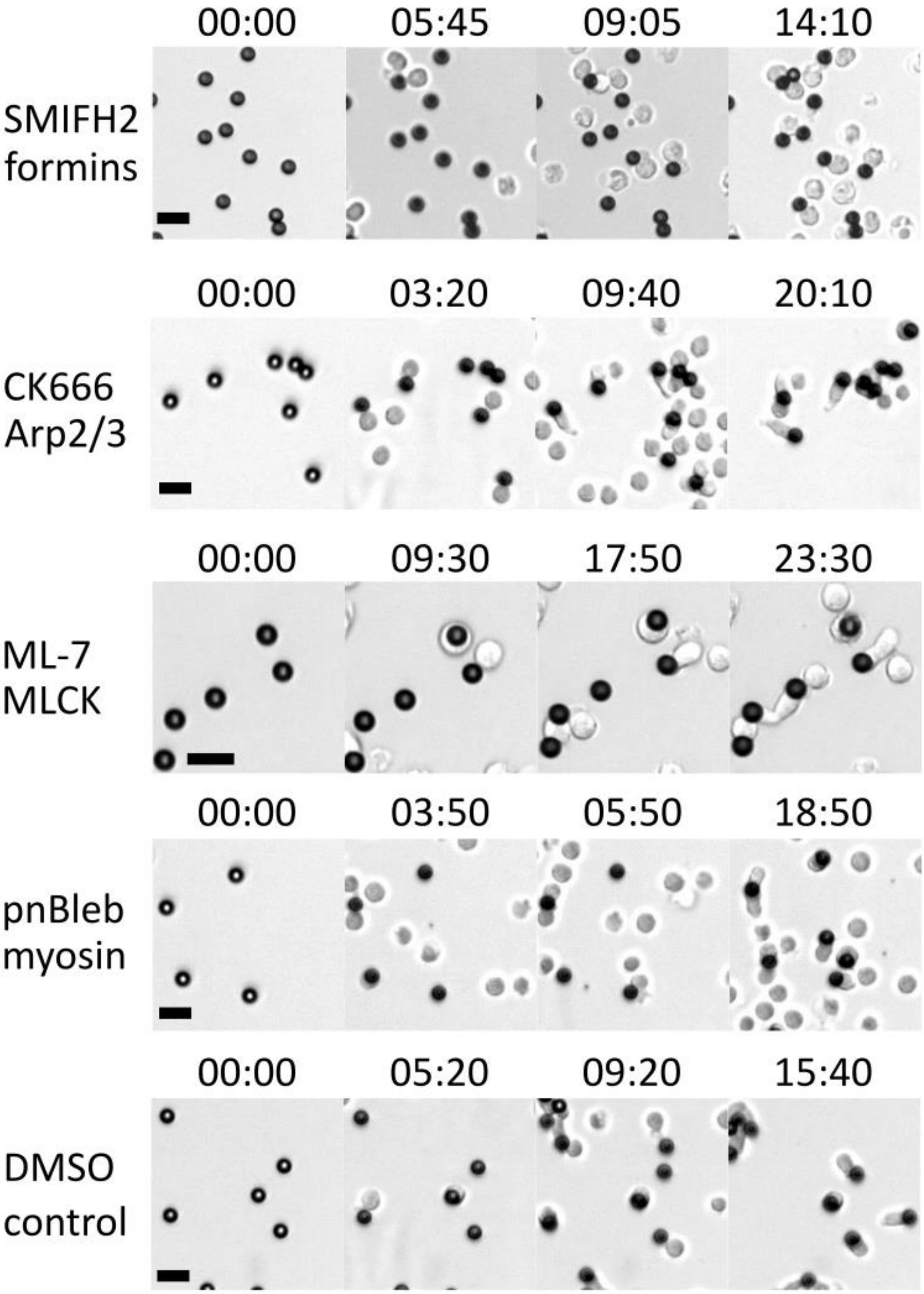

Figure 35. See legend on the previous page.

The three inhibitors (ML-7, CK666 and SMIFH2) changed the waiting time (time between the contact and the onset of pushing protrusion, Figure 36). The time was not different for the blebbistatin. The change in median times for ML-7 and CK666, although statistically significant, corresponds to the difference in only one or two frames of the recorded movies (which were recorded at 1 frame every 10 s), suggesting that the biological effect of the inhibition was small. The effect was the largest in case of SMIFH2, suggesting that the nucleation of actin by formins plays an important role in the beginning of the growth of the punch.

Figure 36. The time between the contact and the onset of the growth of the pushing protrusion (punch). A. The way in which the waiting time was measured for the individual cells. Time in minutes:seconds, scale bar is 10 μm. Last frame shows the elongated shape of the activated cell – of the type nepenthes. B. Quantification of the waiting time for the different inhibitors used. The times were measured in two independent experiments, the concentration of inhibitors and number of cells are indicated below the chart. n.s. not significant * p<0,05 **** p<0,0001 Mann-Whitney U test. One value at 580 s for ML-7, one value at 330 s for CK666 and one value at 355 s for SMIFH2 are not shown for clarity of the chart; these values were included in the calculation of the median (red number) and interquartile range shown on the boxplot.

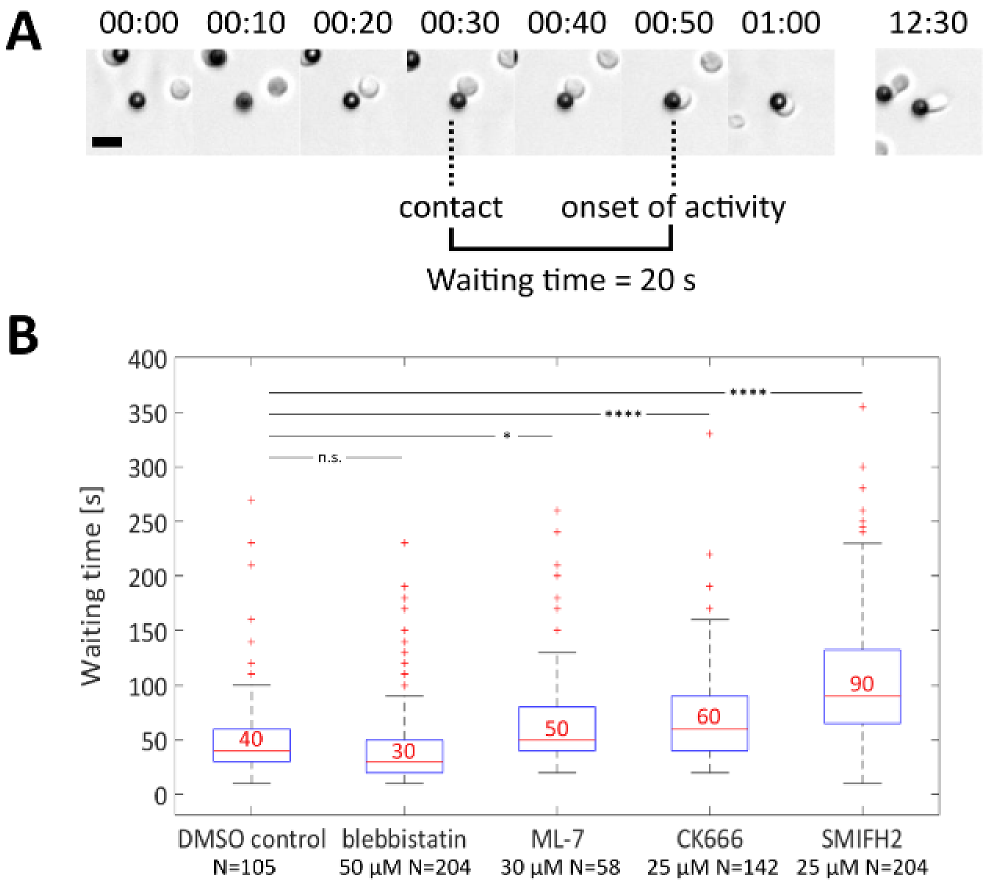

In summary, in MFP experiments we observed a strong influence of SMIFH2 on changes in cell morphology and on force generation, and a small influence of ML-7 on changes in cell morphology and on force generation. In the microchamber experiments we observed a small influence of CK666 on the waiting time, and no influence of CK666 on the cell morphology, and no influence of blebbistatin on the cell morphology or the waiting time. These results suggest that formins are an important effector for force generation and morphology changes in T cell activation, and will be further addressed in the Discussion section.

## 3.3 Signalling cascade

The results of the MFP experiments with beads coated only with antibodies against CD3 molecule showed that binding to the CD3 molecule was the first step to generate forces. It is known that this binding triggers a signalling cascade inside T cells. We asked what is the link between this signalling cascade and the sequence of force generation and changes in cell morphology that we observed. This link should lead from the CD3 molecule in the T cell membrane to the cytoskeleton effectors. We decided to study the phosphorylation of the proteins downstream of the CD3 molecule when T cells were incubated with different cytoskeleton inhibitors.

To our surprise, western blot analysis revealed that the phosphorylation of ζ chains disappeared both in cells treated with ML-7 (Figure 37A on the next page), and in cells treated with SMIFH2 (Figure 37B). The basal level of phosphorylation, in non-activating conditions, was also reduced, suggesting that both MLCK and formins are necessary to sustain the tonic signalling.

Figure 37. The cytoskeleton inhibitors perturb the phosphorylation of ζ chains. Human primary CD4+ T cells were pre-incubated for 30 minutes at 37°C with 30 µM ML-7, the MLCK inhibitor (A), 25 µM SMIFH2, the formins inhibtor (B), or the vehicle (DMSO) alone. Cells were then activated for 10 to 30 minutes with beads coated with anti-CD3 and anti-CD28 antibodies (activation) at 37°C in the presence of inhibitors. Phosphorylation of the ζ chains was measured by western blot analysis. The gp96 protein (A) and LAT protein (B) in each lane are shown as loading controls. In control conditions (DMSO), the phosphorylation of the ζ chains increased with the activation time. In comparison, across all time points, the cells incubated with ML-7 or SMIFH2 show less phosphorylation of ζ chains, indicating that treatment with cytoskeleton inhibitors perturbed this early (close to the cell membrane) signalling event in T cell activation. The results shown are representative of two independent experiments with three (A) or four (B) different cell donors. The ML-7 experiments were performed by Claire Hivroz.

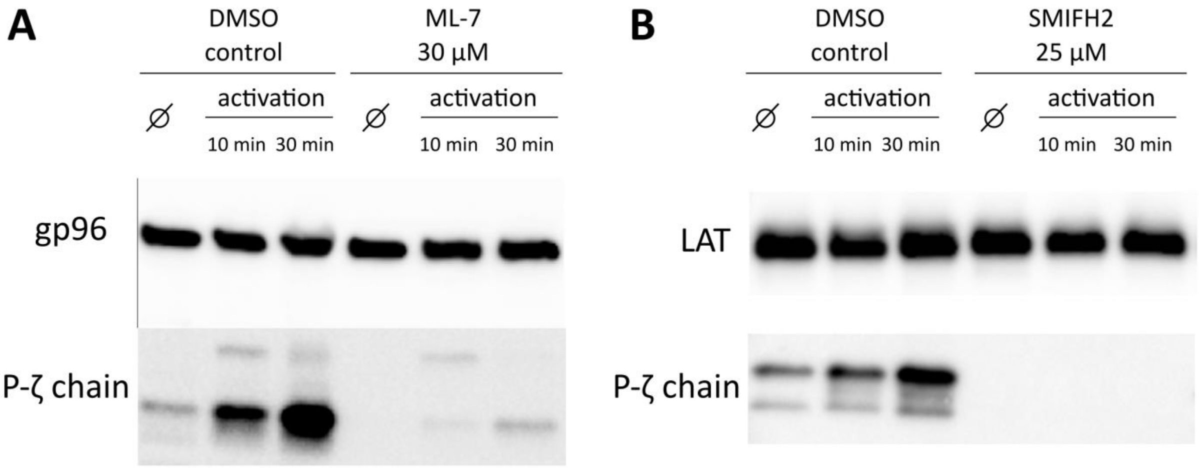

These results indicate that cytoskeleton activity (the activity of formins and MLCK) is required for the phosphorylation of the ζ chains, one of the earliest signalling events triggered after CD3 engagement. By combining these results with the ones obtained with the MFP experiments we can also conclude that the phosphorylation of the ζ chains is not required for force generation, as cells treated with ML-7 pushed and pulled, with only small quantitative changes in the observed sequence of force generation; also cells treated with SMIFH2 were able to push, although the maximal force was diminished – while for both these inhibitors there was no detectable phosphorylation of ζ chains.

To further investigate the role of signalling in the morphology changes and force generation, we used PP2, a small molecule inhibitor of Src family kinases, which include Lck, in microchamber experiments. PP2 completely abrogated the expected sequence in morphology changes after T cells contacted the beads coated with anti-CD3 and anti-CD28 antibodies. (Figure 38 on the next page). This aligns with the results obtained in the experiments on micropillars, in which the use of PP2 substantially decreased the in-plane forces generated by CD4+ T cells (Bashour et al., 2014), and suggests that kinase activity is essential to trigger the sequence of changes in cell morphology and of force generation. PP2 significantly inhibits many different kinases (Brandvold, Steffey, Fox, & Soellner, 2012), which for now does not allow to conclude on the specific protein involved in the process.

These preliminary results open a perspective for the study of the way through which the activating signal passes from the CD3 and CD28 molecules, which bind to the extracellular receptors, to the cytoskeleton effectors, which generate forces and change the morphology of T cells during their activation.

Figure 38. PP2 blocked the sequence of changes in morphology during T cell activation. Human primary CD4+ T cells were pre-incubated for 30 minutes with 25 µM PP2, or the same volume of DMSO, and then used in microchamber experiments (see Figure 33) with the beads coated with anti-CD3 and anti-CD28 antibodies. The pie charts show the proportion of active and inactive cells in the recordings, "contact not seen" means that a cell floated into the field of view with a bead attached to it, and showed no activity afterwards. The active cells were those which followed the sequence of changes in morphology (a pushing protrusion followed with a spread, cup-like form on the bead). The proportions are shown as a percentage of all the cells that attached to at least one bead. N=105 cells in one experiment (PP2) and N=411 cells in two experiments (DMSO control). The brightfield images show examples of cell morphology during the experiment, for "control" morphology see also Figures 33C, top row and Figure 35, bottom row. Time in minutes:seconds, scale bar is 10 µm.

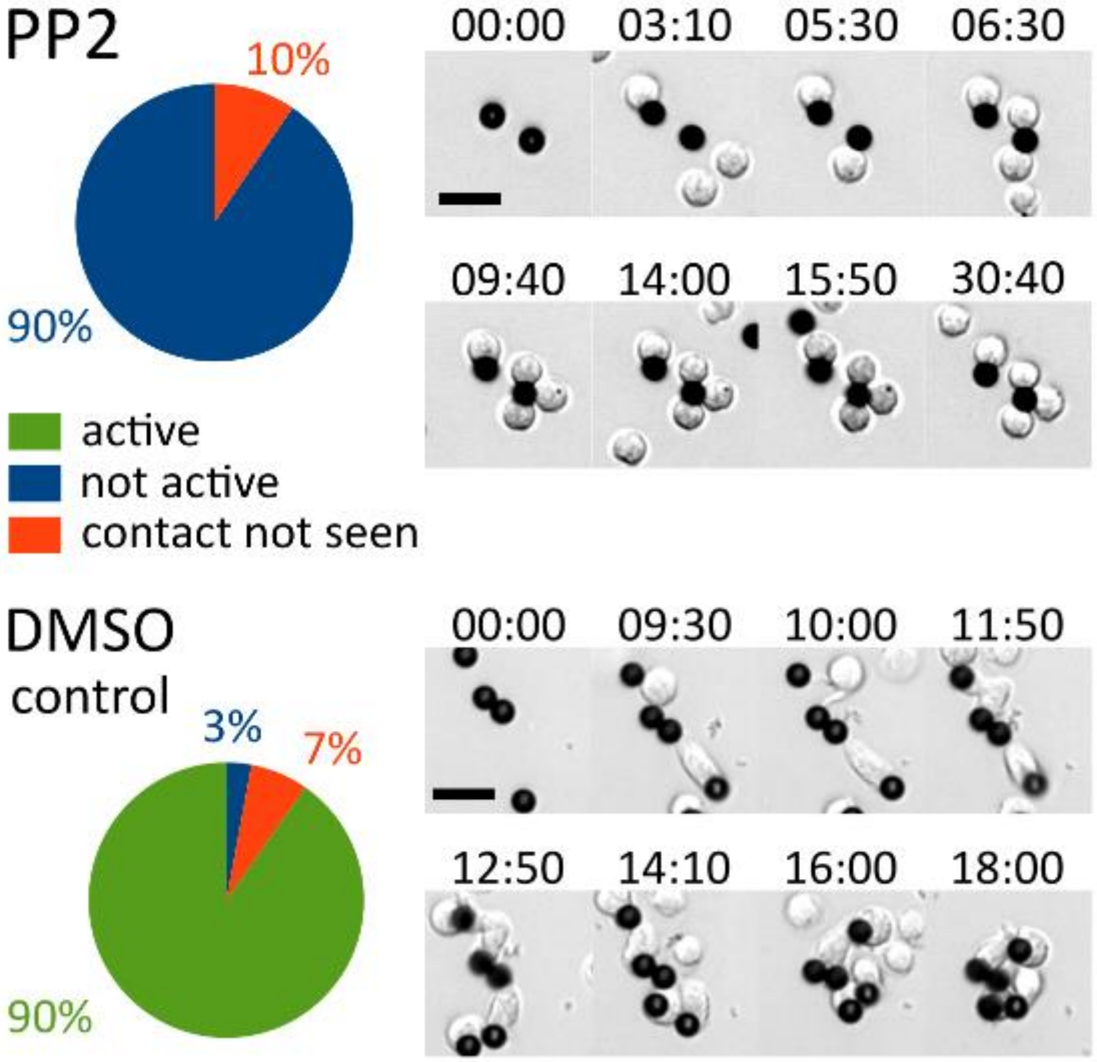

# Discussion

## 1. Sequence of morphology changes in T cell activation

In this work, I characterised the sequence of early events in T cell activation that included the force generation and changes in cell morphology. The changes in cell morphology can be summarised as follows: the formation of the punch, the collapse of the punch, and the spreading of the cell on the bead to form the cup. This sequence repeated qualitatively for lymphoblasts, for primary T cells activated with anti-CD3 antibodies, and for T cells co-stimulated with anti-CD3 and anti-CD28 antibodies, with only some quantitative differences. This sequence repeated also qualitatively for all 17 donors tested. There may be some quantitative differences between the donors, but for now the way in which I acquired the data (different donors were used in different conditions) did not allow to analyse it quantitatively. This standard order of morphology changes was thus robust in my experimental model – human CD4+ T cells activated with antibodies attached to a bead.

As these changes in cell morphology develop over time, the description of forces and the explanation of the mechanism of the formation of the immunological synapse need to take into account the time at which the events happen. Thus, to provide a general framework (a general timeline) for the description of T cell activation, I validate here the sequence of events obtained in my experiments, against the morphology changes described previously in the different studies of T cell activation (Figure 39).

Figure 39. Conceptual drawings of the sequence of changes in T cell morphology during their activation – during the formation of the immunological synapse. A. My drawings showing the changes in T cell morphology (see Figure 18 in Chapter 2). B. Model drawings reproduced from Fig. S16 in (Ueda et al., 2011). C. Model drawings reproduced from Fig. 6 in (Grakoui et al., 1999), by permission from AAAS. D. Model drawings reproduced from graphical abstract of (Ritter et al., 2015), under the CC-BY 4.0 license. The studies were done on different timescales – time since contact for the last image is about 2-3 minutes for A, 4 hours for B, more than 5 minutes for C, and 30 minutes for D.

Figure 39 is shown on the next page.

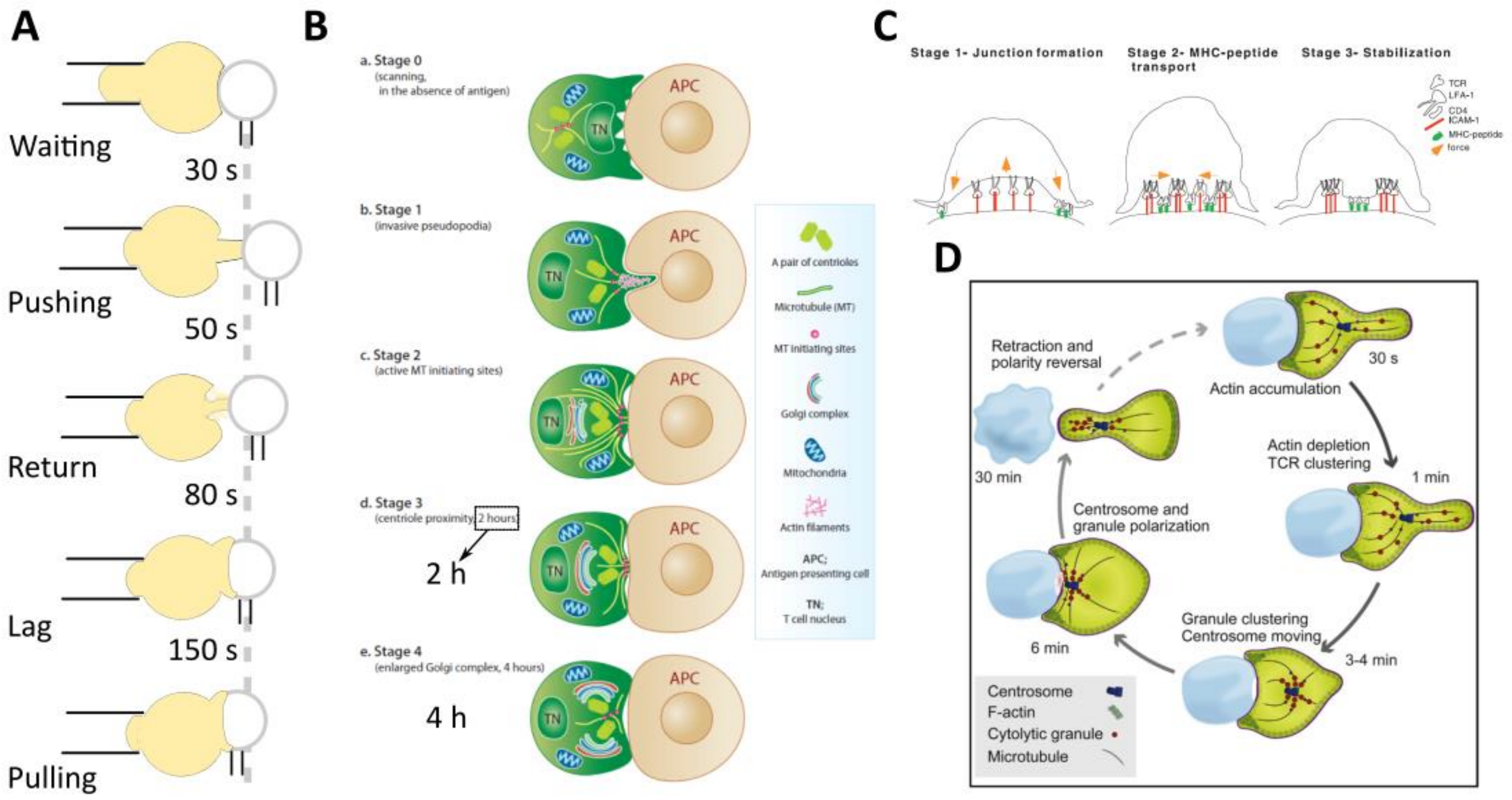

Figure 39. See the legend on the previous page.

In early observations, done on the molecular level, the morphological changes during the formation of the immunological synapse were described with the spatial organisation of the different proteins. In a “citation classic”, one of the first papers to use the notion “immunological synapse” in the title ((Grakoui et al., 1999), see also Figure 6 in Introduction), in which T cells from different transgenic lines of mice formed synapses with peptide-MHCs and ICAM-1 embedded in the supported lipid bilayer, TCRs were described to attach to peptide-MHCs on the periphery, and then to be transported towards the centre of the synapse. Thus, the central supramolecular activation cluster (cSMAC) containing TCRs was formed, surrounded by the adhesive pSMAC containing LFA-1 (Figure 39C). The researchers proposed that the initial binding of LFA-1 to ICAM-1 in the centre of the synapse (the first contact area) serves to anchor the T cell to the surface. This anchoring was speculated to be necessary for the actin cytoskeleton activity, which then facilitated the antigen recognition and transported the TCRs towards the cSMAC (although no experiments targeting cytoskeleton were reported in this study).

These three drawings – initial contact followed with a major reorganisation of the contact area leading to the formation of the "mature synapse" (Figure 39C) – are reminiscent of pushing (punch), collapse and then pulling (cup). The timing reported in (Grakoui et al., 1999)approximates the sequence found in the MFP experiments (the central cluster of LFA-1 appeared 30 seconds after the first contact between T cell and the lipid bilayer, and gave way to cSMAC of TCRs about 3 minutes from the first contact). However, an important difference between the studies is the lack of ICAM-1 on the beads used in my MFP experiments, so the lack of integrins triggering. As the engagement of LFA-1 with antibodies on the bead changed completely the punch morphology (Husson et al., 2011), we can postulate that punch, as a localised, long protrusion, shows only when the integrins are not triggered. This seems to be corroborated by the study with DNA tension probes (Liu et al., 2016) in which the OT-1 mouse T cells interacted with immobilised antigens on a glass surface. The signal from the tension probes attached to peptide-MHCs increased in the central point of the contact area around 40 s after the initial contact (punch), then the contact area increased, and the tension signal increased uniformly over the whole contact area (cup). When ICAM-1 was added on the surface this pattern was lost, and the cells assumed a migratory phenotype, with tension signal localised at the rear of the cell, within 2 minutes from the initial contact.

Punch is not the only protrusion reported on the interface between T cell and the activating surface. In a study where mouse CD4+ T cells formed conjugates with CH27 cells (mouse B cell lymphoma line) and were imaged with transmission electron microscopy (Ueda et al., 2011), thin, finger-like protrusions were engulfed deeply into the CH27 cells. These protrusions, although reminiscent of the punch in the conceptual drawing (Figure 39B), were reported also when CH27 cells did not bear the cognate peptide for the T cells. The protrusions were therefore postulated to be involved in the scanning of the surface of the antigen-presenting cell, and not in the formation of the immunological synapse. Accordingly, a conceptual drawing from a recent study (Ritter et al., 2015), in which a suite of high-resolution fluorescence microscopy techniques was used to image the synapse between mouse OT-I T cells and the target cells (EL4 mouse lymphoma cell line), shows no protrusions on the contact area (Figure 39D). The imaging in this study showed however an initial increase in filamentous actin over the whole contact area, the timing of which is similar to the formation of the punch. Again, we can postulate that the engagement of the integrins prevented the formation of a single, long punch.

In summary, all the studies mentioned above are consistent with the picture in which TCR triggering leads initially to the intensive actin polymerisation at the contact area. The polymerisation shows as a localised protrusion (punch) if integrins are not triggered. This first step is deemed to establish the initial firm contact between the T cell and the activating surface. Then T cells spread on the surface, which showed as the cup in the MFP experiments. At this stage the centrosome translocates close to the immunological synapse and T cells perform their physiological functions.

The biophysical measurements allowed to associate these changes in cell morphology with forces that T cells exert on the activating surface. The initial polymerisation of actin on the contact area shows as the pushing force against the substrate; during the subsequent spreading T cells exert traction forces, which can be measured both in-plane and out-of-plane. I will now discuss which information about the process of T cell activation we can gather from the mechanical analysis of these forces exerted by T cells.

## 2. Mechanosensitive forces generated by T cells

With the MFP experiments we showed that the pushing and pulling forces generated by T cells changed with the bending stiffness of the measuring micropipette. More specifically, the speed of force generation (force rate) on average increased from 0,014 to 0,038 nN/s for pushing, and from 0,008 to 0,019 nN/s for pulling, over the stiffness range from 0,2 to 1,1 nN/µm (Figure 24in Chapter 2). It is known that T cells interact with different antigen-presenting cells, including B cells, dendritic cells, and macrophages. In a study previously done in our group, these different cell types were shown to have different mechanical properties that were modified in inflammatory conditions(Bufi et al., 2015). In this context, it is valuable to compare the bending stiffness of the measuring micropipette, k [nN/µm], to the Young's modulus, E [Pa], a measure of cell stiffness reported in this study. The simple approximation for the "conversion factor" between these two measures of stiffness (Julien Husson, personal communication) can be described as follows:

Young's modulus is a coefficient which for elastic objects relates stress and strain, i.e. the force per unit area applied to the contact surface and the deformation of the object:$\sigma = E\varepsilon$ (1), where $\sigma$ is the stress, $E$ is the Young's modulus, and $\varepsilon$ is the strain. In the context in which we are working, a T cell would exert forces deforming an antigen-presenting cell, which we approximate with an elastic sphere (Figure 40, right). The strain of this sphere can be described as $\varepsilon = \frac{\delta}{L_0}$ (2) where $\delta$ is the deformation and $L_0$ is the initial, resting diameter of the sphere. The force exerted by the T cell$F$ causes the stress: $\sigma = \frac{F}{S}$ (3), where $S$ is the surface of the contact area between the T cell and the antigen-presenting cell. By equating (1) and (3), and substituting (2) into it we obtain:

$$\sigma = E\frac{\delta}{L_0} = \frac{F}{S}$$

$$F = \frac{ES}{L_0}\delta \qquad (4)$$

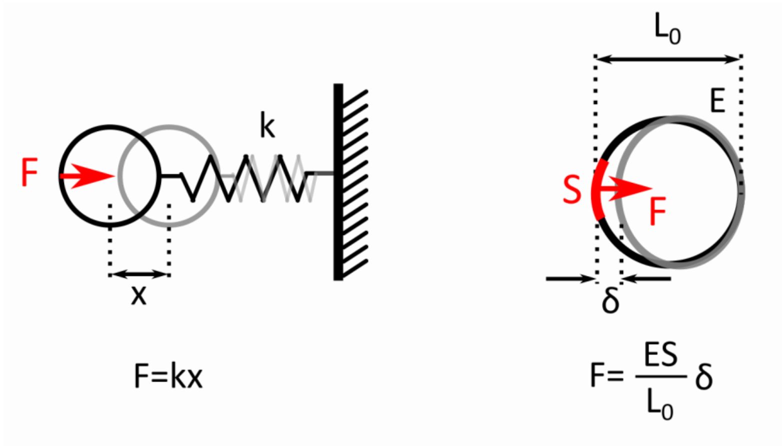

Figure 40. Schematic drawings of the force deforming an elastic spring of stiffness k (left) and an elastic sphere of Young's modulus E (right). The equations below the drawings show the relationship between force and change of length in both situations.

Equation (4) relates the force to the displacement, as measured in the image (Figure 40). Thus, the relationship between the bending stiffness of the micropipette k and the equivalent Young's modulus can be written as $k = \frac{ES}{L_0}$. For this approximation we assume $L_0$ to be on the order of 10 µm, a value comparable to the size of the bead and to the diameter of the cells. The surface of the contact area $S$ changed during the recorded activation process. For the pushing phase it can be approximated as $\pi R_{punch}^2$ where $R_{punch}$ is the radius of the punch, on average equal 0,85 µm (see resting T cells in Table 4 in Chapter 2), which gives $S \approx$ 2,2µm$^2$. For the pulling phase, assuming the radial symmetry of the cup, and the cup angle being equal 120° (on average it was 125° for resting T cells, Table 4 in Chapter 2), we get a simple geometric relation $S = \pi R_{bead}^2 \left(1 + \frac{\sqrt{3}}{2}\right)$ where $R_{bead}$ is the radius of the bead, equal to 2,25 µm, which gives $S \approx 29{,}7$ µm$^2$. For the simplicity of calculations $S$ can be approximated as 20 µm$^2$. In summary, for the range of the bending stiffness of the measuring micropipette ($k$) from 0,2 to 1,1 nN/µm, which was covered in the experiments, we obtain an equivalent Young's modulus range of 0,1 to 0,55 nN/µm$^2$, or 100 to 550 Pa. This result represents the order of magnitude of the effective stiffness of the measuring micropipettes used in the MFP experiments. It is included in the range of reported Young's modulus of the antigen-presenting cells (240 to 1500 Pa, (Bufi et al., 2015)), which suggests that our experiments were conducted at a range of stiffness relevant to the physiological conditions.

The influence of the target stiffness on the forces generated by T cells was tested in two in-plane studies. In a study with traction force microscopy (Hui et al., 2015), the total traction force generated by Jurkat T cells increased with the stiffness of polyacrylamide gels in the range of 200-6000 Pa. The "conversion factor" for the stiffness of the gels reported in this paper (turning the stiffness of the gels used into the range from 0,1 to 10 nN/µm) encompasses the range of stiffness of the micropillars used in another study (Bashour et al., 2014), in which no difference in force per pillar was found for the pillars of the bending stiffness in the range from 0,6 to 2,4 nN/µm. This discrepancy of results may be due to the different experimental model used (Jurkat T cells versus primary human and mouse T cells; stimulation with anti-CD3 antibodies only versus costimulation with both anti-CD3 and anti-CD28 antibodies).Also, T cells plated on a coated gel have a uniform contact with the activating surface, whereas it is more point-like on the micropillars (the diameter of the micropillars used was 1 µm). This could have influenced the pattern of force generation by T cells. There is also an important difference in timing of the measurement, as the force per micropillar was measured over a 20-minute window beginning 20 minutes after seeding, whereas the traction force on the gel was measured over a 1-minute window 14 minutes after the contact was formed. This opens an interesting possibility that the in-plane traction forces responded to the stiffness of the substrate at the earlier stages of the formation of the immunological synapse, but then the traction stabilised to a value comparable for different stiffness.

For the out-of-plane forces, a direct comparison is possible between the results for the pulling force rate obtained in MFP experiments and in BFP experiments previously done in our group (Husson et al., 2011). The results are in good agreement (Figure 41 on the next page). The range of stiffness covered in the MFP experiments extends above the range covered in the BFP experiments. The trend of force rate increasing with the target stiffness continues in this extended range, suggesting that the upper limit of the pulling force rate generated by T cells was not yet reached. This is in agreement with the traction forces measured in (Hui et al., 2015), which plateaued at the gel stiffness of 4 kPa, well above the range covered in Figure 41, by any of the "conversion factors" discussed above.

Figure 41. Comparison between the micropipette force probe (MFP) and the biomembrane force probe (BFP). The pulling force rate was measured for the activation of human primary CD4+ T cells with anti-CD3/anti-CD28 beads (MFP) and anti-CD3 beads (BFP). The BFP data was published before (Husson et al., 2011), the MFP data is in Figure 24 in Chapter 2. Each data point shows mean±s.d. over one day of experiments, representing 3 to 10 cells. The second X axis below the chart shows the equivalent Young's modulus for the probe stiffness used in the experiments, calculated according to the "conversion factor" discussed above. Figure and the caption text adapted from the Supplemental Figure S2 in (Sawicka et al., 2017).

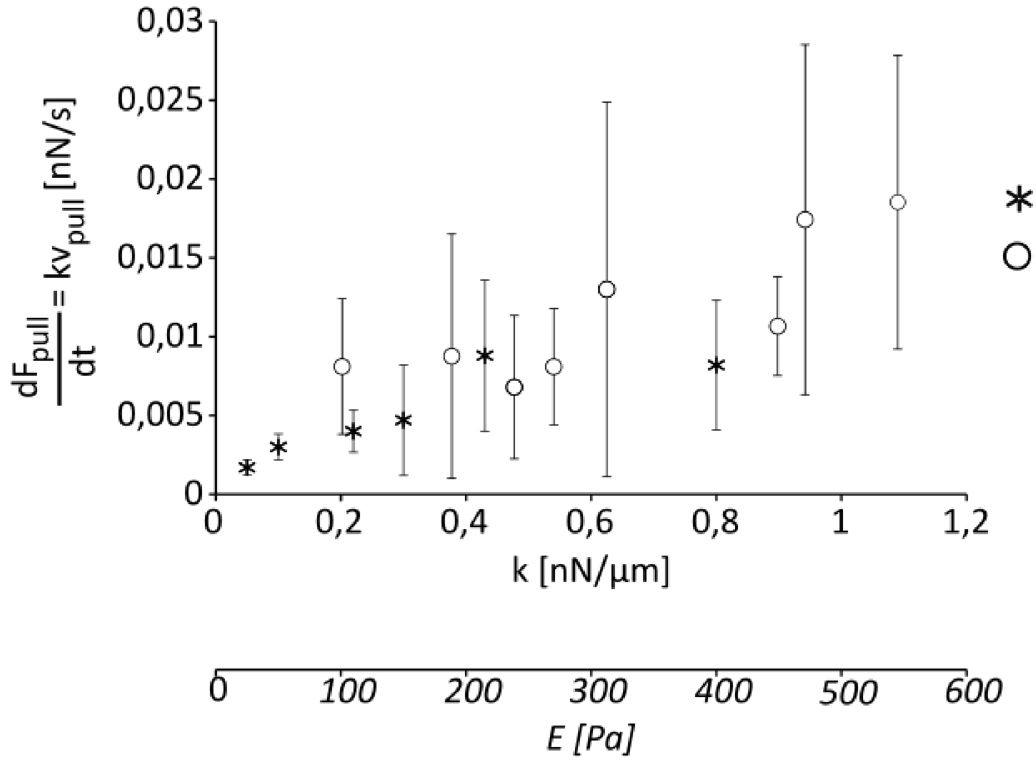

These results show that T cells are able to tune the forces that they generate to the stiffness of the target with which they are interacting, and do so over a large range of stiffness (two orders of magnitude).As a similar range of stiffness can cause different functional responses of T cells (Judokusumo et al., 2012; Saitakis et al., 2017), the results of the force measurements support the concept that T cells use mechanical forces to sense the stiffness of the target, which then modifies the ongoing activation process. If forces are the mechanosensitive unit of T cells, then the understanding of the mechanism of force generation will lead to the understanding of T cell mechanosensitivity.

# 3. Role of cytoskeleton reorganisation in force generation

To answer how T cells generate forces, we ran MFP experiments with T cells treated with small molecule inhibitors of different cytoskeleton-related proteins. The largest effect was found with SMIFH2, inhibitor of formins; we found also quantitative differences with ML-7, inhibitor of myosin light chain kinase (MLCK), which phosphorylates the regulatory light chain of myosin, leading to the activation of myosin.

The role of myosin in force generation by T cells seems quite clear as in most of the studies the use of blebbistatin, the inhibitor of myosin activity, or of ML-7, the inhibitor of MLCK, reduced the forces generated by T cells (Table 8). As myosin is a molecular motor responsible for pulling of the actin filaments this result is expected.

Table 8. Comparison of several studies of the effect of blebbistatin and ML-7 on the forces in T cell activation.

| Reference | Inhibitor used | Technique for force measurement | T cells used | Activation signal | Effect on forces (compared to DMSO control) |
|---|---|---|---|---|---|
| (Basu et al., 2016) | 50 µM blebbistatin | Micropillars, in-plane | OT-I mouse lymphoblasts | Peptide-MHC and ICAM-1 | Reduced total force |
| (Hu & Butte, 2016) | 10 µM ML-7 | AFM, out-of-plane | OT-II mouse lymphoblasts | Antibodies against CD3 | Reduced total pushing and pulling force |
| (Sawicka et al., 2017) | 30µM ML-7 | MFP, out-of-plane | Human resting CD4+ | Antibodies against CD3 and CD28 | Reduced return and pulling speed |
| (Hui et al., 2015) | 50 µM blebbistatin<br>10 µM ML-7 | Traction force microscopy, in-plane | Jurkat | Antibodies against CD3 | No effect on total force |

Somewhat to the contrary, in the last study reported in Table 8, both blebbistatin and ML-7 had no effect on traction forces exerted by Jurkat T cells (Hui et al., 2015). In this study, however, the inhibitor was added to the medium during the experiment, and in the other studies the cells were pre-treated for 15 to 30 minutes with the inhibitor. This may have influenced the initial state of the cytoskeleton of T cells when they contacted the activating surface; also, it is difficult to compare the concentration of inhibitor inside the cells in these two situations. Quite a surprising result was obtained with the DNA tension probes (Liu et al., 2016): the tension transmitted through the TCR complexes increased when resting OT-I T cells were treated during the experiment with 40 μM ML-7. It is difficult to compare this result, obtained on the molecular level, with the results listed in Table 8. It suggests a possible additional level of complexity in the description of the forces, where the global measured output does not correspond directly to the force transmitted through individual molecules.

MLCK may have other functions in cells than phosphorylation of myosin light chain (Chen Chen et al. 2014), however, in the results compiled in Table 8, ML-7 and blebbistatin show similar effects, suggesting that the effect of ML-7 is primarily due to the action of MLCK on myosin. The morphology of T cells observed in microchamber experiments (Figure 35 in Chapter 3) was similar for cells incubated with ML-7 and with blebbistatin, it was also comparable to the control cells, suggesting that the inhibition of myosin modified the ongoing activation process, but did not stop it completely. Accordingly, the measured forces were reduced in inhibitor-treated cells, but not abolished. In summary, myosin is important for the forces generated by T cells, but it is not the only driving factor for forces, and its activity is not necessary for the observed changes in cell morphology.

The role of formins in force generation by T cells, to the best of our knowledge, had not been directly investigated before. For T cells pre-treated with SMIFH2, inhibitor of formin homology domain 2, we measured reduced maximal pushing force. The return speed was also reduced, leading to the cup being formed at a later timepoint, and some cells did not form the cup at all (Table 7 in Chapter 3). These results indicate an important role of formins in the force generation in T cell activation. The effect of formin inhibition was quantitatively marked already at the end of the pushing phase (about 1 minute from the contact), earlier than the centrosome translocation, for which the activity of formins is necessary(Andrés-Delgado et al., 2012; Gomez et al., 2007), and which occurs within several minutes from the first contact. The centre of the immunological synapse, where the centrosome docks, is relatively depleted in actin (Ritter et al., 2015). This is consistent with the postulated inhibitory role of microtubules on the actin network in the immunological synapse (Hui & Upadhyaya, 2017). The disruption of activity of formins, which interact both with microtubules and with actin, could deregulate this cytoskeleton organisation at the immunological synapse, leading to the significant effect on forces and cell morphology that we observed in the MFP experiments.

The results for ML-7 and SMIFH2 obtained in the MFP experiments are somewhat different from the ones obtained in the study of actomyosin arcs (Murugesan et al., 2016). In this study, 50 μM blebbistatin and 10 μM SMIFH2 had a similar effect on the morphology of the immunological synapse, formed by Jurkat T cells on the supported lipid bilayers with antibodies against CD3 molecule. For both inhibitors, the actomyosin arcs did not form anymore on the boundary between the dSMAC and the pSMAC. Thus, the arcs were postulated to be nucleated by formins, and then pulled towards the centre of the synapse by the myosin. CK666, the inhibitor of Arp2/3 complex, had an opposite effect, suggesting that Arp2/3 and formins compete for the same pool of actin. In the MFP experiments, the effect on return speed observed with ML-7 repeated for SMIFH2-treated cells, suggesting a possible parallel between these in-plane and out-of-plane observations. However, the observed morphology of cells was different for ML-7 and SMIFH2, and the effect of SMIFH2 on forces was more pronounced (showed also in maximal pushing forces). In summary, this suggests that the effect of SMIFH2 measured and observed out-of-plane is larger than the effect observed in-plane.

The important role of formins in T cell biology was found with the mice knock-out for the formin mDia1, in two independent reports (Eisenmann et al., 2007; Sakata et al., 2007). In these mice, the T cell count in spleen and lymph nodes was reduced, although the size of the spleen and the thymus was normal. The T cells isolated from these spleens failed to spread on glass slides coated with anti-CD3 and anti-CD28 antibodies, which is reminiscent of the lack of cup in our experiments. The T cells from mDia1-/- mice also migrated less in a transwell assay, and exited less from the bloodstream to peripheral lymphoid organs when transferred adoptively to a wild type or knock-out recipient. These T cells also proliferated less in vitro upon stimulation with concanavalin A or anti-CD3 and anti-CD28 antibodies. Thus, the large effect of formin inhibition on T cell forces and morphology obtained in our setup is consistent with the impairment of different functions of T cells in these knock-out studies.

Further investigation of the actin organisation is needed to understand the contribution of different cytoskeleton-related proteins to force generation. As a first step, the measurement of forces in T cells treated with CK666 would be interesting, as this inhibitor of Arp2/3 was reported to reduce traction forces on polyacrylamide gels exerted by Jurkat T cells (Hui et al., 2015), and to increase the tension on the TCRs measured with the DNA probes (Liu et al., 2016). In our microchamber setup, the use of inhibitors of formins and Arp2/3 increased the waiting time between the contact with the bead and the onset of activity (Figure 36 in Chapter 3), suggesting that both types of actin nucleators are implicated in the early stages of the activation process. Arp2/3 and formins were found to have complementary roles in the nucleation of cortical actin (Bovellan et al., 2014); it would be thus interesting to study the interplay between the two in the force generation in T cell activation.

# Conclusions & perspectives

In this work I showed that T cells during their activation followed a sequence of changes in morphology and of force generation. This sequence was qualitatively the same for the human resting CD4+ T cells, and for CD4+ T lymphoblasts, an in vitro model of effector T cells, suggesting that the initial events after TCR triggering are similar for the different subpopulations of T cells. The resting CD4+ T cells isolated from the peripheral blood form a heterogeneous population by itself, as they comprise naive T cells and memory T cells. In a preliminary experiment, we tested the forces generated by these two subpopulations, sorted from the peripheral blood based on the expression of the two isoforms of CD45: CD45RA on naive cells, and CD45RO on memory cells (see details in Supplement 2). As the differences between the two subpopulations were not statistically significant, the results from both were pooled for the data point at k = 0,2 nN/μm. It seems thus that the mechanism of force generation is similar in both subpopulations. Another important functional subpopulation of CD4+ T cells are regulatory T cells. As they play an immuno-suppressive role, it would be interesting to see if they generate similar forces as the "standard", immuno-enhancing CD4+ T cells.

The results obtained with SMIFH2 and ML-7 allow to say that the different proteins linked with the actin cytoskeleton play different roles at different stages of the process of T cell activation. This line of research could be pursued with the application of the inhibitors in a particular moment of the activation process. Such a study would be feasible as the order of events and their timing in the sequence are well defined. An example of such an experiment would be to apply SMIFH2 after the formation of the cup, to check if the activity of formins is necessary only at the initial stages, like the collapse of the punch, or also for the continuation of the process. More broadly, this type of studies could require new tools, such as photo-activatable inhibitors, or proteins, which can be (de)activated with the laser beam applied locally to the cell. For example, blebbistatin is known to be unstable when irradiated with blue light (Sakamoto, Limouze, Combs, Straight, & Sellers, 2005). This prompted the development of a photostable derivative of the compound (Képiró et al., 2014); it would be interesting, instead, to use this photosensitivity to have the possibility to switch on and off the activity of blebbistatin during the ongoing activation process. The rapid activation or inactivation of the inhibitors is particularly important as the changes in T cell morphology happen within seconds, or a few minutes, making them difficult to study with a change of the medium.

The broad goal of this approach would be to provide the integrated description of the machinery behind the force generation and changes in morphology in T cell activation, with a good spatial and temporal resolution. This description would involve the modifications of the cytoskeleton, and the chemical signalling passing through the different molecules and the second messengers like calcium ions. The full description can be thought of as consisting of two elements: a 3D map, showing the localisation of the different molecular players, and a script describing their activities step by step.

By knowing the role of the different players at each stage of the formation of the immunological synapse, we can address the different pathologies stemming from the incorrect activation of T cells. The primary human cells were used in this study to provide basic information on the mechanics of the process in a relevant model. The results thus obtained will enable in the future a direct comparison with the T cells affected by different pathologies. Several immunodeficiencies in human have been related to the malfunctioning of the TCR-triggered signalling (reviewed in (Notarangelo, 2014)) or the cytoskeleton reorganisation in T cell activation, like in Wiskott-Aldrich syndrome (reviewed in (Rivers & Thrasher, 2017)).

This study focused on the CD4+ T cells, but the involvement of the CD4 molecule in the force generation was not addressed. It is known that forces are generated when T cells are put in contact with peptide-MHCs, which engage CD4, and with anti-CD3 antibodies, which do not. In a study with AFM (Hu & Butte, 2016) some quantitative differences were reported between these two ways of triggering the force generation by T cells. The relative impact of CD4 and CD8 on the TCR-peptide-MHC bond is also different (Hong et al., 2015). The involvement of CD4 in the force generation would be interesting in the context of the infection by HIV. The activity of cytoskeleton triggered and exploited by HIV has been studied extensively (reviewed in (Ospina Stella & Turville, 2018)), however, not much is known on the role of forces in the process. The understanding of this pathological process could shed some light on the physiological process of T cell activation, for example, understanding of the signalling and the mechanical pathways leading to the entry of HIV into the cell would tell us which processes are guiding the membrane dynamics on T cell surface.

We and the others showed that the forces exerted by T cells change with the stiffness of their target. It is consistent with T cells using the mechanical forces to sense the stiffness of their target, which then changes the functional outcome of the activation process. Recently, the development of new classes of cancer treatments, such as anti-checkpoint therapy or CAR T cells, led to substantial interest in finding the "optimal conditions" for T cell activation. In this context, it is of particular interest to understand the mechanism through which the T cells sense the stiffness of their target and respond to it, so that these mechanical aspects can be tuned to potentiate the anti-tumour T cell response.

In this thesis I discussed the forces exerted by T cells on the activating substrate, which mimicked the antigen-presenting cell. However, there are also forces exerted inside the T cell, linked for example to the intracellular traffic of different cargos towards the immunological synapse (reviewed in (Martín-Cófreces & Sánchez-Madrid, 2018)). This is another biophysical aspect of T cell activation which could be an interesting area to explore.

Basic information about the forces generated by T cells during their activation process are already known. More research is required to establish the function of forces in T cell activity, in physiological and pathological conditions.

# Supplements

## Supplement 1: Micropipettes

Apart from providing the technical details of the micropipette setups used in our laboratory, this supplement contains also some practical advice on the experimental setups, including some of the troubleshooting that was done during my thesis research.

### S1.1 Micropipette fabrication

The micropipettes were prepared from borosilicate glass. To explain the choice of this material for the fabrication of an experimental tool, I provide a few details on the glass as a material. Glass is any non-crystalline, or amorphous, solid (https://en.wikipedia.org/wiki/Glass , accessed 2018-07-11). Silica glass, popularly referred to as "glass", has been processed by humans for at least 3 000 years (Shortland, Kirk, Eremin, Degryse, & Walton, 2018), which gained us practical experience in dealing with this material. As pure silica ($SiO_2$) has a melting point over 1000°C, silica is typically mixed with different additives, which make it easier to process, at several hundred Celsius degrees. Sodium borosilicate glass – with sodium, boron, and aluminium oxides added – is used in cooking equipment and in lab utensils, as it resists better to heat expansion. Thus, to be able to heat-process a thin capillary, without closing it, we used capillaries made from sodium borosilicate glass (1 mm outer diameter, 0,78 mm inner diameter; Harvard Apparatus, USA); each such glass capillary served to fabricate two micropipettes.

A micropipette puller (P-97,Sutter Instruments, USA) heats up a capillary in the middle part, and pulls the two ends away, sharply. The melted capillary stretches then in the heated part – forming what I call micropipette shafts – and finally breaks, leaving two pre-micropipettes. By tuning the heating time, heat intensity, and pulling speed we tune the length and width of the shafts. For example, if the parts are pulled away faster, the micropipette shafts will be shorter, which means that along the micropipette shaft its diameter increases faster, and also that the shaft is stiffer.

I used two main programmed sets of parameters, obtaining the two main micropipette types:

- holding micropipettes: rigid, with short shaft, used to hold in place the object of interest.
- measuring micropipettes, or microindenters: flexible, with long shaft, used to exert and measure forces in the piconewton to nanonewton range.

A pre-pipette as pulled from capillary needs to be adapted to the particular experimental setup. This is done with the microforges, the devices built by adding a metal loop to a standard, table-top microscope. Electrical current flowing through the loop heats it up; the loop then serves as the "forge" for the micropipettes. I used two different microforges: MF-200 (World Precision Instruments, USA; Figure 42A) and MF-900 (Narishige, Japan; Figure 42B).

Figure 42. Microforgery. Schematic drawings showing the preparation of the tip (A) and bending of the shaft of the micropipettes (B). Top view: looking down from the ceiling, Side view: standing in the laboratory.

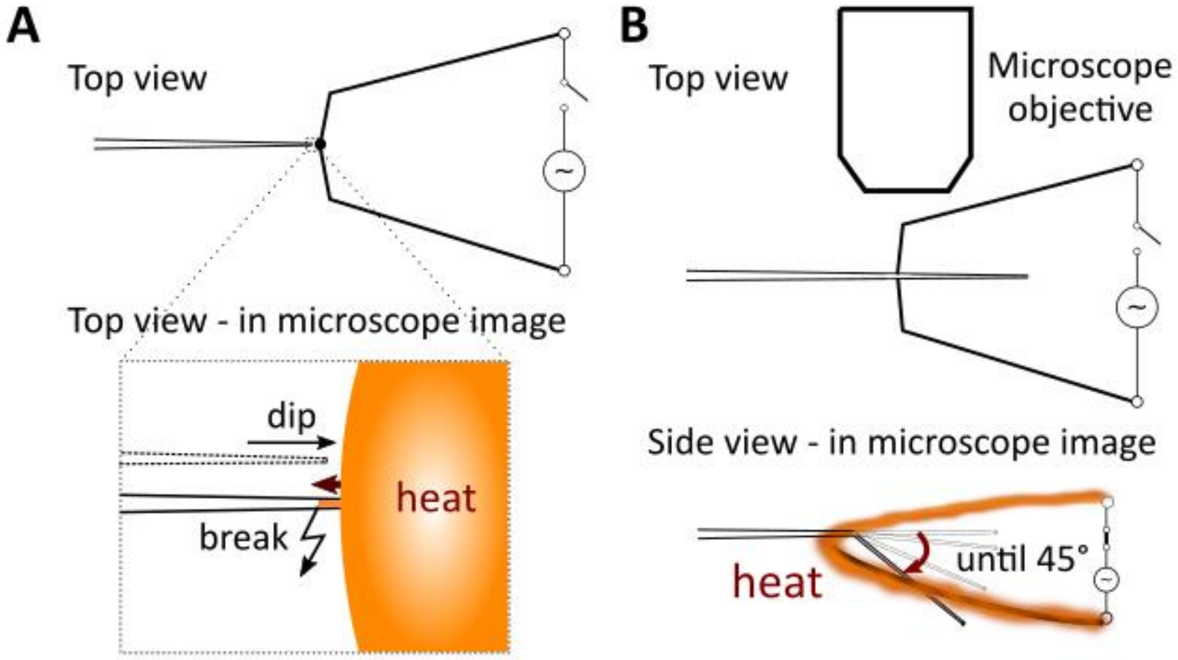

In the first microforge (Figure 42A), a glass bead is added on the metal loop. The bead melts when the electrical current is flowing through the loop, which allows us to shape the tip of the micropipette. In this step we tune the tip diameter (see Figure 13 in Chapter 1), and we polish the tip so that it is symmetric with blunt ends, then it holds stably the aspirated object. A pre-micropipette is dipped into molten, heated glass bead. The glass from the bead then flows inside the micropipette shaft, which is visible in the microscope image. When the heating is off, and glass solidifies again, pulling the pre-micropipette away breaks it at the point reached by the molten glass. As the pre-micropipettes gradually increase their diameter, the further the micropipette is broken the larger diameter it has. The measuring micropipettes with increasing diameter get also stiffer, so the cutting needs to be adapted to the desired bending stiffness, rather than desired diameter. In practice, this means that making a thinner or a more flexible micropipette is always more challenging, as a clean tip needs to be obtained in a few cuts, with a narrow error margin.

A microindenter tip is obtained by pulling the pre-micropipette away sharply while the glass is still liquid. A drop of glass stays then on the tip of the micropipette, and solidifies as a microindenter (Figure 13 in Chapter 1, right). See the movie S6 in (Gonzalez-Rodriguez et al., 2016) for an example of a microindenter fabrication.

During my experiments I established that a holding micropipette for a primary T cell should have a diameter of 2,5-3,5 µm, thinner micropipettes "pinch" the cell, broader ones can aspirate it completely during the experiment (see also (Guillou, Babataheri, Saitakis, et al., 2016)). For measuring micropipettes I used the bending stiffness in the range of 0,1-1,2 nN/µm, this was varied within the range needed to obtain a measurable displacement (up to several micrometers) for a single T cell that generates forces up to 1 nN.

Figure 42B shows the bending of the shaft of the micropipette. The micropipette is held above the metal loop, without contacting it. When the loop heats up, the shaft heats on one side and bends. A 45° bend is needed to position the micropipette tip in the focal plane of the microscope (see Figure 43 below and Figure 14A in Chapter 1); for a bent micropipette (inset in Figure 13 in Chapter 1, middle) another bend, 90°, is introduced in the thin part of the shaft.

Prepared micropipettes can be stored for months if needed. Microindenters can also be reused for different experiments; micropipettes unfortunately are used only once, as after the experiment the medium evaporating from the tip leaves behind enough of proteins and lipids to clog the micropipette completely.

## S1.2 Micropipette calibration

The last step of the preparation of measuring micropipettes is the calibration, or the measurement of the bending stiffness of particular micropipette. Measuring micropipettes are calibrated against a standard microindenter of a known stiffness.

To obtain this standard – first-generation standard – we used a commercial force probe 406A from Aurora Scientific, Canada (the force probe was calibrated, by the company, against a standard of a known stiffness), or we weighted pieces of paper on the tip of the micropipette (Guillou, Babataheri, Puech, et al., 2016). The second-generation standards, calibrated against the first-generation ones, are used for working purposes to calibrate micropipettes in a series of experiments. As the measurement error propagates across generations, using the same standard for all the experiments is advisable. The standards are microindenters, for two reasons: 1) microindenter tip shows for each calibration that the standard did not break and so that it still has the same bending stiffness; 2) the bead on the tip of the microindenter is bigger in diameter than a micropipette tip and thus better visible in the image and easier to position with the tip pointing downwards (Figure 43 on the next page). In this configuration, microindenter and micropipette bend each other in the same way as during the experiment (bending the long thin part).

Figure 43. Micropipette calibration. A. Configuration of the micropipettes on the microscope table, drawn in 3D projection and in symbolic 2D representation, used also in Figures 14 and 16 in Chapter 1. Inset: microscope image showing a positioned micropipette and microindenter, scale bar is 20 µm. B. Calculation of the bending stiffness of the micropipette, $k_p$. The force causing the bending of the standard microindenter by a distance $d_{standard}$, is the same as the force causing the bending of the calibrated micropipette by a distance $d_{pipette}$. This equation relates the measured displacements and the bending stiffness of the micropipette and the microindenter. At each time point during calibration, the position of the tip of the micropipette (x) is detected in the image and plotted against the position of the base (z), read from the piezoelectric controller. $k_p$ is calculated from the slope of the plot. Adapted from Supplemental Figure S8 in (Sawicka et al., 2017).

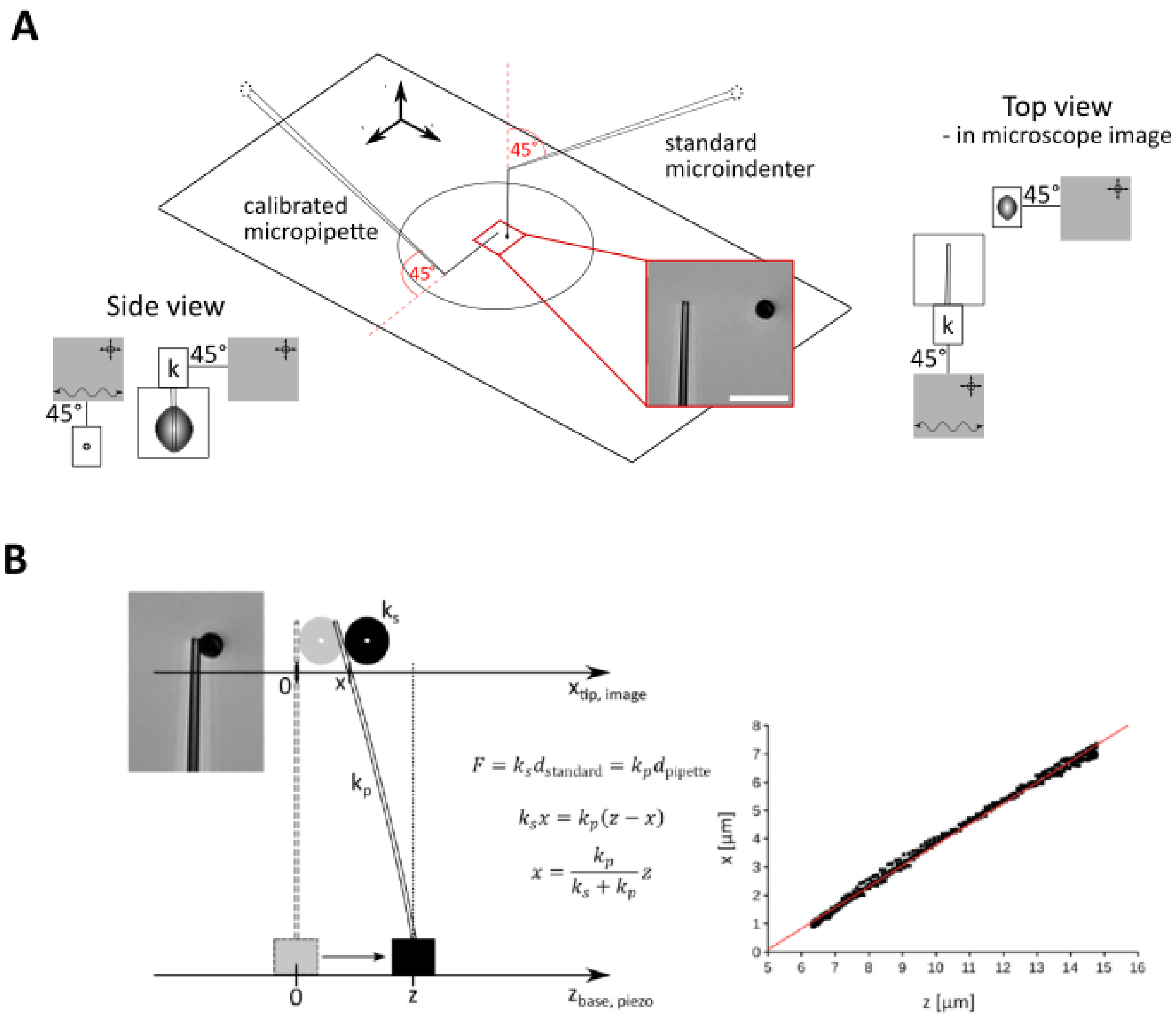

Micropipette and microindenter are held and moved with motorized micropositioners (Sensapex, Finland or Sutter Instruments, USA) placed above the sample table of an inverted microscope (Nikon Eclipse Ti-U; Nikon Instruments, Japan) with an ORCA-Flash 4.0 CMOS camera (Hamamatsu Photonics, Japan) mounted on an optical table (Newport, USA). The microscope is equipped with 4×, 10× and 20× air objectives for positioning, and with 40× air objective for calibration. The camera is controlled with the MicroManager software (Edelstein, Amodaj, Hoover, Vale, & Stuurman, 2010).

The microindenter and the micropipette tip are first put in contact by the operator, this sets the initial position on the X axis. During the calibration the micropipettes follow the programmed movement of the micropositioner with a piezoelectric controller and a strain gauge reader (Thorlabs, USA).When the base of the micropipette is moved by a distance $z$, set on the piezoelectric controller, the tip of the micropipette moves together with the tip of the microindenter by a smaller distance $x$. The value of $x$ is obtained at each time point by cross-correlating the line of current image against the template line obtained in the first image, and finding the maximum peak of the resulting cross-correlation function. One full calibration measurement takes approximately 12 seconds, during which approximately 4000 images are acquired. The bending stiffness of the calibrated micropipette, $k_p$, is calculated from the slope of the line fitted to the $x(z)$ chart (Figure 43B). The standard deviation over 5 measurements of the $k_p$ usually do not exceed 5% of the measured value.

Typically I prepare and calibrate the pipettes in advance, so that on the experimental day I can focus on the setup.

## S1.3 What can go wrong with the micropipettes

To set up the MFP experiment, the holding micropipette needs to be filled with water, to control the aspiration pressure inside it. Then, both pipettes need to be positioned with the tips in the focal plane of the microscope, meaning very close to the bottom of the dish (see Figure 14A in Chapter 1). This, combined with the multi-step fabrication protocol, creates opportunities to make mistakes. None of these mistakes really impair the experiment as such, they just delay an inexperienced experimenter. In other words, these mistakes do not influence the results, they prevent from obtaining the results in the first place.

During the first months of my experiments I started using the abbreviation PP&A, which means “pipettes positioned and aspirating”: it denotes the moment when I can inject the cells to the Petri dish and start the measurements, so the "real experiment". On average, I reached this checkpoint in 96±37 minutes during the calendar years 2016 and 2017 (mean±s.d., N=53 experimental days). This time extends mostly due to different problems with holding micropipettes, which are summarised in Figure 44. A problematic micropipette needs to be replaced with a new one, increasing the total number for this day. Although the average number of holding micropipettes per experimental day decreased from 2,6 in 2016 to 1,9 in 2017, this difference did not reach the statistical significance (p=0,172; Mann-Whitney U-test, N=37 vs N=29 experimental days). Still, for around one half of the experimental days I needed only one micropipette (zero problematic pipettes).

Figure 44. All the colours of micropipette problems. Percentages over the problematic holding micropipettes in a calendar year (total number in the corners). See text for the explanation of categories of problems. The total number of holding micropipettes used can be calculated as: 67 problematic micropipettes + 37 working ones in 2016 + 29 problematic micropipettes + 29 working ones in 2017 = 162 holding micropipettes.

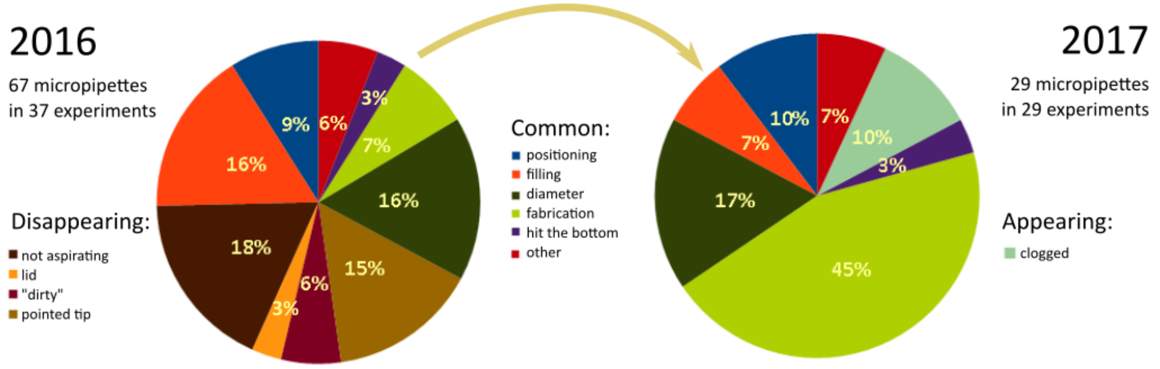

Four categories were troubleshot and disappeared in 2017. The "not aspirating" micropipettes were the most mysterious, as they failed to aspirate, otherwise looking normally. We speculated that there could be a clog of serum proteins at the tip or further up the micropipette, which appeared while filling the micropipette tip with medium. Indeed, the category disappeared shortly after we started filling the tip with PBS. Other possibility is that "not aspirating" micropipettes were similar to "lid" micropipettes, which were visibly closed at the tip with, probably, the leftovers of glass bead used in the fabrication. Micropipettes with "pointed tip" usually could not be used, as the point "scratched" cells; "dirty" is an umbrella term for all similar problems with the tip.

One category appeared in 2017: "clogged" micropipettes, which, usually after several hours of experiment, aspirated cell debris. The category is absent from 2016, because back then when the micropipette clogged I quitted the experiment. In 2017 I continued with a new micropipette.

The remaining categories are: micropipettes broken during "filling" or "positioning"; micropipettes either too thin or too broad, so with incorrect tip "diameter", and micropipettes that "hit the bottom" when their main angle was bigger than 45° and the micropipette tip was pointing upwards, never reaching the focal plane of the microscope. The vast increase in the prevalence of the "fabrication" category in 2017 can be due to growing experience, which allowed me to eliminate some faulty micropipettes in fabrication already (for example, the "pointed tip" and "dirty" categories), or due to the simple omission of this category in my notes in 2016 (a micropipette discarded in fabrication does not delay much).

# Supplement 2: Cells

This supplement re-uses the Materials and Methods part from (Sawicka et al., 2017), under the CC-BY-NC-SA 3.0 license, with some modifications as needed.

All cells I used in the research were human cells. The research was conducted according to the Helsinki Declaration, with informed consent obtained from the blood donors, as requested by the Etablissement Français du Sang.

The blood was separated with a standard Ficoll procedure. T cells were obtained from the layer of peripheral blood mononuclear cells by negative selection with following kits:

- primary CD4+ T cells (resting T cells): 130-096-533CD4+ T Cell Isolation Kit, human (Miltenyi Biotec, Bergisch Gladbach, Germany). Excludes cells with CD8, CD14, CD15, CD16, CD19, CD36, CD56, CD123, TCR γ/δ, and glycophorin A. Targets the population of (CD3+CD4+) cells.

- naïve CD4+ T cells: 19555 EasySep Human Naïve CD4+ T cell isolation kit, (Stemcell Technologies, Vancouver, Canada). Excludes cells with CD8, CD14, CD16, CD19, CD20, CD25, CD36, CD56, CD61, CD66b, CD123, HLA-DR, TCRγ/δ, glycophorin A,and CD45RO. Targets the population of (CD3+CD4+CD45RA+CD45RO-) cells.

- memory CD4+ T cells: 130-091-893 Memory CD4+ T Cell Isolation Kit, human (Miltenyi Biotec). Excludes cells with CD45RA, CD8, CD14, CD16, CD19, CD56, CD36, CD123, TCRγ/δ, and glycophorin A. Targets the population of (CD3+CD4+CD45RO+) cells.

T cells were purified by Stéphanie Dogniaux and Michael Saitakis.

The complete medium used in all the experiments was RPMI 1640 with GlutaMax, supplemented with 10% heat-inactivated fetal bovine serum (FBS) and 1% penicillin-streptomycin (all from Life Technologies ThermoFisher Scientific, Waltham, USA).

Isolated T cells were either used directly for experiments, or suspended in FBS:DMSO (90%:10% vol/vol) and kept frozen in liquid nitrogen. One to seven days before the experiment the cells were thawed, mixed with preheated complete medium, washed once, and then kept in the complete medium at 37°C, 5% $CO_2$, at a concentration around $10^6$ cells/ml.

To obtain CD4+ T lymphoblasts, six-well plastic plates were coated with anti-CD3 antibody (OKT3 clone, #16-0037-85; eBioscience, ThermoFisher Scientific; 2,5 µg/ml in 1,3 ml final) overnight at 4°C. Wells were washed, and $5{,}4 \times 10^6$ freshly purified primary CD4+ T cells were plated per well in the presence of soluble anti-CD28 antibody (LEAF Purified anti-human CD28 #BLE302923; Biolegend, San Diego, USA; 2,5 µg/ml) and recombinant IL-2 (Proleukin; Novartis, Basel, Switzerland; 20 U/ml). Fresh medium containing IL-2 (20 U/ml) was added every 3 days, and lymphoblasts were used from day 6 or frozen on day 6 and thawed before the experiment, as described above.

# Supplement 3: Additional methods

Parts of this supplement re-use the Materials and Methods part from (Sawicka et al., 2017) , under the CC-BY-NC-SA 3.0 license, with some modifications as needed.

## S3.1 Western blot analysis of protein phosphorylation

Human primary CD4+ T-cells ($4 \times 10^6$/ml) were pre-incubated for 15 to 30 min at 37°C with 30 µM ML-7, 25 µM SMIFH2, or in DMSO (vehicle 1/67, vol/vol). Cells were then activated by addition of beads coated withanti-CD3 and anti-CD28 antibodies at a ratio of one bead per cell. After the described time (10 or 30 min), activation was stopped on ice by addition of cold PBS. After centrifugation, cells were lysed in Pierce radioimmunoprecipitation assay (RIPA) buffer (ThermoFisher Scientific) supplemented with 1× complete, Mini, EDTA-free Protease Inhibitor Cocktail Tablet (Roche, Basel, Switzerland) and Halt Phosphatase

Inhibitor Cocktail (ThermoFisher Scientific). The lysates were resolved by SDS-PAGE on Mini- PROTEAN TGX Precast Gels (Bio-Rad, Hercules, USA) and were transferred to membranes (Immunoblot PVDF membranes; Bio-Rad) with the Trans-Blot turbo system (Bio-Rad). Membranes were blocked for 2 h in Tris-buffered saline (TBS), 5% bovine serum albumin (BSA), 0,05% Tween and incubated overnight at 4°C with primary antibodies diluted in TBS, 5% BSA, 0,05% Tween: anti-phospho-myosin light chain 2 (Thr18/Ser19) rabbit antibody (#3674; Cell Signaling Technology, Danvers, USA; 1:1000), anti-phospho-ζ chain (Tyr142) mouse antibody (BD558402; BD Biosciences, Franklin Lakes, USA; 1:1000), anti-LAT rabbit antibody (06-807; Merck Milipore, Darmstadt, Germany; 1 μg/ml), and anti-gp96 rat antibody (9G10 monoclonal rat antibody; Abcam, Cambridge, UK; 0,5 μg/ml). After several washes in TBS, 0,05% Tween, membranes were incubated 1 h at room temperature with horseradish peroxidase (HRP)-conjugated secondary antibodies (Jackson Immuno Research, West Grove, USA; 1:10000) diluted in TBS, 5% BSA, 0,05% Tween. Membranes were then washed again, incubated for 5 min in Clarity Western ECL Blotting Substrates (Bio-Rad), and revealed with the ChemiDoc Touch Imaging system (Bio-Rad). Western blot experiments were performed by Claire Hivroz, Stéphanie Dogniaux and me.

## S3.2 Scanning electron microscopy

Human primary CD4+ T-cells ($1{,}5 \times 10^5$ cells per slide) were plated on 12 mm round slides precoated with 0,02% poly-L-lysine and incubated for 20 min at room temperature. Then the beads coated with anti-CD3 and anti-CD28 antibodies were added, at a ratio of one bead per cell, and incubated for 5 min at room temperature. The samples were then washed in phosphate buffer, pH 7.4 (PB), fixed overnight at 4°C in PB + 2% glutaraldehyde, and, finally, washed in PB. Samples were then dehydrated by passing through a graded series of ethanol solutions, then dried by the $CO_2$ critical-point method (CPD75 Quorum Technologies, Lewes, UK) and coated by sputtering with a 20- to 40-nm thin gold layer with a Scancoat Six (Edwards Vacuum, HHV, Crawley, UK). Acquisitions were performed with a GeminiSEM 500 microscope (Zeiss, Oberkochen, Germany). The slides were prepared by Claire Hivroz and me until the fixation in glutaraldehyde, and then prepared for imaging and imaged by Virginie Bazin from IBPS, at Université Pierre et Marie Curie.

## S3.3 Software used

The optical microscope was controlled with MicroManager (https://micro-manager.org/). For the fast tracking of the position of the tip of the measuring micropipette, a custom script in Matlab (https://en.mathworks.com/products/matlab.html) controlled both the MicroManager and the piezoelectric micropositioner. The microscope images were analysed and prepared for publication with ImageJ, version 1.50b (https://imagej.nih.gov/ij/). The numerical data was stored, analysed, and visualised with OpenOffice (https://www.openoffice.org/?redirect=soft), Microsoft Excel (https://products.office.com/en-us/excel), and R, used with the help of JGR (Java GUI for R, https://www.rforge.net/JGR/). The charts were plotted with Matlab or with OpenOffice. The statistical tests were performed in Matlab or with the online calculators available on the Social Science Statistics website (http://www.socscistatistics.com/), after a verification that they provide the same results as the built-in Matlab functions. The schematic drawings and the compilation of multi-panel figures for publication were done in Inkscape (https://inkscape.org/en/). Mendeley (https://www.mendeley.com/) was used to manage papers and references. I would like to acknowledge the Citation Gecko (http://citationgecko.com/) for a different look at the references. The thesis was written in Microsoft Word, and formatted with the template provided by the Paris Descartes University. The equations in separate lines were typeset with LaTeX, used with the help of LyX (https://www.lyx.org/).

# Supplement 4: Editorial choices for text

When people write about T cells and T lymphocytes, they write about the same cells, and these notions were already interchangeable in the 1980s (for example, both forms appear in the same Nature News&Views article (Robertson, 1986)). As a purely editorial choice, I use T cells throughout the thesis.

The origin of the name "western blot" is an interesting piece in the history of science. The technique for the transfer of DNA from the agarose gel to nitrocellulose membrane, on which it is subsequently detected with a complementary RNA strand, was described by Edwin

Southern (Southern, 1975), and, as the technique became immediately popular, the researchers began calling it the "Southern blot". By convention, a play with words, and an intelligent tribute to Edwin Southern, a similar technique for the transfer of RNA got the name of the "Northern blot"; although it was not called this way in the original paper (Alwine, Kemp, & Stark, 1977). When W. Neal Burnette described a technique for the analogous transfer of proteins, this is the way he motivated the choice of the name: "With due respect to Southern (Southern, 1975), the established tradition of “geographic” naming of transfer techniques (“Southern,” “Northern”) is continued; the method described in this manuscript is referred to as “Western” blotting." (Burnette, 1981) (this is not the first paper that described the technique of protein transfer and detection, see references 7-9 in it).

More than 35 years later, the western blots are still in use, with both spellings: "western" (Lin, Fan, et al., 2015; Martin, Veloso, Wu, Katrukha, & Akhmanova, 2018; Tajik et al., 2016), and "Western" (Engel et al., 2015; Murugesan et al., 2016; Roybal, Buck, Ruan, et al., 2016) (examples only; I did not check which form is more popular). The choice between the two spellings is complicated by the fact that English orthography allows both "western" and "Western"; with, potentially, a slight change in meaning (Oxford English Living Dictionary, https://en.oxforddictionaries.com/definition/western

see also the Q&A of the Chicago Manual of Style,

http://www.chicagomanualofstyle.org/qanda/data/faq/topics/Capitalization/faq0034.html

both links accessed on 2018-06-29). I chose to use "western blots", to align with all the other names for laboratory techniques, which are spelled in small caps, and to stress that no person by the name of Western was implicated in the development of the technique (although W. Neal Burnette worked at the time at the Fred Hutchinson Cancer Research Center in Seattle, so on the West Coast of the USA).

# Supplement 5: Sample charts from MFP experiments

During the ongoing research work for my thesis, Julien Husson developed a fast-tracking system for the MFP experiments. As a result, some of the data presented in this thesis come from the experiments in which the position of the measuring micropipette was tracked manually in the sequence of images (with one data point every 2 seconds) and some from the experiments in which the position of the measuring micropipette was tracked automatically (with about 800 data points every 2 seconds). The change in tracking system meant also the change in the micropipette setup, as shown in Figure 14 in Chapter 1. For the manual tracking we used the face-to-face setup (Figure 14C), whereas for the automatic tracking we used the 90° setup (Figure 14B), as the automatic tracking relies on the cross-correlation of the successive images, and it requires a clear pattern on the image, which was in this case provided by the tip of the measuring micropipette.

To show that the two setups give the same order of events on the chart (although the automatic tracking system enables to study the force sequence in more detail), and to provide some estimate of the cell-to-cell variability in the experiments, I attach to the thesis the montage of the charts obtained with the two approaches. First montage (Figure 45) shows all the active cells in one manual tracking experiment, with the measuring micropipette stiffness $k = 0{,}202$ nN/μm. Second montage (Figure 46) shows all the active cells in two automatic tracking experiments, with the measuring micropipette stiffness $k = 0{,}285$ nN/μm and $k = 0{,}256$ nN/μm; yellow line is a window average over 50 data points; note that first six and the latter six charts have a different scale on the Y axis. Time is shown in seconds from the beginning of the recording on the X axis, the position of the measuring micropipette in micrometers from its position on the first frame on the Y axis.

As it can be seen in the charts, the initial pushing and return are usually clearly marked. However, the beginning of the pulling phase is sometimes difficult to mark, and sometimes it cannot be traced at all, for example when the cell pushed itself out of the holding micropipette during the pushing phase, which blocks the possibility of force measurement (charts were cut in this situation). The onset of pulling was not associated with an abrupt change of cell morphology. Therefore, for the analysis of pulling speed I used only the charts in which a clear, linear pulling is visible, and there is no drift of the baseline of the chart. This led unfortunately to few cells analysed for pulling per one experiment; a more thorough analysis of pulling would require more experiments.

Figure 45. Montage of all charts obtained in one experiment with manual tracking.

Figure 46. Montage of all charts obtained in two experiments with automatic tracking.

Figures 45 and 46 are shown on the two next pages.

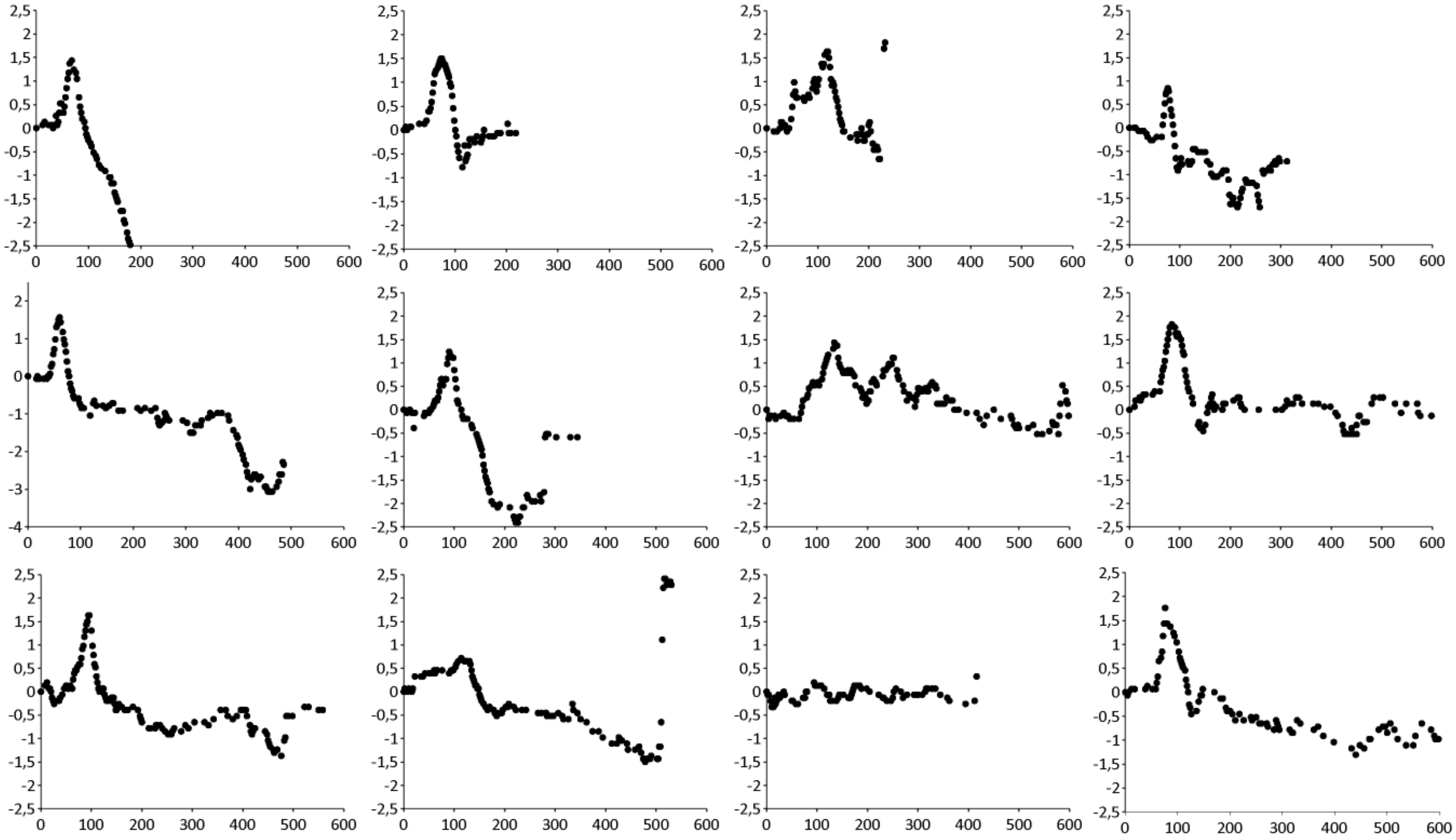

Figure 45. See the legend and the description on the previous page.

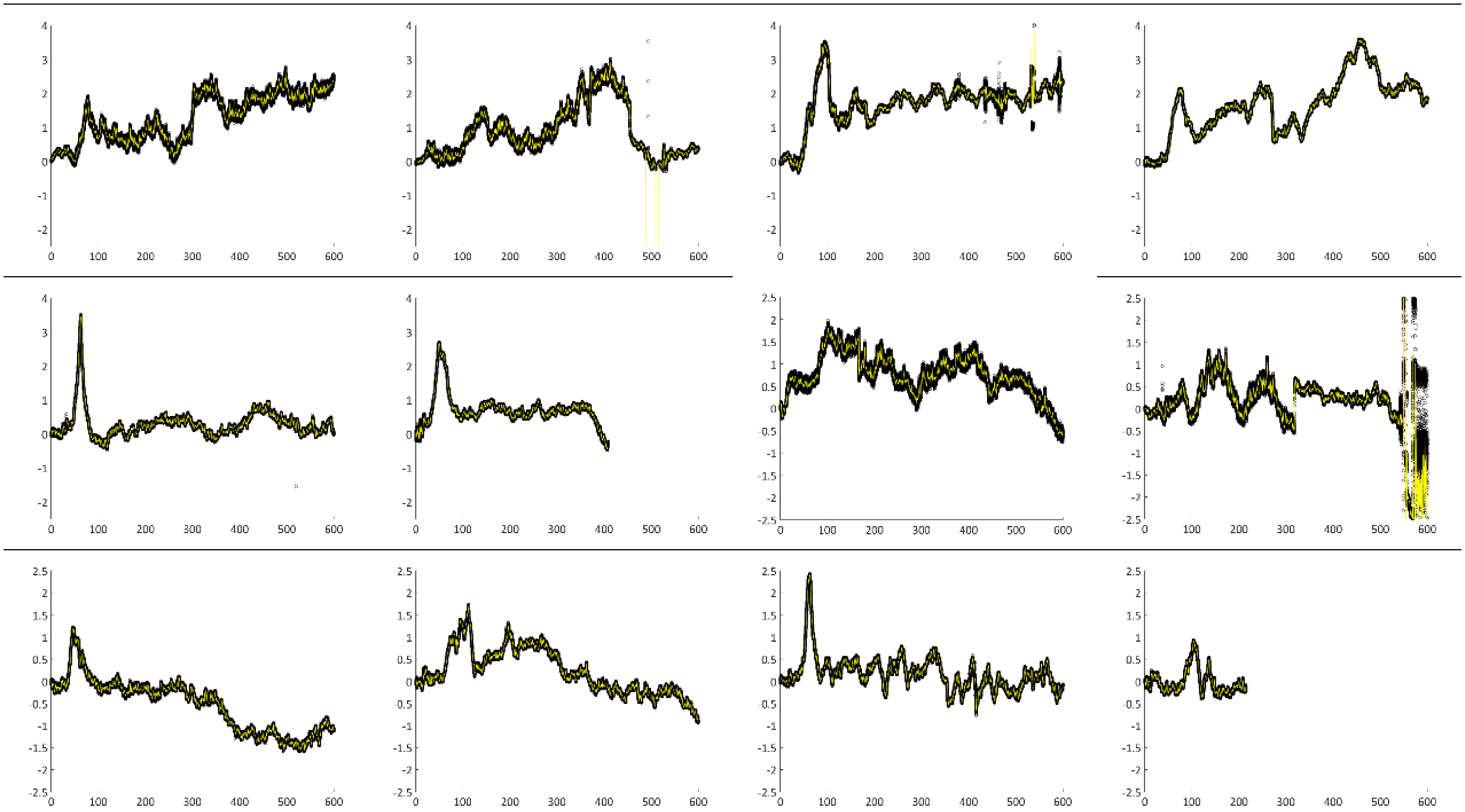

Figure 46. See the legend and the description on the page 123.

# Bibliography

Acuto, O., & Cantrell, D. (2000). T cell activation and the cytoskeleton. *Annual Reviews in Immunology*, *18*, 165–184. https://doi.org/10.1146/annurev.immunol.18.1.165

Al-Aghbar, M. A., Chu, Y. S., Chen, B. M., & Roffler, S. R. (2018). High-affinity ligands can trigger T cell receptor signaling without CD45 segregation. *Frontiers in Immunology*, *9*, 713. https://doi.org/10.3389/fimmu.2018.00713

Allen, P. M., Matsueda, G. R., Haber, E., & Unanue, E. R. (1985). Specificity of the T cell receptor: two different determinants are generated by the same peptide and the I-Ak molecule. *Journal of Immunology*, *135*(1), 368–373. Retrieved from http://www.jimmunol.org/content/135/1/368

Alwine, J. C., Kemp, D. J., & Stark, G. R. (1977). Method for detection of specific RNAs in agarose gels by transfer to diazobenzyloxymethyl-paper and hybridization with DNA probes. *Proceedings of the National Academy of Sciences*, *74*(12), 5350–5354. https://doi.org/10.1073/pnas.74.12.5350

Andrés-Delgado, L., Antón, O. M., Bartolini, F., Ruiz-Sáenz, A., Correas, I., Gundersen, G. G., & Alonso, M. A. (2012). INF2 promotes the formation of detyrosinated microtubules necessary for centrosome reorientation in T cells. *Journal of Cell Biology*, *198*(6), 1025–1037. https://doi.org/10.1083/jcb.201202137

Ashkin, A. (1970). Acceleration and Trapping of Particles by Radiation Pressure. *Physical Review Letters*, *24*(4), 156–159. https://doi.org/10.1103/PhysRevLett.24.156

Barda-Saad, M., Braiman, A., Titerence, R., Bunnell, S. C., Barr, V. A., & Samelson, L. E. (2005). Dynamic molecular interactions linking the T cell antigen receptor to the actin cytoskeleton. *Nature Immunology*, *6*(1), 80–89. https://doi.org/10.1038/ni1143

Bartolini, F., Moseley, J. B., Schmoranzer, J., Cassimeris, L., Goode, B. L., & Gundersen, G. G. (2008). The formin mDia2 stabilizes microtubules independently of its actin nucleation activity. *Journal of Cell Biology*, *181*(3), 523–536. https://doi.org/10.1083/jcb.200709029

Bashour, K. T., Gondarenko, A., Chen, H., Shen, K., Liu, X., Huse, M., … Kam, L. C. (2014). CD28 and CD3 have complementary roles in T-cell traction forces. *Proceedings of the National Academy of Sciences*, *111*(6), 2241–2246. https://doi.org/10.1073/pnas.1315606111

Basu, R., Whitlock, B. M., Husson, J., Le Floc'h, A., Jin, W., Oyler-Yaniv, A., … Huse, M. (2016). Cytotoxic T Cells Use Mechanical Force to Potentiate Target Cell Killing. *Cell*, *165*(1), 100–110. https://doi.org/10.1016/j.cell.2016.01.021

Bernard, A., & Boumsell, L. (1984). The Clusters of Differentiation (CD) defined by the First International Workshop on Human Leucocyte Differentiation Antigens. *Human Immunology*, *11*(1), 1–10. https://doi.org/10.1016/0198-8859(84)90051-X

Bhaumik, S., & Basu, R. (2017). Cellular and molecular dynamics of Th17 differentiation and its developmental plasticity in the intestinal immune response. *Frontiers in Immunology*, *8*, 254. https://doi.org/10.3389/fimmu.2017.00254

Billadeau, D. D., Nolz, J. C., & Gomez, T. S. (2007). Regulation of T-cell activation by the cytoskeleton. *Nature Reviews Immunology*, *7*(2), 131–143. https://doi.org/10.1038/nri2021

Binnig, G., Quate, C. F., & Gerber, C. (1986). Atomic force microscope. *Physical Review Letters*, *56*(9), 930–933. https://doi.org/10.1103/PhysRevLett.56.930

Bohineust, A., Garcia, Z., Beuneu, H., Lemaître, F., & Bousso, P. (2018). Termination of T cell priming relies on a phase of unresponsiveness promoting disengagement from APCs and T cell division. *Journal of Experimental Medicine*, *215*(5), 1481–1492. https://doi.org/10.1084/jem.20171708

Bovellan, M., Romeo, Y., Biro, M., Boden, A., Chugh, P., Yonis, A., … Charras, G. (2014). Cellular control of cortical actin nucleation. *Current Biology*, *24*(14), 1628–1635. https://doi.org/10.1016/j.cub.2014.05.069

Brain, P., Gordon, J., & Willetts, W. A. (1970). Rosette formation by peripheral lymphocytes. *Clinical and Experimental Immunology*, *6*(5), 681–688. Retrieved from https://www.ncbi.nlm.nih.gov/pmc/articles/PMC1712724/

Brandvold, K. R., Steffey, M. E., Fox, C. C., & Soellner, M. B. (2012). Development of a highly selective c-Src kinase inhibitor. *ACS Chemical Biology*, *7*(8), 1393–1398. https://doi.org/10.1021/cb300172e

Brownlie, R. J., & Zamoyska, R. (2013). T cell receptor signalling networks: branched, diversified and bounded. *Nature Reviews Immunology*, *13*(4), 257–269. https://doi.org/10.1038/nri3403

Bufi, N., Saitakis, M., Dogniaux, S., Buschinger, O., Bohineust, A., Richert, A., … Asnacios, A. (2015). Human primary immune cells exhibit distinct mechanical properties that are modified by inflammation. *Biophysical Journal*, *108*(9), 2181–2190. https://doi.org/10.1016/j.bpj.2015.03.047

Burnette, W. N. (1981). “Western blotting”: electrophoresis of protein from sodium dodecyl sulphate polyacrylamide gels to unmodified nitrocellulose and radiographic detection with antibody and radioiodinated protein A. *Analytical Biochemistry*, *112*, 195–203. https://doi.org/10.1177/104063870601800613

Cai, E., Marchuk, K., Beemiller, P., Beppler, C., Rubashkin, M. G., Weaver, V. M., … Krummel, M. F. (2017). Visualizing dynamic microvillar search and stabilization during ligand detection by T cells. *Science*, *356*(6338), eaal3118. https://doi.org/10.1126/science.aal3118

Carbone, C. B., Kern, N., Fernandes, R. A., Hui, E., Su, X., Garcia, K. C., & Vale, R. D. (2017). In vitro reconstitution of T cell receptor-mediated segregation of the CD45 phosphatase. *Proceedings of the National Academy of Sciences*, *114*(44), E9338–E9345. https://doi.org/10.1073/pnas.1710358114

Chang, V. T., Fernandes, R. A., Ganzinger, K. A., Lee, S. F., Siebold, C., McColl, J., … Davis, S. J. (2016). Initiation of T cell signaling by CD45 segregation at “close contacts.” *Nature Immunology*, *17*(5), 574–582. https://doi.org/10.1038/ni.3392

Chaudhuri, O., Parekh, S. H., Lam, W. A., & Fletcher, D. A. (2009). Combined atomic force microscopy and side-view optical imaging for mechanical studies of cells. *Nature Methods*, *6*(5), 383–387. https://doi.org/10.1038/nmeth.1320

Chen, C., Tao, T., Wen, C., He, W.-Q., Qiao, Y.-N., Gao, Y.-Q., … Zhu, M.-S. (2014). Myosin light chain kinase (MLCK) regulates cell migration in a myosin regulatory light chain phosphorylation-independent mechanism. *Journal of Biological Chemistry*, *289*(41), 28478–28488. https://doi.org/10.1074/jbc.M114.567446

Chen, L., & Flies, D. B. (2013). Molecular mechanisms of T cell co-stimulation and co-inhibition. *Nature Reviews Immunology*, *13*, 227–242. https://doi.org/10.1038/nri3405

Chen, Y., Ju, L., Rushdi, M., Ge, C., & Zhu, C. (2017). Receptor-mediated cell mechanosensing. *Molecular Biology of the Cell*, *28*(23), 3134–3155. https://doi.org/10.1091/mbc.E17-04-0228

Chugh, P., Clark, A. G., Smith, M. B., Cassani, D. A. D., Dierkes, K., Ragab, A., … Paluch, E. K. (2017). Actin cortex architecture regulates cell surface tension. *Nature Cell Biology*, *19*(6), 689–697. https://doi.org/10.1038/ncb3525

Comrie, W. A., & Burkhardt, J. K. (2016). Action and Traction: Cytoskeletal Control of

Receptor Triggering at the Immunological Synapse. *Frontiers in Immunology, 7*, 68. https://doi.org/10.3389/fimmu.2016.00068

Courtney, A. H., Lo, W.-L., & Weiss, A. (2018). TCR Signaling: Mechanisms of Initiation and Propagation. *Trends in Biochemical Sciences*, *43*(2), 108–123. https://doi.org/10.1016/J.TIBS.2017.11.008

Davies, A. J. (1993). The tale of T cells. *Immunology Today*, *14*(3), 137–140. https://doi.org/10.1016/0167-5699(93)90216-8

Davis, S. J., & van der Merwe, P. A. (2006). The kinetic-segregation model: TCR triggering and beyond. *Nature Immunology*, *7*(8), 803–809. https://doi.org/10.1038/ni1369

Delon, J., Bercovici, N., Liblau, R., & Trautmann, A. (1998). Imaging antigen recognition by naive CD4+T cells: Compulsory cytoskeletal alterations for the triggering of an intracellular calcium response. *European Journal of Immunology*, *28*(2), 716–729. https://doi.org/10.1002/(SICI)1521-4141(199802)28:02<716::AID-IMMU716>3.0.CO;2-E

Delon, J., & Germain, R. N. (2000). Information transfer at the immunological synapse. *Current Biology*, *10*(24), R923-33. https://doi.org/10.1016/S0960-9822(00)00870-8

Dembo, M., & Wang, Y.-L. (1999). Stresses at the Cell-to-Substrate Interface during Locomotion of Fibroblasts. *Biophysical Journal*, *76*(4), 2307–2316. https://doi.org/10.1016/S0006-3495(99)77386-8

Dillard, P., Varma, R., Sengupta, K., & Limozin, L. (2014). Ligand-mediated friction determines morphodynamics of spreading T cells. *Biophysical Journal*, *107*(11), 2629–2638. https://doi.org/10.1016/j.bpj.2014.10.044

Dustin, M. L., & Cooper, J. A. (2000). The immunolgical synapse and the actin cyroskeleton: molecular hardware for T cell signaling. *Nature Immunology*, *1*(1), 23–29. https://doi.org/10.1038/76877

Edelstein, A., Amodaj, N., Hoover, K., Vale, R., & Stuurman, N. (2010). Computer control of microscopes using µManager. *Current Protocols in Molecular Biology, Supplement*, 14.20.1-14.20.17. https://doi.org/10.1002/0471142727.mb1420s92

Eisenmann, K. M., West, R. A., Hildebrand, D., Kitchen, S. M., Peng, J., Sigler, R., … Alberts, A. S. (2007). T cell responses in mammalian diaphanous-related formin mDia1 knock-out mice. *Journal of Biological Chemistry*, *282*(34), 25152–25158. https://doi.org/10.1074/jbc.M703243200

Engel, P., Boumsell, L., Balderas, R., Bensussan, A., Gattei, V., Horejsi, V., … Clark, G. (2015). CD Nomenclature 2015: Human Leukocyte Differentiation Antigen Workshops as a Driving Force in Immunology. *The Journal of Immunology*, *195*(10), 4555–4563. https://doi.org/10.4049/jimmunol.1502033

Evans, E., Leung, A., & Zhelev, D. (1993). Synchrony of cell spreading and contraction force as phagocytes engulf large pathogens. *Journal of Cell Biology*, *122*(6), 1295–1300. https://doi.org/10.1083/jcb.122.6.1295

Evans, E., Ritchie, K., & Merkel, R. (1995). Sensitive force technique to probe molecular adhesion and structural linkages at biological interfaces. *Biophysical Journal*, *68*(6), 2580–2587. https://doi.org/10.1016/S0006-3495(95)80441-8

Evans, E., & Yeung, A. (1989). Apparent viscosity and cortical tension of blood granulocytes determined by micropipet aspiration. *Biophysical Journal*, *56*(1), 151–160. https://doi.org/10.1016/S0006-3495(89)82660-8

Evavold, B. D., & Allen, P. M. (1991). Separation of IL-4 production from Th cell proliferation by an altered T cell receptor ligand. *Science*, *252*(5010), 1308–1310. https://doi.org/10.1126/SCIENCE.1833816

Feng, Y., Brazin, K. N., Kobayashi, E., Mallis, R. J., Reinherz, E. L., & Lang, M. J. (2017).

Mechanosensing drives acuity of αβ T-cell recognition. *Proceedings of the National Academy of Sciences*, *114*(39), E8204–E8213. https://doi.org/10.1073/pnas.1703559114

Ferreira, L. M. R. (2013). Gammadelta T Cells: Innately adaptive immune cells? *International Reviews of Immunology*, *32*(3), 223–248. https://doi.org/10.3109/08830185.2013.783831

Fesnak, A. D., June, C. H., & Levine, B. L. (2016). Engineered T cells: The promise and challenges of cancer immunotherapy. *Nature Reviews Cancer*, *16*(9), 566–581. https://doi.org/10.1038/nrc.2016.97

Gaud, G., Lesourne, R., & Love, P. E. (2018). Regulatory mechanisms in T cell receptor signalling. *Nature Reviews Immunology*. https://doi.org/10.1038/s41577-018-0020-8

Gomez, T. S., Kumar, K., Medeiros, R. B., Shimizu, Y., Leibson, P. J., & Billadeau, D. D. (2007). Formins Regulate the Actin-Related Protein 2/3 Complex-Independent Polarization of the Centrosome to the Immunological Synapse. *Immunity*, *26*(2), 177–190. https://doi.org/10.1016/j.immuni.2007.01.008

Gonzalez-Rodriguez, D., Guillou, L., Cornat, F., Lafaurie-Janvore, J., Babataheri, A., de Langre, E., … Husson, J. (2016). Mechanical Criterion for the Rupture of a Cell Membrane under Compression. *Biophysical Journal*, *111*(12), 2711–2721. https://doi.org/10.1016/j.bpj.2016.11.001

Good, R. A., Gabrielsen, A. E., Cooper, M. D., & Peterson, R. D. A. (1966). The role of the thymus and bursa of Fabricius in the development of effector mechanisms. *Annals of the New York Academy of Sciences*, *129*(1), 130–154. https://doi.org/10.1111/j.1749-6632.1966.tb12847.x

Grakoui, A., Bromley, S. K., Sumen, C., Davis, M. M., Shaw, A. S., Allen, P. M., & Dustin, M. L. (1999). The immunological synapse: a molecular machine controlling T cell activation. *Science*, *285*(5425), 221–227. https://doi.org/10.1126/science.285.5425.221

Grossman, Z., & Paul, W. E. (2015). Dynamic Tuning of Lymphocytes: Physiological Basis, Mechanisms, and Function. *Annual Review of Immunology*, *33*(1), 677–713. https://doi.org/10.1146/annurev-immunol-032712-100027

Guck, J., Schinkinger, S., Lincoln, B., Wottawah, F., Ebert, S., Romeyke, M., … Bilby, C. (2005). Optical deformability as an inherent cell marker for testing malignant transformation and metastatic competence. *Biophysical Journal*, *88*(5), 3689–3698. https://doi.org/10.1529/biophysj.104.045476

Guillou, L., Babataheri, A., Puech, P.-H., Barakat, A. I., & Husson, J. (2016). Dynamic monitoring of cell mechanical properties using profile microindentation. *Scientific Reports*, *6*(1), 21529. https://doi.org/10.1038/srep21529

Guillou, L., Babataheri, A., Saitakis, M., Bohineust, A., Dogniaux, S., Hivroz, C., … Husson, J. (2016). T-lymphocyte passive deformation is controlled by unfolding of membrane surface reservoirs. *Molecular Biology of the Cell*, *27*(22), 3574–3582. https://doi.org/10.1091/mbc.E16-06-0414

Hammer, J. A., & Burkhardt, J. K. (2013). Controversy and Consensus Regarding Myosin II Function at the Immunological Synapse. *Current Opinion in Immunology*, *25*(3), 300–306. https://doi.org/10.1016/j.coi.2013.03.010

Herant, M., Heinrich, V., & Dembo, M. (2005). Mechanics of neutrophil phagocytosis: behavior of the cortical tension. *Journal of Cell Science*, *118*(9), 1789–1797. https://doi.org/10.1242/jcs.02275

Hirose, K., Iwata, A., Tamachi, T., & Nakajima, H. (2017). Allergic airway inflammation: key players beyond the Th2 cell pathway. *Immunological Reviews*, *278*, 145–161. https://doi.org/10.1111/imr.12540

Hivroz, C., & Saitakis, M. (2016). Biophysical Aspects of T Lymphocyte Activation at the Immune Synapse. *Frontiers in Immunology, 7*, 46. https://doi.org/10.3389/fimmu.2016.00046

Hochweller, K., Wabnitz, G. H., Samstag, Y., Suffner, J., Hammerling, G. J., & Garbi, N. (2010). Dendritic cells control T cell tonic signaling required for responsiveness to foreign antigen. *Proceedings of the National Academy of Sciences*, *107*(13), 5931–5936. https://doi.org/10.1073/pnas.0911877107

Hong, J., Murugesan, S., Betzig, E., & Hammer, J. A. (2017). Contractile actomyosin arcs promote the activation of primary mouse T cells in a ligand-dependent manner. *PLoS ONE*, *12*(8), e0183174. https://doi.org/10.1371/journal.pone.0183174

Hong, J., Persaud, S. P., Horvath, S., Allen, P. M., Evavold, B. D., & Zhu, C. (2015). Force-Regulated In Situ TCR–Peptide-Bound MHC Class II Kinetics Determine Functions of CD4 $^+$ T Cells. *The Journal of Immunology*, *195*(8), 3557–3564. https://doi.org/10.4049/jimmunol.1501407

Hu, K. H., & Butte, M. J. (2016). T cell activation requires force generation. *Journal of Cell Biology*, *213*(5), 535–542. https://doi.org/10.1083/jcb.201511053

Huang, J., Brameshuber, M., Zeng, X., Xie, J., Li, Q., Chien, Y., … Davis, M. M. (2013). A single peptide-major histocompatibility complex ligand triggers digital cytokine secretion in CD4+ T Cells. *Immunity*, *39*(5), 846–857. https://doi.org/10.1016/j.immuni.2013.08.036

Hui, K. L., Balagopalan, L., Samelson, L. E., & Upadhyaya, A. (2015). Cytoskeletal forces during signaling activation in Jurkat T-cells. *Molecular Biology of the Cell*, *26*(4), 685–695. https://doi.org/10.1091/mbc.E14-03-0830

Hui, K. L., & Upadhyaya, A. (2017). Dynamic microtubules regulate cellular contractility during T-cell activation. *Proceedings of the National Academy of Sciences*, *114*(21), E4175–E4183. https://doi.org/10.1073/pnas.1614291114

Huse, M., Klein, L. O., Girvin, A. T., Faraj, J. M., Li, Q. J., Kuhns, M. S., & Davis, M. M. (2007). Spatial and Temporal Dynamics of T Cell Receptor Signaling with a Photoactivatable Agonist. *Immunity*, *27*(1), 76–88. https://doi.org/10.1016/j.immuni.2007.05.017

Husson, J., Chemin, K., Bohineust, A., Hivroz, C., & Henry, N. (2011). Force generation upon T cell receptor engagement. *PLoS ONE*, *6*(5), e19680. https://doi.org/10.1371/journal.pone.0019680

Irvine, D. J., Purbhoo, M. A., Krogsgaard, M., & Davis, M. M. (2002). Direct observation of ligand recognition by T cells. *Nature*, *419*(6909), 845–849. https://doi.org/10.1038/nature01076

Ishizaki, T., Morishima, Y., Okamoto, M., Furuyashiki, T., Kato, T., & Narumiya, S. (2001). Coordination of microtubules and the actin cytoskeleton by the Rho effector mDia1. *Nature Cell Biology*, *3*(1), 8–14. https://doi.org/10.1038/35050598

Iskratsch, T., Wolfenson, H., & Sheetz, M. P. (2014). Appreciating force and shape-the rise of mechanotransduction in cell biology. *Nature Reviews Molecular Cell Biology*, *15*(12), 825–833. https://doi.org/10.1038/nrm3903

Jager, A., Dardalhon, V., Sobel, R. A., Bettelli, E., & Kuchroo, V. K. (2009). Th1, Th17, and Th9 Effector Cells Induce Experimental Autoimmune Encephalomyelitis with Different Pathological Phenotypes. *The Journal of Immunology*, *183*(11), 7169–7177. https://doi.org/10.4049/jimmunol.0901906

Judokusumo, E., Tabdanov, E., Kumari, S., Dustin, M. L., & Kam, L. C. (2012). Mechanosensing in T lymphocyte activation. *Biophysical Journal*, *102*(2), L5–L7. https://doi.org/10.1016/j.bpj.2011.12.011

Jurlander, J. (1998). The cellular biology of B-cell chronic lymphocytic leukemia. *Critical*

*Reviews in Oncology/Hematology*, *27*(1), 29–52. Retrieved from http://www.ncbi.nlm.nih.gov/pubmed/9548016

Képiró, M., Várkuti, B. H., Végner, L., Vörös, G., Hegyi, G., Varga, M., & Málnási-Csizmadia, A. (2014). Para-nitroblebbistatin, the non-cytotoxic and photostable myosin II inhibitor. *Angewandte Chemie - International Edition*, *53*(31), 8211–8215. https://doi.org/10.1002/anie.201403540

Kim, A. S., Kakalis, L. T., Abdul-Manan, N., Liu, G. A., & Rosen, M. K. (2000). Autoinhibition and activation mechanisms of the Wiskott-Aldrich syndrome protein. *Nature*, *404*(6774), 151–158. https://doi.org/10.1038/35004513

Kim, S. T., Takeuchi, K., Sun, Z. Y. J., Touma, M., Castro, C. E., Fahmy, A., … Reinherz, E. L. (2009). The αβ T cell receptor is an anisotropic mechanosensor. *Journal of Biological Chemistry*, *284*(45), 31028–31037. https://doi.org/10.1074/jbc.M109.052712

Köhler, G., & Milstein, C. (1975). Continuous cultures of fused cells secreting antibody of predefined specificity. *Nature*, *256*(5517), 495–497. https://doi.org/10.1038/256495a0

Kumari, S., Depoil, D., Martinelli, R., Judokusumo, E., Carmona, G., Gertler, F. B., … Dustin, M. L. (2015). Actin foci facilitate activation of the phospholipase C-γ in primary T lymphocytes via the WASP pathway. *ELife*, *4*, e04953. https://doi.org/10.7554/eLife.04953

Kung, P., Goldstein, G., Reinherz, E. L., & Schlossman, S. F. (1979). Monoclonal antibodies defining distinctive human T cell surface antigens. *Science*, *206*(4416), 347–349. https://doi.org/10.1126/SCIENCE.314668

Kupfer, A., & Dennert, G. (1984). Reorientation of the microtubule-organizing center and the Golgi apparatus in cloned cytotoxic lymphocytes triggered by binding to lysable target cells. *Journal of Immunology*, *133*(5), 2762–2766. Retrieved from http://www.jimmunol.org/content/133/5/2762

Kupfer, A., & Kupfer, H. (2003). Imaging immune cell interactions and functions: SMACs and the Immunological Synapse. *Seminars in Immunology*, *15*(6), 295–300. https://doi.org/10.1016/j.smim.2003.09.001

Kupfer, A., Swain, S. L., Janeway Jr., C. A., & Singer, S. J. (1986). The specific direct interaction of helper T cells and antigen-presenting B cells. *Proceedings of the National Academy of Sciences*, *83*(16), 6080–6083. https://doi.org/10.1073/pnas.83.16.6080

Laurent, V. M., Hénon, S., Planus, E., Fodil, R., Balland, M., Isabey, D., & Gallet, F. (2002). Assessment of Mechanical Properties of Adherent Living Cells by Bead Micromanipulation: Comparison of Magnetic Twisting Cytometry vs Optical Tweezers. *Journal of Biomechanical Engineering*, *124*(4), 408–421. https://doi.org/10.1115/1.1485285

Laurent, V. M., Kasas, S., Yersin, A., Schäffer, T. E., Catsicas, S., Dietler, G., … Meister, J. J. (2005). Gradient of rigidity in the lamellipodia of migrating cells revealed by atomic force microscopy. *Biophysical Journal*, *89*(1), 667–675. https://doi.org/10.1529/biophysj.104.052316

Lawand, M., Déchanet-Merville, J., & Dieu-Nosjean, M. C. (2017). Key features of gamma-delta T-cell subsets in human diseases and their immunotherapeutic implications. *Frontiers in Immunology*, *8*, 761. https://doi.org/10.3389/fimmu.2017.00761

Lee, C.-Y., Herant, M., & Heinrich, V. (2011). Target-specific mechanics of phagocytosis: protrusive neutrophil response to zymosan differs from the uptake of antibody-tagged pathogens. *Journal of Cell Science*, *124*(7), 1106–1114. https://doi.org/10.1242/jcs.078592

Lee, C.-Y., Thompson, G. R., Hastey, C. J., Hodge, G. C., Lunetta, J. M., Pappagianis, D., & Heinrich, V. (2015). Coccidioides endospores and spherules draw strong chemotactic, adhesive, and phagocytic responses by individual human neutrophils. *PLoS ONE*, *10*(6), e0129522. https://doi.org/10.1371/journal.pone.0129522

Lever, M., Lim, H.-S., Kruger, P., Nguyen, J., Trendel, N., Abu-Shah, E., … Dushek, O. (2016). Architecture of a minimal signaling pathway explains the T-cell response to a 1 million-fold variation in antigen affinity and dose. *Proceedings of the National Academy of Sciences*, *113*(43), E6630–E6638. https://doi.org/10.1073/pnas.1608820113

Lever, M., Maini, P. K., Van Der Merwe, P. A., & Dushek, O. (2014). Phenotypic models of T cell activation. *Nature Reviews Immunology*, *14*(9), 619–629. https://doi.org/10.1038/nri3728

Li, M., Dang, D., Liu, L., Xi, N., & Wang, Y. (2017). Atomic force microscopy in characterizing cell mechanics for biomedical applications: A review. *IEEE Transactions on Nanobioscience*, *16*(6), 523–540. https://doi.org/10.1109/TNB.2017.2714462

Lieber, A. D., Yehudai-Resheff, S., Barnhart, E. L., Theriot, J. A., & Keren, K. (2013). Membrane tension in rapidly moving cells is determined by cytoskeletal forces. *Current Biology*, *23*(15), 1409–1417. https://doi.org/10.1016/j.cub.2013.05.063

Lin, W., Fan, Z., Suo, Y., Deng, Y., Zhang, M., Wang, J., … Chu, Y. (2015). The bullseye synapse formed between CD4+ T-cell and staphylococcal enterotoxin B-pulsed dendritic cell is a suppressive synapse in T-cell response. *Immunology and Cell Biology*, *93*(1), 99–110. https://doi.org/10.1038/icb.2014.76

Liu, Y., Blanchfield, L., Ma, V. P., Andargachew, R., Galior, K., Liu, Z., … Salaita, K. (2016). DNA-based nanoparticle tension sensors reveal that T-cell receptors transmit defined pN forces to their antigens for enhanced fidelity. *Proceedings of the National Academy of Sciences*, *113*(20), 5610–5615. https://doi.org/10.1073/pnas.1600163113

Liu, Y., Yehl, K., Narui, Y., & Salaita, K. (2013). Tension Sensing Nanoparticles for Mechano-imaging at the Living Non-living Interface. *Journal of American Chemical Society*, *135*(14), 5320–5323. https://doi.org/10.1021/ja401494e

Lowery, J., Kuczmarski, E. R., Herrmann, H., & Goldman, R. D. (2015). Intermediate filaments play a pivotal role in regulating cell architecture and function. *Journal of Biological Chemistry*, *290*(28), 17145–17153. https://doi.org/10.1074/jbc.R115.640359

Malissen, B., & Bongrand, P. (2015). Early T Cell Activation: Integrating Biochemical, Structural, and Biophysical Cues. *Annual Review of Immunology*, *33*(1), 539–561. https://doi.org/10.1146/annurev-immunol-032414-112158

Marklein, R. A., Lam, J., Guvendiren, M., Sung, K. E., & Bauer, S. R. (2018). Functionally-Relevant Morphological Profiling: A Tool to Assess Cellular Heterogeneity. *Trends in Biotechnology*, *36*(1), 105–118. https://doi.org/10.1016/j.tibtech.2017.10.007

Martín-Cófreces, N. B., & Sánchez-Madrid, F. (2018). Sailing to and docking at the immune synapse: Role of tubulin dynamics and molecular motors. *Frontiers in Immunology*, *9*, 1174. https://doi.org/10.3389/fimmu.2018.01174

Martin, M., Veloso, A., Wu, J., Katrukha, E. A., & Akhmanova, A. (2018). Control of endothelial cell polarity and sprouting angiogenesis by noncentrosomal microtubules. *ELife*, *7*, e33864. https://doi.org/10.7554/eLife.33864

McKeithan, T. W. (1995). Kinetic proofreading in T-cell receptor signal transduction. *Proceedings of the National Academy of Sciences*, *92*(11), 5042–5046. https://doi.org/10.1073/pnas.92.11.5042

Mendes, N. F., Tolnai, M. E., Silveira, N. P., Gilbertsen, R. B., & Metzgar, R. S. (1973). Technical aspects of the rosette tests used to detect human complement receptor (B) and sheep erythrocyte-binding (T) lymphocytes. *Journal of Immunology*, *111*(3), 860–867. Retrieved from http://www.jimmunol.org/content/111/3/860

Mitrossilis, D., Fouchard, J., Pereira, D., Postic, F., Richert, A., Saint-Jean, M., & Asnacios, A. (2010). Real-time single-cell response to stiffness. *Proceedings of the National Academy of Sciences*, *107*(38), 16518–16523. https://doi.org/10.1073/pnas.1007940107

Monks, C. R., Freiberg, B. A., Kupfer, H., Sciaky, N., & Kupfer, A. (1998). Three-dimensional segregation of supramolecular activation clusters in T cells. *Nature*, *395*(6697), 82–86. https://doi.org/10.1038/25764

Moogk, D., Natarajan, A., & Krogsgaard, M. (2018). T cell receptor signal transduction: affinity, force and conformational change. *Current Opinion in Chemical Engineering*, *19*, 43–50. https://doi.org/10.1016/j.coche.2017.12.007

Moreau, H. D., Lemaître, F., Terriac, E., Azar, G., Piel, M., Lennon-Dumenil, A. M., & Bousso, P. (2012). Dynamic in situ cytometry uncovers T cell receptor signaling during immunological synapses and kinapses in vivo. *Immunity*, *37*(2), 351–363. https://doi.org/10.1016/j.immuni.2012.05.014

Mosmann, T. R., Cherwinski, H., Bond, M. W., Giedlin, M. A., & Coffman, R. L. (1986). Two types of murine helper T cell clone. I. Definition according to profiles of lymphokine activities and secreted proteins. *Journal of Immunology*, *136*(7), 2348–2357. Retrieved from http://www.jimmunol.org/content/136/7/2348

Murugesan, S., Hong, J., Yi, J., Li, D., Beach, J. R., Shao, L., … Hammer, J. A. (2016). Formin-generated actomyosin arcs propel t cell receptor microcluster movement at the immune synapse. *Journal of Cell Biology*, *215*(3), 383–399. https://doi.org/10.1083/jcb.201603080

Nolen, B. J., Tomasevic, N., Russell, A., Pierce, D. W., Jia, Z., McCormick, C. D., … Pollard, T. D. (2009). Characterization of two classes of small molecule inhibitors of Arp2/3 complex. *Nature*, *460*(7258), 1031–1034. https://doi.org/10.1038/nature08231

Norcross, M. A. (1984). A synaptic basis for T-lymphocyte activation. *Annales d'Immunologie*, *135*(2), 113–134. Retrieved from https://www.ncbi.nlm.nih.gov/pmc/articles/PMC2551763/

Notarangelo, L. D. (2014). Immunodeficiency and immune dysregulation associated with proximal defects of T cell receptor signaling. *Current Opinion in Immunology*, *31*, 97–101. https://doi.org/10.1016/j.coi.2014.10.003

O'Connor, R. S., Hao, X., Shen, K., Bashour, K., Akimova, T., Hancock, W. W., … Milone, M. C. (2012). Substrate Rigidity Regulates Human T Cell Activation and Proliferation. *The Journal of Immunology*, *189*(3), 1330–1339. https://doi.org/10.4049/jimmunol.1102757

Ortega-Carrion, A., & Vicente-Manzanares, M. (2016). Concerning immune synapses: a spatiotemporal timeline. *F1000Research*, *5*, 418. https://doi.org/10.12688/f1000research.7796.1

Ospina Stella, A., & Turville, S. (2018). All-round manipulation of the actin cytoskeleton by HIV. *Viruses*, *10*(2), 63. https://doi.org/10.3390/v10020063

Ounkomol, C., Xie, H., Dayton, P. A., & Heinrich, V. (2009). Versatile horizontal force probe for mechanical tests on pipette-held cells, particles, and membrane capsules. *Biophysical Journal*, *96*(3), 1218–1231. https://doi.org/10.1016/j.bpj.2008.10.047

Paul, W. E., & Seder, R. A. (1994). Lymphocyte responses and cytokines. *Cell*, *76*(2), 241–251. https://doi.org/10.1016/0092-8674(94)90332-8

Ponjavic, A., McColl, J., Carr, A. R., Santos, A. M., Kulenkampff, K., Lippert, A., … Lee,

S. F. (2018). Single-Molecule Light-Sheet Imaging of Suspended T Cells. *Biophysical Journal*, *114*(9), 2200–2211. https://doi.org/10.1016/j.bpj.2018.02.044

Reinherz, E. L., Kung, P. C., Goldstein, G., & Schlossman, S. F. (1979a). A monoclonal antibody with selective reactivity with functionally mature human thymocytes and all peripheral human T cells. *Journal of Immunology*, *123*(3), 1312–1317. Retrieved from http://www.jimmunol.org/content/123/3/1312

Reinherz, E. L., Kung, P. C., Goldstein, G., & Schlossman, S. F. (1979b). Separation of functional subsets of human T cells by a monoclonal antibody. *Proceedings of the National Academy of Sciences*, *76*(8), 4061–4065. https://doi.org/10.1073/PNAS.76.8.4061

Remmerbach, T. W., Wottawah, F., Dietrich, J., Lincoln, B., Wittekind, C., & Guck, J. (2009). Oral cancer diagnosis by mechanical phenotyping. *Cancer Research*, *69*(5), 1728–1732. https://doi.org/10.1158/0008-5472.CAN-08-4073

Ritter, A. T., Asano, Y., Stinchcombe, J. C., Dieckmann, N. M. G., Chen, B. C., Gawden-Bone, C., … Griffiths, G. M. (2015). Actin Depletion Initiates Events Leading to Granule Secretion at the Immunological Synapse. *Immunity*, *42*(5), 864–876. https://doi.org/10.1016/j.immuni.2015.04.013

Rivers, E., & Thrasher, A. J. (2017). Wiskott-Aldrich syndrome protein: Emerging mechanisms in immunity. *European Journal of Immunology*, *47*(11), 1857–1866. https://doi.org/10.1002/eji.201646715

Rizvi, S. A., Neidt, E. M., Cui, J., Feiger, Z., Skau, C. T., Margaret, L., … Kovar, D. R. (2009). Identification and Characterization of a Small Molecule Inhibitor of Formin-Mediated Actin Assembly. *Chemical Biology*, *16*(11), 1158–1168. https://doi.org/10.1016/j.chembiol.2009.10.006

Robertson, M. (1986). T-cell receptor: gamma gene product surfaces. *Nature*, *322*, 110–111. https://doi.org/10.1038/324227a0

Roca-Cusachs, P., Conte, V., & Trepat, X. (2017). Quantifying forces in cell biology. *Nature Cell Biology*, *19*(7), 742–751. https://doi.org/10.1038/ncb3564

Rosenbluth, M. J., Lam, W. A., & Fletcher, D. A. (2006). Force microscopy of nonadherent cells: A comparison of leukemia cell deformability. *Biophysical Journal*, *90*(8), 2994–3003. https://doi.org/10.1529/biophysj.105.067496

Rotsch, C., Braet, F., Wisse, E., & Radmacher, M. (1997). AFM imaging and elasticity measurements on living rat liver macrophages. *Cell Biology International*, *21*(11), 685–696. https://doi.org/10.1006/cbir.1997.0213

Roybal, K. T., Buck, T. E., Ruan, X., Cho, B. H., Clark, D. J., Ambler, R., … Murphy, R. F. (2016). Computational spatiotemporal analysis identifies WAVE2 and cofilin as joint regulators of costimulation-mediated T cell actin dynamics. *Science Signaling*, *9*(424), rs3. https://doi.org/10.1126/scisignal.aad4149

Sadelain, M., Brentjens, R., & Rivière, I. (2009). The promise and potential pitfalls of chimeric antigen receptors. *Current Opinion in Immunology*, *21*(2), 215–223. https://doi.org/10.1016/j.coi.2009.02.009

Saitakis, M., Dogniaux, S., Goudot, C., Bufi, N., Asnacios, S., Maurin, M., … Hivroz, C. (2017). Different TCR-induced T lymphocyte responses are potentiated by stiffness with variable sensitivity. *ELife*, *6*, e23190. https://doi.org/10.7554/eLife.23190

Saitoh, M., Ishikawa, T., Matsushima, S., Naka, M., & Hidaka, H. (1987). Selective inhibition of catalytic activity of smooth muscle myosin light chain kinase. *The Journal of Biological Chemistry*, *262*(16), 7796–7801. Retrieved from http://www.jbc.org/content/262/16/7796.long

Sakamoto, T., Limouze, J., Combs, C. A., Straight, A. F., & Sellers, J. R. (2005). Blebbistatin, a myosin II inhibitor, is photoinactivated by blue light. *Biochemistry*, *44*(2), 584–588. https://doi.org/10.1021/bi0483357

Sakata, D., Taniguchi, H., Yasuda, S., Adachi-Morishima, A., Hamazaki, Y., Nakayama, R., … Narumiya, S. (2007). Impaired T lymphocyte trafficking in mice deficient in an actin-nucleating protein, mDia1. *The Journal of Experimental Medicine*, *204*(9), 2031–2038. https://doi.org/10.1084/jem.20062647

Salter, A. I., Pont, M. J., & Riddell, S. R. (2018). Chimeric antigen receptor modified T cells : CD19 and the road beyond. *Blood*, *131*(24), 2621–2629. https://doi.org/10.1182/blood-2018-01-785840

Sawicka, A., Babataheri, A., Dogniaux, S., Barakat, A. I., Gonzalez-Rodriguez, D., Hivroz, C., & Husson, J. (2017). Micropipette force probe to quantify single-cell force generation: application to T-cell activation. *Molecular Biology of the Cell*, *28*(23), 3229–3239. https://doi.org/10.1091/mbc.E17-06-0385

Schönichen, A., & Geyer, M. (2010). Fifteen formins for an actin filament: A molecular view on the regulation of human formins. *Biochimica et Biophysica Acta - Molecular Cell Research*, *1803*(2), 152–163. https://doi.org/10.1016/j.bbamcr.2010.01.014

Shamir, M., Bar-On, Y., Phillips, R., & Milo, R. (2016). SnapShot: Timescales in Cell Biology. *Cell*, *164*(6), 1302. https://doi.org/10.1016/j.cell.2016.02.058

Shortland, A. J., Kirk, S., Eremin, K., Degryse, P., & Walton, M. (2018). The Analysis of Late Bronze Age Glass from Nuzi and the Question of the Origin of Glass-Making. *Archaeometry*, *60*(4), 764–783. https://doi.org/10.1111/arcm.12332

Southern, E. M. (1975). Detection of specific sequences among DNA fragments separated by gel electrophoresis. *Journal of Molecular Biology*, *98*(3), 503–517. https://doi.org/10.1016/S0022-2836(75)80083-0

Tajik, A., Zhang, Y., Wei, F., Sun, J., Jia, Q., Zhou, W., … Wang, N. (2016). Transcription upregulation via force-induced direct stretching of chromatin. *Nature Materials*, *15*(12), 1287–1296. https://doi.org/10.1038/nmat4729

Tan, J. L., Tien, J., Pirone, D. M., Gray, D. S., Bhadriraju, K., & Chen, C. S. (2003). Cells lying on a bed of microneedles: An approach to isolate mechanical force. *Proceedings of the National Academy of Sciences*, *100*(4), 1484–1489. https://doi.org/10.1109/TDEI.2009.5211872

Taylor, M. J., Husain, K., Gartner, Z. J., Mayor, S., & Vale, R. D. (2017). A DNA-Based T Cell Receptor Reveals a Role for Receptor Clustering in Ligand Discrimination. *Cell*, *169*, 108–119. https://doi.org/10.1016/j.cell.2017.03.006

Thoumine, O., & Ott, A. (1997). Time scale dependent viscoelastic and contractile regimes in fibroblasts probed by microplate manipulation. *Journal of Cell Science*, *110*, 2109–2116. Retrieved from http://jcs.biologists.org/content/110/17/2109

Toepfner, N., Herold, C., Otto, O., Rosendahl, P., Jacobi, A., Kräter, M., … Guck, J. (2018). Detection of human disease conditions by single-cell morpho-rheological phenotyping of blood. *ELife*, *7*, e29213. https://doi.org/10.7554/eLife.29213

Tse, H. T. K., Gossett, D. R., Moon, Y. S., Masaeli, M., Sohsman, M., Ying, Y., … Di Carlo, D. (2013). Quantitative diagnosis of malignant pleural effusions by single-cell mechanophenotyping. *Science Translational Medicine*, *5*(212), 212ra163. https://doi.org/10.1126/scitranslmed.3006559

Ueda, H., Morphew, M. K., McIntosh, J. R., & Davis, M. M. (2011). CD4+ T-cell synapses involve multiple distinct stages. *Proceedings of the National Academy of Sciences*, *108*(41), 17099–17104. https://doi.org/10.1073/pnas.1113703108

Valberg, P. A., & Feldman, H. A. (1987). Magnetic particle motions within living cells. Measurement of cytoplasmic viscosity and motile activity. *Biophysical Journal*, *52*(4), 551–561. https://doi.org/10.1016/S0006-3495(87)83244-7

Valitutti, S., Dessing, M., Aktories, K., Gallati, H., & Lanzavecchia, A. (1995). Sustained

Signaling Leading to T Cell Activation Results from Prolonged T Cell Receptor Occupancy. Role of T Cell Actin Cytoskeleton. *Journal of Experimental Medicine, 181*(2), 577–584. https://doi.org/10.1084/jem.181.2.577

Wan, Y. Y., & Flavell, R. A. (2009). How Diverse — CD 4 Effector T Cells and their Functions. *Journal of Molecular Cell Biology, 1*(1), 20–36. https://doi.org/10.1093/jmcb/mjp001

Wang, H., Wei, B., Bismuth, G., & Rudd, C. E. (2009). SLP-76-ADAP adaptor module regulates LFA-1 mediated costimulation and T cell motility. *Proceedings of the National Academy of Sciences*, *106*(30), 12436–12441. https://doi.org/10.1073/pnas.0900510106

Wang, X., & Ha, T. (2013). Defining single molecular forces required to activate integrin and Notch signaling. *Science, 340*(6135), 991–994. https://doi.org/10.1126/science.1231041

Wu, P.-H., Aroush, D. R.-B., Asnacios, A., Chen, W.-C., Dokukin, M. E., Doss, B. L., … Wirtz, D. (2018). A comparison of methods to assess cell mechanical properties. *Nature Methods*, *15*, 491–498. https://doi.org/10.1038/s41592-018-0015-1

Wülfing, C., & Davis, M. M. (1998). A Receptor / Cytoskeletal Movement Triggered by Costimulation During T Cell Activation. *Science*, *282*(5397), 2266–2269. https://doi.org/10.1126/science.282.5397.2266

Yamada, S., Wirtz, D., & Kuo, S. C. (2000). Mechanics of living cells measured by laser tracking microrheology. *Biophysical Journal*, *78*(4), 1736–1747. https://doi.org/10.1016/S0006-3495(00)76725-7

Zhu, J., & Paul, W. E. (2008). CD4 T cells: fates, functions, and faults. *Blood, 112*(5), 1557–1569. https://doi.org/10.1182/blood-2008-05-078154

# Table of contents

# List of figures

# List of tables

# Supplement 6: Published paper

The publication (Sawicka et al., 2017), published in the journal Molecular Biology of the Cell by the American Society for Cell Biology, is reproduced here under the Attribution–Noncommercial–Share Alike 3.0 Unported Creative Commons License (CC-BY-NC-SA). See details at http://creativecommons.org/licenses/by-nc-sa/3.0

MBoC | ARTICLE

# Micropipette force probe to quantify single-cell force generation: application to T-cell activation

**Anna Sawicka[a,b], Avin Babataheri[a], Stéphanie Dogniaux[b], Abdul I. Barakat[a], David Gonzalez-Rodriguez[c], Claire Hivroz[b,*], and Julien Husson[a,*]**
[a]Laboratoire d'Hydrodynamique (LadHyX), Department of Mechanics, Ecole polytechnique-CNRS UMR7646, 91128 Palaiseau, France; [b]Institut Curie Section Recherche, INSERM U932 and PSL Research University, 75005 Paris, France; [c]LCP-A2MC, Institut Jean Barriol, Université de Lorraine, 57078 Metz, France

**ABSTRACT In response to engagement of surface molecules, cells generate active forces that regulate many cellular processes. Developing tools that permit gathering mechanical and morphological information on these forces is of the utmost importance. Here we describe a new technique, the micropipette force probe, that uses a micropipette as a flexible cantilever that can aspirate at its tip a bead that is coated with molecules of interest and is brought in contact with the cell. This technique simultaneously allows tracking the resulting changes in cell morphology and mechanics as well as measuring the forces generated by the cell. To illustrate the power of this technique, we applied it to the study of human primary T lymphocytes (T-cells). It allowed the fine monitoring of pushing and pulling forces generated by T-cells in response to various activating antibodies and bending stiffness of the micropipette. We further dissected the sequence of mechanical and morphological events occurring during T-cell activation to model force generation and to reveal heterogeneity in the cell population studied. We also report the first measurement of the changes in Young's modulus of T-cells during their activation, showing that T-cells stiffen within the first minutes of the activation process.**

**Monitoring Editor**
Manuel Théry
CEA, Hopital Saint Louis

Received: Jun 19, 2017
Revised: Sep 8, 2017
Accepted: Sep 12, 2017

## INTRODUCTION

In a variety of biological functions such as adhesion (Liu *et al.*, 2015), migration (Sheetz, 1994; Plotnikov and Waterman, 2013), mechanotransduction (Ingber, 1997), probing of the mechanical environment (Schaefer and Hordijk, 2015), or communication between cells (Basu and Huse, 2017) receptor-ligand binding triggers cells to generate forces. Understanding the interplay between biochemical and mechanical signals requires methods capable of quantification of forces in different biochemical and cellular environments.

To measure and characterize forces generated by cells, several techniques have been applied. They can be distinguished mostly by the type of force probe they use. Atomic force microscopy (AFM) uses a flexible cantilever coated with molecules of interest to measure forces exerted by cells attached to a flat surface (Pelling *et al.*, 2007; Ossola *et al.*, 2015; Rigato *et al.*, 2017). In traction force microscopy (Dembo and Wang, 1999; Hui *et al.*, 2015; Hui and Upadhyaya, 2017), flexible substrates with embedded fluorescent beads or flexible micropillars are deformed by the cells plated on them. DNA tension probes use a ligand immobilized to a surface through a DNA tether that is unfolded when a sufficient force is applied by the cell, leading to a change in fluorescence signal (Wang and Ha, 2013; Liu *et al.*, 2016). Last, the biomembrane force probe (BFP) uses a red blood cell to which molecules of interest are bound via an attached coated bead (Simson *et al.*, 1998; Merkel *et al.*, 1999; Pincet and Husson, 2005; Heinrich and Ounkomol, 2007; Gourier *et al.*, 2008; Husson *et al.*, 2011; Sun *et al.*, 2011; Šmít *et al.*, 2017).

Micropipettes are most often used to probe by aspiration the passive mechanical properties of cells (Evans and Kukan, 1984; Sato *et al.*, 1987; Needham and Hochmuth, 1992; Shao and Hochmuth, 1996; Sit *et al.*, 1997; Hochmuth, 2000; Spillmann *et al.*, 2004; Hogan *et al.*, 2015) or their dynamical response on controlled stimulation (Evans *et al.*, 1993; Herant *et al.*, 2005, 2006; Lee *et al.*, 2015). We herein describe the micropipette force probe (MFP) that uses a flexible micropipette directly as the force probe. It allows spanning a large range of probe stiffness with micropipettes of different geometry. Holding the cell and its target allows us to dynamically

---

*Address correspondence to: Claire Hivroz (claire.hivroz@curie.fr), Julien Husson (julien.husson@ladhyx.polytechnique.fr).

Abbreviations used: AFM, atomic force microscopy; BFP, biomembrane force probe; MFP, micropipette force probe.

Supplemental Material can be found at:
http://www.molbiolcell.org/content/suppl/2017/09/18/mbc.E17-06-0385v1.DC1

follow the morphological and mechanical properties of the triggered cells while measuring the forces generated. We illustrate the advantages of MFP by applying it to the study of T-cell activation, following our previous studies in the field (Husson *et al.*, 2011; Guillou *et al.*, 2016b; Hivroz and Saitakis, 2016; Saitakis *et al.*, 2017) We provide new insights into this process of pivotal importance in the adaptive immune response.

## RESULTS

### Micropipette force probe

***Concept/principle.*** The principle of the micropipette force probe is to use a glass micropipette as a cantilever of known bending stiffness to measure forces generated by a single cell. The use of a micropipette instead of a filled microfiber or lamella (Meyhöfer and Howard, 1995; Tees *et al.*, 2001; Marcy *et al.*, 2004; Guillou *et al.*, 2016a) allows us to form a force probe tailored to the particular experiment, with a bead covered with antibodies of interest aspirated at the tip of the micropipette (called the bead micropipette herein). Then, a cell held by a second, rigid micropipette (called the cell micropipette herein) is brought in contact with the bead, and the response of the cell to the bead is recorded. Of practical importance, once the response of the cell is finished, both bead and cell can be released from their respective micropipettes, and another bead and cell can be selected within a couple of minutes to perform another experiment. The technique thus allows testing tens of different bead-cell couples with a single set of micropipettes, minimizing uncertainty due to micropipette variability. Moreover, the technique allows using virtually any kind of bead: commercially available or custom made with any chemical coupling (Husson *et al.*, 2011). Experiments are performed on an inverted microscope with two micropositioners holding and moving both micropipettes, the tips of which lie in the focal plane of the microscope where both cell and bead are observed (Figure 1, A and B). During a standard experiment, the contact between a cell and the bead micropipette is ensured by compressing the cell against the bead (Figure 1B, top, and Supplemental Video 1). The base of the bead micropipette remains immobile, so any movement of the bead is due to the forces generated by the cell (pushing or pulling on the bead, Figure 1B, bottom).

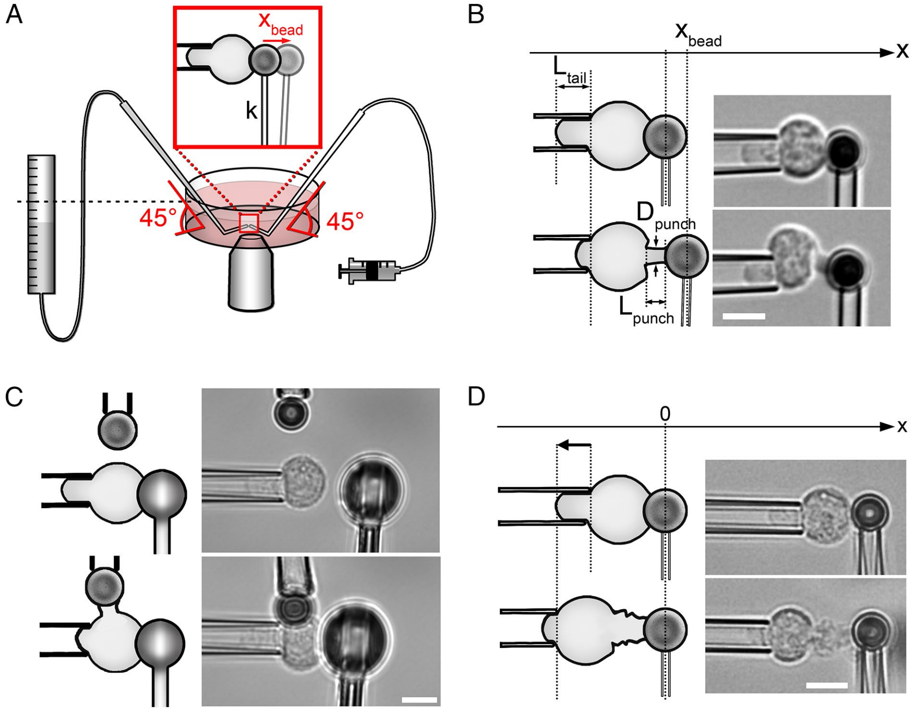

FIGURE 1: Micropipette setups used in the experiments. (A) Micropipette force probe: overview. The tip of a flexible micropipette holding an activating bead (bead micropipette) is positioned close to the tip of a stiff micropipette holding a cell (cell micropipette). Both micropipettes have a 45° bend, so their tips are in the focal plane of the inverted microscope. During the experiment, the bending of the bead micropipette shows as the displacement of the bead along the *x*-axis ($x_{bead}$, see B). The aspiration pressure in the cell micropipette is controlled by the height of a water reservoir. The aspiration pressure in the bead micropipette is controlled with a syringe filled with air. (B) Micropipette force probe: geometrical measurements. Drawings of an activated T-cell (left) with corresponding brightfield microscopy images (right). Top: the cell is brought in contact with the bead at time $t = 0$. Bottom: the cell pushes the bead away during activation. The position $x_{bead}$ of the center of the bead along the *x*-axis is tracked over time, leading to speed and force measurement. The dimensions of the pushing protrusion called a punch (length $L_{punch}$ and diameter $D_{punch}$) and the part of the cell inside the micropipette called a tail (length $L_{tail}$) are measured manually only at the selected frames of the recording. (C) Profile microindentation of a cell during its activation. Drawings (left) and corresponding brightfield images (right). A microindenter replaces the bead micropipette; the bead is held by a third, stiff micropipette. During the experiment, the cell is indented once every 10 s, each indentation providing a measurement of the Young's modulus, describing the effective stiffness of the cell. After measuring the Young's modulus baseline value for several cycles (top), the bead is brought in contact with the cell; the indentations continue during the activation (bottom, see Figure 2D). (D) Activation of a cell with no resisting bead micropipette. Drawings (left) and corresponding brightfield images (right). A cell is brought in contact with a bead, and when the punch starts growing from the cell, the cell micropipette is retracted to keep the bead micropipette at its initial position, simulating the cell pushing against a bead micropipette of zero bending stiffness. (B–D) Scale bar is 5 μm.

***Range of application and limitations.*** The measured force is proportional to the bead micropipette's tip displacement in the microscopy image. To achieve a measurable displacement, the bending stiffness of the bead micropipette needs to be adapted to the range of forces exerted by the cell. With different shapes of bead micropipettes, a wide range of bending stiffness can be attained: from 0.01 to >100 nN/μm. This range is wider than for existing force probes: optical tweezers have a typical stiffness in the 0.01–0.5 nN/μm range, and AFM cantilevers are usually stiffer than 10 nN/μm. In practice, when studying T-cells as demonstrated in this paper, we used a typical bending stiffness ranging from 0.15 to 1.10 nN/μm. Our detection accuracy is better than 0.05 μm, leading to a resolution in force from 0.008–0.06 nN depending on the bending stiffness of the bead micropipette. Here we apply the technique to nonadherent blood cells, but it can also be applied to adherent cells grown on a large bead substrate such as dextran beads, as already shown for endothelial cells (Guillou *et al.*, 2016a). The technique also allows monitoring cell morphology seen from profile during the force measurements.

We detect displacement of the bead micropipette by live analysis of camera images, with a limited time resolution (typically 400 Hz, see *Materials and Methods*) as opposed to superior time resolution of laser diodes used in AFM. The bead micropipettes have a several-millimeter-long, flexible shaft subjected to several sources of vibrations. The softer the micropipette, the larger the vibration amplitude. The major source of vibrations is a free medium-air interface in an open Petri dish in which the experiments are performed. These vibrations can be controlled with an experimental chamber made of glass slides holding a liquid droplet by capillarity (Pincet and Husson, 2005; Gourier *et al.*, 2008) (Supplemental Figure S1). Since the use of the chamber makes experiments less easy to implement, we used open Petri dishes for all experiments reported in this paper. Vibrations can also come from vibrating devices such as the fan of the camera cooling system. Altogether, these vibrations limit the accuracy of force and displacement measurement. The bead micropipette, while firmly holding the bead, does not form a perfectly tight joint with it and can thus aspirate small pieces of cell membrane. Once such aspiration is clearly visible, we stop the measurements for this cell, although aspiration of micron-size parts of the cell membrane does not appear to affect the cell behavior. These cell debris, however, might block the bead micropipette, precluding its further use.

***Comparison with the biomembrane force probe.*** We previously studied the mechanics of T-cell activation using a BFP (Husson *et al.*, 2011). This device uses a red blood cell as a spring of calibrated stiffness ranging from ~0.05 to ~0.5 nN/µm (Simson *et al.*, 1998; Merkel *et al.*, 1999; Pincet and Husson, 2005; Heinrich and Ounkomol, 2007; Gourier *et al.*, 2008; Sun *et al.*, 2011; Šmít *et al.*, 2017). The range of stiffness is similar to the one used with the MFP, but the measurements with the BFP are limited to pulling forces and to displacements smaller than ~0.3 µm. The MFP was designed to overcome these two important limitations of the BFP. With MFP we are able to measure pushing forces over larger displacements (more than 2 µm). On the practical side, we wanted to use any kind of bead size and coverage and reuse the same probe (bead micropipette) with several cells in a row. We validated that results obtained with the MFP and BFP were consistent by measuring the pulling forces generated by human primary CD4+ T-cells (Supplemental Figure S2).

## Application to T-cell activation

There is growing interest in the forces generated by T-cells, because these forces are involved in formation of the immune synapse and T-cell activation (reviewed in Depoil and Dustin [2014], Comrie and Burkhardt [2016], Hivroz and Saitakis [2016]). Using the BFP, we were among the first to show that human T-cells exert forces when their T-cell receptor (TCR) is engaged (Husson *et al.*, 2011).

To further study these forces, we applied the MFP technique to the events occurring during the first 5 to 10 min after TCR/CD3 triggering (the first events during T-cell activation). We used human primary CD4+ T-cells (called resting T-cells herein, see *Materials and Methods*) and beads covered with anti-CD3 antibodies. An experiment with the MFP started by bringing the cell in contact with the bead, thus inducing a slight compression of the cell (compressive force up to 0.15 nN, see $x_{contact}$ in Figure 2A). We defined the time origin as the instant when this compression was applied, and we measured other times parameters described below relative to this initial contact time.

***Pushing forces.*** The first measurable mechanical event during T-cell activation was the appearance of a pushing protrusion that we call a punch. The punch pushed the bead away at a speed $v_{push}$ that was constant to a first approximation (Figure 2A). The punch appeared, and the pushing force started, at instant $t_{push} = 31$ s (median, interquartile range [IQR]: 22–42 s, $N = 112$ cells across 14 experiments) with resting T-cells and anti-CD3/anti-CD28 beads. This

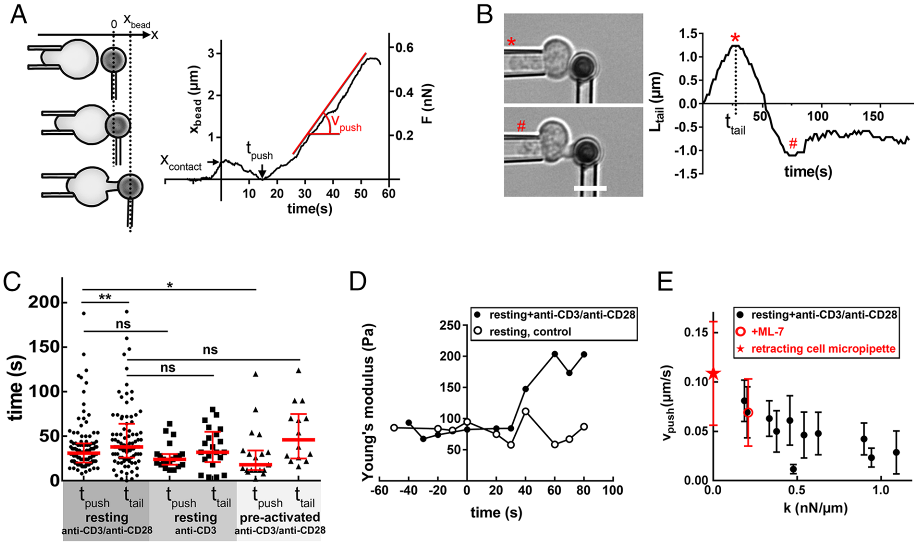

**FIGURE 2:** First events during T-cell activation. (A) Onset of pushing force. Drawings of a T-cell during the beginning of the activation process (left) with the corresponding position of the bead $x_{bead}$ (right). At the beginning of the experiment, the bead was located at $x_{bead} = 0$ (top drawing); at time $t = 0$ contact was made between the cell and the bead (middle drawing), leading to a small displacement of the bead ($x_{contact}$). The cell then reorganized and started growing a protrusion (called a punch, bottom drawing) at time $t_{push}$ and with a speed $v_{push}$. (B) Measurement of tail length. Brightfield images of a T-cell during activation (left), with the corresponding length of the part of the cell that is aspirated in the cell micropipette, $L_{tail}$ (see Figure 1B). At time $t = t_{tail}$, the tail started retracting inside the cell micropipette (red star). In this example, the retraction lasted ~40 s and stopped at t~70s (red #). Scale bar is 5 µm. (C) Comparison of timings. Two time points, $t_{push}$ and $t_{tail}$, were measured from contact to the onset of mechanical changes (see A and B), and for activation of human primary CD4+ T-cells (resting) with anti-CD3/anti-CD28 beads, or only anti-CD3 beads, and for human CD4+ T lymphoblasts (preactivated) with anti-CD3/anti-CD28 beads. Each data point represents one cell, red thick line shows median, whiskers span the interquartile range. $*p = 0.02$, $**p = 0.04$, two-tailed Mann-Whitney test. (D) Increase in the Young's modulus of a T-cell (in its effective stiffness). Full circles: example showing the Young's modulus of a resting T-cell during its activation measured with profile microindentations (see Figure 1C). Open circles: a control resting T-cell indented with no activating bead. (E) Pushing speed $v_{push}$ depends on the bending stiffness of the bead micropipette $k$. Full circles: MFP experiments with various bending stiffness of the bead micropipette. Red star: experiment where the cell micropipette was retracted during punch growth in order to simulate zero bending stiffness (see Figure 1D). Open red circle: resting T-cells treated with 30 µM ML-7 (inhibitor of myosin light chain kinase). Each data point shows mean ± SD over one experimental day (the same bead micropipette), representing 4–13 cells ($N = 9 \pm 3$ cells, mean ± SD).

$t_{push}$ was similar for resting T-cells activated with beads covered with only anti-CD3 antibodies ($t_{push}$ = 24 s median, IQR: 18–30 s, $N = 20$ cells across two experiments). On reactivation of T-cells the $t_{push}$ was shorter, as shown for the CD4+ T lymphoblasts (called preactivated herein) with anti-CD3/anti-CD28 beads ($t_{push}$ = 18 s median, IQR: 12–33 s, $N = 19$ cells across two experiments) (Figure 2C). The punch grew initially at an approximately right angle from the cell body (Supplemental Video 1), which we confirmed by scanning electron microscopy (Supplemental Figure S3A). No punch formed when we put resting T-cells in contact with beads covered with anti-CD45 antibodies (Supplemental Video 2), showing that the pushing force required TCR/CD3 engagement.

***Tail retraction.*** The cell was partly aspirated in the cell micropipette due to an aspiration pressure of typically 80 Pa that was kept constant throughout the experiment. We called the part of the cell inside the micropipette the tail and measured its length, $L_{tail}$ (Figure 1B). A shortening of the tail indicates an increase in cell tension, which is itself directly linked to the effective Young's modulus, or effective stiffness, of the cell that we can directly quantify using profile microindentation (Guillou *et al.*, 2016a,b). During T-cell activation, we observed a shortening of the tail (Figure 2B) beginning at instant $t_{tail}$ = 38 s (median, IQR: 27–61 s, $N = 103$ cells across 14 experiments). The time at which the tail begins to retract is similar for resting CD4+ T-cells activated with anti-CD3 beads. The measured $t_{tail}$ is also similar for resting and preactivated CD4+ T-cells in contact with anti-CD3/anti-CD28 beads (Figure 2C). To directly quantify changes in cell tension related to these changes in tail length, we performed profile microindentations (Guillou *et al.*, 2016a) during the activation of resting T-cells (Figure 1C). The effective Young's modulus of T-cells increased from 128 ± 16 to 292 ± 44 Pa (mean ± SEM, time points $t = -10$ and 70 s, $N = 15$ and 9 cells, respectively, across two experiments, Figure 2D). This increase began 30–40 s after the contact (Figure 2D), consistent with the measured time of retraction, $t_{tail}$. Although pushing and tail retraction began within a narrow time window (Figure 2C), for the majority of resting T-cells activated with anti-CD3/anti-CD28 beads pushing preceded tail retraction ($t_{push} < t_{tail}$ for 76 cells, $t_{push} > t_{tail}$ for 26 cells, across 14 experiments).

***Cell forces and speeds depend on bending stiffness of the bead micropipette.*** In a previous study, we showed that T-cells could adapt their pulling forces to the stiffness of the substrate against which they develop these forces (Husson *et al.*, 2011). The MFP allowed us to investigate the dependence of both pushing and pulling forces on the stiffness of the substrate. We found that for each cell the pushing speed, hence the loading rate $dF/dt = kv$, were relatively constant over time (Figure 2A) but depended on the bending stiffness of the bead micropipette (Figure 2E). We then wanted to measure the growth speed of the punch when no resisting force was applied (approximating $k = 0$). We first attempted to do so by releasing the bead from the bead micropipette right after the contact was established. In this case a punch grew but quickly either became very curved or grew out of the focal plane, so we could not quantify its growth speed. We therefore used the approach shown in Figure 1D, in which a cell was brought in contact with the bead, and when the punch started growing from the cell, the cell micropipette was manually retracted to keep the bead micropipette at its initial position. This allowed us to observe the punch growing against no notable resisting force, which simulates a bead micropipette with a vanishing bending stiffness. Hence, we measured a data point that would correspond to $k = 0$ in Figure 2E (red star). Consistent with the trend of growth speed diminishing with increasing bending stiffness $k$, this growing speed at $k = 0$ was the largest.

***Buckling and end of punch growth.*** After 10 s (median, IQR: 8–18 s, $N = 79$ cells across 14 experiments) of pushing at a constant speed, the punch suddenly stopped growing and stalled for 2 s (median, IQR: 1–4 s, $N = 36$ cells across six experiments), as can be seen on the $x_{bead}(t)$ chart (inset at the top in Figure 3A). The punch then usually resumed its growth but in another direction and with a broader shape (Supplemental Video 1 and Supplemental Figure S4). In most of the cases, this stalling corresponded to a kink appearing close to the middle of the punch (arrow in Supplemental Video 1). We called this event buckling. The force measured at this moment, $F_{buckling}$, in the range of 0.15–0.30 nN, depended on the bending stiffness of the bead micropipette, $k$ (Figure 3B). The mathematical shape of this dependence was consistent with the theory of mechanical buckling: the critical force $F_{buckling}$ to induce buckling of an elastic beam of elastic modulus $E$, moment of inertia $I$, and length $L$ is given by Euler's formula as follows:

$$F_{buckling} = \frac{\pi^2 EI}{L^2} \tag{1}$$

The compressive force exerted on the punch by the probe is $F = kL$, where $k$ is the bending stiffness of the bead micropipette. Therefore, the expected dependence of the buckling force on bending stiffness of the bead micropipette is

$$F_{buckling} = k^{2/3}\left(\pi^2 EI\right)^{1/3} \tag{2}$$

Figure 3B shows a comparison between force predicted by Eq. 2 and the $F_{buckling}$ measured for different values of bending stiffness of the bead micropipette. To yield the predictions shown in Figure 3B, Eq. 2 was applied for $E = 130$ Pa (mean value measured by profile microindentations, see above under *Tail retraction*), the punch was assumed to be a cylinder with a moment of inertia $I = \pi D^4/64$, and the punch diameter $D$ was adjusted to fit the experimental data, leading to $D = 1.3$ µm, slightly smaller than the measured final diameter of 1.9 µm (see below). The fact that Euler's formula correctly described the observed dependence between force and bending stiffness of the bead micropipette supported our hypothesis that the observed warping of the punch corresponds to mechanical buckling.

After buckling, the punch usually resumed its growth, with similar pushing speed (0.086 ± 0.025 µm/s vs. 0.098 ± 0.029 µm/s, mean ± SD, $N = 21$ cells across five experiments, $p = 0.05$, two-tailed paired $t$ test; see Supplemental Figure S5) but a different morphology. For larger bending stiffness of the bead micropipette (above 0.35 nN/µm) the punch did not regrow after buckling, it buckled only at its maximal length. On average, the punch reached a maximal length of 2.0 ± 0.7 µm (mean ± SD, $N = 106$ cells across 14 experiments) with a diameter of 1.9 ± 0.5 µm (mean ± SD, $N = 105$ cells across 14 experiments, Figure 3D), that is, roughly half the diameter of the 4.5-µm-wide bead. At this point, the cell generated a maximal pushing force, $F_{push}^{max}$, up to 0.8 nN. This force also depended on the bending stiffness of the bead micropipette (Figure 3B). The maximal pushing forces were similar in amplitude when resting T-cells were activated with anti-CD3/anti-CD28 beads and with anti-CD3 beads. Pushing forces were also similar for resting and preactivated CD4+ T-cells activated with anti-CD3/anti-CD28 beads (Figure 3B). Treatment with ML-7, the myosin light chain kinase inhibitor, led to longer punches (Figure 3D, ML-7: 2.35 ± 0.12 µm, $N = 17$ cells across three experiments, control: 1.97 ± 0.07 µm, $N = 106$ cells across 14 experiments), but to the

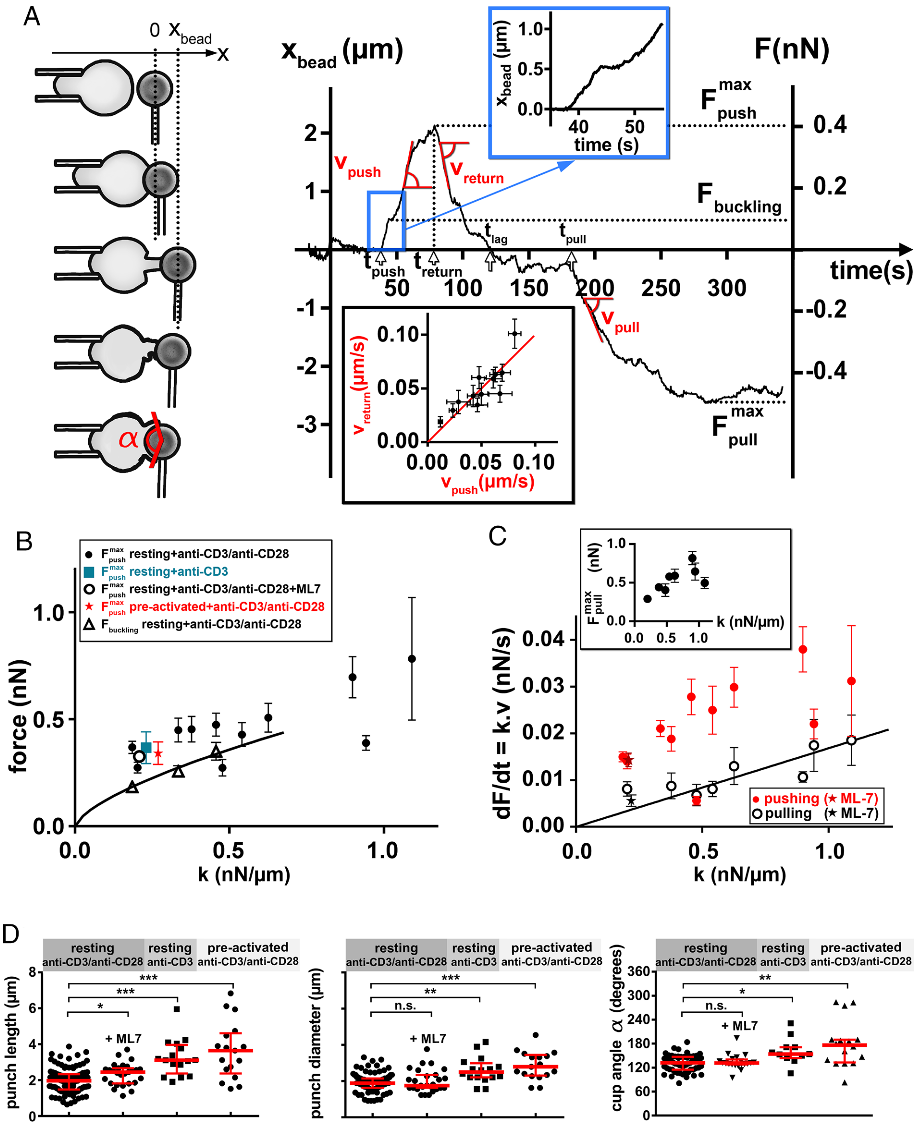

**FIGURE 3:** Sequence of mechanical early events during T-cell activation. (A) Drawings of a T-cell (left) and time trace of the bead position, $x_{bead}$, and force, $F$, in the first minutes of T-cell activation (right). Inset at bottom: return speed $v_{return}$ vs. pushing speed $v_{push}$. The line is a linear regression, with a slope of 1.0. Inset on top: magnification of the stalling of the bead when the punch buckled. (B) Maximal pushing force and buckling force. The continuous line corresponds to the buckling force of an elastic beam (see the text). Each data point shows mean ± SEM over one experimental day, representing 5–14 cells ($N = 9 \pm 3$, mean ± SD). (C) Loading rate $dF/dt$ (force in absolute value) during pushing (full circles) or pulling (open circles) vs. bending stiffness of the bead micropipette $k$. The line corresponds to a linear fit of the pulling loading rate (see the text). Each data point shows mean ± SEM over one experimental day, representing 3–10 cells ($N = 7 \pm 2$, mean ± SD). Inset: maximal pulling force $F_{pull}^{max}$ vs. bending stiffness of the bead micropipette $k$. (D) Dimensions of the pushing protrusion (punch, left and middle) and the pulling protrusion (cup, right). The punch length and diameter were measured when the punch was the longest (see Figure 1B), and the cup coverage angle on the bead, $\alpha$, was measured as soon as the cup was formed (see the bottom drawing in A). $*p < 0.05$, $**p < 0.01$, $***p < 0.001$ two-tailed unpaired $t$ test with Welch's correction.

same maximal pushing force (Figure 3C, see below for further observations with ML-7).

***Collapse of the punch and formation of a cup.*** Once the punch had reached its maximal length, it gradually became broader while collapsing at a constant speed, $v_{return}$ (Figure 3A) and then formed a cuplike structure on the bead (called a cup herein; Supplemental Video 1). Some cells did not form the cup but kept on pushing instead, growing and collapsing several punches in a row. These cells did not reach the further stages described below. During the collapse of the punch, the bead moved backward to its initial position (Figure 3A). Even though the punch underwent a large morphological change, for a given cell and bending stiffness of the bead micropipette, the return speed and pushing speed had the same absolute value (Figure 3A, inset at bottom). Interestingly, ML-7 treatment did not change the pushing speed (Figure 3C showing pushing and pulling loading rate). However, it reduced both the return speed (ML-7: $v_{return} = 0.044 \pm 0.006$ μm/s, $N = 21$ cells across three experiments, at $k = 0.208$ nN/μm as averaged over $k = 0.189$–$0.218$ nN/μm, control: $v_{return} = 0.085 \pm 0.009$ μm/s, mean ± SEM, $N = 25$ cells across four experiments, at $k = 0.195$ nN/μm as averaged over $k = 0.146$–$0.202$ nN/μm) and the pulling speed (ML-7: $v_{pull} = 0.021 \pm 0.004$ μm/s, $N = 10$ cells across three experiments, control: $v_{pull} = 0.042 \pm 0.006$ μm/s, mean ± SEM, $N = 11$ cells across three experiments).

The cup contacted the bead with a larger area than the punch. The cup reached a covering angle $\alpha = 121 \pm 21°$ (mean ± SD, $N = 27$ cells across six experiments, cup angle $\alpha$ defined in Figure 3A), with the rim of the cup sometimes reaching the tip of the bead micropipette (Supplemental Video 1). To check whether this perturbed the normal spreading of the cup, we used a different bead micropipette shape, with a 90° bend at the tip. This way, the bead was aspirated at the intersection with the $x$-axis, further away from the cell than in the standard situation, leaving more space for eventual cup spreading (Supplemental Figure S6). In this configuration, the measured cup angle was $140 \pm 17°$ (mean ± SD, $N = 30$ cells across four experiments), showing that the cell spreading on the bead was not strongly perturbed by the tip of the bead micropipette. Preactivated T-cells visibly spread more on the bead (Supplemental Video 3) than resting T-cells; in that case, the measured cup angle reached $179 \pm 58°$ (mean ± SD $N = 18$ cells across two experiments, Figure 3D).

***Lag phase.*** After the punch collapsed and the cup formed as described above, the cell entered what we called a lag phase. During this phase, the cell exerted no large forces on the bead, which stayed close to its initial position ($x_{bead} = 0$). However, the cell remained active as shown by its morphology: waves and/or ruffles formed on the cell surface and traveled seemingly from the cup toward the tail (Supplemental Video 1). The lag phase lasted for 51 s (median, IQR: 16–76 s, $N = 56$ cells across 14 experiments, measured as $\Delta t_{lag} = t_{pull} - t_{lag}$, Figure 3A) and ended with the onset of a pulling force exerted by the cell on the bead at $t_{\text{pull}}$ = 148 s (median, IQR: 104–226 s, $N$ = 63 cells across 14 experiments).

***Pulling phase.*** As when T-cells pushed, they pulled the bead at a relatively constant speed, $v_{\text{pull}}$, or a constant loading rate $dF/dt = kv_{\text{pull}}$, that depended on the bending stiffness of the bead micropipette $k$. For the same bending stiffness of the bead micropipette, the pulling loading rate was roughly twice smaller in absolute value than the pushing loading rate (Figure 3C). Maximal pulling forces reached 0.8 nN in magnitude (Figure 3C, inset), comparable to maximal pushing force.

We investigated whether the pulling phase dynamics could be described by a recent model by Etienne *et al.* (2015), which was developed to characterize contractile forces of different cell types (rat embryonic fibroblasts and the mouse myogenic cell line) adhering to two opposite glass lamella. Etienne *et al*. proposed a minimal model, accounting for cell viscoelasticity, actomyosin contractility, and actin treadmilling, to explain the dependence of pulling forces on the stiffness of the substrate against which cells develop forces. In this model, at the early times of pulling, when the pulling force is significantly below its maximum, the rate of force increase over time is described by

$$\frac{dF}{dt} = \begin{cases} kv_c & \text{if } k < k_{\text{crit}} \\ \dfrac{\sigma_a S}{\tau_\alpha} & \text{otherwise} \end{cases} \tag{3}$$

Here $k$ is the stiffness of the substrate, $v_c$ is the typical actomyosin contractile velocity, $\sigma_a$ is the maximum active contractile tension that can be developed, $S$ is the cross-section of the cup (contact area between the cell and the substrate), and $\tau_\alpha$ is the typical time for actomyosin stress relaxation. According to Eq. 3, the pulling loading rate $dF/dt$ increases linearly with the stiffness of the substrate $k$, provided that $k$ remains small compared with the cell stiffness, $k_{\text{crit}} = ES/L_0$, where $E$ is the Young's modulus and $L_0$ is the maximal probe deformation allowed by the geometry of the experiment. Beyond $k = k_{\text{crit}}$, the probe would be more rigid than the cell, and the rate of pulling would become independent of the probe and limited by the rate of actomyosin relaxation. We applied the model to our experimental data on the dependence of $dF/dt$ on $k$ during the pulling phase, shown in Figure 3C. As predicted by the model, experiments in the range of bending stiffness of the bead micropipette studied here were satisfactorily described by a proportionality relation, represented by a straight line of slope $v_c$ = 0.017 µm/s (95% c.i. 0.013 ÷ 0.020 µm/s). This value is consistent with the $v_c$ = 0.025 µm/s deduced by Etienne *et al.* (2015) for experiments on mouse myoblasts. For myoblasts, Etienne *et al*. observed a second regime, corresponding to a constant rate of pulling force generation, in experiments with very stiff probes of $k > k_{\text{crit}} \approx 10$ nN/µm, which is beyond the range of bending stiffness explored here. The fact that this second regime was not attained in our experiments using bending stiffness of the bead micropipette up to 1 nN/µm implies that the final Young's modulus of the mature T-cell's cup is larger than 1 kPa. Overall, the ability of Etienne *et al*.'s model to describe our experimental results suggests that T-cell force generation during the pulling phase arises from biophysical mechanisms shared by other cell types.

***Identification of two different cell morphologies after pulling.*** At the end of the pulling phase, at $t_{\text{end}}$ = 202 s (median, IQR: 136–290 s, $N$ = 49 cells across eight experiments), we observed two different T-cell morphologies (Figure 4 and Supplemental Video 4). We called the first morphological type nepenthes, after the shape of the nepenthes flower, and the second one flytrap, by analogy, as it seemingly closed on the bead and rounded up around it. The flytrap cells usually extracted themselves from the cell micropipette within 5 min from contact (Supplemental Video 4). The nepenthes cells usually stayed in their micropipette, remained elongated, and showed extensive activity in the form of waves traveling along the cell body. Some flytrap cells showed some waves but not as clearly and over a shorter period of time than nepenthes cells. The tail of nepenthes cells regrew in the cell micropipette for 40% of nepenthes cells (12 of 30 nepenthes cells across eight experiments) and never for flytrap cells (23 flytrap cells across eight experiments). Nepenthes cells had a clear uropod morphology at the opposite side to the bead (Supplemental Video 5), whereas flytrap cells did not have any clear uropod. This different morphology could be clearly seen with SiR-actin, a fluorescent dye binding F-actin: it showed a crescent shape structure for flytrap cells and a pointlike uropod for nepenthes cells (Supplemental Figure S7 and Supplemental Video 6). With anti-CD3 beads, we observed both types (6 nepenthes cells and 9 flytrap cells across 22 cells in two experiments). Preactivated T-cells showed a

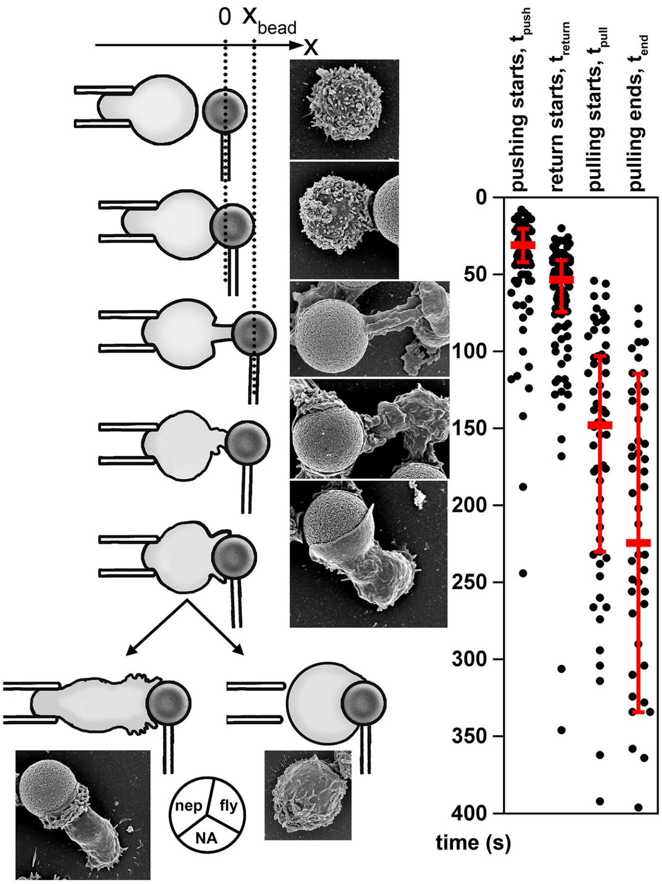

FIGURE 4: Morphology of T-cells during early stages of activation. Drawings of T-cells (left) with corresponding examples of cells imaged with scanning electron microscopy (right). The scanning electron microscopy images were cropped from larger fields of view, see Supplemental Figure S3B. Beads are 4.5 µm in diameter. The pie chart shows the proportion of the two morphological types in the population; nep, nepenthes, fly, flytrap, NA, not assigned ($N$ = 77 resting T-cells activated with anti-CD3/anti-CD28 beads in eight experiments). Timeline shows the different phases of the activation process (see chart in the Figure 3A) for resting T-cells activated with anti-CD3/anti-CD28 beads. Each dot is a single cell; red thick line shows the median; whiskers span the IQR.

clear tendency toward the flytrap type (20 cells, all flytrap cells in two experiments).

The assignment of a cell to the flytrap or nepenthes type was not possible in ~30% of cells in micropipette experiments (24 of 77 resting T-cells activated with anti-CD3/anti-CD28 beads in eight experiments, 7 of 22 resting T-cells activated with anti-CD3 beads in two experiments), usually when the cell was not well aligned with the bead at the contact or pushed itself out of the focal plane during the activation process. Images with no micropipettes (Supplemental Videos 5 and 6 and scanning electron microscopy images in Figure 4) showed that both phenotypes were not an artifact due to the micropipette setup. These two archetypal morphologies reveal a heterogeneity of behavior of resting CD4+ T-cells in the very early stages of activation.

## DISCUSSION

### MFP as a new technique for the measurement of forces generated by cells

Several micromanipulation techniques have been developed to measure forces actively generated by cells. Some are limited by the range of forces they can measure (e.g., optical tweezers, for forces lower than ~100 pN) and are thus best suited for single-molecule measurements or specific studies such as forces generated by single filopodia (Bornschlogl *et al.*, 2013). Single cells generate active forces ranging from tens of piconewtons to several nanonewtons. Relevant techniques to measure these forces rely mainly on the tracking of the deflection of a calibrated spring: AFM cantilevers (Binnig *et al.*, 1986; Puech, 2005), microfibers or glass lamella (Howard and Hudspeth, 1987; Ishijima *et al.*, 1996; Tees *et al.*, 2001; Marcy *et al.*, 2004; Desprat *et al.*, 2006; Tsukasaki *et al.*, 2007; Mitrossilis *et al.*, 2010), or flexible substrates or micropillars (Dembo and Wang, 1999; Hui *et al.*, 2015; Hui and Upadhyaya, 2017).

While micropipettes were often used to aspirate cells to probe their passive mechanical properties (Evans and Kukan, 1984; Sato *et al.*, 1987; Needham and Hochmuth, 1992; Shao and Hochmuth, 1996; Sit *et al.*, 1997; Hochmuth, 2000; Spillmann *et al.*, 2004; Hogan *et al.*, 2015) or their dynamical response on controlled stimulation (Evans *et al.*, 1993; Herant *et al.*, 2005, 2006; Lee *et al.*, 2015), they were seldom used as flexible cantilevers, as it was done for instance to measure adhesion (Colbert *et al.*, 2009). The MFP described here uses the micropipette as a flexible cantilever to measure forces generated by single cells. This study highlights the possibilities brought up by MFP. Thanks to the observation of the morphology of the cells during the force measurement, we describe in detail the various phases of force generation during T-cell activation. For instance, we identified the pushing protrusion, punch, thanks to the bead micropipette, which held the punch along a fixed axis during its growth. Without this support punch rapidly bent and was barely noticeable (Supplemental Video 5). Importantly, the simultaneous observation of cell morphology allows fine control of the cell-bead contact time, which is not possible when injecting beads and cells in a Petri dish. A modified version of AFM (lateral AFM [Ounkomol *et al.*, 2009]), allows sideways imaging while measuring forces, but the experiments with cells require replacing the AFM cantilever for every cell. This arguably becomes easier with MFP, as the bead micropipette can be reused multiple times.

The application of MFP to the study of T-cell activation led to measurements consistent with previous studies. Our measurements of human T-cells performed at the whole-cell (and nanonewton) level are highly complementary to recent measurements by Liu *et al.* using DNA tension probes (Liu *et al.*, 2016), who showed that around 40 s after mouse OT-1 resting T-cells came into contact with the activating surface, piconewton pulling forces were generated at the TCR. A more direct comparison to our MFP measurements is provided by the results of Hu and Butte (2016), who performed AFM measurements on mouse OT-1 preactivated T-cells (lymphoblasts). They measured similar pushing forces (0.1–1.2 nN) and somewhat larger (0.5–2.5 nN) pulling forces. This suggests that forces of the described magnitude and timing form integral part of the process of T-cell activation.

### New information on T-cell activation obtained with MFP

MFP was particularly useful for identifying and measuring the pushing forces developed by human T-cells on TCR/CD3 triggering. Like pulling forces, pushing forces were sensitive to bending stiffness of the bead micropipette. The maximal measured pushing force was ~0.4 nN, comparable to the force required to deform the glycocalyx, whose reported Young's modulus is 400–700 Pa (Bai and Wang, 2012; Marsh and Waugh, 2013). Thus, the pushing forces could serve to compress the glycocalyx covering the antigen-presenting cell (APC) and to form a stable contact between the T-cell and the APC. On the molecular level, the pushing forces are also probably needed to "push away" the bulky phosphatase CD45 that needs to be excluded from the TCR microclusters to allow signaling in T-cells (Varma *et al.*, 2006).

The model we propose to understand the observed buckling of the growing punch is compatible with the structure of the punch we described earlier (Husson *et al.*, 2011), a hollow tube of polymerized actin. Together with the reported minor role of myosin activity (see results obtained with ML-7), the observed buckling behavior may provide insight into the molecular mechanisms involved in the formation of this structure. The punch is also probably involved in the ability of T-cells to "palpate" their environment and, in particular, as shown herein, to sense its stiffness. This stiffness sensing is important since it leads to functional programming of the T-cells (Saitakis *et al.*, 2017). The development of forces perpendicular to the contact area is probably also important for T-cells to cross the endothelial barrier by the path of least resistance (Martinelli *et al.*, 2014).

Our results also show that the presence of the activating CD28 antibody together with the activating TCR/CD3 antibody altered the pushing forces developed by the resting T-cells by modifying the length and diameter of the growing punch. These data add to the reported effect of the engagement of CD28, which has been shown by traction force microscopy to increase the traction forces developed by human primary T-cells activated by TCR/CD3 (Bashour *et al.*, 2014). This is in agreement with the known effect of CD28 on actin remodeling (Wülfing, 1998). It would thus be particularly interesting to investigate the role of WAVE2 and cofilin, two regulators of CD28-induced actin dynamics (Roybal *et al.*, 2016), on the pushing forces reported herein.

The MFP experimental setup also allowed us to compare primary, resting, and preactivated effector T-cells in terms of their ability to develop forces. Our results reveal that preactivated T-cells, when their CD3 and CD28 receptors were triggered again, developed pushing forces earlier and grew a longer and broader punch (Figures 2C and 3D). This probably enables them to better probe their environment. Since forces were linked to the killing efficiency of mouse cytotoxic T-cells (Basu *et al.*, 2016), this may also explain the better efficiency of effector T-cells in killing their targets.

Finally, as the experiments with MFP are conducted in open Petri dishes, the technique is versatile and complementary experiments can be implemented, such as profile microindentation during activation (with a third micropipette added, Figure 1C). This way, we were able to measure the Young's modulus of T-cells during their activation and to show that they got stiffer when activated

(Figure 2D). This change in the mechanical properties means that the actomyosin cytoskeleton undergoes drastic modifications during T-cell activation. As a result, an extremely soft T-cell (80–100 Pa) (Bufi *et al.*, 2015; Guillou *et al.*, 2016b) becomes more rigid, which may well be sensed by the APC and participate in the cross-talk between the T-cell and the APC.

We applied the MFP technique to investigate the role of myosin in the development of both pushing and pulling forces by T-cells. Our results show that pushing speeds (and hence pushing loading rates) remain unchanged for resting T-cells treated with the myosin light chain kinase inhibitor ML-7 (Figure 3C). These data are in agreement with results obtained with AFM showing a relatively low effect of ML-7 on the pushing forces (Hu and Butte, 2016). They suggest that the pushing forces are essentially due to the actin polymerization. This is in agreement with reports showing that inhibition of the phosphorylation of the myosin light chain with the Rho kinase inhibitor Y-27632 or inhibition of the myosin II ATPase activity with blebbistatin does not alter actin retrograde flow at the immune synapse (Babich *et al.*, 2012; Ashdown *et al.*, 2017). In contrast, ML-7 treatment affects the punch length, which is longer (Figure 3D), and both the return and the pulling speeds, which are reduced, suggesting that myosin activity controls the shrinkage of the punch and the subsequent generation of pulling forces. These data are consistent with results obtained by traction force microscopy on Jurkat cells (Hui *et al.*, 2015; Hui and Upadhyaya, 2017) and by AFM on preactivated mouse T-cells (Hu and Butte, 2016), which both show that pulling forces developed by T-cells are affected by pharmacological inhibitors of myosin.

In the present study, we identified and characterized two different morphologies adopted by T-cells during their activation. The difference in nepenthes versus flytrap formation did not correlate with the naive versus memory phenotype of the T-cells (unpublished data). However, this difference of behavior may well be due to the presence of different T-cell subpopulations in the purified CD4+ T-cells used herein. Alternatively, the different phenotypes may also correlate with the difference between kinapse and synapse formation (Dustin, 2008). Indeed, waves of actin have been associated with a migratory phenotype (Inagaki and Katsuno, 2017), whereas phagocytic synapse (flytrap morphology) requires T-cell arrest (Niedergang *et al.*, 2016). It would also be interesting to investigate if these two archetypal phenotypes lead to different functional outcomes.

Our results show that the MFP is particularly well suited to the analysis of pushing and pulling forces that cells generate in response to various triggering signals and various stiffness of the substrate they contact. It can also be coupled to profile microindentation to provide in real time the measurement of changes in mechanical properties of cells and gather many dynamic morphological parameters. Together, these parameters reveal heterogeneity in the studied cell population and can be used to develop models explaining the forces generated at the cellular level in response to a given stimulus.

## MATERIALS AND METHODS

### Micropipette pulling and calibration

Micropipettes used to hold the cells (cell micropipettes) were prepared as described previously (Guillou *et al.*, 2016a): borosilicate glass capillaries (1 mm OD, 0.78 mm ID; Harvard Apparatus, Holliston, MA) were pulled with a P-97 micropipette puller (Sutter Instruments, Novato, CA). An MF-200 microforge (World Precision Instruments [WPI], Sarasota, FL) was used to cut the tip of pulled capillaries to the desired inner diameter (2.5–3.5 µm). The diameter was first assessed optically with calibrated graduations in the microforge's ocular and then measured under the inverted microscope with the 100× objective. The micropipettes were then bent at a 45° angle with an MF-900 microforge (Narishige, Tokyo, Japan) so their tip was in the microscope's focal plane (Figure 1A).

Flexible micropipettes used to hold the beads (bead micropipettes) were pulled with a thin tip whose geometry determines the bending stiffness of the bead micropipette, *k*. We first cut the tip of the micropipette to the desired length with a melted glass bead on the MF-200 microforge. We then either bent the tip at right angle for the face-to-face cell-bead presentation (Supplemental Figure S6) or left it straight, as used in most of the experiments (Figure 1). Last, we bent the micropipette at a 45° angle with the MF-900 microforge to place the tip in the focal plane, as with the cell micropipette.

Microindenters were prepared from the bead micropipettes, as described previously (Guillou *et al.*, 2016a,b) (see video in Guillou *et al.* [2016b]). In brief, the MF-200 microforge was used to melt glass at the tip of the micropipette, producing a glass bead of 5–10 µm in diameter. The diameter was then precisely determined under the microscope with the 100× objective.

The bending stiffness of microindenters and bead micropipettes was measured against standard microindenters that had been previously calibrated (Supplemental Figure S8). The standard microindenters were calibrated with a commercial force probe (model 406A with a force range of 0–500 nN; Aurora Scientific, Aurora, ON, Canada). The microindenters used in this paper had typically the rigidity of 0.5 nN/µm and the bead micropipettes in the range of 0.15–1.10 nN/µm.

### Beads and inhibitors

Dynabeads Human T-activator CD3/CD28, Dynabeads CD3, and Dynabeads CD45 (referred to as anti-CD3/anti-CD28, anti-CD3, and anti-CD45 beads, respectively) were purchased from Invitrogen Life Technologies (Carlsbad, CA). ML-7 was purchased from Merck Millipore (Billerica, MA) and suspended in dimethyl sulfoxide (DMSO) (Pan-Biotech, Aidenbach, Germany). Cells were preincubated with 30 µM ML-7 for 15 min and kept in the same concentration of the inhibitor throughout the experiment.

### Cell purification and culture

All cells used in this study were human cells. This study was conducted according to the Helsinki Declaration, with informed consent obtained from the blood donors, as requested by the Etablissement Français du Sang. The complete medium was RPMI 1640 with GlutaMax, supplemented with 10% heat-inactivated fetal bovine serum (FBS) and 1% penicillin-streptomycin (all from Life Technologies ThermoFisher Scientific, Waltham, MA). Human primary CD4+ T-cells were negatively selected from peripheral blood mononuclear cells isolated from the blood of healthy donors with the CD4+ T-cell isolation kit (Miltenyi Biotec, Bergisch Gladbach, Germany). Isolated T-cells were suspended in FBS:DMSO (90%:10% vol/vol) and kept frozen in liquid nitrogen. One to seven days before the experiment the cells were thawed, mixed with preheated complete medium, washed once, and then kept in the complete medium at 37°C, 5% $CO_2$, at a concentration of ~106 cells/ml.

To obtain CD4+ T lymphoblasts, six-well plastic plates were coated with anti-CD3 antibody (OKT3 clone, #16-0037-85; eBioscience, ThermoFisher Scientific; 2.5 µg/ml in 1.3 ml final) overnight at 4°C. Wells were washed, and $5.4 \times 10^6$ freshly purified human primary CD4+ T-cells were plated per well in the presence of soluble anti-CD28 antibody (LEAF Purified anti-human CD28 # BLE302923; Biolegend, San Diego, CA; 2.5 µg/ml) and recombinant IL-2 (Proleukin; Novartis, Basel, Switzerland; 20 U/ml). Fresh medium containing

IL-2 (20 U/ml) was added every 3 d, and lymphoblasts were used from day 6 or frozen on day 6 and thawed before the experiment, as described above.

### Western blot analysis of phosphorylation of the myosin light chain

Human primary CD4+ T-cells ($4 \times 10^6$/ml) were preincubated 15 min at 37°C with 30 μM ML-7 or in DMSO (vehicle 1/67, vol/vol). Cells were then activated by addition of anti-CD3/anti-CD28 beads at a ratio of one bead per cell. After described time (10 or 30 min), activation was stopped on ice by addition of cold PBS. After centrifugation, cells were lysed in Pierce radioimmunoprecipitation assay buffer (ThermoFisher Scientific) supplemented with 1× complete, Mini, EDTA-free Protease Inhibitor Cocktail Tablet (Roche, Basel, Switzerland) and Halt Phosphatase Inhibitor Cocktail (ThermoFisher Scientific). Postnuclear lysates were resolved by SDS–PAGE on Mini-PROTEAN TGX Precast Gels (Bio-Rad, Hercules, CA) and were transferred to membranes (Immunblot PVDF membranes; Bio-Rad) with the Trans-Blot turbo system (Bio-Rad). Membranes were blocked for 2 h in Tris-buffered saline (TBS), 5% bovine serum alumin (BSA), 0.05% Tween and incubated overnight at 4°C with primary antibodies diluted in TBS, 5% BSA, 0.05% Tween: anti-phospho-myosin light chain 2 (Thr18/Ser19) rabbit antibody (#3674; Cell Signaling Technology, Danvers, MA, 1/1000) and anti-gp96 rat antibody (9G10 monoclonal rat antibody; Abcam, Cambridge, UK, 0.5 μg/ml). After several washes in TBS, 0.05% Tween, membranes were incubated 1 h at room temperature with horseradish peroxidase–conjugated secondary antibodies (Jackson ImmunoResearch, West Grove, PA, 1/10 000) diluted in TBS, 5% BSA, 0.05% Tween. Membranes were then washed again, incubated for 5 min in Clarity Western ECL Blotting Substrates (Bio-Rad), and revealed with the ChemiDoc Touch Imaging system (Bio-Rad). Membranes are shown in Supplemental Figure S9.

### Optical microscopy

A glass-bottom Petri dish (Fluorodish; WPI) containing cells and activating beads was mounted on an inverted microscope (Nikon Eclipse Ti-U; Nikon Instruments, Tokyo, Japan) placed on an air table (Newport, Irvine, CA). The microscope was equipped with a 100× oil immersion, 1.3 NA objective (Nikon) for monitoring the experiments and lower magnification objectives (40×, 20×, 10×, and 4×; Nikon) for micropipette positioning. Images were acquired with an ORCA-Flash 4.0 complementary metal oxide semiconductor camera (Hamamatsu Photonics, Hamamatsu City, Japan) controlled with the MicroManager software (Edelstein *et al.*, 2014). The micropipettes were attached to two motorized micropositioners (Sensapex, Oulu, Finland). Beads were aspirated into the tip of the calibrated micropipette by capillarity forces with no aspiration pressure added. Cells were aspirated with 60–100 Pa of hydrostatic pressure applied with a water reservoir placed on a vertical linear slider (A1512DM-S1.5; Velmex, Bloomfield, NY). The experiments were conducted close to 37°C; the dish was heated with heating pads (RS Components, Corby, UK) attached to the microscope table and an objective heating ring (Okolab, Pozzuoli, NA, Italy). No $CO_2$ buffering was used; instead, we replaced every hour during the experiment the medium in the dish. Time-lapse recordings were started just before the cell was gently brought into contact with the bead.

### Micropositioning and detection

The bead was pushed or pulled by the cell along the *x*-axis. The position of the bead, $x_{bead}$, is the same as the position of the tip of the bead micropipette. To track it, we developed a custom Matlab (Mathworks, Natick, MA) code calling the Micromanager software. The gray levels along a line parallel to the *x*-axis intersecting the micropipette were retrieved at acquisition frequency of ~300–500 Hz (depending on the size of the acquisition window). The gray levels along this line were cross-correlated with the gray levels of a template line acquired at the beginning of each recording (a strategy already used by the authors; Laan *et al.*, 2008; Husson *et al.*, 2009). The position of the maximum of the cross-correlation function was locally fitted to a parabola and led to subpixellic precision of bead micropipette localization (one camera pixel represents 64 nm with the 100× objective). In addition, a whole image was saved every 2 s for the visualization of the activation process.

### Profile microindentation

Profile microindentation was performed as described previously (Guillou *et al.*, 2016a). Briefly, the setup consisted of a cell micropipette, a microindenter (see above in micropipette pulling), and a rigid bead micropipette coming at a right angle (Figure 1C). Microindentation algorithm used the same method as in Guillou *et al.* (2016a), except that the software part was now implemented in Matlab to control directly the MicroManager software and obtain a higher acquisition frequency.

### Scanning electron microscopy

For scanning electron microscopy, the primary CD4+ T-cells ($1.5 \times 10^5$ cells per slide) were plated on slides precoated with 0.02% poly-L-lysine and incubated for 20 min at room temperature. Then the anti-CD3/anti-CD28 beads were added, at a ratio of one bead per cell and incubated for 5 min at room temperature. The samples were then washed in phosphate buffer, pH 7.4 (PB), fixed overnight at 4°C in PB + 2% glutaraldehyde, and, finally, washed in PB. Samples were then dehydrated by passing through a graded series of ethanol solutions, then dried by the $CO_2$ critical-point method (CPD75 Quorum Technologies, Lewes, UK) and coated by sputtering with a 20- to 40-nm thin gold layer with a Scancoat Six (Edwards Vacuum, HHV, Crawley, UK). Acquisitions were performed with a GeminiSEM 500 microscope (Zeiss, Oberkochen, Germany).

### Data analysis

From all the cells recorded in the micropipette experiments, we excluded nonresponding cells, which did not show any activity after the contact with the bead, and cells dead during recording, which retract the tail very fast, visibly grow larger in diameter and show no activity afterward, presumably because they lose membrane integrity. Across all the experiments with anti-CD3/anti-CD28 and anti-CD3 beads we recorded 486 cells from 10 different donors, of which 84 cells were nonresponding, 26 cells were dead during recording, and 376, or 77% of all cells, were active and were analyzed.

Morphological parameters of cells during activation (the diameter and the length of the punch, cup angle) were measured manually in the microscopy images, with the ImageJ software (Schneider *et al.*, 2012). For all experiments the contact time, used as instant *t* = 0, was established in the image sequence. The onset of pushing and the onset of tail retraction were also marked in the images and were used to calculate the $t_{push}$ and $t_{tail}$ (Figure 2, A and B). The onset of pulling was established in the chart $x_{bead}(t)$ (as it is not associated with an abrupt change in cell morphology) and was used to determine $t_{pull}$. The lag time $\Delta t_{lag}$ was calculated as the $t_{pull}$ minus $t_{lag}$, which was also marked in the chart as the instant when $x_{bead}$ = 0 (Figure 3A). For force experiments, on the resulting $x_{bead}(t)$ charts we manually chose the beginning and the end of the pushing, return, and pulling phases and fitted a line for every slope. As the early experiments were performed with low sampling frequency ($x_{bead}$ noted only once every 2 s, in the full image), the high-sampling-frequency data were appropriately averaged to consistently fit the $v_{push}$ and $v_{return}$ for all experiments that are shown in Figures 2E and 3, B and C. Maximal pushing and pulling force was taken from the $x_{bead}(t)$ chart, as shown in the Figure 3A. Buckling force was also taken from the chart, and the step in the pushing slope was verified with the corresponding frame in the image sequence, to check whether it shows the described buckling morphology.

The profile microindentation experiments were analyzed as described previously (Guillou *et al.*, 2016a). Briefly, force–indentation curves were fitted with the Hertz model to obtain the effective Young's modulus of the cell, assuming the Poisson's ratio equal 0.5. As the indentations continued during activation of the T-cells, we discarded some experimental curves, for example, when the bead interfered with the moving microindenter or when the cell escaped from the cell micropipette.

### Statistics

We report median times for all the events because the distribution is usually skewed with a few outliers with a very long time (see the timeline in Figure 4). In the boxplots boxes span from the first to the third quartile, with median marked with a thicker line. In the timing scatter plot (Figure 2C), we did not show (for resting T-cells + anti-CD3/anti-CD28 beads) 1 $t_{push}$ and 2 $t_{tail}$ values larger than 200 s for clarity of the chart; in the plot in Figure 4 we also did not show five data points at times >400s. All these values were included in the median and IQR calculations shown in the text. The Mann-Whitney test was used for comparing data in Figure 2C. Unpaired *t* test with Welch's correction was used for comparing data in Figure 3D.

## ACKNOWLEDGMENTS

We thank Virginie Bazin (IBPS, Université Pierre et Marie Curie, Paris) for her help in obtaining scanning electron microscopy images. We acknowledge Caroline Frot, Antoine Garcia, Daniel Guy, Delphine L'Huillier, Sandrine Laguerre, Thérèse Lescuyer, Magali Tutou, and Do Chi Toai Vu, at LadHyX, for technical support. We also thank Morgan Huse and Audrey Le Floc'h for fruitful discussions and Pierre-Henri Puech for critical reading of the manuscript. This work has benefited from the financial support of the LabeX LaSIPS (ANR-10-LABX-0040-LaSIPS) managed by the French National Research Agency under the "Investissements d'avenir"program (ANR-11-IDEX-0003-02). This work was also supported by GEFLUC Paris-Ile-de-France funding, a CNRS PEPS funding, an endowment in cardiovascular cellular engineering from the AXA Research Fund, and funds from the DC-BiolLabex (ANR-10-IDEX-0001-02 PSL* and ANR-11-LABX-0043) and from the Fondation pour la Recherche Médicale (FRM DEQ20140329513). A.S. is supported by a PhD fellowship from ITMO Cancer and funds from the PhD Program Frontières du Vivant (FdV)–Cursus Bettencourt.

## REFERENCES

Ashdown GW, Burn GL, Williamson DJ, PandžićE, Peters R, Holden M, Ewers H, Shao L, Wiseman PW, Owen DM (2017). Live-cell super-resolution reveals F-actin and plasma membrane dynamics at the T cell synapse. Biophys J 112, 1703–1713.

Babich A, Li S, O'Connor RS, Milone MC, Freedman BD, Burkhardt JK (2012). F-actin polymerization and retrograde flow drive sustained PLC?1 signaling during T cell activation. J Cell Biol 197, 775–787.

Bai K, Wang W (2012). Spatio-temporal development of the endothelial glycocalyx layer and its mechanical property in vitro. J R Soc Interface 9, 2290–2298.

Bashour KT, Gondarenko A, Chen H, Shen K, Liu X, Huse M, Hone JC, Kam LC (2014). CD28 and CD3 have complementary roles in T-cell traction forces. Proc Natl Acad Sci USA 111, 2241–2246.

Basu R, Whitlock BM, Husson J, Le Floc'h A, Jin W, Oyler-Yaniv A, Dotiwala F, Giannone G, Hivroz C, Biais N, *et al.* (2016). Cytotoxic T cells use mechanical force to potentiate target cell killing. Cell 165, 100–110.

Basu R, Huse M (2017). Mechanical communication at the immunological synapse. Trends Cell Biol 27, 241–254.

Binnig G, Quate CF, Gerber C (1986). Atomic force microscope. Phys Rev Lett 56, 930–933.

Bornschlogl T, Romero S, Vestergaard CL, Joanny J-F, Van Nhieu GT, Bassereau P (2013). Filopodial retraction force is generated by cortical actin dynamics and controlled by reversible tethering at the tip. Proc Natl Acad Sci USA 110, 18928–18933.

Bufi N, Saitakis M, Dogniaux S, Buschinger O, Bohineust A, Richert A, Maurin M, Hivroz C, Asnacios A (2015). Human primary immune cells exhibit distinct mechanical properties that are modified by inflammation. Biophys J 108, 2181–2190.

Colbert M-J, Raegen AN, Fradin C, Dalnoki-Veress K (2009). Adhesion and membrane tension of single vesicles and living cells using a micropipette-based technique. Eur Phys J E Soft Matter 30, 117–121.

Comrie WA, Burkhardt JK (2016). Action and traction: cytoskeletal control of receptor triggering at the immunological synapse. Front Immunol 7, 1–25.

Dembo M, Wang YL (1999). Stresses at the cell-to-substrate interface during locomotion of fibroblasts. Biophys J 76, 2307–2316.

Depoil D, Dustin ML (2014). Force and affinity in ligand discrimination by the TCR. Trends Immunol 35, 597–603.

Desprat N, Guiroy A, Asnacios A (2006). Microplates-based rheometer for a single living cell. Rev Sci Instrum 77, 55111.

Dustin ML (2008). Hunter to gatherer and back: Immunological synapses and kinapses as variations on the theme of amoeboid locomotion. Annu Rev Cell Dev Biol 24, 577–596.

Edelstein AD, Tsuchida MA, Amodaj N, Pinkard H, Vale RD, Stuurman N (2014). Advanced methods of microscope control using μManager software. J Biol Methods 1, 10.

Étienne J, Fouchard J, Mitrossilis D, Bufi N, Durand-Smet P, Asnacios A (2015). Cells as liquid motors: mechanosensitivity emerges from collective dynamics of actomyosin cortex. Proc Natl Acad Sci USA 112, 2740–2745.

Evans E, Kukan B (1984). Passive material behavior of granulocytes based on large deformation and recovery after deformation tests. Blood 64, 1028–1035.

Evans E, Leung A, Zhelev D (1993). Synchrony of cell spreading and contraction force as phagocytes engulf large pathogens. J Cell Biol 122, 1295–1300.

Gourier C, Jegou A, Husson J, Pincet F (2008). A nanospring named erythrocyte. The biomembrane force probe. Cell Mol Bioeng 1, 263–275.

Guillou L, Babataheri A, Puech P-H, Barakat AI, Husson J (2016a). Dynamic monitoring of cell mechanical properties using profile microindentation. Sci Rep 6, 21529.

Guillou L, Babataheri A, Saitakis M, Bohineust A, Dogniaux S, Hivroz C, Barakat AI, Husson J (2016b). T lymphocyte passive deformation is controlled by unfolding of membrane surface reservoirs. Mol Biol Cell 27, 3574–3582.

Heinrich V, Ounkomol C (2007). Force versus axial deflection of pipette-aspirated closed membranes. Biophys J 93, 363–372.

Herant M, Heinrich V, Dembo M (2005). Mechanics of neutrophil phagocytosis: behavior of the cortical tension. J Cell Sci 118, 1789–1797.

Herant M, Heinrich V, Dembo M (2006). Mechanics of neutrophil phagocytosis: experiments and quantitative models. J Cell Sci 119, 1903–1913.

Hivroz C, Saitakis M (2016). Biophysical aspects of t lymphocyte activation at the immune synapse. Front Immunol 7, 1–12.

Hochmuth RM (2000). Micropipette aspiration of living cells. J Biomech 33, 15–22.

Hogan B, Babataheri A, Hwang Y, Barakat AI, Husson J (2015). Characterizing cell adhesion by using micropipette aspiration. Biophys J 109, 209–219.

Howard J, Hudspeth AJ (1987). Mechanical relaxation of the hair bundle mediates adaptation in mechanoelectrical transduction by the bullfrog's saccular hair cell. Proc Natl Acad Sci USA 84, 3064–3068.

Hu KH, Butte MJ (2016). T cell activation requires force generation. J Cell Biol 213, 535–542.

Hui KL, Balagopalan L, Samelson LE, Upadhyaya A (2015). Cytoskeletal forces during signaling activation in Jurkat T-cells. Mol Biol Cell 26, 685–695.

Hui KL, Upadhyaya A (2017). Dynamic microtubules regulate cellular contractility during T-cell activation. Proc Natl Acad Sci USA 114, E4175–E4183.

Husson J, Chemin K, Bohineust A, Hivroz C, Henry N (2011). Force generation upon T cell receptor engagement. PLoS One 6, e19680.

Husson J, Dogterom M, Pincet F (2009). Force spectroscopy of a single artificial biomolecule bond: the Kramers' high-barrier limit holds close to the critical force. J Chem Phys 130, 2–5.

Inagaki N, Katsuno H (2017). Actin waves: origin of cell polarization and migration? Trends Cell Biol 27, 515–526.

Ingber DE (1997). Tensegrity: the architectural basis of cellular mechanotransduction. Annu Rev Physiol 59, 575–599.

Ishijima A, Kojima H, Higuchi H, Harada Y, Funatsu T, Yanagida T (1996). Multiple- and single-molecule analysis of the actomyosin motor by nanometer-piconewton manipulation with a microneedle: unitary steps and forces. Biophys J 70, 383–400.

Laan L, Husson J, Munteanu EL, Kerssemakers JWJ, Dogterom M (2008). Force-generation and dynamic instability of microtubule bundles. Proc Natl Acad Sci USA 105, 8920–8925.

Lee CY, Thompson GR, Hastey CJ, Hodge GC, Lunetta JM, Pappagianis D, Heinrich V (2015). Coccidioides endospores and spherules draw strong chemotactic, adhesive, and phagocytic responses by individual human neutrophils. PLoS One 10, 1–28.

Liu B, Chen W, Zhu C (2015). Molecular force spectroscopy on cells. Annu Rev Phys Chem 66, 427–451.

Liu Y, Blanchfield L, Ma VP-Y, Andargachew R, Galior K, Liu Z, Evavold B, Salaita K (2016). DNA-based nanoparticle tension sensors reveal that T-cell receptors transmit defined pN forces to their antigens for enhanced fidelity. Proc Natl Acad Sci USA 113, 5610–5615.

Marcy Y, Prost J, Carlier M-F, Sykes C (2004). Forces generated during actin-based propulsion: a direct measurement by micromanipulation. Proc Natl Acad Sci USA 101, 5992–5997.

Marsh G, Waugh RE (2013). Quantifying the mechanical properties of the endothelial glycocalyx with atomic force microscopy. J Vis Exp 2013, e50163.

Martinelli R, Zeiger AS, Whitfield M, Sciuto TE, Dvorak A, Van Vliet KJ, Greenwood J, Carman CV (2014). Probing the biomechanical contribution of the endothelium to lymphocyte migration: diapedesis by the path of least resistance. J Cell Sci 127, 3720–3734.

Merkel R, Nassoy P, Leung A, Ritchie K, Evans E (1999). Energy landscapes of receptor-ligand bonds explored with dynamic force spectroscopy. Nature 397, 50–53.

Meyhöfer E, Howard J (1995). The force generated by a single kinesin molecule against an elastic load. Proc Natl Acad Sci USA 92, 574–578.

Mitrossilis D, Fouchard J, Pereira D, Postic F, Richert A, Saint-Jean M, Asnacios A (2010). Real-time single-cell response to stiffness. Proc Natl Acad Sci USA 107, 16518–16523.

Needham D, Hochmuth RM (1992). A sensitive measure of surface stress in the resting neutrophil. Biophys J 61, 1664–1670.

Niedergang F, Di Bartolo V, Alcover A (2016). Comparative anatomy of phagocytic and immunological synapses. Front Immunol 7, 1–9.

Ossola D, Amarouch MY, Behr P, Vörös J, Abriel H, Zambelli T (2015). Force-controlled patch clamp of beating cardiac cells. Nano Lett 15, 1743–1750.

Ounkomol C, Xie H, Dayton PA, Heinrich V (2009). Versatile horizontal force probe for mechanical tests on pipette-held cells, particles, and membrane capsules. Biophys J 96, 1218–1231.

Pelling AE, Veraitch FS, Pui-Kei Chu C, Nicholls BM, Hemsley AL, Mason C, Horton MA (2007). Mapping correlated membrane pulsations and fluctuations in human cells. J Mol Recognit 20, 467–475.

Pincet F, Husson J (2005). The solution to the streptavidin-biotin paradox: The influence of history on the strength of single molecular bonds. Biophys J 89, 4374–4381.

Plotnikov SV, Waterman CM (2013). Guiding cell migration by tugging. Curr Opin Cell Biol 25, 619–626.

Puech P-H (2005). Measuring cell adhesion forces of primary gastrulating cells from zebrafish using atomic force microscopy. J Cell Sci 118, 4199–4206.

Rigato A, Miyagi A, Scheuring S, Rico F (2017). High-frequency microrheology reveals cytoskeleton dynamics in living cells. Nat Phys 13, 771–775.

Roybal KT, Buck TE, Ruan X, Cho BH, Clark DJ, Ambler R, Tunbridge HM, Zhang J, Verkade P, Wulfing C, *et al.* (2016). Computational spatiotemporal analysis identifies WAVE2 and cofilin as joint regulators of costimulation-mediated T cell actin dynamics. Sci Signal 9, rs3.

Saitakis M, Dogniaux S, Goudot C, Bufi N, Asnacios S, Maurin M, Randriamampita C, Asnacios A, Hivroz C (2017). Different TCR-induced T lymphocyte responses are potentiated by stiffness with variable sensitivity. Elife 6, 1–29.

Sato M, Levesque MJ, Nerem RM (1987). Micropipette aspiration of cultured bovine aortic endothelial cells exposed to shear stress. Arterioscler Thromb Vasc Biol 7, 276–286.

Schaefer A, Hordijk PL (2015). Cell-stiffness-induced mechanosignaling - a key driver of leukocyte transendothelial migration. J Cell Sci 128, 2221–2230.

Schneider CA, Rasband WS, Eliceiri KW (2012). NIH Image to ImageJ: 25 years of image analysis. Nat Methods 9, 671–675.

Shao JY, Hochmuth RM (1996). Micropipette suction for measuring piconewton forces of adhesion and tether formation from neutrophil membranes. Biophys J 71, 2892–2901.

Sheetz MP (1994). Cell migration by graded attachment to substrate and contraction. Semin Cell Biol 5, 149–155.

Simson DA, Ziemann F, Strigl M, Merkel R (1998). Micropipet-based pico force transducer: in depth analysis and experimental verification. Biophys J 74, 2080–2088.

Sit P, Spector A, Lue A, Popel A, Brownell W (1997). Micropipette aspiration on the outer hair cell lateral wall. Biophys J 72, 2812–2819.

Šmít D, Fouquet C, Doulazmi M, Pincet F, Trembleau A, Zapotocky M (2017). BFPTool: a software tool for analysis of Biomembrane Force Probe experiments. BMC Biophys 10, 2.

Spillmann CM, Lomakina E, Waugh RE (2004). Neutrophil adhesive contact dependence on impingement force. Biophys J 87, 4237–4245.

Sun L, Cheng Q-H, Gao H, Zhang Y-W (2011). A nonlinear characteristic regime of biomembrane force probe. J Biomech 44, 662–668.

Tees DF, Waugh RE, Hammer DA (2001). A microcantilever device to assess the effect of force on the lifetime of selectin-carbohydrate bonds. Biophys J 80, 668–682.

Tsukasaki Y, Kitamura K, Shimizu K, Iwane AH, Takai Y, Yanagida T (2007). Role of multiple bonds between the single cell adhesion molecules, nectin and cadherin, revealed by high sensitive force measurements. J Mol Biol 367, 996–1006.

Varma R, Campi G, Yokosuka T, Saito T, Dustin ML (2006). T cell receptor-proximal signals are sustained in peripheral microclusters and terminated in the central supramolecular activation cluster. Immunity 25, 117–127.

Wang X, Ha T (2013). Defining single molecular forces required to activate integrin and notch signaling. Science 340, 991–994.

Wülfing C (1998). A receptor/cytoskeletal movement triggered by costimulation curing T cell activation. Science 282, 2266–2269.